From atomic-scale imaging to quantum fault-tolerance with spins in diamond

Abobeih, Mohamed

DOI
10.4233/uuid:cce8dbcb-cfc2-4fa2-b78b-99c803dee02d

Publication date
2021

Document Version
Final published version

Citation (APA)
Abobeih, M. (2021). *From atomic-scale imaging to quantum fault-tolerance with spins in diamond*. [Dissertation (TU Delft), Delft University of Technology]. https://doi.org/10.4233/uuid:cce8dbcb-cfc2-4fa2-b78b-99c803dee02d

FROM ATOMIC-SCALE IMAGING TO QUANTUM FAULT-TOLERANCE WITH SPINS IN DIAMOND

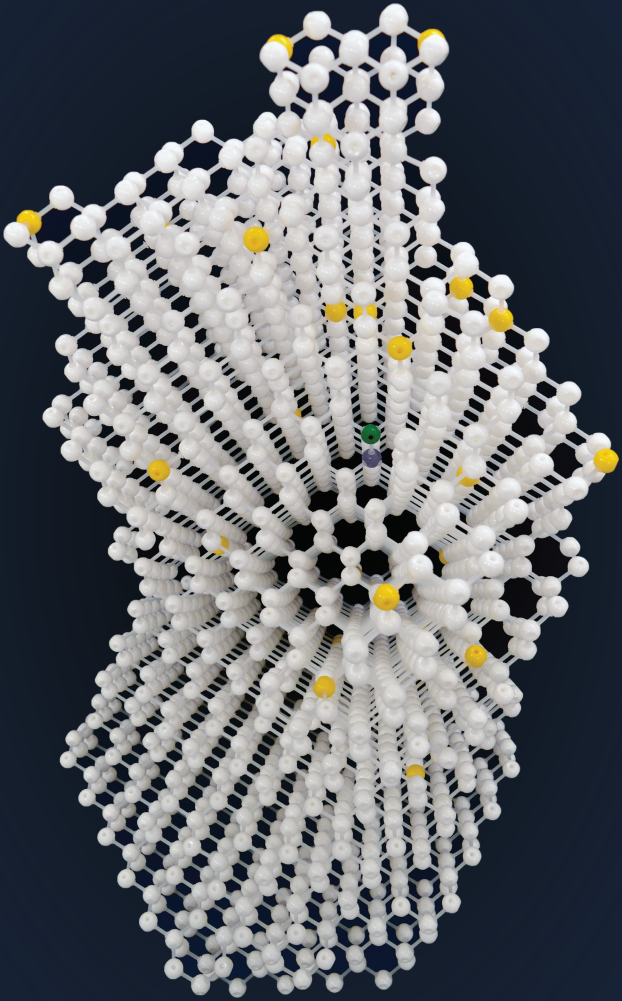

MOHAMED ABOBEIH

FROM ATOMIC-SCALE IMAGING TO QUANTUM FAULT-TOLERANCE WITH SPINS IN DIAMOND

Dissertation

for the purpose of obtaining the degree of doctor
at Delft University of Technology,
by the authority of the Rector Magnificus prof.dr.ir. T.H.J.J. van der Hagen,
Chair of the Board for Doctorates,
to be defended publicly on
Thursday 21 January 2021 at 15:00 o'clock

by

Mohamed ABOBEIH

Master of Science in Optics and Photonics,
Karlsruhe Institute of Technology, Karlsruhe, Germany,
born in Dakahliya, Egypt.

This dissertation has been approved by the promotor:
Prof. dr. ir. R. Hanson

Composition of the doctoral committee:

Rector Magnificus,	chairperson
Prof. dr. ir. R. Hanson	Delft University of Technology, promotor
Dr. ir. T.H. Taminiau	Delft University of Technology, copromotor
Independent members:	
Assoc. prof. C.L. Degen	ETH Zürich, Switzerland
Assoc. prof. S.J.J.M.F. Kokkelmans	Eindhoven University of Technology
Prof. dr. M. Plenio	Ulm University, Germany
Prof. dr. G.A. Steele	Delft University of Technology
Prof. dr. ir. L.M.K. Vandersypen	Delft University of Technology

Printed by: Gildeprint – Enschede

Cover design: Joe Randall, Lucy Matthes-Buck, Mohamed Abobeih

Casimir PhD Series, Delft-Leiden 2020-36

ISBN 978-90-8593-461-5

An electronic version of this dissertation is available at
`http://repository.tudelft.nl/`.

CONTENTS

SUMMARY

Owing to its exceptional spin properties and bright spin-photon interface, the nitrogen-vacancy (NV) center in diamond has emerged as a promising platform for quantum science and technology, including quantum communication, quantum computation and quantum sensing. In this thesis we develop novel methods for atomic-scale imaging and high-fidelity control of complex nuclear-spin systems coupled to the electron spin of an NV center in diamond. This well-controlled quantum system provides new opportunities in quantum sensing, quantum information processing, and may also form the building block of a large-scale quantum network, one of the key goals in quantum technology.

We first study and enhance the coherence properties of the NV electron spin. By using dynamical decoupling spectroscopy techniques, we probe and characterize the nuclear-spin environment of a single NV center. We find that this spin environment can be described by seven individual ^{13}C nuclear spins and six ^{13}C-^{13}C nuclear-spin pairs. We then utilize this knowledge to demonstrate a record-long coherence time of the NV center electron spin (> 1.5 seconds)—the longest coherence time for single electron spins in the solid state—by using tailored dynamical decoupling sequences that avoid unwanted interactions.

Following from these results, we develop novel control and multidimensional spectroscopy techniques, which isolate individual nuclear-nuclear spin interactions within this complex spin bath with high accuracy. With these methods we demonstrate atomic-scale magnetic resonance imaging of a cluster of 27 ^{13}C nuclear spins in diamond. This experiment provides a proof-of-principle towards the magnetic imaging of individual molecules or complex spin structures, one of the visionary goals in the field of quantum sensing.

Furthermore, we develop the NV center and this surrounding cluster of ^{13}C nuclear spins as a promising quantum register with exceptional coherence properties. We demonstrate a fully connected 10-qubit register with high-fidelity control, coherence times up to one minute, and genuine multipartite entanglement of up to 7 qubits. These results enable high-fidelity control of multi-qubit quantum registers.

Additionally, this developed quantum register is used to realize the smallest fault-tolerant logical qubit of a complete error correction code (the [[5,1,3]] code with an additional ‘flag’ qubit). We utilize multiple non-destructive parity measurements in addition to a flag ancilla measurement to demonstrate fault-tolerant encoding of the logical states. We measure a logical-state fidelity of 95(2)% for the fault-tolerant encoding compared to 81(2)% for the non-fault-tolerant encoding, thus demonstrating a significant improvement. Furthermore, we demonstrate fault-tolerant operations on the logical qubit by applying a set of transversal logical gates. These results present a key step towards fault-tolerant quantum computations.

Finally, we introduce ^{13}C-^{13}C nuclear-spin pairs as a novel intrinsically coherence-protected qubits with extraordinary coherence properties. We demonstrate high-fidelity control and single-shot readout ($> 98\%$) of these pairs using the NV center electron spin. We demonstrate an inhomogeneous dephasing time, $T_2^* = 1.9(3)$ minutes—the longest reported for an individually controlled qubit. Moreover, we demonstrate entanglement between two spin pairs through projective parity measurements. These new qubits have the potential to provide extremely robust quantum memories for quantum networks.

The work presented in this thesis advances the NV center and its surrounding nuclear-spin environment as a promising quantum system for quantum information processing, quantum simulations, and quantum sensing. The characterization and control methods developed here can likely be extended to other new defect systems. Therefore, when combined with fast progress in research groups around the world on, for example, developing photonic cavities, controlled surfaces, and fabrication methods, these results provide new opportunities for atomic-scale magnetic resonance imaging as well as large-scale quantum networks.

SAMENVATTING

Door zijn uitzonderlijke spin eigenschappen en spin-selectieve optische transities, is het stikstof-gat defect (nitrogen vacancy, NV) in diamant uitgegroeid tot een veelbelovend platform voor quantum technologie, waaronder quantum communicatie, quantum computatie en quantum sensoren. In dit proefschrift ontwikkelen we nieuwe methodes voor de beeldvorming op atomaire schaal en uitstekende controle van complexe kernspin systemen gekoppeld aan het elektron spin van een NV in diamant. Dit gecontroleerde quantum systeem biedt nieuwe mogelijkheden voor quantum sensoren, quantum informatica en zou ook als bouwsteen kunnen functioneren in grootschalige quantum netwerken.

Ten eerste bestuderen en verbeteren we de coherentie van het NV elektron spin. Door het gebruik van dynamische ontkoppelingstechnieken, onderzoeken en karakteriseren we de kernspin omgeving van een enkel NV. Hieruit concluderen we dat de omgeving goed kan worden beschreven door zeven individuele ^{13}C kernspins en zes ^{13}C-^{13}C kernspin paren. We gebruiken deze kennis om een record in coherentie tijd van het NV elektron spin te demonstreren (>1.5 seconden) – de langste coherentie tijd voor een enkele elektron spin in vaste stof– door middel van op maat gemaakte dynamische ontkoppelingssequenties die ongewenste interacties vermijden.

Als vervolg op deze resultaten, ontwikkelen we nieuwe multidimensionale spectroscopie en controle technieken, die individuele kernspin-kernspin interacties isoleren binnenin het complexe spin bad met hoge nauwkeurigheid. Met deze methodes demonstreren we beeldvorming op atomaire schaal door middel van magnetische resonantie van een cluster bestaande uit 27 ^{13}C kernspins in diamant. Dit experiment toont de principiële bruikbaarheid van deze techniek aan voor het in kaart brengen van enkele moleculen of complexe spin structuren, een van de visionaire doelen in het gebied van quantum sensoren.

Daarnaast ontwikkelen we van het NV en omliggende cluster van ^{13}C kernspins een quantum register met uitzonderlijke coherentie eigenschappen. We demonstreren een volledig verbonden 10-qubit register met uitstekende controle, coherentie tijden tot een minuut lang, en verstrengeling van 7 qubits. Deze resultaten maken uitstekende controle van multi-qubit quantum registers mogelijk.

Bovendien gebruiken we het ontwikkelde quantum register om de kleinste fouttolerante logische qubit van een complete fouten correctie code (de [[5,1,3]] code met een extra 'vlag' qubit) te realiseren. Door het gebruik van meerdere niet-destructieve pariteitsmetingen en een vlag ancilla meting, demonsteren we de fouttolerante codering van logische quantum toestanden. We meten de preparatie van een logische quantum toestand met een zekerheid van 95(2)% voor een fouttolerante codering in vergelijking met 81(2)% voor een niet-fouttolerante codering, en demonstreren daarmee een significante verbetering. Daarnaast, implementeren we fouttolerante operaties op de logische qubit door het toepassen van een set van transversale logische quantum operaties. Deze resultaten demonstreren een belangrijke stap in de richting van fouttolerante quantum computaties.

Tot slot introduceren we ^{13}C-^{13}C kernspin paren als nieuwe en intrinsiek tegen decoherentie beschermde qubits, met buitengewone coherentie eigenschappen. We demonstreren uitstekende controle en het betrouwbaar uitlezen ($> 98\%$) van de spin paren door het gebruik van het NV. Ook meten we een inhomogene decoherentie tijd van $T_2^* = 1.9(3)$ minuten, de langste gerapporteerd voor een individueel gecontroleerde qubit. Daarnaast laten we verstrengeling zien van twee spin paren door projectieve pariteitsmetingen. Deze nieuwe qubits hebben de potentie om als extreem robuuste quantum geheugens voor quantum netwerken te functioneren.

Het werk gepresenteerd in dit proefschrift demonstreert een belangrijke vooruitgang van het NV en omliggende kernspins als een veelbelovend quantum systeem voor quantum informatica, quantum simulaties, en quantum sensoren. De ontwikkelde karakterisatie en controlemethodes komen in aanmerking om gebruikt te worden in andere systemen bestaande uit defecten. Hierdoor, indien gecombineerd met de snelle vooruitgang van onderzoeksgroepen vanuit de hele wereld in bijvoorbeeld het ontwikkelen van optische trilholtes, gecontroleerde oppervlaktes, en fabricatie methodes, zullen deze resultaten nieuwe mogelijkheden voor atomaire-schaal magnetische resonantie beeldvorming methodes én grootschalige quantum netwerken creëren.

1

INTRODUCTION

1.1. THE RISE OF QUANTUM SCIENCE AND TECHNOLOGY

Quantum mechanics is one of the most successful theories describing physical phenomena in our world. Several key technologies in the last century rely on mechanisms that can only be explained in the framework of quantum mechanics. For example, semiconductor technologies, lasers, photodectors, nuclear magnetic resonance (NMR) and magnetic resonance imaging (MRI), just to name a few.

Owing to remarkable progress made over the last few decades in isolating and manipulating individual quantum systems [1, 2] (such as single electrons, atoms, molecules or photons), a newer version of this field—often referred to as quantum science and technology—has emerged. Most of the earlier technologies are best described by mesoscopic or even microscopic quantum theory, they were typically developed following a top-down approach. In contrast, the emerging field of quantum science and technology takes the peculiar phenomena of quantum mechanics, such as quantum superposition and quantum entanglement, and aims to build quantum devices which exploit these phenomena. Such an approach requires building from the bottom-up level of individual quantum systems. These devices can —in principle— be much faster, more secure or more efficient than what is ever possible with their classical counterparts. These new quantum technologies manifest in four main categories: quantum simulation, quantum computation, quantum communication, and quantum sensing and metrology [3].

Quantum computation is perhaps the most famous one of these categories [4]. While classical computers use bits (that are defined in either the state ‘0’ or ‘1’), quantum computers use quantum bits (‘qubits’) which can exist in arbitrary superposition states of ‘0’ and ‘1’. Many quantum algorithms which show an exponential speed-up compared to the best known classical algorithms have been theoretically proposed [5], and proof-of-principle experiments that show the validity of such algorithms have been demonstrated [4, 6, 7]. Moreover, these quantum computers can be used to simulate and understand complex many-body quantum systems [8, 9], which are typically impractical to simulate by classical computers. The reason is that the computational power required to fully describe quantum systems scales exponentially with the number of its constituents.

Although quantum computers might still be a long-term goal, scientists have come up with another category of devices that are less complex than general-purpose quantum computers, but can still efficiently simulate complex quantum systems; these so-called quantum simulators are special purpose devices designed to study the behaviour of specific quantum systems or learn more about certain physical phenomena [10]. By building controllable quantum systems where some of the physical parameters can be tuned, we can simulate certain physical problems and get more insights about them [10, 11].

Another important category of emerging quantum technologies is quantum communication, which deals with transmitting the quantum states of particles or qubits from one place to another [12, 13]. This can enable fundamentally secure ways of communications guaranteed by the laws of quantum mechanics such as quantum key distribution [14].

Finally, the quantum technology, which is already penetrating various markets, is quantum sensing and metrology. Quantum sensors are devices or systems that utilize quantum properties or phenomena to measure a certain physical quantity. The applications of quantum sensors range from measuring magnetic and electric fields to measuring temperatures, frequencies, time or pressure [15]. The essence of quantum sensing is that it utilizes the extreme sensitivity of quantum systems to disturbances in their environment to measure these physical phenomena with high accuracy and resolution that might not even be possible with the best classical devices [15].

For each of these applications, the main building block is often a controllable individual quantum system (usually referred to as qubit). These qubits can be realized using several experimental platforms, for example the state of a photon, an electron spin, a nuclear spin, an atom, an ion, or even artificial atoms such as a quantum dot or a superconducting qubit [3]. Each of these platforms come with their own fascinating physics, challenges and opportunities.

1.2. SPINS IN DIAMOND: A VERSATILE QUANTUM SYSTEM

Solid-state spins associated to optically active defect centers are among the most advanced and reliable systems for quantum technologies due to their relatively long coherence times [16–20], compatibility for on-chip integration [21, 22] and suitability to work over a wide range of temperatures [16]. Among these systems, the nitrogen-vacancy (NV) center in diamond—a lattice defect in diamond which consists of a substitutional nitrogen atom (replacing a carbon atom) next to a vacant lattice site—has received great attention as it combines a number of these properties [16, 23].

The NV electron spin has exceptional coherence properties [17, 19], can be initialized and read-out with high fidelity via optical means [21], and it provides an optical interface for creating remote entanglement [23–25]. Due to spin-spin couplings, this electron spin can be used to detect and control ^{13}C nuclear spins in its vicinity, which can serve as excellent quantum registers or memories [26–28]. This opens up several interesting applications in quantum communication [24, 29], quantum computation and simulation [28, 30], and quantum sensing [15, 31], but also enables performing fundamental studies in spin physics or fundamental tests of quantum mechanics [25, 32, 33].

1.3. QUANTUM NETWORKS WITH SPINS IN DIAMOND

One of the long-term goals for solid-state defects in general (and for NV centers in particular) is to use them to build a large-scale quantum network [16, 34]. This envisioned quantum network is a promising approach for large-scale distributed quantum computing and secure quantum communications [35–37]. Such a network would consist of multiple nodes, where each of them might contain several nuclear-spin qubits to store and process quantum information, and that are connected together through optical entanglement links based on photons, see Fig. 1.1.

In this thesis, we study and develop one of the building blocks of such a network: the multi-qubit node. Each node consists of an NV center which is coupled to a ^{13}C nuclear-spin environment (Fig. 1.1). We study this nuclear-spin environment and develop novel methods to control the nuclear-spins and to image them with atomic-scale resolution. This provides a precise understanding and description of the quantum node (the full system Hamiltonian) and paves the way towards using this for building a large-scale quantum network but also opens up new opportunities in quantum information processing, quantum sensing, and quantum simulation. The nuclear spins can be used to realize an excellent quantum register to store and process quantum information, and may ultimately be used to improve the efficiency and quality of optical links between the nodes via entanglement distillation [38] or quantum error correction [36, 37, 39].

1.4. THESIS OVERVIEW

Here, we outline the contents of the thesis:

In **chapter 2**, we introduce the NV center in diamond, and give an overview of the main theoretical and experimental methods used throughout the rest of this thesis.

In **chapter 3**, we study and enhance the coherence properties of an NV electron-spin coupled to a multi-qubit nuclear spin environment. We demonstrate a record-long coherence time of the NV center electron spin (1.5 second)—the longest coherence time for single electron spins in the solid state—by precise understanding of (and decoupling from) the interactions with individual ^{13}C nuclear spins and ^{13}C-^{13}C nuclear spin pairs in the environment. We develop basic initialization, control and readout of the ^{13}C-^{13}C pairs in order to directly reveal their coupling strength. We then exploit this knowledge to store quantum states in the electron spin for over a second using tailored dynamical decoupling sequences that carefully avoid unwanted interactions.

In **chapter 4**, we demonstrate atomic-scale magnetic imaging of a cluster of 27 ^{13}C nuclear spins in diamond using the NV center as a quantum sensor. This cluster provides a model system for the magnetic imaging of single molecules or atomic structures outside the diamond, an outstanding goal in the field of quantum sensing. We present a multidimensional spectroscopy method that isolates individual nuclear–nuclear spin interactions in the cluster with high spectral resolution and high accuracy, and develop methods to extract the three-dimensional structure of the cluster from these measurements with sub-ångström resolution.

In **chapter 5**, we show that the NV center combined with this cluster of ^{13}C nuclear spins is a promising platform for quantum information processing applications. We demonstrate a fully connected 10-qubit register with high-fidelity control, coherence

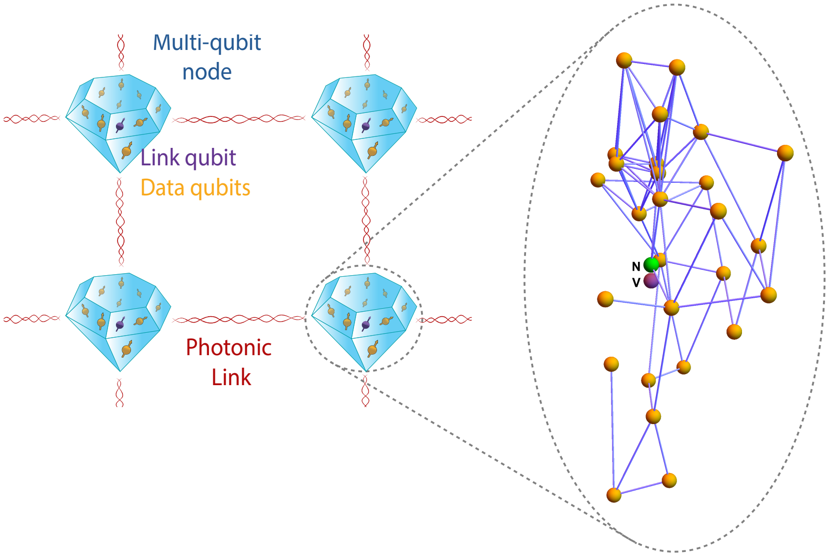

Figure 1.1: A quantum network with spins in diamond. Constructing quantum networks with defect centers is a promising approach for large-scale distributed quantum computing and secure quantum communications. Such a network would consist of multiple nodes that each contain several qubits to store and process quantum states, and that are connected together through optical entanglement links based on photons. In this thesis we focus one of the building blocks of this network: the multi-qubit node. Each node is made of an NV center which is coupled to a nuclear-spin environment. This spin environment provides a quantum register to store and process quantum information, and is also promising to improve the network quality through entanglement purification or error correction.

times up to one minute, and genuine multipartite entanglement of up to 7-qubits.

In **chapter 6**, we use the developed quantum register to demonstrate a fault-tolerant logical qubit with spins in diamond. We utilize multiple non-destructive parity measurements to demonstrate fault-tolerant encoding of a complete logical qubit. Afterwards, we demonstrate transversal fault-tolerant logical gates on the encoded state. Such a fault-tolerant logical qubit is a key building block for large-scale quantum information processing.

In **chapter 7**, we introduce ^{13}C-^{13}C nuclear-spin pairs as a novel qubit with intrinsic coherence protection. We demonstrate high-fidelity control and single-shot readout (> 98%) of these pairs using the NV center electron spin. Furthermore, we demonstrate an inhomogeneous dephasing time, $T_2^* = 1.9(3)$ minutes, the longest reported for any individual qubit. Finally, we demonstrate entanglement between two spin pairs through projective parity measurements.

In **chapter 8**, we summarize the main findings and conclusions of this thesis and discuss the near-term potential improvements and avenues. We then give an outlook for the continued development of this platform.

REFERENCES

[1] S. Haroche, *Nobel lecture: Controlling photons in a box and exploring the quantum to classical boundary,* Rev. Mod. Phys. **85**, 1083 (2013).

[2] D. J. Wineland, *Nobel lecture: Superposition, entanglement, and raising schrödinger's cat,* Rev. Mod. Phys. **85**, 1103 (2013).

[3] A. Acín, I. Bloch, H. Buhrman, T. Calarco, C. Eichler, J. Eisert, D. Esteve, N. Gisin, S. J. Glaser, F. Jelezko, *et al.*, *The quantum technologies roadmap: a european community view,* New J. Phys. **20**, 080201 (2018).

[4] T. D. Ladd, F. Jelezko, R. Laflamme, Y. Nakamura, C. Monroe, and J. L. O'Brien, *Quantum computers,* Nature **464**, 45 (2010).

[5] A. Montanaro, *Quantum algorithms: an overview,* npj Quantum Inf. **2**, 1 (2016).

[6] M. Nielsen and I. L. Chuang, *Quantum computation and quantum information* (Cambridge University Press, Cambridge, 2000).

[7] F. Arute, K. Arya, R. Babbush, D. Bacon, J. C. Bardin, R. Barends, R. Biswas, S. Boixo, F. G. Brandao, D. A. Buell, *et al.*, *Quantum supremacy using a programmable superconducting processor,* Nature **574**, 505 (2019).

[8] R. P. Feynman, *Simulating physics with computers,* Int. J. Theor. Phys. **21**, 467.

[9] S. Lloyd, *Universal quantum simulators,* Science , 1073 (1996).

[10] J. I. Cirac and P. Zoller, *Goals and opportunities in quantum simulation,* Nat. Phys. **8**, 264 (2012).

[11] I. Buluta and F. Nori, *Quantum simulators,* Science **326**, 108 (2009).

[12] N. Gisin, G. Ribordy, W. Tittel, and H. Zbinden, *Quantum cryptography,* Rev. Mod. Phys. **74**, 145 (2002).

[13] N. Gisin and R. Thew, *Quantum communication,* Nat. photon. **1**, 165 (2007).

[14] V. Scarani, H. Bechmann-Pasquinucci, N. J. Cerf, M. Dušek, N. Lütkenhaus, and M. Peev, *The security of practical quantum key distribution,* Reviews of modern physics **81**, 1301 (2009).

[15] C. L. Degen, F. Reinhard, and P. Cappellaro, *Quantum sensing,* Rev. Mod. Phys. **89**, 035002 (2017).

[16] D. D. Awschalom, R. Hanson, J. Wrachtrup, and B. B. Zhou, *Quantum technologies with optically interfaced solid-state spins,* Nat. Photonics **12**, 516 (2018).

[17] N. Bar-Gill, L. M. Pham, A. Jarmola, D. Budker, and R. L. Walsworth, *Solid-state electronic spin coherence time approaching one second,* Nat. Commun. **4**, 1743 (2013).

[18] P. C. Maurer, G. Kucsko, C. Latta, L. Jiang, N. Y. Yao, S. D. Bennett, F. Pastawski, D. Hunger, N. Chisholm, Markham, *et al.*, *Room-Temperature Quantum Bit Memory Exceeding One Second,* Science **336**, 1283 (2012).

[19] M. H. Abobeih, J. Cramer, M. A. Bakker, N. Kalb, M. Markham, D. Twitchen, and T. H. Taminiau, *One-second coherence for a single electron spin coupled to a multi-qubit nuclear-spin environment,* Nat. commun. **9**, 2552 (2018).

[20] C. E. Bradley, J. Randall, M. H. Abobeih, R. C. Berrevoets, M. J. Degen, M. A. Bakker, M. Markham, D. J. Twitchen, and T. H. Taminiau, *A ten-qubit solid-state spin register with quantum memory up to one minute,* Phys. Rev. X **9**, 031045 (2019).

[21] L. Robledo, L. Childress, H. Bernien, B. Hensen, P. F. A. Alkemade, and R. Hanson, *High-fidelity projective read-out of a solid-state spin quantum register,* Nature **477**, 574 (2011).

[22] N. H. Wan, T.-J. Lu, K. C. Chen, M. P. Walsh, M. E. Trusheim, L. De Santis, E. A. Bersin, I. B. Harris, S. L. Mouradian, I. R. Christen, *et al.*, *Large-scale integration of artificial atoms in hybrid photonic circuits,* Nature **583**, 226 (2020).

[23] W. B. Gao, A. Imamoglu, H. Bernien, and R. Hanson, *Coherent manipulation, measurement and entanglement of individual solid-state spins using optical fields,* Nat. Photon. **9**, 363 (2015).

[24] H. Bernien, B. Hensen, W. Pfaff, G. Koolstra, M. Blok, L. Robledo, T. Taminiau, M. Markham, D. Twitchen, L. Childress, *et al.*, *Heralded entanglement between solid-state qubits separated by three metres,* Nature **497**, 86 (2013).

[25] B. Hensen, H. Bernien, A. E. Dréau, A. Reiserer, N. Kalb, M. S. Blok, J. Ruitenberg, R. F. Vermeulen, R. N. Schouten, C. Abellán, *et al.*, *Loophole-free bell inequality violation using electron spins separated by 1.3 kilometres,* Nature **526**, 682 (2015).

[26] T. H. Taminiau, J. J. T. Wagenaar, T. van der Sar, F. Jelezko, V. V. Dobrovitski, and R. Hanson, *Detection and control of individual nuclear spins using a weakly coupled electron spin,* Phys. Rev. Lett. **109**, 137602 (2012).

[27] T. H. Taminiau, J. Cramer, T. van der Sar, V. V. Dobrovitski, and R. Hanson, *Universal control and error correction in multi-qubit spin registers in diamond,* Nat. Nanotechnol. **9**, 171 (2014).

[28] J. Cramer, N. Kalb, M. A. Rol, B. Hensen, M. S. Blok, M. Markham, D. J. Twitchen, R. Hanson, and T. H. Taminiau, *Repeated quantum error correction on a continuously encoded qubit by real-time feedback,* Nat. Commun. **7**, 11526 (2016).

[29] W. Pfaff, B. J. Hensen, H. Bernien, S. B. v. Dam, M. S. Blok, T. H. Taminiau, M. J. Tiggelman, R. N. Schouten, M. Markham, D. J. Twitchen, and R. Hanson, *Unconditional quantum teleportation between distant solid-state quantum bits,* Science **345**, 532 (2014).

[30] G. Waldherr, Y. Wang, S. Zaiser, M. Jamali, T. Schulte-Herbruggen, H. Abe, T. Ohshima, J. Isoya, J. F. Du, P. Neumann, and J. Wrachtrup, *Quantum error correction in a solid-state hybrid spin register,* Nature **506**, 204 (2014).

[31] R. Schirhagl, K. Chang, M. Loretz, and C. L. Degen, *Nitrogen-vacancy centers in diamond: nanoscale sensors for physics and biology,* Annu. Rev. Phys. Chem. **65**, 83 (2014).

[32] T. K. Unden, D. Louzon, M. Zwolak, W. H. Zurek, and F. Jelezko, *Revealing the emergence of classicality using nitrogen-vacancy centers,* Physical review letters **123**, 140402 (2019).

[33] S. B. van Dam, J. Cramer, T. H. Taminiau, and R. Hanson, *Multipartite entanglement generation and contextuality tests using nondestructive three-qubit parity measurements,* Phys. Rev. Lett. **123**, 050401 (2019).

[34] S. Wehner, D. Elkouss, and R. Hanson, *Quantum internet: A vision for the road ahead,* Science **362** (2018).

[35] H. J. Kimble, *The quantum internet,* Nature **453**, 1023 (2008).

[36] N. H. Nickerson, Y. Li, and S. C. Benjamin, *Topological quantum computing with a very noisy network and local error rates approaching one percent,* Nat. Commun. **4**, 1756 (2013).

[37] N. H. Nickerson, J. F. Fitzsimons, and S. C. Benjamin, *Freely scalable quantum technologies using cells of 5-to-50 qubits with very lossy and noisy photonic links,* Phys. Rev. X **4**, 041041 (2014).

[38] N. Kalb, A. A. Reiserer, P. C. Humphreys, J. J. W. Bakermans, S. J. Kamerling, N. H. Nickerson, S. C. Benjamin, D. J. Twitchen, M. Markham, and R. Hanson, *Entanglement distillation between solid-state quantum network nodes,* Science **356**, 928 (2017).

[39] J. Cramer, *Quantum error correction with spins in diamond* (Delft, Delft University of Technology, 2016).

2

BACKGROUND AND METHODS

In this chapter, we introduce the NV center in diamond, which is the system used for all experiments in this thesis. We also give an overview of the main theoretical background and experimental methods used throughout this thesis.

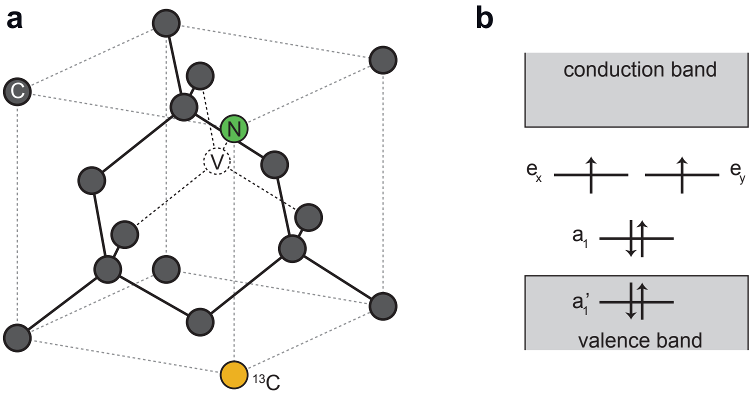

Figure 2.1: The nitrogen-vacancy (NV) center in diamond. a) The crystal structure of diamond. The NV center is formed by a substitutional nitrogen atom next to a vacant lattice side. About 1.1% of the carbon atoms in the diamond lattice are ^{13}C isotopes (yellow). b) The NV molecular orbitals and their occupation in the electronic ground state. Figures adapted from Pfaff [25], Bernien [26].

2.1. THE NV CENTER IN DIAMOND

The nitrogen-vacancy (NV) center in diamond is a common lattice defect in diamond. It consists of a substitutional nitrogen atom (replacing a carbon atom) next to a vacant lattice site (Fig. 2.1). This defect can occur naturally in the diamond, or can be formed by ion implantation [1, 2], or electron irradiation [3]. More recently, it was also shown that it can be formed by direct laser writing [4–6]. The NV center mainly exists in one of two charge states: neutrally-charged (NV^0) and negatively-charged (NV^-) [7]. In the neutral charge state, there are 5 unbound electrons coming from the nearby nuclei (2 from the nitrogen and 3 from the carbons) [7]. The defect can also capture an additional electron from nearby charge traps in its environment which lead to the negatively charged state NV^- [7]. The NV^- charge state is a particularly interesting and versatile platform for quantum technologies [8] with many applications ranging from quantum sensing [9–15] to quantum information processing [16–19], and quantum networks and communications [8, 20–24].

In this thesis we focus on NV^- (hereafter denoted NV). The electronic structure of this NV center is shown in Fig. 2.1b. The electronic wavefunction can be approximated by a linear combination of the available atomic orbitals from the neighbouring nitrogen and carbon atoms [27–29], see Fig.2.1b. In the ground state, the six electrons are distributed among the orbitals as shown in Fig. 2.1b. The two lowest-energy levels (a_1' and a_1) are doubly occupied, and the molecular orbitals $e_{x,y}$ have one electron each. In the excited state, one electron from the orbital a_1 is promoted to one of the e orbitals [27–29].

In both the ground and excited states, two unpaired electron spins can combine into triplet or singlet states. Due to Coulomb repulsion, the triplet states are lower in energy; therefore, the lowest energy ground state is the triplet state ($S = 1$) in the ground molecular orbital [27, 30]. Figure 2.2 shows the energy level diagram of the ground and excited states, for which the fine structure will be described in the following section.

Excitation of the NV from the spin-triplet ground state to one of the six excited states can occur by resonant optical excitations, or off-resonantly via the phonon-sideband. The relaxation can also occur in a similar manner by emitting photons resonantly through the zero phonon line (ZPL), or off-resonantly via the phonon-sideband or singlet states. Note that an important feature of the NV center is that both the ground and first excited state levels have unoccupied energy levels only inside the diamond bandgap. This gives the NV center optical properties similar to those of ions trapped in vacuum [31].

2.2. SYSTEM HAMILTONIAN: NV IN A SPIN BATH

Beyond the central NV electron spin, our quantum system additionaly comprises the host ^{14}N nuclear spin and the surrounding bath of ^{13}C spins. A significant part of this thesis is focused on exploring, understanding, and controlling this complex quantum system. So, we start here by giving a detailed description of the system Hamiltonian.

In the orbital ground state of the NV, the system Hamiltonain can be described by the summation of the Hamiltonians of each of the individual subsystems (components of the system) in addition to the interaction terms between them:

$$H = H_e + H_N + H_c + H_{eN} + H_{ec} + H_{cc} + H_{Nc}, \tag{2.1}$$

where H_e is the NV electron spin ground state Hamiltonian; H_N is the Hamiltonian of the ^{14}N nuclear spin; H_c is the Hamiltonian of the ^{13}C spins; H_{eN} is the hyperfine interaction between the electron spin and the host ^{14}N nuclear spin; H_{ec} is the hyperfine interaction between the electron spin and the ^{13}C nuclear spins; H_{cc} is the nuclear-nuclear coupling between the ^{13}C spins; H_{Nc} is the coupling between the ^{14}N and ^{13}C nuclear spins. In the following, we shall take a closer look at each term of this Hamiltonian.

Electron spin. The NV electron spin ground state is a spin triplet ($S = 1$) and its Hamiltonian can be described as (neglecting second order spin-orbit coupling) [30, 32]:

$$H_e = \Delta_{\mathrm{ZFS}} S_z^2 + \gamma_e (\mathbf{B} \cdot \mathbf{S}), \tag{2.2}$$

where $\Delta_{\mathrm{ZFS}} \approx 2.88$ GHz is the electron zero field splitting (due to spin-spin interactions), $\gamma_e \approx 2.8$ MHz/G is the electron gyromagnetic ratio, $\mathbf{B} = (B_x, B_y, B_z)$ is the magnetic field vector, $\mathbf{S} = (S_x, S_y, S_z)$ are the electron spin-1 operators. The spin states $m_s = 0$ and $m_s = \pm 1$ are split by Δ_{ZFS} at zero applied magnetic field; applying an external magnetic field lifts the degeneracy of the $m_s = \pm 1$ states due to the Zeeman term (see Fig. 2.2). We can then define a qubit between two of these three spin states. In this thesis, we typically define our electron-spin qubit between the states $m_s = 0$ ($|0\rangle$) and $m_s = -1$ ($|1\rangle$).

Nitrogen spin. The ^{14}N nuclear-spin Hamiltonian H_N and its interaction with the electron spin H_{eN} can be written as:

$$H_N + H_{eN} = -Q_N I_{N,z}^2 + \gamma_n (\mathbf{B} \cdot \mathbf{I_N}) + \mathbf{S} \cdot \mathbf{A_N} \cdot \mathbf{I_N}, \tag{2.3}$$

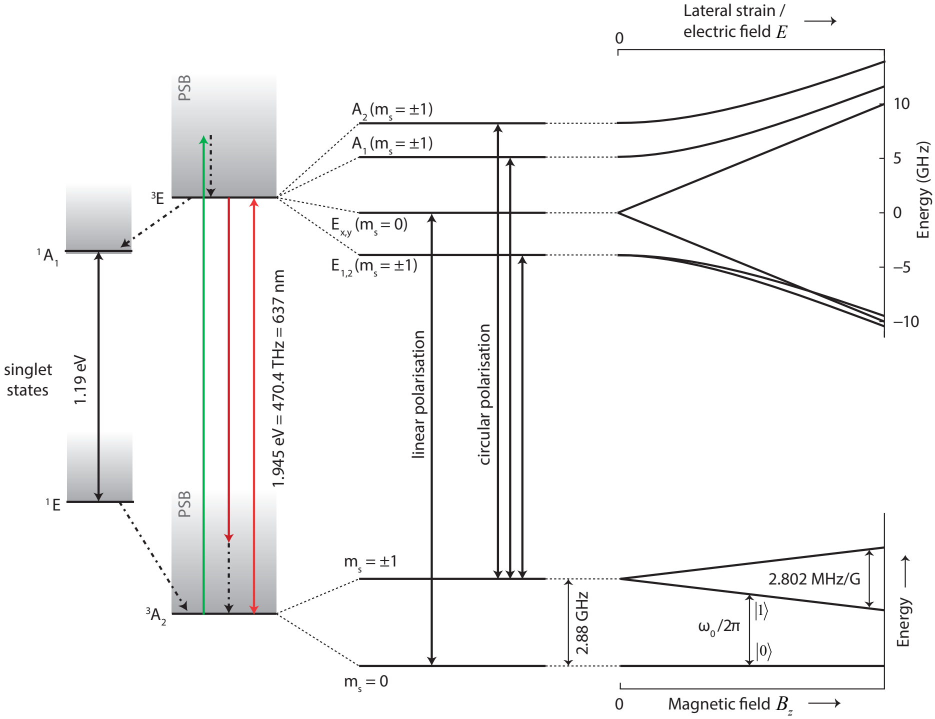

Figure 2.2: Energy level diagram of the negatively charged NV center (ground and excited states). **Bottom center**: The NV ground state is a spin triplet ($S = 1$). The zero field splitting ($\Delta_{\mathrm{ZFS}} \approx 2.88$ GHz) separates the $m_s = 0$ state and the two degenerate states $m_s = \pm1$. **Bottom right**: Applying an external magnetic field (along the NV axis) lifts this degeneracy by Zeeman splitting and allows the definition of a qubit within the ground state triplet. **Top center**: The fine structure of the excited states (which can only be observed at cryogenic temperatures). There are two levels ($E_{x,y}$) that correspond to $m_s = 0$ and four levels that correspond to $m_s = \pm1$ ($E_{1,2}, A_{1,2}$); $E_{x,y}$, $E_{1,2}$ are both doubly degenerate. Excitation of the NV from the ground state to one of the six excited states can occur by optical excitations resonantly (light red line), or off resonantly via the phonon-sideband (green line). The relaxation can also occur in a similar manner by emitting photons resonantly through the zero phonon line (ZPL), or off-resonantly via the phonon-sideband or the singlet states (**Left**). **Top right**: The effect of lateral strain or electric field (up to first order) on the excited state levels. The lateral strain has no effect on the ground state levels to first order. Figure adapted from Pfaff, Bernien, Hensen [25, 26, 30].

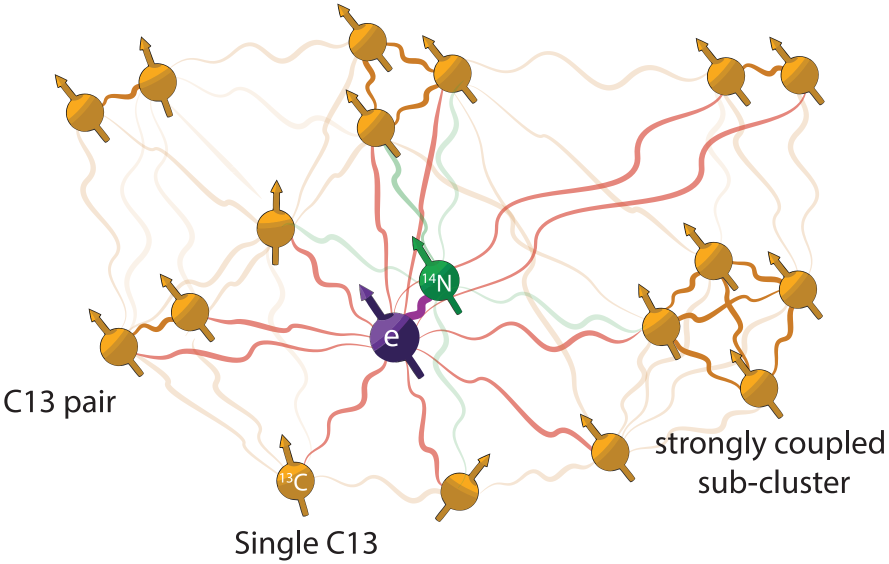

Figure 2.3: Sketch of the quantum system: the NV in a spin bath. The NV electron spin ($S = 1$) is the central spin in the system. It couples to the host ^{14}N nuclear spin ($I = 1$) via hyperfine coupling (purple line; Hamiltonian: H_{eN}). There is a natural abundance (1.1%) of spin-1/2 ^{13}C atoms in the diamond. The electron spin couples to the ^{13}C spins via hyperfine coupling (red lines, Hamiltonian term: H_{ec}), which depends on the relative positions of these ^{13}C spins. These couplings shift the energy of the ^{13}C spins, and can be used as a way to detect, polarize and coherently control the ^{13}C spins via the electron spin. In addition, the nuclear spins in the environment (i.e., ^{13}C and ^{14}N spins) interact with each other via dipolar coupling (green lines, Hamiltonian: H_{Nc}; yellow lines, Hamiltonian: H_{cc}). The nuclear-nuclear couplings depend on the relative positions of the spins (distance and angle with respect to the external magnetic field). When two spins are close to each other, this lead to a strong coupling (i.e., coupling $> 1/T_2^*$) and we call such spins a ^{13}C pair (chapter 3 in this thesis). In some cases three or more spins happen to be close to each other forming strongly coupled subclusters (chapter 4).

where $Q_N \approx 4.98$ MHz is the quadrupole splitting (separates the nitrogen-spin states $m_I = 0$ and $m_I = \pm 1$ under zero magnetic field) [32], $\gamma_n = 0.3077$ kHz/G is the nitrogen-spin gyromagnetic ratio, $\mathbf{I_N} = (I_{N,x}, I_{N,y}, I_{N,z})$ are the spin-1 operators for the ^{14}N nuclear spin, and $\mathbf{A_N}$ is the hyperfine tensor describing the electron-^{14}N interaction. Note that under the secular approximation, H_{eN} can be approximated to $A_\parallel \hat{S}_z \hat{I}_{N,z}$, where $A_\parallel = 2.16$ MHz is the parallel component of the hyperfine interaction.

Carbon-13 spins. The ^{13}C spins Hamiltonian H_c and their hyperfine interaction with the electron-spin H_{ec} can be written as:

$$H_c + H_{ec} = \sum_i \gamma_c \mathbf{B} \cdot \mathbf{I}_i + \sum_i \mathbf{S} \cdot \mathbf{A}_i \cdot \mathbf{I}_i, \tag{2.4}$$

where $\gamma_c = 1.0705$ kHz/G is the carbon-spin gyromagnetic ratio, $\mathbf{I}_i = (I_{i,x}, I_{i,y}, I_{i,z})$ are the spin-1/2 operators for the ^{13}C nuclear spins, and $\mathbf{A}_i$ is the hyperfine tensor describing the electron-^{13}C interaction.

Nuclear-nuclear interactions. In addition to their interactions with the NV electron spins, the nuclear spins in the environment (i.e., ^{13}C and ^{14}N spins) interact with each other via dipolar coupling.

$$H_{cc} = \sum_{i,j} \mathbf{I}_i \cdot \mathbf{C_{ij}} \cdot \mathbf{I}_j, \tag{2.5}$$

$$H_{Nc} = \sum_j \mathbf{I}_N \cdot \mathbf{C_{N,j}} \cdot \mathbf{I}_j, \tag{2.6}$$

where $\mathbf{C_{i,j}}$, $\mathbf{C_{N,j}}$ are the tensors describing the ^{13}C-^{13}C and ^{14}N-^{13}C nuclear-nuclear interactions respectively.

2.3. EXPERIMENTAL SETUP

Our setup consists of five main parts: 1) control electronics: used to run the control cycle and to communicate between different components of the setup; 2) optics: used for initialization and readout of the NV electron spin; 3) microwave and RF: used for manipulating the spin states of the electron and nuclear spins; 4) external magnetic field: to create controllable energy splittings through the Zeeman effect; 5) cryogenics: to cool down the diamond sample to 3.7 K. See Figure 2.4 for a detailed sketch of the main components of the setup and how they communicate with each other.

2.4. DIAMOND DEVICES AND OPTICAL ADDRESSING

2.4.1. DIAMOND DEVICES

The experiments in this thesis are performed on a single, naturally occurring NV center in a high-purity chemical-vapor-deposition homoexpitaxially grown diamond (type IIa) with a natural abundance of ^{13}C (1.1%) and a <111> crystal orientation. Figure 2.5 shows a typical device similar to the one used in this thesis. To improve the photon-collection efficiency, a solid immersion lens (SIL) is fabricated on top of the NV center, by milling

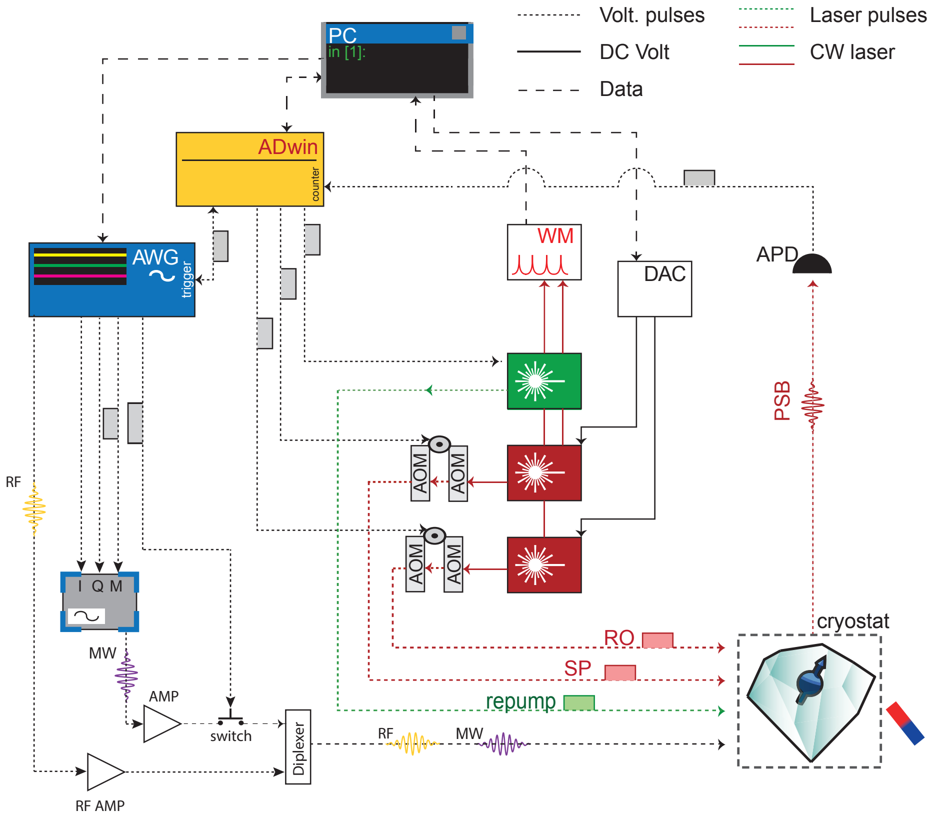

Figure 2.4: Schematic of the experimental setup. **Control electronics**: We use a PC to program the control cycle onto a micro-controller (Jaeger ADwin Pro II) and to program the pulse sequence with nanosecond resolution onto an arbitrary waveform generator (Tektronix AWG 5014, 4.5V pk-pk). The communication between the different components of the setup is mainly done by the ADwin, including triggering the AWG to start the pulse sequence. **Optics**: We use a green laser (515 nm, Cobolt MLD, on/off ratio of >135 dB) for charge state control and two resonant lasers (Toptica DL Pro and New Focus TLB-6704-P) for initialization and readout. To generate optical pulses, the green laser can be directly modulated by the ADwin. For the two resonant lasers, we use Acousto-optic modulators (AOM). To suppress the optical background noise we cascade two AOM's (Gooch and Housego Fibre Q, total on/off ratio >100 dB) for each of the lasers. The frequencies of the two resonant lasers are measured using a wavemeter (HF-ANGSTROM WS/U-10U) and stabilized using a PC-controlled feedback loop (PID loop) to 2 MHz accuracy. We use a home-built confocal microscope to focus light onto the sample and to collect the emission. The microscope objective is mounted on XYZ piezo scanner (PI) that can be used to make 3-dimensional scans and to precisely align the NV center to the optical path. **Microwave and RF**: Microwave pulses are generated using a vector source (SGS100). The frequencies, timings, shapes and phases of theses pulses are controlled via the AWG through IQ- and pulse-modulation. The signal is amplified by a microwave amplifier (AR 25S1G6). We use a fast microwave switch (TriQuint TGS2355-SM, suppression ratio of 40 dB, controlled by the AWG) to protect the NV from the amplifier noise while idling. Video leakage noise generated by the switch is filtered with a high pass filter. The RF signal is generated directly by the AWG; in some experiments in this thesis (only parts of Chapter 5) we use an RF amplifier to achieve higher Rabi frequencies (Analog Devices ADA4870). However, for the rest of the multi-qubit experiments, we do not use the RF amplifier to avoid heating of the chip and to allow shorter RF pulses without ringing from filters in the RF electronics. In both cases, the MW and RF signals are then combined using a diplexer and the output is then fed to the diamond sample. **External magnetic field**: We apply a static magnetic field, $B_z \approx 403$ G, along the NV-axis using a permanent room-temperature neodymium magnet. We stabilize the magnetic field strength to < 3 mG and the magnet is aligned to the NV-axis with uncertainty of 0.07° using thermal echo sequences (see chapter 4 or ref. [33] for details of magnetic field stability and the alignment procedure). **Cryogenics**: The sample is held in a closed cycle cryostat (Montana Cryostation) at a temperature of 3.7 K. Figure adapted from pfaff, Cramer [25, 34].

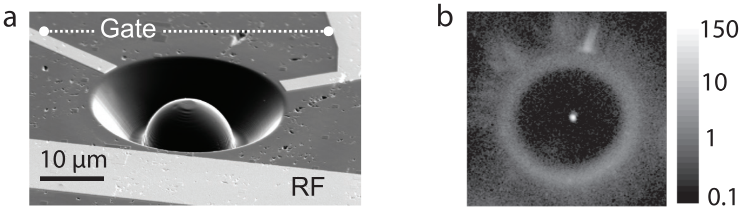

Figure 2.5: a) Scanning electron microscope image of a solid immersion lens (SIL) in the diamond chip. The stripline close to the SIL is used to send MW and RF pulses for driving the electron and nuclear spin resonances. The gates are used to apply DC voltages for strain tuning (not used in this work). b) A scanning confocal microscope image of the SIL using green laser light. The bright spot in the middle of the SIL shows the emission of a single NV center in the phonon-sideband. Figure from Bernien [26].

away diamond using focused ion beam [35] (Fig. 2.5). In addition, an aluminum-oxide anti-reflection coating layer (grown by atomic-layer-deposition) is used [35].

Lithographically-defined, on-chip striplines are fabricated close to the solid immersion lenses by metal evaporation. These striplines are used to apply microwave and RF fields for driving the electron- and nuclear-spin transitions. Gold gate-electrodes are fabricated near the SILs to apply static electric fields. This allows tuning the strain in the NV-centre which can be used for fine-tuning of the optical resonances [36]. Note that these gates are not used throughout this work.

2.4.2. OPTICAL ADDRESSING

For the work presented in this thesis, we work at low temperatures (3.7 K) and therefore we use spin-selective resonant optical excitations for high-fidelity initialization and readout of the NV electron spin [35]. We typically initialize the NV electron spin into the $m_s = 0$ state (Fidelity $> 99.7\%$) through a spin pumping process. We use a resonant laser (spin pump (SP) laser) that excites the ground states $m_s = \pm 1$ into the optically excited states $E_{1,2}$ (see Fig. 2.2, Fig. 2.8a). Initialization into $m_s = \pm 1$ is done by applying resonant microwave pulses that drive the electron spin from the initialized $m_s = 0$ state into the desired state.

We read out the electron spin state in a single shot by shining a laser in resonance with the transition $m_s = 0$ to E_x (RO laser) [35]. Ideally, this leads to emission of one or more photons if the electron spin is in $m_s = 0$ or zero photons if the state is $m_s = \pm 1$ (average readout fidelity here $\approx 94.5\%$).

2.5. DETECTION AND CONTROL OF ^{13}C NUCLEAR SPINS

As discussed in section 2.2, the NV center in diamond is surrounded by a bath of ^{13}C nuclear spins (with natural abundance of 1.1%). While this bath of ^{13}C nuclear spins is the main source of decoherence for the NV electron spin [9, 37], recent advances in quantum control methods have enabled the detection and universal control of individual ^{13}C nuclear spins in the bath [17, 38–40], thus transforming these spins into a promising resource (a quantum register). Additionally, this bath provides a model system to study and develop methods for quantum sensing and atomic-scale magnetic resonance imaging, which are among the main applications areas of the NV center [9–13, 38, 41–45] (see also ch. 4). In this chapter, we will give an overview of the main methods used in this thesis for the detection (sensing) and control of these ^{13}C spins. Note that a significant part of this thesis is focused on developing better detection and control methods. These novel methods will be discussed in detail in their dedicated chapters.

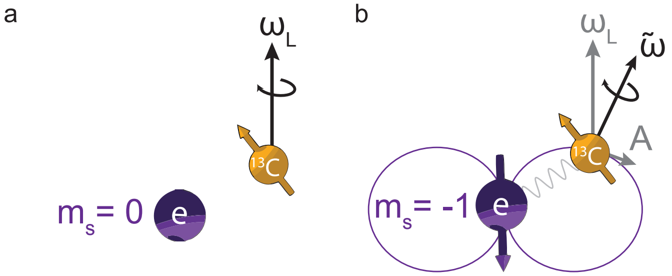

Figure 2.6: Dependence of the ^{13}C nuclear spin precession on the electron spin state. a) For $m_s = 0$, the ^{13}C nuclear spin rotates along an axis parallel to the external magnetic field direction and with the bare Larmor frequency $\omega_0 = \gamma_c B_z$ (the hyperfine coupling is effectively turned off). b) For $m_s = -1$, and for non-zero $A_\perp$, the rotation axis is tilted and the evolution frequency is $\tilde{\omega} = \sqrt{(\omega_0 - A_\parallel)^2 + A_\perp^2}$. This leads to two anti-commuting rotation axes based on the electron spin state [17, 38]. Figure adapted from Cramer [34].

2.5.1. SIMPLIFIED INTERACTION HAMILTONIAN

To develop a better understanding of the detection and control of ^{13}C spins, let us first consider the simple scenario of a single nuclear spin in the vicinity of an NV center. The Hamiltonian describing the electron-carbon system (a simplified version of eq. 2.1), in the interaction picture with respect to the electron energy splitting and under the secular approximation can be described by [17, 38]:

$$H = \omega_0 I_z + A_\parallel S_z I_z + A_\perp S_z I_x, \tag{2.7}$$

where ω_o $(= \gamma_c B_z)$ is the bare Larmor frequency, and $A_\parallel$ $(A_\perp)$ is the parallel (perpendicular) hyperfine coupling between the electron and the ^{13}C nuclear spin with respect to the applied static magnetic field. Note that these hyperfine components have contributions from two different effects: a dipolar coupling term and a Fermi-contact term [46].

We can rewrite the above Hamiltonian as follows:

$$H = |0\rangle\langle 0| H_0 + |1\rangle\langle 1| H_1, \tag{2.8}$$

$$H_0 = \omega_0 I_z, \tag{2.9}$$

$$H_1 = (\omega_0 - A_\parallel) I_z + A_\perp I_x, \tag{2.10}$$

where H_0 (H_1) is the Hamiltonian describing the evolution of the nuclear spin if the electron is in the state $m_s = 0$ ($m_s = -1$).

From this Hamiltonian, we note that the ^{13}C nuclear spin evolution depends on the electron spin state (see Fig. 2.6 for illustration). For $m_s = 0$, the ^{13}C nuclear spin rotates along an axis parallel to the external magnetic field and with the Larmor frequency ω_0. For $m_s = -1$, and for non-zero $A_\perp$, the rotation axis is tilted and the evolution frequency is $\tilde{\omega} = \sqrt{(\omega_0 - A_\parallel)^2 + A_\perp^2}$. This leads to two non-commuting rotation axes based on the electron spin state. By utilizing dynamical decoupling (DD) sequences that switch between the electron spin states, we can engineer the average Hamiltonian to produce certain controlled (or uncontrolled) rotations for the ^{13}C nuclear spin. This allows us to design controlled-gates which can be further used to make maximally entangled electron-nuclear spin states, and can also be used for ancilla-based initialization and readout of the nuclear spins [17, 34, 38]. In the following sections, we shall look into each of these elements in more detail.

2.5.2. DETECTION AND CHARACTERIZATION OF SINGLE NUCLEAR SPINS

Each NV center is surrounded by a unique ^{13}C nuclear spin environment because the spins are randomly located in the diamond lattice. The hyperfine coupling parameters ($A_\parallel$, $A_\perp$) depend on the position of the spins with respect to the NV center. Strongly coupled spins ($A_\parallel > 1/T_{2,e}^*$, $T_{2,e}^*$ is the electron spin dephasing time) will be distinct from the rest of the bath in the typical electron spin resonance (ESR) experiments and can be directly detected and controlled using resonant microwave fields [18, 38, 47–49]. However, to detect and control weakly coupled spins ($A_\parallel < 1/T_{2,e}^*$), which are the vast majority spins in the environment, other techniques are required. Pioneering work has used multipulse dynamical decoupling sequences to detect such weakly coupled spins [38, 39, 50]. These multipulse sequences enhance the electron spin coherence by decoupling it from the spin bath [51, 52], and at the same time isolate the weak signals from specific nuclear spins, by tuning the sequence to be resonant with their dynamics [38, 39, 50].

The dynamical decoupling sequences that are typically used in this thesis can be decomposed into primitive units of the form: (τ - π - 2τ - π - τ), see Fig. 2.7a. The unitary describing the evolution of the nuclear spin during this operation can be written as [38]:

$$V_0 = \exp[-iH_0\tau]\exp[-iH_1 2\tau]\exp[-iH_0\tau], \tag{2.11}$$

$$V_1 = \exp[-iH_1\tau]\exp[-iH_0 2\tau]\exp[-iH_1\tau], \tag{2.12}$$

where V_0 (V_1) is the unitary evolution for an initial electron spin state $m_s = 0$ ($m_s = -1$).

These unitaries can also be written as single-qubit rotations [38]:

$$\begin{aligned} V_0 =& \exp[-i\phi(\mathbf{I}\cdot\hat{\mathbf{n}}_\mathbf{0})], \\ V_1 =& \exp[-i\phi(\mathbf{I}\cdot\hat{\mathbf{n}}_\mathbf{-1})], \end{aligned} \tag{2.13}$$

where $\hat{\mathbf{n}}_\mathbf{0}$ ($\hat{\mathbf{n}}_\mathbf{-1}$) is the rotation axis for the initial electron-spin state $m_s = 0$ ($m_s = -1$). Importantly, these rotation axes depend on the interpulse delay τ, and by selecting specific τ resonant with the electron-nuclear spin dynamics, these rotation axes can be anti-parallel (see Fig. 2.7b). The rotation angle ϕ does not depend on the input electron state but it does depend on the number of dynamical decoupling pulses N [38]. Thus, by selecting a specific combination of τ and N values, we can tailor the desired unitary operation on the nuclear spin [17].

If the two rotation axes ($\hat{\mathbf{n}}_\mathbf{0}$ and $\hat{\mathbf{n}}_\mathbf{-1}$) are not parallel, a non-trivial conditional rotation of the nuclear spins is realized, which can lead to entanglement between the electron and nuclear spins. This can be used to probe the nuclear spins in the environment. First, the electron spin is prepared into a superposition state, e.g. $|x\rangle = (|0\rangle + |1\rangle)/\sqrt{2}$. After applying a dynamical decoupling sequence with $N\pi$-pulses with a variable pulse delay τ, the remaining electron coherence is measured (see Fig. 2.8a). When the interpulse delay 2τ is in resonance with one of the nuclear spins in the environment, a dip (coherence collapse) in the signal is observed (see Fig. 2.8b for an example).

The obtained dynamical decoupling signal from such experiments can be described by [38]:

$$P_x = (M+1)/2, \tag{2.14}$$

where, for a single nuclear spin j,

$$M = \mathrm{Re}[\mathrm{Tr}[(V_0^{N/2}(V_1^{N/2})^\dagger]]. \tag{2.15}$$

For multiple nuclear spins (with negligible nuclear-nuclear interaction), the coherence term M will just be the multiplication of those of the individual ones:

$$M = \prod_{i=1}^{n} M_i. \tag{2.16}$$

A more detailed treatment, which takes into account nuclear-nuclear interactions is presented in chapter 3.

Note that, in principle, we can use the dynamical decoupling signals for different values of N, τ to obtain the hyperfine parameters $A_\parallel$, $A_\perp$, by matching simulated signals with experiment [19, 38]. More recently, automatic algorithmic methods and machine-learning-enhanced techniques have been realised to obtain these parameters more accurately (see our recent work [55, 56]). Note that there are also other more advanced spectroscopy methods that can directly obtain these hyperfine parameters with high accuracy (see for example refs. [33, 43, 57].)

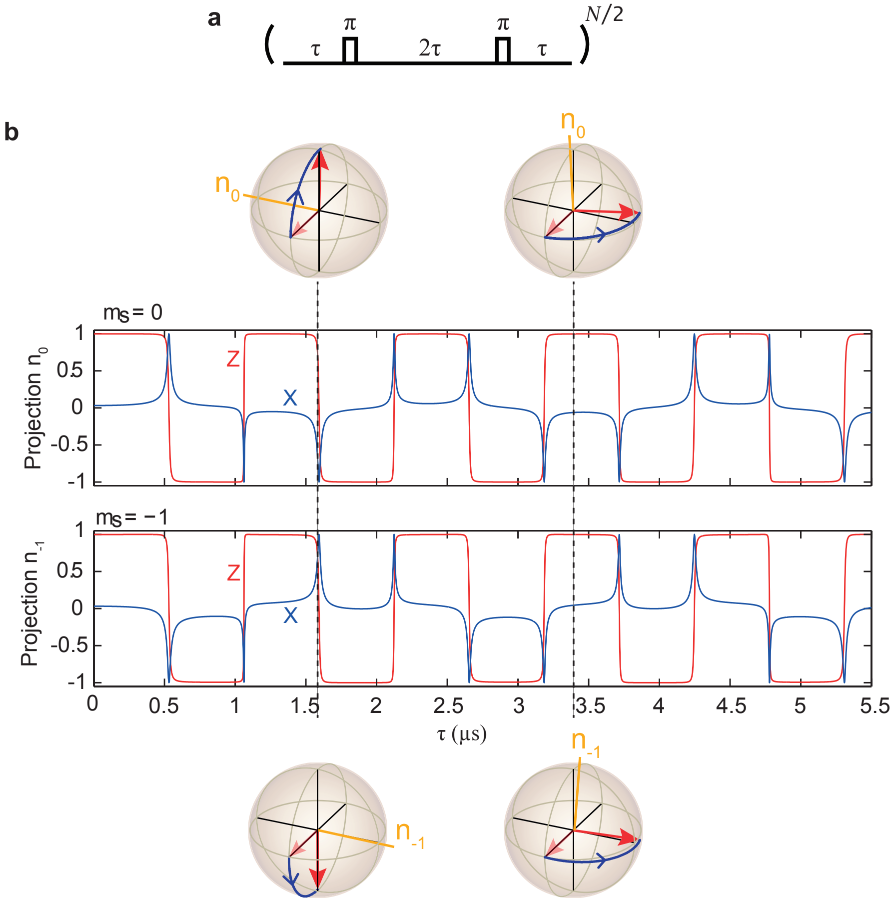

Figure 2.7: Nuclear-spin dynamics under dynamical decoupling sequences. a) The dynamical decoupling sequences that are typically used in this thesis can be decomposed into primitive units of the form: (τ - π - 2τ - π - τ). b) Example showing the dynamics of a single nuclear spin ($A_{\parallel}$ = 78.2 kHz, $A_{\perp}$ = 30 kHz) under a single dynamical decoupling unit (i.e., $N = 2$) for variable interpulse delay τ. The middle panels show the X and Z projections of the nuclear-spin rotation-axes for $m_s = 0$ ($\mathbf{\hat{n}_0}$) and $m_s = -1$ ($\mathbf{\hat{n}_{-1}}$). For specific τ values (e.g., left dashed line and corresponding Bloch spheres) the nuclear-spin rotation-axes for $\mathbf{\hat{n}_0}$ and $\mathbf{\hat{n}_{-1}}$ are anti-parallel; by selecting the right number of pulses the rotation angle can be adjusted to certain values (e.g. $\pi/2$) [17]. For most of the other values of τ, the nuclear spin undergoes simple Z-rotations independent of the electron spin state (e.g. the right dashed line and corresponding Bloch spheres). Figure adapted from Taminiau et. al. [17], Cramer [34].

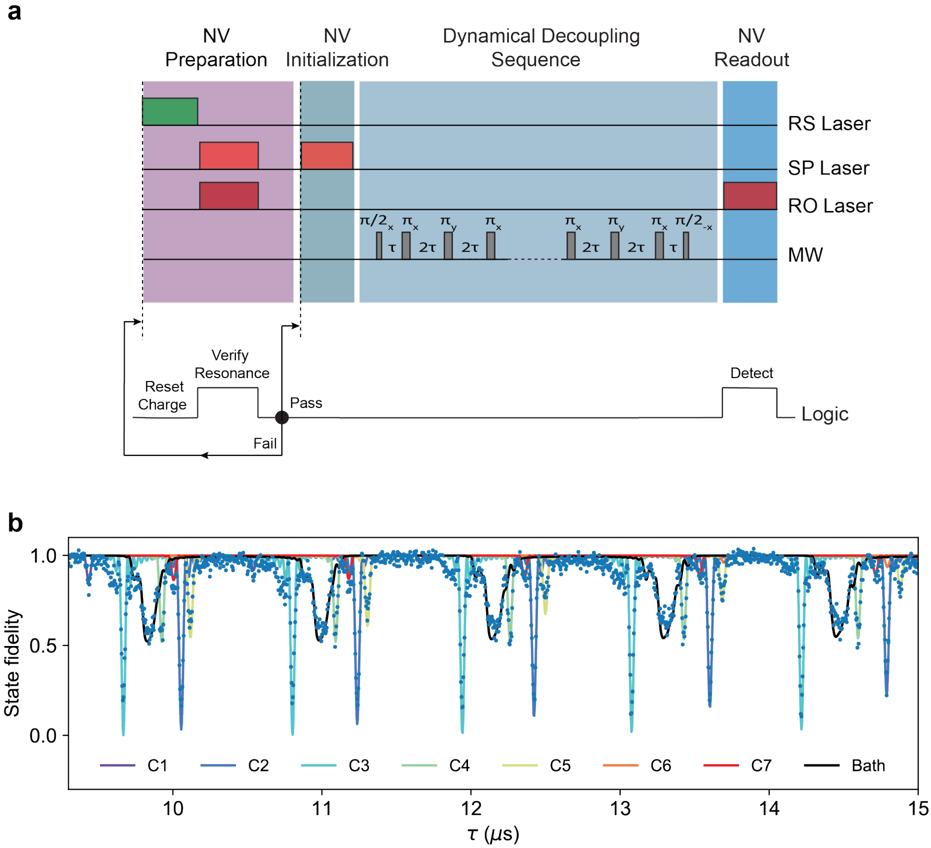

Figure 2.8: Dynamical decoupling spectroscopy. a) Detailed experimental sequence. The pulse sequence consists of four main parts: NV preparation, NV initialization, Dynamical decoupling sequence, NV readout. **NV preparation**: the NV centre is prepared in the negative charge state and brought on resonance with the lasers used for the initialization (SP laser) and Readout (RO laser) steps. We simultaneously apply the SP and RO lasers for 150 µs and count the number of detected photons (wavelength 637 nm, RO laser resonant with $m_s = 0$ to E_x transition and SP laser resonant with $m_s = \pm 1$ to $E_{1,2}$ transition) [35]. If the number of detected photons exceeds a certain threshold, the NV is in the negative charge state and on resonance with both lasers, and the sequence proceeds to the next step. If not, the charge reset laser (RS, wavelength 515 nm) is applied for 1 ms and the same process is repeated until success [35]. **NV initialization**: the NV electron spin is initialized into the $m_s = 0$ state through spin pumping on the $E_{1,2}$ transition (SP laser, 100 µs) [35]. **Dynamical decoupling sequence**: the electron spin is prepared into a superposition state by applying a $\pi/2$-pulse. Afterwards, a sequence of $N\pi$-pulses is applied on the electron spin with the form $(\tau\text{-}\ \pi\ \text{-}\ \tau)^N$. To reduce the effect of pulse errors, we alternate the phases of the π-pulses according to the XY-8 scheme [53]. **NV readout**: we apply the RO laser for 10 µs and count the number of detected photons in this period. This allows us to read out the NV electron spin state in a single shot (fidelity ≈ 94.5%). b) Example showing the obtained dynamical decoupling signal for $N = 32$ pulses. Loss of coherence indicates the interaction of the electron spin with nuclear spins in the environment. Here, the total signal is described by seven ^{13}C spins and a bath of 200 randomly generated spins with hyperfine couplings below 10 kHz. For the seven spins, the hyperfine parameters $A_\parallel$, $A_\perp$, are obtained by matching simulated signal with experiment. Blue: data. Solid lines: theory. Figure adapted from Abobeih et al. [54] and Jung et al. [55]

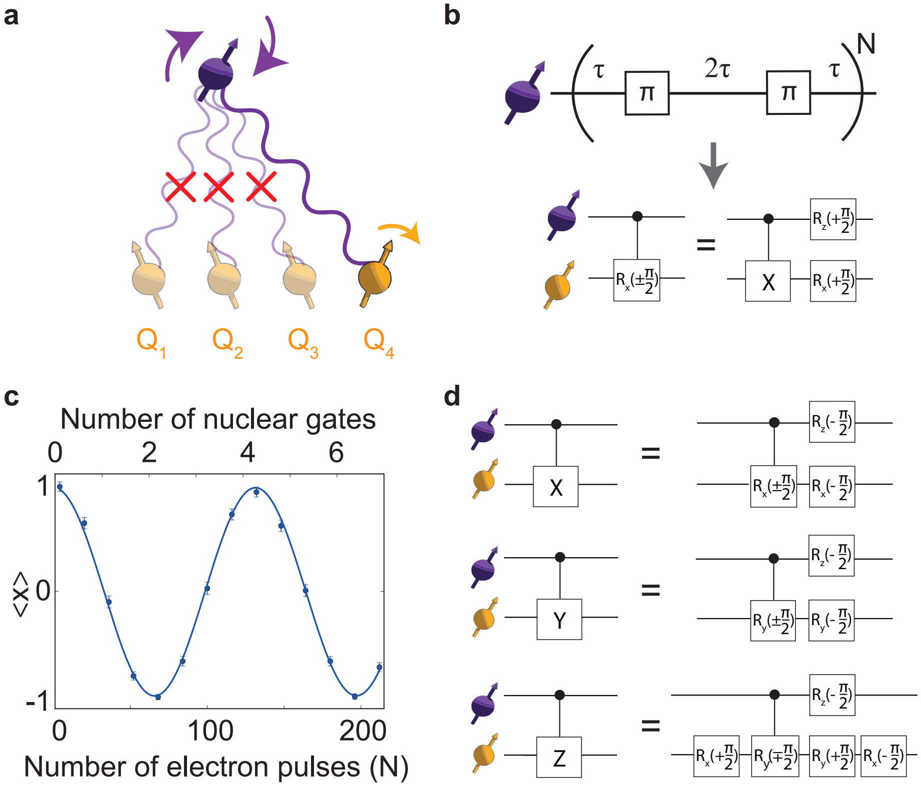

Figure 2.9: Nuclear-spin control using dynamical decoupling sequences. a) Sketch demonstrating the basic idea. Dynamical decoupling can be used to isolate the interaction between the electron spin and a certain nuclear spin while decoupling it from the rest of the spin bath. b) By selecting τ to be resonant with one of the carbon spins, and selecting the right number of pulses, the dynamical decoupling sequence leads to an electron-controlled nuclear gate $R_x(\pm\pi/2)$ which is equivalent to a standard CNOT gate up to single qubit rotations. Note that $R_x(\pm\pi/2) = |0\rangle\langle 0| \otimes R_x(+\pi/2) + |1\rangle\langle 1| \otimes R_x(-\pi/2)$. c) Sweeping the number of pulses N, with τ being resonant with one of the spins, leads to a coherent oscillation due to the nuclear spin undergoing differing rotation angles, ϕ, at different number of pulses N, which is then reflected in the measured $\langle X\rangle$ for the electron spin. One quarter of a period corresponds to a maximally entangling gate $R_x(\pm\pi/2)$. d) Implementation of the standard controlled gates using our two-qubit gate schemes and extra single qubit rotations. $R_y(\pm\pi/2)$ can be directly implemented using $R_x(\pm\pi/2)$ by adding phase-shift gates.

2.5.3. UNIVERSAL CONTROL OF ^{13}C NUCLEAR SPINS

As discussed in the previous section, a careful choice of τ and N can be used to tailor the desired unitary operations on the nuclear spin, including controlled rotation gates (see Fig. 2.9). These controlled-rotations are equivalent to the standard CNOT gate up to single qubit rotations (Fig. 2.9b) and can be used to create maximally entangled states between the electron and nuclear spins [17, 19]. These two-qubit gates can also be used to initialize and readout the nuclear spins via the electron spin ancilla (see sections 2.5.4,2.5.5). In addition, entanglement of multiple nuclear spins can be realized by sequential entanglement with the electron spin [17, 19] (more details in chapter 5).

If the electron is in an eigenstate, single qubit rotations along Z axis (phase-shift gates) are achieved by free precession (the evolution frequencies can be calibrated with high accuracy [19, 54]). Single qubit rotations along X or Y can be done by applying a resonant dynamical decoupling gate (which effectively acts as a single qubit rotation in this case). Alternatively, direct radio frequency (RF) pulses resonant with the nuclear spin transition can be used [58]. Otherwise, if the electron is in an arbitrary quantum state, single qubit rotations along X, Y or Z can be done by off-resonant dynamical decoupling sequences (as shown in Fig. 2.7b) which also mitigate the electron decoherence.

Therefore, we have a universal gate-set for the electron and nuclear spins which make them appealing muti-qubit quantum registers.

2.5.4. ANCILLA-BASED INITIALIZATION OF THE NUCLEAR SPINS

For both quantum information processing and quantum sensing applications, initialization (or polarization) of the nuclear spins is a key step for many experiments. In our work, we typically use two methods for initialization: 1) measurement-based initialization (MBI), and 2) SWAP initialization (see Fig. 2.10 for illustration of both methods).

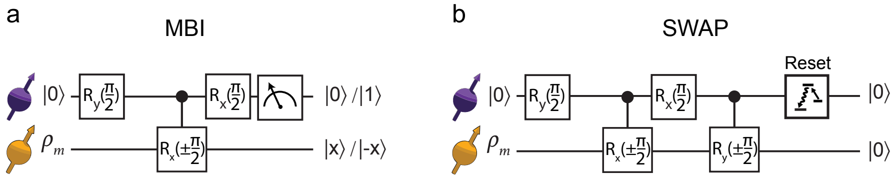

Figure 2.10: Carbon initialization methods. a) Measurement-based initialization (MBI). The electron spin is brought into superposition using a $\pi/2$ pulse, and then a resonant DD gate is applied. A final $\pi/2$ pulse brings the electron to its eigenbasis. Measuring the electron spin projects the nuclear spin into $|x\rangle_n$ or $|-x\rangle_n$ depending on the measurement outcome. b) SWAP initialization. Here an extra controlled $R_y(\pm\pi/2)$ is applied (compared to the MBI initialization) which brings the nuclear spin to the state $|0\rangle$ independent of the electron spin state. Finally, an optical pulse is used to reset the electron state to $|0\rangle$.

For MBI, the electron spin is initialized in a superposition state (e.g., $|x\rangle = (|0\rangle + |1\rangle)/\sqrt{2}$), before application of a resonant DD gate which effectively applies an electron-controlled gate on the nuclear spin (Fig. 2.10).

Assuming the nuclear spins are in a fully mixed state (in this thesis we operate in the infinite temperature regime $k_b T \gg \hbar\gamma B_z$), the density matrix describing its state can be written as $\rho_m = I/2 = (|x\rangle\langle x| + |-x\rangle\langle -x|)/2$. The combined electron-nuclear state after the rotation $R_y^{\pi/2}$ on the electron spin can be written as [59]:

$$|x\rangle\langle x|_e \otimes \frac{1}{2}(|x\rangle\langle x|_n + |-x\rangle\langle -x|_n), \tag{2.17}$$

with $|-x\rangle = (|0\rangle - |1\rangle)/\sqrt{2}$. After applying the electron-nuclear gate, the state can be written as:

$$\frac{1}{2}(\left|-y\right\rangle\left\langle -y\right|_e \otimes |x\rangle\langle x|_n + \left|y\right\rangle\left\langle y\right|_e \otimes |-x\rangle\langle -x|_n) \tag{2.18}$$

with $\left|y\right\rangle = (|0\rangle + i\,|1\rangle)/\sqrt{2}$ and $\left|-y\right\rangle = (|0\rangle - i\,|1\rangle)/\sqrt{2}$. Effectively, the electron-controlled nuclear gate effectively adds a conditional phase shift to the electron state dependent on the nuclear state. Finally, an $R_x(\pi/2)$-rotation brings back the electron to the eigenbasis:

$$\frac{1}{2}(|0\rangle\langle 0|_e \otimes |x\rangle\langle x|_n + |1\rangle\langle 1|_e \otimes |-x\rangle\langle -x|_n) \tag{2.19}$$

A projective measurement on the electron (via resonant optical excitation) would thus project the nuclear-spin state into a certain state. For an outcome $|0\rangle_e$ ($|1\rangle_e$) for the electron, the nuclear spin is projected into $|x\rangle_n$ ($|-x\rangle_n$). Note this initialization method is probabilistic as the nuclear-spin state depends on the outcome of the electron measurement. However, we can make it deterministic by applying feedback depending on the measurement outcome.

The second initialization method is SWAP, in which the electron and nuclear spin states are swapped. This method deterministically initializes the nuclear-spin into an eigenstate. From equation 2.19, it can be seen that applying a controlled rotation $R_y(\pm\pi/2)$ will cause the nuclear spin to end up in the state $|0\rangle$, independent of the electron-spin state.

$$\frac{1}{2}(|0\rangle\langle 0|_e \otimes |0\rangle\langle 0|_n + |1\rangle\langle 1|_e \otimes |0\rangle\langle 0|_n) \tag{2.20}$$

The electron spin, however, ends up in a mixed state, and we reinitialize it by optical pumping which generally does not perturb the nuclear spin eigenstate for the relatively weak hyperfine couplings used here.

2.5.5. ANCILLA-BASED READOUT OF THE NUCLEAR SPINS

The readout of the nuclear spin state in the X basis can be performed in a similar way to the MBI scheme. From equation 2.19, we can see that if the input nuclear spin state is $|x\rangle_n$ ($|-x\rangle_n$), the outcome of the electron measurement is 0 (1). Measuring the nuclear-spin along different axes (e.g., Y or Z) is achieved by extra basis rotations (single qubit gates).

Measuring multi-qubit nuclear-spin operators can be realized in a similar way (Fig. 2.11). As each additional electron-controlled nuclear gate adds a $\pi/2$ phase shift to the electron spin (Fig. 2.9), the final phase of the $\pi/2$ readout pulse has to account for the number of the spins being measured (i.e., the phase depends on the number of non-trivial terms in the measured tomography operator). A few examples are given in Fig. 2.11.

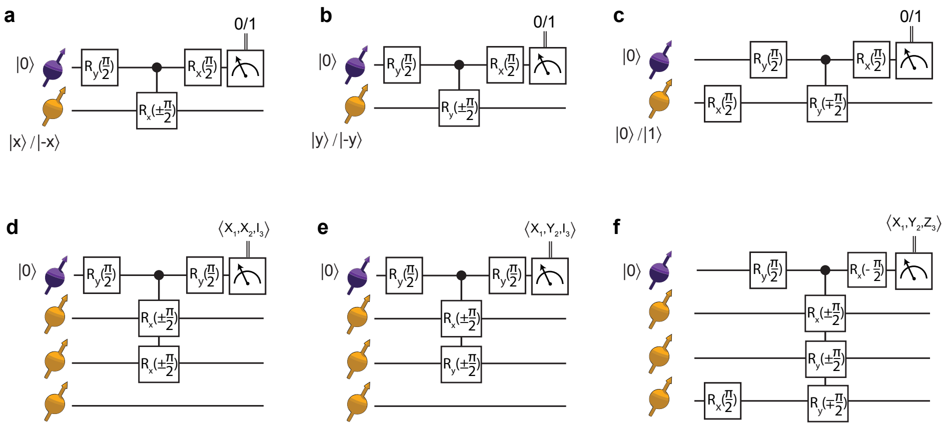

Figure 2.11: Ancilla-based tomography of nuclear spin states. a) Reading out a single nuclear spin in the X-basis is done in a similar way to MBI; if the input nuclear spin state is $|x\rangle_n$ ($|-x\rangle_n$), the outcome of the electron measurement is 0 (1). Reading out the nuclear spin in the Y-basis (b), and Z-basis (c) is done by simple extra basis rotation. d,e,f) Measuring multi-qubit operators. As each measured nuclear spin (the electron-controlled nuclear gate) adds a $\pi/2$ phase shift to the electron, the final phase of the $\pi/2$ readout pulse has to account for the number of the spins being measured (i.e., depends on the number of non-identity terms in the tomography process).

2.5.6. STABILIZER (PARITY) MEASUREMENTS

Non-destructive parity measurements are important components in quantum information processing, providing a mechanism to engineer entangled states, but also as the key ingredient for quantum error detection and correction protocols [60, 61]. In general, the circuits for implementing parity measurements are very similar to those used in the tomography steps discussed in section 2.5.5. The key difference is that, the parity measurement requires a quantum non-demolition (QND) measurement of the nuclear spins (data qubits). The main challenge in our system is that optically reading out the electron spin (ancilla) could lead to undesired spin flips, which—due to the hyperfine interaction—translates to dephasing of the nuclear spins and would diminish the QND nature of the measurement. To mitigate this, we use a QND-type readout of the ancilla by resonant optical excitation and dynamically stopping the excitation process (within 2 μs) upon photon collection [19]. This reduces undesired spin flips during the excitation process (the probability that the electron spin is in the same state after the measurement is 0.992 [19]).

Note that directly applying our gate scheme similar to Fig. 2.11 leads to an extra basis rotation for the nuclear spins. When measuring multiple stabilizers in a row, this extra basis rotation has to be taken into account. This can be done by updating the following stabilizer measurements such that the final output state would be the originally targeted one up to single-qubit rotations. For instance, if we want to measure multiple stabilizers $P_1, P_2, .., P_N$ in a row, we can simplify the implementation given our own gate schemes as follows.

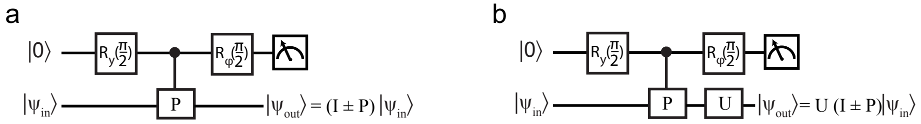

Figure 2.12: Measuring stabilizers. a) General scheme for ancilla-based measurement of a stabilizer P. The phase ϕ of the final $\pi/2$ pulse will depend on the operator P as discussed earlier. b) Given our experimental implementation of controlled gates, the most straightforward way to measure an operator P (i.e., with least amount of applied single qubit gates) usually leads to extra single qubit rotations U. If we want to measure multiple stabilizers in a row, we either undo the extra rotation by applying the unitary $U^\dagger$ first, or instead update the next stabilizers to be measured to account for this.

First, we measure the stabilizer P_1. If the measurement outcome is +1, we project into the state with +1 eigenvalue. The state after that measurement would thus be (up to a normalization factor):

$$\bar{\psi}_1 = U_1(I+P_1)\left|\psi_{in}\right\rangle. \tag{2.21}$$

To take into account the extra rotation U_1, for the second stabilizer to be measured, we measure $\bar{P_2} = U_1 P_2 U_1^\dagger$ instead of P_2. The obtained state after measuring $\bar{P_2}$ will therefore be:

$$\begin{aligned} \bar{\psi}_2 \quad &= U_2 \cdot (I + U_1 P_2 U_1^\dagger) \cdot U_1 \cdot (I + P1)\left|\psi_{in}\right\rangle \\ &= U_2 U_1 \cdot (I + P_2) \cdot (I + P1)\left|\psi_{in}\right\rangle \\ &= U_2 U_1 \left|\psi_2\right\rangle \end{aligned} \tag{2.22}$$

We can generalize this for the N stabilizers. For the N_{th} stabilizer we measure:

$$\bar{P_N} = (U_{N-1}...U_1) \cdot P_N \cdot (U_{N-1}...U_1)^\dagger \tag{2.23}$$

The final output state will be:

$$\bar{\psi}_{out} = (U_N U_{N-1}...U_1)\left|\psi_{out}\right\rangle, \tag{2.24}$$

which is the target output state up to single qubit rotations ($U = U_N U_{N-1}...U_1$).

Another method to measure multiple stabilizers in a row is to replace each controlled X, Y or Z gate by its equivalent in our scheme following Figure 2.9d and finally compile the circuit to reduce the total number of gates (see chapter 6 for an example).

2.5.7. TWO-QUBIT GATE OPTIMIZATION

As shown in the previous sections, by selecting τ in resonance with the electron-nuclear dynamics, and selecting the number of pulses N such that the rotation angle is $\pi/2$, we can obtain the two qubit gate $R_x(\pm\pi/2)$. As there are many periodic resonances in the dynamical decoupling spectrum (as shown in Fig. 2.8), we aim to select the resonant τ which would lead to the best gate performance. In addition, for practical reasons, we

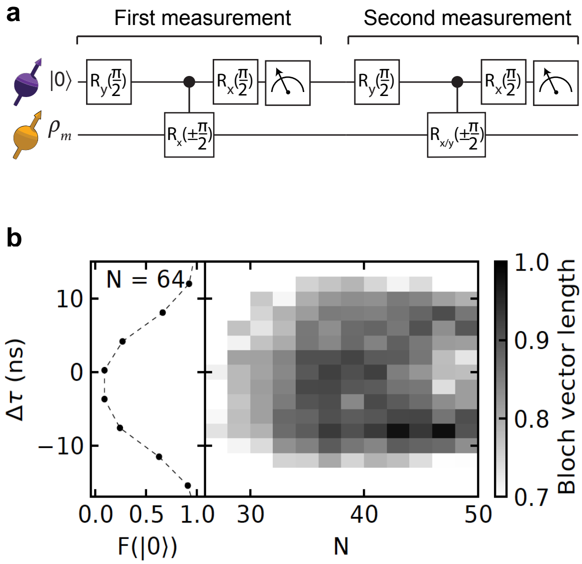

Figure 2.13: Optimization of the electron-nuclear two-qubit gates. a) Experimental sequence used for gate optimization. Two sequential measurements of the nuclear spin are performed using DD gates with roughly chosen parameters near a certain resonance. The second measurement is performed in both X- and Y-bases (to get $\langle I_x \rangle$,$\langle I_y \rangle$). b) An example showing the dependence of the measured Bloch vector length ($\sqrt{\langle I_x \rangle^2 + \langle I_y \rangle^2}$) with N and $\Delta\tau$. The previous process is then repeated for other potentially promising resonances and we then choose the optimal gate configuration. Figure adapted from Kalb [31].

can allow slight detuning in the resonance condition τ which provides more flexibility to optimize τ and N for a better gate performance [17, 19, 31]. Ideally, the combination of (τ, N) maximizes the gate fidelity by 1) Minimizing the interaction with non-targeted spins such that the electron only entangles with the target (i.e. minimizes crosstalk); 2) Setting the rotation angle ϕ as close as possible to $\pi/2$, such that a maximally entangled state is produced. Therefore, having flexibility in changing τ can help in reducing the discretization errors as N can only change in steps of 2 pulses.

To this end, we optimize our two-qubit gates by performing the sequence shown in Fig. 2.13a. We perform two sequential measurements of the nuclear spin using a DD gate with a (τ, N) combination that is roughly chosen near a certain resonance. To avoid systematic phase shifts on the nuclear spin due to detunings of the applied DD gate, we perform the second measurement in both X and Y bases and we then calculate the Bloch vector length in the XY-plane of the Bloch sphere $\sqrt{\langle I_x \rangle^2 + \langle I_y \rangle^2}$. Note that this constant phase shift is calibrated away after selecting the optimal parameters [31]. We then make 2D scans of τ and N used to implement the controlled rotation gates in both initialization and readout steps, and find the parameters that maximize the Bloch vector length. We then repeat the previous procedure for other potentially promising resonances and finally select the optimal gate configuration.

REFERENCES

[1] B. Naydenov, V. Richter, J. Beck, M. Steiner, P. Neumann, G. Balasubramanian, J. Achard, F. Jelezko, J. Wrachtrup, and R. Kalish, *Enhanced generation of single optically active spins in diamond by ion implantation,* App. Phys. Lett. **96**, 163108 (2010).

[2] S. Pezzagna, B. Naydenov, F. Jelezko, J. Wrachtrup, and J. Meijer, *Creation efficiency of nitrogen-vacancy centres in diamond,* New J. Phys. **12**, 065017 (2010).

[3] D. Twitchen, D. Hunt, M. Newton, J. Baker, T. Anthony, and W. Banholzer, *Electron paramagnetic resonance (EPR) and optical absorption studies of defects created in diamond by electron irradiation damage at 100 and 350 k,* PHYSICA B **273**, 628 (1999).

[4] Y.-C. Chen, P. S. Salter, S. Knauer, L. Weng, A. C. Frangeskou, C. J. Stephen, S. N. Ishmael, P. R. Dolan, S. Johnson, B. L. Green, *et al.*, *Laser writing of coherent colour centres in diamond,* Nat. Photon. **11**, 77 (2017).

[5] Y.-C. Chen, B. Griffiths, L. Weng, S. S. Nicley, S. N. Ishmael, Y. Lekhai, S. Johnson, C. J. Stephen, B. L. Green, G. W. Morley, M. E. Newton, M. J. Booth, P. S. Salter, and J. M. Smith, *Laser writing of individual nitrogen-vacancy defects in diamond with near-unity yield,* Optica **6**, 662 (2019).

[6] J. M. Smith, S. A. Meynell, A. C. B. Jayich, and J. Meijer, *Colour centre generation in diamond for quantum technologies,* Nanophotonics **8**, 1889 (2019).

[7] M. W. Doherty, N. B. Manson, P. Delaney, F. Jelezko, J. Wrachtrup, and L. C. L. Hollenberg, *The nitrogen-vacancy colour centre in diamond,* Phys. Rep. **528**, 1 (2013).

[8] D. D. Awschalom, R. Hanson, J. Wrachtrup, and B. B. Zhou, *Quantum technologies with optically interfaced solid-state spins,* Nat. Photonics **12**, 516 (2018).

[9] J. R. Maze, J. M. Taylor, and M. D. Lukin, *Electron spin decoherence of single nitrogen-vacancy defects in diamond,* Phys. Rev. B **78**, 094303 (2008).

[10] J. Taylor, P. Cappellaro, L. Childress, L. Jiang, D. Budker, P. Hemmer, A. Yacoby, R. Walsworth, and M. Lukin, *High-sensitivity diamond magnetometer with nanoscale resolution,* Nat. Phys. **4**, 810 (2008).

[11] G. de Lange, *Quantum control and coherence of interacting spins in diamond* (PhD Thesis, Delft, University of Technology, 2012).

[12] R. Schirhagl, K. Chang, M. Loretz, and C. L. Degen, *Nitrogen-vacancy centers in diamond: nanoscale sensors for physics and biology,* Annu. Rev. Phys. Chem. **65**, 83 (2014).

[13] C. L. Degen, F. Reinhard, and P. Cappellaro, *Quantum sensing,* Rev. Mod. Phys. **89**, 035002 (2017).

[14] N. Aslam, M. Pfender, P. Neumann, R. Reuter, A. Zappe, F. Fávaro de Oliveira, A. Denisenko, H. Sumiya, S. Onoda, J. Isoya, and J. Wrachtrup, *Nanoscale nuclear magnetic resonance with chemical resolution,* Science **357**, 67 (2017).

[15] D. R. Glenn, D. B. Bucher, J. Lee, M. D. Lukin, H. Park, and R. L. Walsworth, *High-resolution magnetic resonance spectroscopy using a solid-state spin sensor,* Nature **555**, 351 (2018).

[16] J. Wrachtrup and F. Jelezko, *Processing quantum information in diamond,* J. Condens. Matter Phys. **18**, S807 (2006).

[17] T. H. Taminiau, J. Cramer, T. van der Sar, V. V. Dobrovitski, and R. Hanson, *Universal control and error correction in multi-qubit spin registers in diamond,* Nat. Nanotech. **9**, 171 (2014).

[18] G. Waldherr, Y. Wang, S. Zaiser, M. Jamali, T. Schulte-Herbrueggen, H. Abe, T. Ohshima, J. Isoya, P. Neumann, and J. Wrachtrup, *Quantum error correction in a solid-state hybrid spin register,* Nature **506**, 204 (2014).

[19] J. Cramer, N. Kalb, M. A. Rol, B. Hensen, M. S. Blok, M. Markham, D. J. Twitchen, R. Hanson, and T. H. Taminiau, *Repeated quantum error correction on a continuously encoded qubit by real-time feedback,* Nat. Commun. **7**, 11526 (2016).

[20] H. Bernien, B. Hensen, W. Pfaff, G. Koolstra, M. S. Blok, L. Robledo, T. H. Taminiau, M. Markham, D. J. Twitchen, L. Childress, and R. Hanson, *Heralded entanglement between solid-state qubits separated by three metres,* Nature **497**, 86 (2013).

[21] W. Pfaff, B. J. Hensen, H. Bernien, S. B. v. Dam, M. S. Blok, T. H. Taminiau, M. J. Tiggelman, R. N. Schouten, M. Markham, D. J. Twitchen, and R. Hanson, *Unconditional quantum teleportation between distant solid-state quantum bits,* Science **345**, 532 (2014).

[22] B. Hensen, H. Bernien, A. E. Dréau, A. Reiserer, N. Kalb, M. S. Blok, J. Ruitenberg, R. F. L. Vermeulen, R. N. Schouten, C. Abellán, W. Amaya, V. Pruneri, M. W. Mitchell, M. Markham, D. J. Twitchen, D. Elkouss, S. Wehner, T. H. Taminiau, and R. Hanson, *Loophole-free Bell inequality violation using electron spins separated by 1.3 kilometres,* Nature **526**, 682 (2015).

[23] W. B. Gao, A. Imamoglu, H. Bernien, and R. Hanson, *Coherent manipulation, measurement and entanglement of individual solid-state spins using optical fields,* Nat. Photon. **9**, 363 (2015).

[24] S. Wehner, D. Elkouss, and R. Hanson, *Quantum internet: A vision for the road ahead,* Science **362** (2018).

[25] W. Pfaff, *Quantum measurement and entanglement of spin quantum bits in diamond* (PhD Thesis, Delft, University of Technology, 2013).

[26] H. Bernien, *Control, measurement and entanglement of remote quantum spin registers in diamond* (PhD Thesis, Delft, University of Technology, 2014).

[27] M. W. Doherty, N. B. Manson, P. Delaney, and L. C. L. Hollenberg, *The negatively charged nitrogen-vacancy centre in diamond: the electronic solution,* New J. Phys. **13**, 025019 (2011).

[28] B. Hensen, *Measurement-based quantum computation with the nitrogen-vacancy centre in diamond* (MSc Thesis, Delft, University of Technology, 2011).

[29] J. R. Maze, A. Gali, E. Togan, Y. Chu, A. Trifonov, E. Kaxiras, and M. D. Lukin, *Properties of nitrogen-vacancy centers in diamond: the group theoretic approach,* New J. Phys. **13**, 025025 (2011).

[30] B. Hensen, *Quantum nonlocality with spins in diamond* (PhD Thesis, Delft, University of Technology, 2016).

[31] N. Kalb, *Diamond-based quantum networks with multi-qubit nodes* (PhD Thesis, Delft, University of Technology, 2018).

[32] M. Doherty, F. Dolde, H. Fedder, F. Jelezko, J. Wrachtrup, N. Manson, and L. Hollenberg, *Theory of the ground-state spin of the nv- center in diamond,* Phys. Rev. B **85**, 205203 (2012).

[33] M. H. Abobeih, J. Randall, C. E. Bradley, H. P. Bartling, M. A. Bakker, M. J. Degen, M. Markham, D. J. Twitchen, and T. H. Taminiau, *Atomic-scale imaging of a 27-nuclear-spin cluster using a quantum sensor,* Nature **576**, 411 (2019).

[34] J. Cramer, N. Kalb, M. A. Rol, B. Hensen, M. S. Blok, M. Markham, D. J. Twitchen, R. Hanson, and T. H. Taminiau, *Repeated quantum error correction on a continuously encoded qubit by real-time feedback,* Nat. Commun. **7**, 1 (2016).

[35] L. Robledo, L. Childress, H. Bernien, B. Hensen, P. F. A. Alkemade, and R. Hanson, *High-fidelity projective read-out of a solid-state spin quantum register,* Nature **477**, 574 (2011).

[36] H. Bernien, B. Hensen, W. Pfaff, G. Koolstra, M. S. Blok, L. Robledo, T. H. Taminiau, M. Markham, D. J. Twitchen, L. Childress, and R. Hanson, *Heralded entanglement between solid-state qubits separated by three metres,* Nature **497**, 86 (2013).

[37] Y. Zhang, C. A. Ryan, R. Laflamme, and J. Baugh, *Coherent control of two nuclear spins using the anisotropic hyperfine interaction,* Phys. Rev. Lett. **107**, 170503 (2011).

[38] T. H. Taminiau, J. J. T. Wagenaar, T. van der Sar, F. Jelezko, V. V. Dobrovitski, and R. Hanson, *Detection and control of individual nuclear spins using a weakly coupled electron spin,* Phys. Rev. Lett. **109**, 137602 (2012).

[39] N. Zhao, J. Honert, B. Schmid, M. Klas, J. Isoya, M. Markham, D. Twitchen, F. Jelezko, R.-B. Liu, H. Fedder, and J. Wrachtrup, *Sensing single remote nuclear spins,* Nat. Nanotech. **7**, 657 (2012).

[40] S. Kolkowitz, Q. P. Unterreithmeier, S. D. Bennett, and M. D. Lukin, *Sensing distant nuclear spins with a single electron spin,* Phys. Rev. Lett. **109**, 137601 (2012).

[41] F. Shi, X. Kong, P. Wang, F. Kong, N. Zhao, R.-B. Liu, and J. Du, *Sensing and atomic-scale structure analysis of single nuclear-spin clusters in diamond,* Nat. Phys. **10**, 21 (2014).

[42] N. Zhao, J.-L. Hu, S.-W. Ho, J. T. K. Wan, and R. B. Liu, *Atomic-scale magnetometry of distant nuclear spin clusters via nitrogen-vacancy spin in diamond,* Nat. Nanotech. **6**, 242 (2011).

[43] J. Zopes, K. S. Cujia, K. Sasaki, J. M. Boss, K. M. Itoh, and C. L. Degen, *Three-dimensional localization spectroscopy of individual nuclear spins with sub-angstrom resolution,* Nat. Commun. **9**, 4678 (2018).

[44] J. Zopes, K. Herb, K. S. Cujia, and C. L. Degen, *Three-dimensional nuclear spin positioning using coherent radio-frequency control,* Phys. Rev. Lett. **121**, 170801 (2018).

[45] A. Ajoy, U. Bissbort, M. D. Lukin, R. L. Walsworth, and P. Cappellaro, *Atomic-scale nuclear spin imaging using quantum-assisted sensors in diamond,* Phys. Rev. X **5**, 011001 (2015).

[46] A. P. Nizovtsev, S. Y. Kilin, A. L. Pushkarchuk, V. A. Pushkarchuk, S. A. Kuten, O. A. Zhikol, S. Schmitt, T. Unden, and F. Jelezko, *Non-flipping* ^{13}*C spins near an NV center in diamond: hyperfine and spatial characteristics by density functional theory simulation of the c510[NV]h252 cluster,* New J. Phys. **20**, 023022 (2018).

[47] L. Childress, M. V. Gurudev Dutt, J. M. Taylor, A. S. Zibrov, F. Jelezko, J. Wrachtrup, P. R. Hemmer, and M. D. Lukin, *Coherent dynamics of coupled electron and nuclear spin qubits in diamond,* Science **314**, 281 (2006).

[48] M. G. Dutt, L. Childress, L. Jiang, E. Togan, J. Maze, F. Jelezko, A. Zibrov, P. Hemmer, and M. Lukin, *Quantum register based on individual electronic and nuclear spin qubits in diamond,* Science **316**, 1312 (2007).

[49] T. van der Sar, *Quantum control of single spins and single photons in diamond* (PhD Thesis, Delft, University of Technology, 2012).

[50] S. Kolkowitz, Q. P. Unterreithmeier, S. D. Bennett, and M. D. Lukin, *Sensing distant nuclear spins with a single electron spin,* Phys. Rev. Lett. **109**, 137601 (2012).

[51] G. d. Lange, Z. H. Wang, D. Ristè, V. V. Dobrovitski, and R. Hanson, *Universal dynamical decoupling of a single solid-state spin from a spin bath,* Science **330**, 60 (2010).

[52] T. van der Sar, Z. H. Wang, M. S. Blok, H. Bernien, T. H. Taminiau, D. M. Toyli, D. A. Lidar, D. D. Awschalom, R. Hanson, and V. V. Dobrovitski, *Decoherence-protected quantum gates for a hybrid solid-state spin register,* Nature **484**, 82 (2012).

[53] T. Gullion, D. B. Baker, and M. S. Conradi, *New, compensated Carr-Purcell sequences,* Journal of Magnetic Resonance **89**, 479 (1990).

[54] M. H. Abobeih, J. Cramer, M. A. Bakker, N. Kalb, M. Markham, D. Twitchen, and T. H. Taminiau, *One-second coherence for a single electron spin coupled to a multi-qubit nuclear-spin environment,* Nat. commun. **9**, 2552 (2018).

[55] K. Jung, M. H. Abobeih, J. Yun, G. Kim, H. Oh, H. Ang, T. H. Taminiau, and D. Kim, *Deep learning enhanced individual nuclear-spin detection,* arXiv:2006.13478 (2020).

[56] H. Oh, J. Yun, M. H. Abobeih, K.-H. Jung, K. Kim, T. H. Taminiau, and D. Kim, *Algorithmic decomposition for efficient multiple nuclear spin detection in diamond,* arXiv:2003.00178 (2020).

[57] J. M. Boss, K. Chang, J. Armijo, K. Cujia, T. Rosskopf, J. R. Maze, and C. L. Degen, *One-and two-dimensional nuclear magnetic resonance spectroscopy with a diamond quantum sensor,* Physical review letters **116**, 197601 (2016).

[58] C. E. Bradley, J. Randall, M. H. Abobeih, R. C. Berrevoets, M. J. Degen, M. A. Bakker, M. Markham, D. J. Twitchen, and T. H. Taminiau, *A ten-qubit solid-state spin register with quantum memory up to one minute,* Phys. Rev. X **9**, 031045 (2019).

[59] M. Bakker, *Frozen core spin dynamics in diamond* (MSc Thesis, Delft, University of Technology, 2015).

[60] D. Gottesman, *Stabilizer Codes and Quantum Error Correction,* arXiv:quant-ph/9705052 (1997).

[61] B. M. Terhal, *Quantum error correction for quantum memories,* Rev. Mod. Phys. **87**, 307 (2015).

3

ONE-SECOND COHERENCE FOR A SINGLE ELECTRON SPIN COUPLED TO A MULTI-QUBIT NUCLEAR-SPIN ENVIRONMENT

M. H. Abobeih, J. Cramer, M. A. Bakker, N. Kalb, M. Markham, D. J. Twitchen, T. H. Taminiau

Single electron spins coupled to multiple nuclear spins provide promising multi-qubit registers for quantum sensing and quantum networks. The obtainable level of control is determined by how well the electron spin can be selectively coupled to, and decoupled from, the surrounding nuclear spins. Here we realize a coherence time exceeding a second for a single nitrogen-vacancy electron spin through decoupling sequences tailored to its microscopic nuclear-spin environment. First, we use the electron spin to probe the environment, which is accurately described by seven individual and six pairs of coupled carbon-13 spins. We develop initialization, control and readout of the carbon-13 pairs in order to directly reveal their atomic structure. We then exploit this knowledge to store quantum states in the electron spin for over a second by carefully avoiding unwanted interactions. These results provide a proof-of-principle for quantum sensing of complex multi-spin systems and an opportunity for multi-qubit quantum registers with long coherence times.

The results of this chapter have been published in Nature Communications **9**, 2552 (2018).

3.1. INTRODUCTION

Coupled systems of individual electron and nuclear spins in solids are a promising platform for quantum information processing [1–6] and quantum sensing [7–11]. Initial experiments have demonstrated the detection and control of several nuclear spins surrounding individual defect or donor electron spins [12–17]. These nuclear spins provide robust qubits that enable enhanced quantum sensing protocols [7–11], quantum error correction [2, 3, 18], and multi-qubit nodes for optically connected quantum networks [19–22].

The level of control that can be obtained is determined by the electron spin coherence and therefore by how well the electron can be decoupled from unwanted interactions with its spin environment. Electron coherence times up to 0.56 s for a single electron spin qubit [5] and ~ 3 seconds for ensembles [23–26] have been demonstrated in isotopically purified samples depleted of nuclear spins, but in those cases the individual control of multiple nuclear-spin qubits is forgone.

Here we realize a coherence time exceeding one second for a single electron spin in diamond that is coupled to a complex environment of multiple nuclear-spin qubits. First, we use the electron spin as a quantum sensor to probe the microscopic structure of the surrounding nuclear-spin environment, including interactions between the nuclear spins. We find that the spin environment is accurately described by seven isolated single ^{13}C spins and six pairs of coupled ^{13}C spins (Fig. 3.1a). We then develop pulse sequences to initialize, control and readout the state of the ^{13}C-^{13}C pairs. We use this control to directly characterize the coupling strength between the ^{13}C spins, thus revealing their atomic structure given by the distance between the two ^{13}C atoms and the angle they make with the magnetic field. Finally, we exploit this extensive knowledge of the microscopic environment to realize tailored decoupling sequences that effectively protect arbitrary quantum states stored in the electron spin for well over a second. This combination of a long electron spin coherence time and selective couplings to a system of up to 19 nuclear spins provides a promising path to multi-qubit registers for quantum sensing and quantum networks.

3.2. SYSTEM

We use a single nitrogen vacancy (NV) center (Fig. 3.1a) in a CVD-grown diamond at a temperature of 3.7 K with a natural 1.1% abundance of ^{13}C and a negligible nitrogen concentration (< 5 parts per billion). A static magnetic field of $B_z \approx 403$ G is applied along the NV-axis with a permanent magnet (see section 3.9). The NV electron spin is read out in a single shot with an average fidelity of 95% through spin-selective resonant excitation [27]. The electron spin is controlled using microwave pulses through an on-chip stripline (see section 3.9).

3.3. LONGITUDINAL RELAXATION

We first address the longitudinal relaxation (T_1) of the NV electron spin, which sets a limit on the maximum coherence time. At 3.7 Kelvin, spin-lattice relaxation due to two-phonon Raman and Orbach-type processes are negligible [28, 29]. No cross relaxation to P1 or other NV centers is expected due to the low nitrogen concentration. The electron

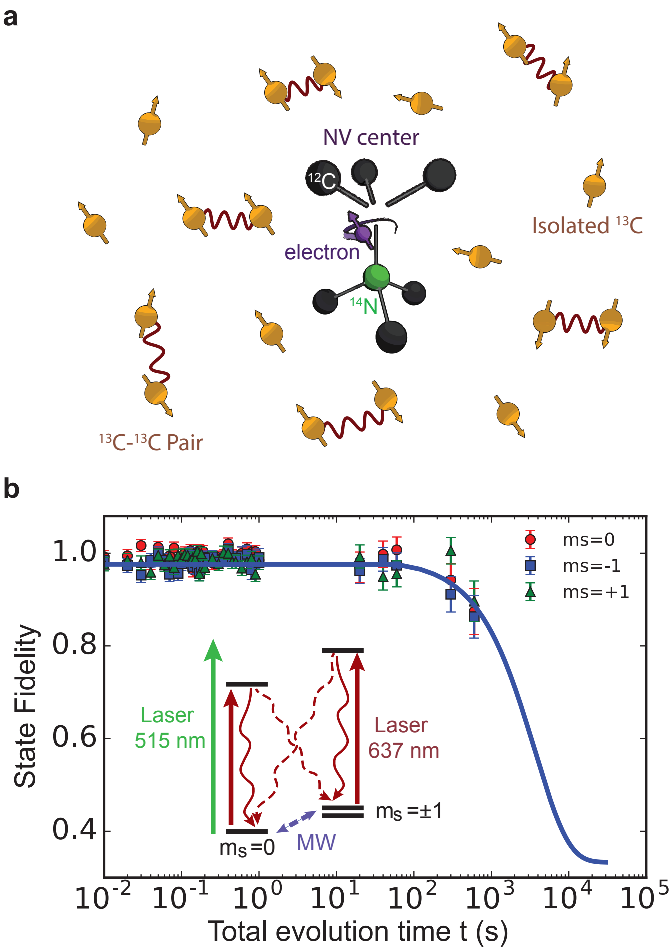

Figure 3.1: **Experimental system and T_1 measurements.** (a) We study a single nitrogen-vacancy (NV) center in diamond surrounded by a bath of ^{13}C nuclear spins (1.1% abundance). In this work, we show that the microscopic nuclear-spin environment is accurately described by 7 isolated ^{13}C spins, 6 pairs of coupled ^{13}C spins and a background bath of ^{13}C spins (not depicted). (b) Longitudinal relaxation of the NV electron spin. The spin is prepared in $m_s = 0, -1$, or $+1$ and the fidelity with the initial state is measured after time t. The inset shows the microwave (MW) and laser controls for the NV spin and charge states, as well as the pathways for spin relaxation induced by potential background noise from these controls. All error bars are one statistical s.d.

spin can, however, relax due to microwave noise and laser background introduced by the experimental controls (Fig. 3.1). We ensure a high on/off ratio of the lasers (> 100 dB) and use switches to suppress microwave amplifier noise (see section 3.9). Figure 3.1b shows the measured electron spin relaxation for all three initial states. We fit the average fidelity F to

$$F = 2/3e^{-t/T_1} + 1/3. \tag{3.1}$$

The obtained decay time T_1 is $(3.6 \pm 0.3) \cdot 10^3$ s. This value sets a lower limit for the spin relaxation time, and is the longest reported for a single electron spin qubit. Remarkably, the observed T_1 exceeds recent theoretical predictions based on single-phonon processes by more than an order of magnitude [30, 31]. To further investigate the origin of the decay, we prepare $m_s = 0$ and measure the total spin population summed over all three states. The total population decays on a similar timescale ($\sim 3.6 \cdot 10^3$ s), indicating that the decay is caused by a reduction of the measurement contrast, possibly due to drifts in the optical setup (see section 3.9), rather than by spin relaxation. This suggests that the spin-relaxation time significantly exceeds the measured T_1 value. Nevertheless, the long T_1 observed here already indicates that longitudinal relaxation is no longer a limiting factor for NV center coherence.

3.4. QUANTUM SENSING OF THE SPIN ENVIRONMENT.

To study the electron spin coherence, we first use the electron spin as a quantum sensor to probe its nuclear-spin environment through dynamical decoupling spectroscopy [12–14]. The electron spin is prepared in a superposition $|x\rangle = (|m_s = 0\rangle + |m_s = -1\rangle)/\sqrt{2}$ and a dynamical decoupling sequence of N π-pulses of the form $(\tau - \pi - \tau)^N$ is applied. The remaining electron coherence is then measured as a function of the time between the pulses 2τ. Loss of electron coherence indicates an interaction with the nuclear-spin environment.

The results in Fig. 3.2a for $N = 32$ pulses reveal a rich structure consisting of both sharp and broader dips in the electron coherence. The sharp dips (Fig. 3.2b) have been identified previously as resonances due to the electron spin undergoing an entangling operation with individual isolated ^{13}C spins in the environment [12–14]. For this NV center, the observed signal is well explained by seven individual ^{13}C spins and a background bath of randomly generated ^{13}C spins (Fig. 3.2b). To verify this explanation we perform direct Ramsey spectroscopy on all seven spins (Fig. 3.6) [3]. For the electron spin in $m_s = \pm 1$, each spin yields a single unique precession frequency due to the hyperfine coupling, indicating that all seven spins are distinct and do not couple strongly to other ^{13}C spins in the vicinity (See Fig. 3.6).

The electron can be efficiently decoupled from the interactions with such isolated ^{13}C spins by setting $\tau = m \cdot \frac{2\pi}{\omega_L}$, with m a positive integer and ω_L the ^{13}C Larmor frequency for $m_s = 0$ [33]. In practice, however, this condition might not be exactly and simultaneously met for all spins due to: the limited timing resolution of τ (here 1 ns), measurement uncertainty in the value ω_L, and differences between the $m_s = 0$ frequencies for different ^{13}C spins, for example caused by different effective g-tensors under a slightly misaligned magnetic field (here < 0.35°, section 3.10.3) [3, 33–35]. We numerically simulate these deviations from the ideal condition and find that, for our range of

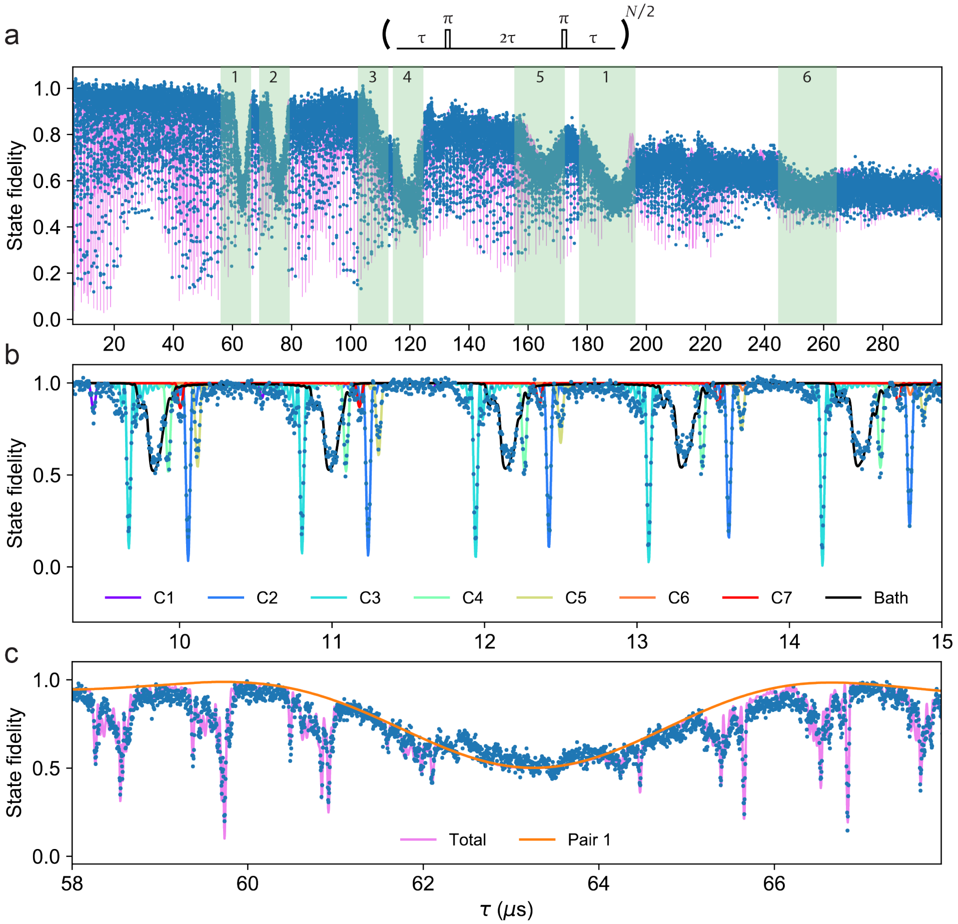

Figure 3.2: **Quantum sensing of the microscopic spin environment.** (a) Dynamical decoupling spectroscopy [13] revealing a rich nuclear-spin environment consisting of individual ^{13}C spins, as well as pairs of coupled ^{13}C spins. The electron spin is prepared in a superposition, $|x\rangle = (|m_s = 0\rangle + |m_s = -1\rangle)/\sqrt{2}$ and a decoupling sequence of $N = 32$ π-pulses separated by 2τ is applied. Loss of coherence indicates the interaction of the electron spin with nuclear spins in the environment. Blue: data. Purple line: theory (see section 3.9). The shaded areas mark the signals due to six ^{13}C-^{13}C pairs labeled 1 to 6. (b) Zoom-in showing sharp signals due to coupling to isolated individual ^{13}C spins [12–14]. The total signal is well described by seven ^{13}C spins (see Table 3.2 for hyperfine parameters) and a bath of 200 randomly generated spins with hyperfine couplings below 10 kHz. (c) Zoom-in showing a broad signal due to ^{13}C-^{13}C pair 1 [16, 32]. Blue: data. The solid orange line is the theoretical signal just due to pair 1, while the purple line includes the seven individual ^{13}C spins and the ^{13}C spin bath as well.

parameters, the effect on the electron coherence is small and can be neglected (Fig. 3.7).

We associate the broader dips in Fig. 3.2a and Fig. 3.2c to pairs of strongly coupled ^{13}C spins. Such ^{13}C - ^{13}C pairs were treated theoretically [32, 36] and the signal due to a single pair of nearest-neighbor ^{13}C spins with particularly strong couplings to a NV center has been detected [16]. In this work, we exploit improved coherence times to detect up to six pairs, including previously undetected non-nearest-neighbor pairs. We then develop pulse sequences to polarize and coherently control these pairs to be able to directly reveal their atomic structure through spectroscopy.

3.5. Direct spectroscopy of nuclear-spin pairs.

The evolution of ^{13}C - ^{13}C pairs can be understood from an approximate pseudo-spin model in the subspace spanned by $|\uparrow\downarrow\rangle = |\Uparrow\rangle$ and $|\downarrow\uparrow\rangle = |\Downarrow\rangle$, following Zhao et al. [32] (sections 3.10.1 and 3.10.2). The pseudo-spin Hamiltonian depends on the electron spin state. For $m_s = 0$ we have:

$$\hat{H}_0 = X\hat{S_x} \tag{3.2}$$

and for $m_s = -1$:

$$\hat{H}_1 = X\hat{S_x} + Z\hat{S_z} \tag{3.3}$$

where $\hat{S_x}$ and $\hat{S_z}$ are the spin-$\frac{1}{2}$ operators. X is the dipolar coupling between the ^{13}C spins and Z is due to the hyperfine field gradient (see section 3.9) [32]. The evolution of the ^{13}C - ^{13}C pair during a decoupling sequence will thus in general depend on the initial electron spin state, causing a loss of electron coherence.

We now show that this conditional evolution enables direct spectroscopy of the ^{13}C - ^{13}C dipolar interaction X. Consider two limiting cases: $X >> Z$ and $Z >> X$, which cover the pairs observed in this work. In both cases, loss of the electron coherence is expected for the resonance condition $\tau = \tau_k = (2k-1)\frac{\pi}{2\omega_r}$, with k a positive integer and resonance frequency $\omega_r = \sqrt{X^2 + (Z/2)^2}$ [13, 32, 37]. For $X >> Z$ the net evolution at resonance is a rotation around the z-axis with the rotation direction conditional on the initial electron state (mathematically analogous to the case of a single ^{13}C spin in a strong magnetic field [13, 38]). For $Z >> X$ the net evolution is a conditional rotation around the x-axis (analogous to the Nitrogen nuclear spin subjected to a driving field [37]). These conditional rotations provide the controlled gate operations required to initialize, coherently control and directly probe the pseudo-spin states.

The measurement sequences for the two cases are shown in Fig. 3.3a. First, a dynamical decoupling sequence is performed that correlates the electron state with the pseudo-spin state. Reading out the electron spin in a single shot then performs a projective measurement that prepares the pseudo-spin into a polarized state. For $X >> Z$ the pseudo-spin is measured along its z-axis and thus prepared in $|\Uparrow\rangle$. For $Z >> X$ the measurement is along the x-axis and the spin is prepared in $(|\Uparrow\rangle + |\Downarrow\rangle)/\sqrt{2}$. Second, we let the pseudo-spin evolve freely with the electron spin in one of its eigenstates ($m_s = 0$ or $m_s = -1$) so that we directly probe the precession frequencies $\omega_0 = X$ (for $m_s = 0$) or $\omega_1 = \sqrt{X^2 + Z^2}$ (for $m_s = -1$). For $Z >> X$, an extra complication is that the initial state $(|\Uparrow\rangle + |\Downarrow\rangle)/\sqrt{2}$ is an eigenstate of $\hat{H}_0$. To access $\omega_0 = X$, we prepare $(|\Uparrow\rangle + i|\Downarrow\rangle)/\sqrt{2}$ - a

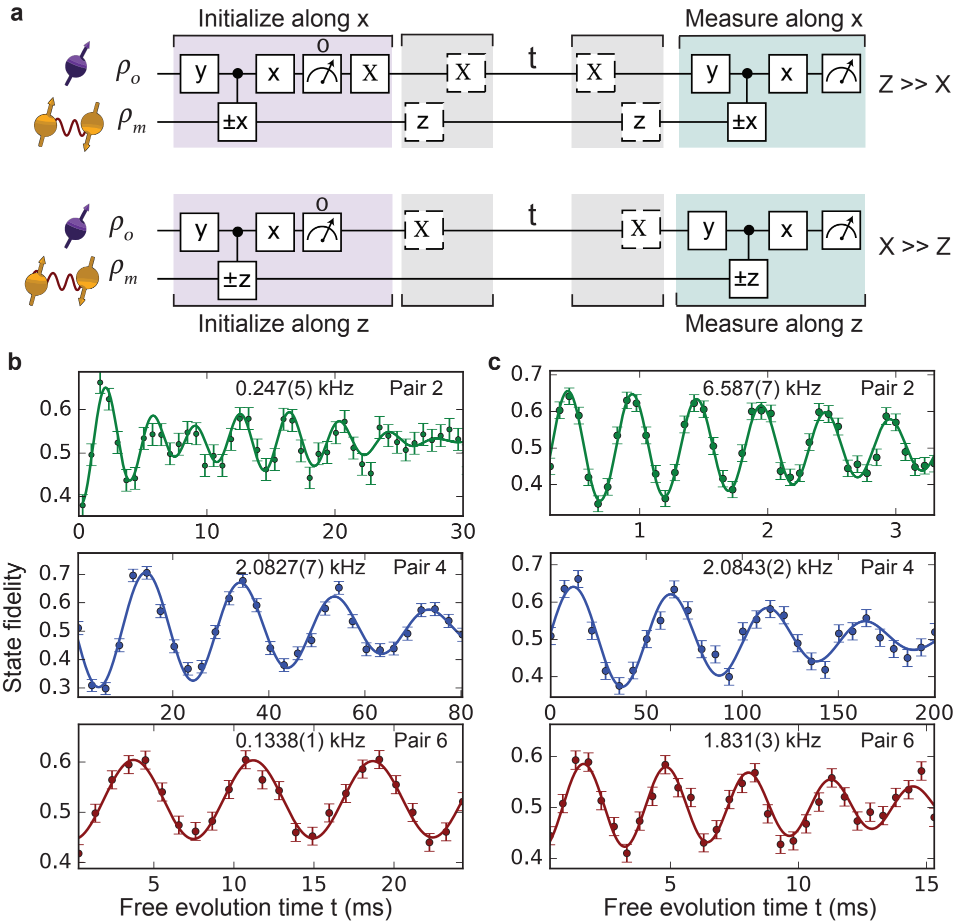

Figure 3.3: **Direct spectroscopy of nuclear-spin pairs.** (a) Measurement sequences for Ramsey spectroscopy of ^{13}C - ^{13}C pairs, for $Z >> X$ and for $X >> Z$. The controlled $\pm x$ ($\pm z$) gates are controlled $\pm\pi/2$ rotations around x (z) with the sign controlled by the electron state. (b,c) Nuclear spin Ramsey measurements and obtained precession frequencies for pairs 2, 4 and 6. The electron spin state during the free evolution time t is set to $m_s = 0$ (b) or $m_s = -1$ (c) and an artificial detuning is applied. Each pair yields a unique set of frequencies, confirming that the pairs are distinct. For pair 2 an additional beating is observed (frequency of 23(3) Hz), indicating a small coupling to one (or more) additional spins. See Fig. 3.8 for the other three pairs and Table 3.4 for fit results. All error bars are one statistical s.d.

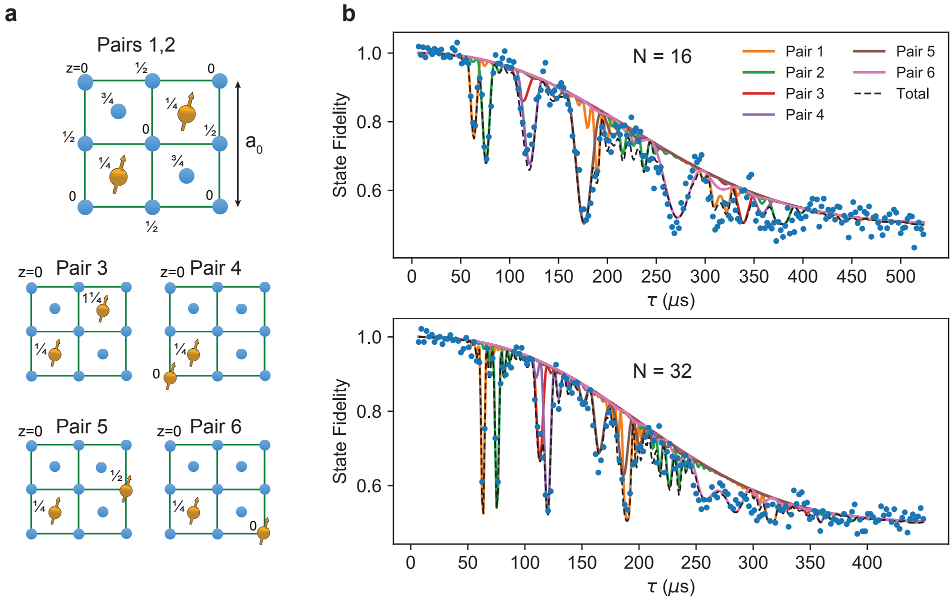

Figure 3.4: **Atomic structure and decoupling signal for the six nuclear-spin pairs.** (a) Structure of the six ^{13}C - ^{13}C pairs within the diamond unit cell (up to symmetries and equivalent orientations). The z values give the height in fractions of the diamond lattice constant a_0. The magnetic field is oriented along the $< 111 >$ direction, i.e. along the axis of pair 4. For pair 3 there is an additional possible structure that yields a similar X, see Table 3.3. (b) The calculated signal for the six individual ^{13}C - ^{13}C pairs accurately describes the measured decoupling signal for different number of pulses N. Data is taken for $\tau = m \cdot \frac{2\pi}{\omega_L}$ to avoid coupling to single ^{13}C spins. See Fig. 3.10 for other values of N.

superposition of $\hat{H}_0$ eigenstates - by first letting the system evolve under $\hat{H}_1$ for a time $\pi/(2\omega_1)$. Finally the state of the pseudo-spin is read out through a second measurement sequence.

We find six distinct sets of frequencies (Fig. 3.3b), indicating that six different ^{13}C - ^{13}C pairs are detected. The measurements for $m_s = 0$ directly yield the coupling strengths X and therefore the atomic structure of the pairs (Fig. 3.4a). We observe a variety of coupling strengths corresponding to nearest-neighbor pairs ($X/2\pi = 2082.7(7)$ Hz, theoretical value 2061 Hz) as well as pairs separated by several bond lengths (e.g. $X/2\pi = 133.8(1)$ Hz, theoretical value 133.4 Hz). The observed number of pairs is consistent with the ^{13}C concentration of the sample (Fig. 3.9). Note that for pair 4 we have $X >> Z$, so the resonance condition is mainly governed by the coupling strength X. This makes it likely that additional pairs with the same dipolar coupling X — but smaller Z values — contribute to the observed signal at $\tau = 120\ \mu$s. Nevertheless, the environment can be described accurately by the six identified pairs, which we verify by comparing the measured dynamical decoupling curves for different values of N to the calculated signal based on the extracted couplings (Fig. 3.4b).

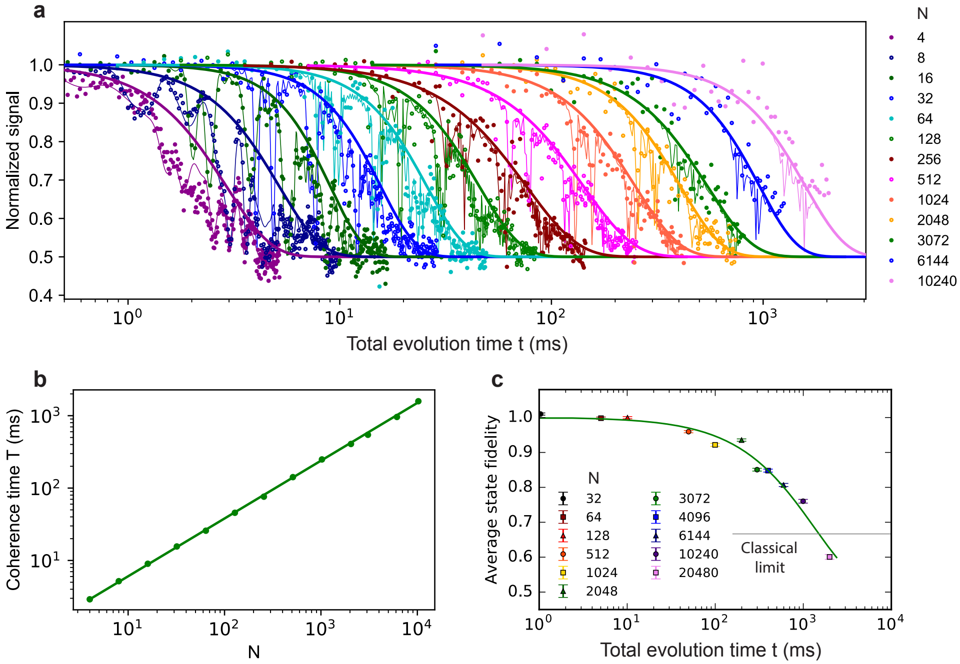

Figure 3.5: **Protecting quantum states with tailored decoupling sequences.** (a) Normalized signal under dynamical decoupling with the number of pulses varying from $N = 4$ to $N = 10240$. The electron is initialized and readout along x. The thin lines are fits to equation (3.4), which takes into account the six $^{13}C - ^{13}C$ pairs identified. We use the extracted amplitudes A to re-normalize the signal. Thick lines are the extracted envelops $(0.5 + 0.5 \cdot e^{-(t/T)^n})$ with T and n obtained from the fits. See Fig. 3.11 for the obtained values n. (b) Scaling of the obtained coherence time T as function of the number of pulses (error bars are $< 5\%$). The solid line is a fit to the power function $T_{N=4} \cdot (N/4)^{\eta}$, where $T_{N=4}$ is the coherence time for $N = 4$. We find $\eta = 0.799(2)$. (c) The average state fidelity obtained for the six cardinal states (Fig. 3.13). Unlike in (a), the signal is shown without any renormalization. The number of pulses N is chosen to maximize the obtained signal at the given total evolution time while avoiding interactions with the ^{13}C environment. The solid green line is a fit to an exponential decay. The horizontal line at $\frac{2}{3}$ fidelity marks the classical limit for storing quantum states. The two curves cross at $t = 1.46$ s demonstrating the protection of arbitrary quantum states well beyond a second. All error bars are one statistical s.d.

3.6. ELECTRON SPIN COHERENCE TIME.

Next, we exploit the obtained microscopic picture of the nuclear spin environment to investigate the electron spin coherence under dynamical decoupling. To extract the loss of coherence due to the remainder of the dynamics of the environment, i.e. excluding the identified signals from the ^{13}C spins and pairs, we fit the results to:

$$F = \frac{1}{2} + A \cdot M(t) \cdot e^{-(t/T)^n}, \tag{3.4}$$

in which $M(t)$ accounts for the signal due to the coupling to the ^{13}C-^{13}C pairs (Fig. 3.4b, see section 3.9). A, T and n are fit parameters that account for the decay of the envelope due to the rest of the dynamics of the environment and pulse errors. As before, effects of interactions with individual ^{13}C spins are avoided by setting $\tau = m \cdot \frac{2\pi}{\omega_L}$. An additional challenge is that at high numbers of pulses the electron spin becomes sensitive even to small effects, such as spurious harmonics due to finite MW pulse durations [39, 40] and non-secular Hamiltonian terms [41], which cause loss of coherence over narrow ranges of τ ($<$ 10 ns). Here, we avoid such effects by scanning a range of $\sim$ 20 ns around the target value to determine the optimum value of τ.

Figure 3.5a shows the electron coherence for sequences from $N = 4$ to 10240 pulses. The coherence times T, extracted from the envelopes, reveal that the electron coherence can be greatly extended by increasing the number of pulses N. The maximum coherence time is $T = 1.58(7)$ seconds for $N = 10240$ (Fig. 3.5b). We determine the scaling of T with N by fitting to $T_{N=4} \cdot (N/4)^{\eta}$, with $T_{N=4}$ the coherence time for $N = 4$ [23, 42–45] which gives $\eta = 0.799(2)$. No saturation of the coherence time T is observed yet, so that longer coherence times are expected to be possible. In our experiments, however, pulse errors become significant at larger N, causing a decrease in the amplitude A (see Fig. 3.12).

3.7. PROTECTING ARBITRARY QUANTUM STATES.

Finally, we demonstrate that arbitrary quantum states can be stored in the electron spin for well over a second by using decoupling sequences that are tailored to the specific microscopic spin environment (Fig. 3.5c). For a given storage time, we select τ and N to maximize the obtained fidelity by avoiding interactions with the characterized ^{13}C spins and ^{13}C-^{13}C pairs. To asses the ability to protect arbitrary quantum states, we average the storage fidelity over the six cardinal states and do not re-normalize the results. The results show that quantum states are protected with a fidelity above the 2/3 limit of a classical memory for at least 0.995 seconds (using $N = 10240$ pulses) and up to 1.46 seconds from interpolation of the results. These are the longest coherence times reported for single solid-state electron spin qubits [5], despite the presence of a dense nuclear spin environment that provides multiple qubits.

3.8. CONCLUSION

These results provide new opportunities for quantum sensing and quantum information processing, and are applicable to a wide variety of solid-state spin systems [4, 5, 17, 46–56]. First, these experiments are a proof-of-principle for resolving the microscopic structure of multi-spin systems, including the interactions between spins [32]. The developed methods might be applied to detect and control spin interactions in samples external to the host material [10, 57–59]. Second, the combination of long coherence times and selective control in an electron-nuclear system containing up to twenty spins enables improved multi-qubit quantum registers for quantum networks. The electron spin coherence now exceeds the time needed to entangle remote NV centers through a photonic link, making deterministic entanglement delivery possible [60]. Moreover, the realized control over multiple ^{13}C-^{13}C pairs provides promising new multi-qubit quantum memories with long coherence times, as the pseudo-spin naturally forms a decoherence-protected subspace [61].

3.9. METHODS

3.9.1. SETUP

The experiments are performed at 3.7 Kelvin (Montana Cryostation) with a magnetic field of ~403 G applied along the NV axis by a permanent magnet. We realize long relaxation ($T_1 > 1$ hour) and coherence times (> 1 second) in combination with fast spin operations (Rabi frequency of 14 MHz) and readout/initialization (~ 10 μs), by minimizing noise and background from the microwave (MW) and optical controls. Amplifier (AR 25S1G6) noise is suppressed by a fast microwave switch (TriQuint TGS2355-SM) with a suppression ratio of 40 dB. Video leakage noise generated by the switch is filtered with a high pass filter. We use Hermite pulse envelopes [62, 63] to obtain effective MW pulses without initialization of the intrinsic ^{14}N nuclear spin. To mitigate pulse errors we alternate the phases of the pulses following the $XY8$ scheme [64]. Laser pulses are generated by direct current modulation (515 nm laser, Cobolt MLD - for charge state control) or by acoustic optical modulators (637 nm Toptica DL Pro and New Focus TLB-6704-P – for spin pumping and single-shot readout [27]). The direct current modulation yields an on/off ratio of > 135 dB. By placing two modulators in series (Gooch and Housego Fibre Q) an on/off ratio of > 100 dB is obtained for the 637 nm lasers. The laser frequencies are stabilized to within 2 MHz using a wavemeter (HF-ANGSTROM WS/U-10U). Possible explanations for the observed decay in Fig. 3.1b are frequency drifts of this wavemeter or spatial drifts of the laser focus over one-hour timescales.

3.9.2. SAMPLE

We use a naturally occurring Nitrogen-Vacancy (NV) center in high-purity type IIa homoepitaxially chemical-vapor-deposition (CVD) grown diamond with a 1.1% natural abundance of ^{13}C and a ⟨111⟩ crystal orientation (Element Six). The NV center studied here has been selected for the absence of very-close-by strongly coupled ^{13}C spins (> 500 kHz hyperfine coupling), but not on any other properties of the nuclear spin environment. To enhance the collection efficiency a solid-immersion lens was fabricated on top of the NV center [27, 65] and a single-layer aluminum-oxide anti-reflection coating was deposited [66, 67].

3.9.3. DATA ANALYSIS.

We describe the total signal for the NV electron spin after a decoupling sequence in Fig. refch3:Figure2 as:

$$F = \frac{1}{2} + A \cdot M_{bath}(t) \cdot \prod_{i=1}^{7} M_C^i(t) \cdot \prod_{j=1}^{6} M_{pair}^j(t) \cdot e^{-(t/T)^n}, \tag{3.5}$$

where t is the total time. M_{bath} is the signal due to a randomly generated background bath of non-interacting spins with hyperfine couplings below 10 kHz. M_C^i are the signals due to the seven individual isolated ^{13}C spins [13]. M_{pair}^j are the signals due to the six $^{13}C - ^{13}C$ pairs and are given by $1/2 + Re(Tr(U_0 U_1^\dagger))/4$, with U_0 and U_1 the evolution operators of the pseudo-spin pair for the decoupling sequence conditional on the initial electron state ($m_s = 0$ or $m_s = -1$) [32]. The coherence time T and exponent n describe the decoherence due to remainder of the dynamics of the spin environment.

Setting $\tau = m \cdot 2\pi/\omega_L$ avoids the resonances due to individual ^{13}C spins, so that equation (3.5) reduces to:

$$F = \frac{1}{2} + A \cdot \prod_{j=1}^{6} M_{pair}^j(t) \cdot e^{-(t/T)^n}. \tag{3.6}$$

The data in Fig. 3.4 and 3.5 are fitted to equation (3.6) and A, T and n are extracted from these fits.

3.10. SUPPLEMENTARY INFORMATION

3.10.1. SYSTEM HAMILTONIAN.

The Hamiltonian describing a system composed of an NV center and a ^{13}C nuclear spin environment, in a suitable rotating frame and under the secular approximation can be described by:

$$\hat{H} = \sum_{i=1}^{n} (\omega_0 \hat{I}_z^i + A_\parallel^i \hat{S}_z \hat{I}_z^i + A_\perp^i \hat{S}_z \hat{I}_x^i) + \hat{H}_{n-n}, \tag{3.7}$$

where ω_o ($= 2\pi \cdot \gamma_c B_z$) is the Larmor frequency, $A_\parallel$ ($A_\perp$) is the parallel (perpendicular) hyperfine coupling between the electron and ^{13}C nuclear spin with respect to the applied static magnetic field. The dipolar interaction between ^{13}C nuclear spins in the environment H_{n-n} is given by:

$$\hat{H}_{n-n} = \sum_{i>j} \frac{\mu_o}{4\pi} \frac{\gamma_c^i \gamma_c^j}{r_{ij}^3} [\mathbf{I}^i \cdot \mathbf{I}^j - 3(\mathbf{I}^i \cdot \hat{r}_{ij})(\mathbf{I}^j \cdot \hat{r}_{ij})], \tag{3.8}$$

where γ_c is the gyromagnetic ratio of the nuclear spin, $\hat{r}_{ij}$ is the unit vector connecting the two nuclear spins and $\mathbf{I}^i$ is the spin-$\frac{1}{2}$ operator. Now we can rewrite the Hamiltonian as follows:

$$\hat{H} = |0\rangle\langle 0|\,\hat{H}_0 + |1\rangle\langle 1|\,\hat{H}_1, \tag{3.9}$$

$$\hat{H}_0 = \hat{H}_{n-n} + \sum_{i=1}^{n} \omega_0 \hat{I}_z^i, \tag{3.10}$$

$$\hat{H}_1 = \hat{H}_{n-n} + \sum_{i=1}^{n} (\omega_0 - A_\parallel^i)\hat{I}_z^i + A_\perp^i \hat{I}_x^i, \tag{3.11}$$

where H_0 (H_1) is the Hamiltonian describing the rest of the system if the electron is in the state $m_s = 0$ ($m_s = -1$).

3.10.2. PSEUDO-SPIN MODEL

Under high magnetic field, the dynamics of a $^{13}C - ^{13}C$ pair can be approximated by a pseudo-spin-$\frac{1}{2}$ model [14, 16], where the two anti-parallel spin states of the pair ($|\uparrow\downarrow\rangle$ and $|\downarrow\uparrow\rangle$) are mapped into spin-up ($|\Uparrow\rangle$) and spin-down ($|\Downarrow\rangle$) states of the pseudo-spin. The polarized states ($|\uparrow\uparrow\rangle$ and $|\downarrow\downarrow\rangle$) have large energy separation (due to large Zeeman energy) with respect to other states and thus do not play a role in the dynamics. Under these assumptions, the dynamics of the pseudo-spin can be described conditional on the electron spin state by the Hamiltonian:

$$\hat{H}_0 = X\hat{S}_x, \text{ and } \hat{H}_1 = X\hat{S}_x + Z\hat{S}_z, \tag{3.12}$$

where $\hat{H}_0$ ($\hat{H}_1$) is the Hamiltonian if the electron is in $m_s = 0$ ($m_s = -1$), X is the dipolar coupling strength between the two nuclear spins [32]:

$$X = \frac{\mu_0}{4\pi}\frac{\gamma_c^2}{r^3}\frac{1}{2}(1 - 3\cos^2\theta), \tag{3.13}$$

where γ_c is the gyromagnetic ratio of the ^{13}C nuclear spin, r is the distance between the two nuclear spins forming the pair, θ is the angle between the pair axis $\vec{r}$ and the external magnetic field direction ([1,1,1] in our case). Z is due to the hyperfine field gradient [16],

$$Z = Z_\parallel + Z_\perp = (A_\parallel^1 - A_\parallel^2) + \frac{(A_\perp^1)^2 - (A_\perp^2)^2}{2\pi \cdot \gamma_C B_0}. \tag{3.14}$$

Table 3.3 shows the calculated set of possible coupling strengths for pairs with different distances, r, and angles, θ, starting from the most strongly coupled pair (2.061 kHz) down to a coupling strength of 61 Hz. This is the range of interest for the pairs that we detect in this work. The values of the coupling strength X are distinct for different possible pairs and thus enable us to determine the distance between the two nuclear spins forming the pair and their orientation with respect to the external field. An exception is pair 3, for which two different types of pairs yield values close to the experimental value (see table 3.4). Although this information is enough to describe the dynamics under dynamical decoupling and the electron spin coherence, the measured value of Z for a single electron-spin state, i.e. $m_s = -1$ in our case, does not yet enable us to uniquely determine the relative position of the pair with respect to the NV. Measuring Z for $m_s = +1$ as well enables obtaining the two quantities $(A_\parallel^1 - A_\parallel^2)$ and $(A_\perp^1)^2 - (A_\perp^2)^2$, which would further narrow down the possible pair positions [16].

3.10.3. EFFECT OF MAGNETIC FIELD MISALIGNMENT ON ^{13}C PRECESSION FREQUENCIES

A misaligned field from the NV-axis would give rise to non-secular terms in the Hamiltonian leading to an effective g-tensor for ^{13}C nuclear spins that depends on the hyperfine coupling strength between the electron and the ^{13}C nuclear spin. For the electron in $m_s = 0$, this effective g-tensor can be calculated as follows [33]:

$$\hat{g}(m_s = 0) = \begin{bmatrix} 1+\eta A_{xx} & \eta A_{xy} & \eta A_{xz} \\ \eta A_{xy} & 1+\eta A_{yy} & \eta A_{yz} \\ 0 & 0 & 1 \end{bmatrix}, \tag{3.15}$$

where $\eta = \frac{2\gamma_e}{2\pi\cdot\gamma_c\Delta} = \frac{1}{2\pi}\cdot 1.824\cdot 10^{-3}\ \text{kHz}^{-1}$, and A_{mn} is the hyperfine tensor between the electron and ^{13}C nuclear spin. The ^{13}C precession frequency can now be calculated as $\omega_0 = \left|2\pi\gamma_c\vec{B}\cdot\hat{g}(0)\right|$ [33]. We estimate our magnetic field alignment to be better than 0.35 degrees, which corresponds to a maximum perpendicular field component of 2.5 G (see Table 3.1). Now if we assume that our field lies in xz-plane, i.e. $\vec{B} = B_z\hat{e_z} + B_x\hat{e_x}$, then $\vec{B}\cdot\hat{g} = B_x(1+\eta A_{xx})\hat{e_x} + \eta B_x A_{xy}\hat{e_y} + (\eta B_x A_{xz} + B_z)\hat{e_z}$, which leads to :

$$\omega_0 = 2\pi\cdot\gamma_c\sqrt{[B_x(1+\eta A_{xx})]^2 + [\eta B_x A_{xy}]^2 + [B_z + \eta B_x A_{xz}]^2} \tag{3.16}$$

In our case A_{xz} and A_{xx} range from $-2\pi\cdot 50$ to $2\pi\cdot 50$ kHz (at maximum), and the maximum value of B_x is 2.5 G. This means that different nuclear spins would have different precession frequencies, ω_0, depending on their hyperfine coupling parameters. The dominant term of change in ω_0 with the hyperfine coupling strengths, for our range of parameters, is $2\pi\cdot\gamma_c\eta B_x A_{xz}$, which would lead to a maximum difference in ω_0 of $2\pi\cdot 500$ Hz between different nuclear spins. This is consistent with what we experimentally observe (see Table 3.2).

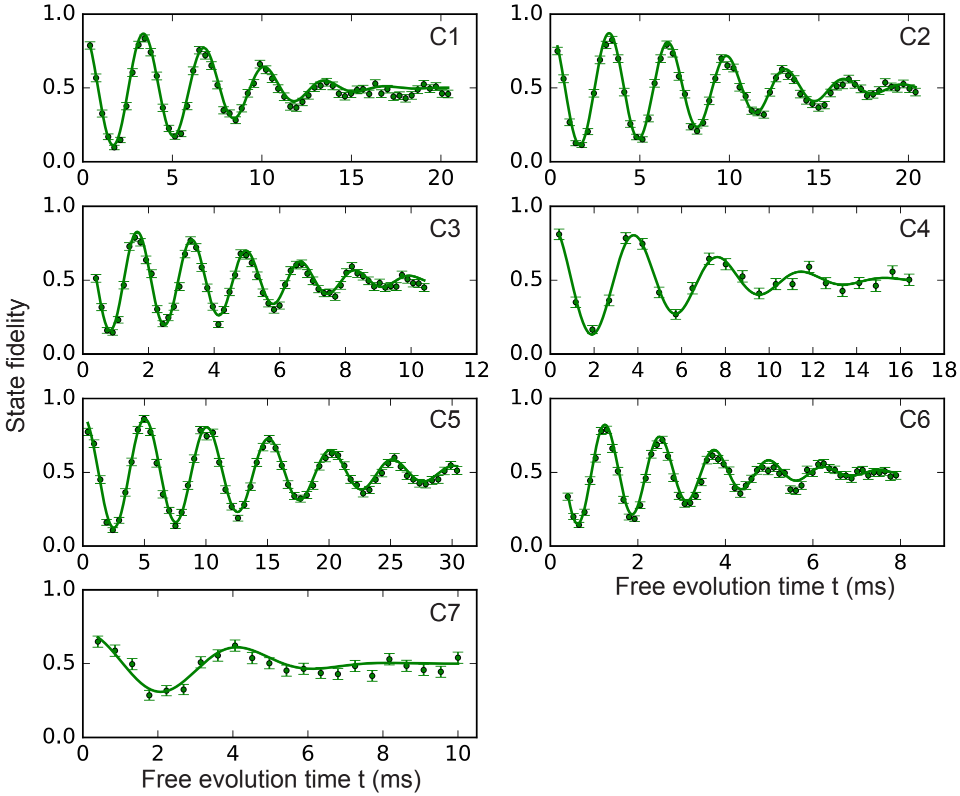

Figure 3.6: **Ramsey experiments for the seven individual ^{13}C spins.** Ramsey interferometry [3] for the ^{13}C nuclear spins. The electron spin state during the free evolution time is $m_s = -1$ (+1 for C4 and C7). Lines are sinusoidal fits with a Gaussian decay: $F = a + A \cdot e^{-(t/T_2^*)^2} \cos(\delta t + \phi)$, with t the free evolution time and δ a detuning. All seven spin signals are well described by a single, unique precession frequency $\omega_{\pm 1} \approx \omega_0 \pm A_\parallel$ (see Table 3.2) and a Gaussian decay, indicating that all seven spins are distinct and that none couple strongly to other ^{13}C spins in the environment. The minimum coupling strength for the observed ^{13}C-^{13}C pairs of 83 Hz (Table 3.4), would already introduce a clear beating in ~ 3 ms, indicating that the seven identified single ^{13}C spins are not part of the 6 detected ^{13}C - ^{13}C pairs.

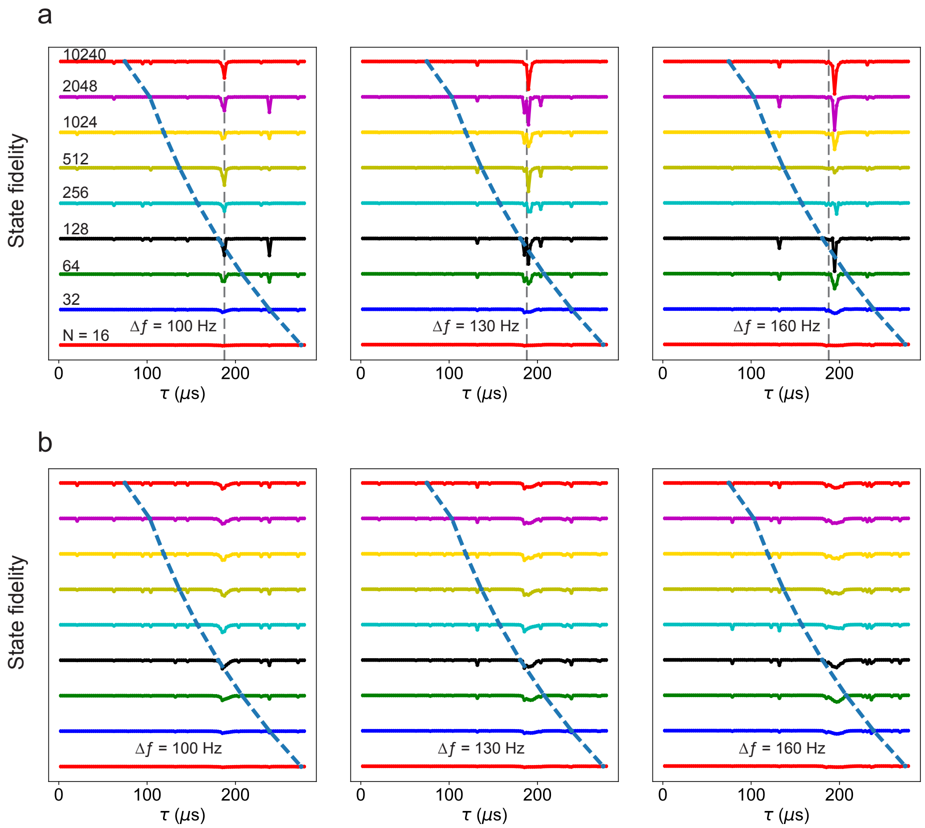

Figure 3.7: **Effect of deviations of τ from** $2\pi/\omega_0$**.** To avoid coupling to the single ^{13}C spins, we aim to set the interpulse spacing to the revival condition $\tau = m \cdot 2\pi/\omega_0$, with m an integer and ω_0 the ^{13}C frequency for $m_s = 0$ [33]. However, this condition is not met exactly and simultaneously in the experiments for all ^{13}C spins (section 3.10.3 and Table 3.2). Here we explore the effect of small deviations from this condition. **a)** Simulated electron spin fidelity after a decoupling sequence with $\tau = m \cdot \frac{2\pi}{\omega_L}$, with ω_L the ^{13}C Larmor frequency estimated from ESR measurements (Table 3.1). In these simulations we include the seven characterized ^{13}C spins and set all precession frequencies to $\omega_0 = \omega_L - \Delta\omega$. The curves show results for $\frac{\Delta\omega}{2\pi} = 100, 130$ and 160 Hz. The y-axis scale is such that the difference between horizontal lines at $\tau = 0$ is 1. The dashed blue line marks the $1/e$ decay times for different values of N (from Fig. 3.5); the main region of interest lies to the left of this line. Note that since the coherence time does not scale linearly with the number of pulses but rather with $N^{0.799}$, the $1/e$ value for τ becomes shorter for larger N. The vertical gray dashed line provides a visual aid to illustrate how the dip positions change with $\Delta\omega$. This shows that a change of 30 Hz in $\frac{\Delta\omega}{2\pi}$ leads to variations of the dip pattern. **b)** The obtained state fidelity averaged over 500 repetitions with ω_0 for the seven spins drawn from a Gaussian distribution with a mean frequency of $\omega_L - \Delta\omega$ and standard deviation of 30 Hz. These fluctuations match the typical observed values of $T_2{}^*$ for the nuclear spins. The result shows that differences in $m_s = 0$ frequencies for different ^{13}C spins are smeared out by dephasing, so that their net effect on the decoupling curves is small. Additionally, the interpulse delay is set with a precision of $\delta_p = 1$ ns. The maximum relative error occurs at short τ ($\tau = \tau_L$) and is of order $\delta_p/2\tau$. This is equivalent to a $\Delta\omega \sim 2\pi \cdot 100$ Hz, for which the simulations show a negligible effect at short τ. At larger τ ($\tau > 10\tau_L$) the relative error in τ quickly becomes negligible.

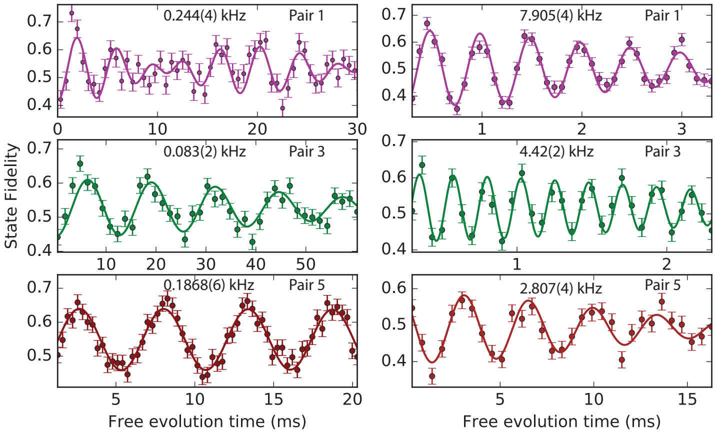

Figure 3.8: **Direct spectroscopy of ^{13}C-^{13}C pairs.** Ramsey spectroscopy for pairs 1, 3 and 5 and for electron state $m_s = 0$ (left) and $m_s = -1$ (right) during the free evolution time. The measurement sequence is shown in Fig. 3.3a. These pairs are all of the type $Z >> X$. For the measurements with $m_s = -1$ an artificial detuning was applied. Pair 1 shows an additional beating (frequency of 22(2) Hz) indicating a small coupling to one (or more) additional spins. Parameters and fit results are summarized in Table 3.4.

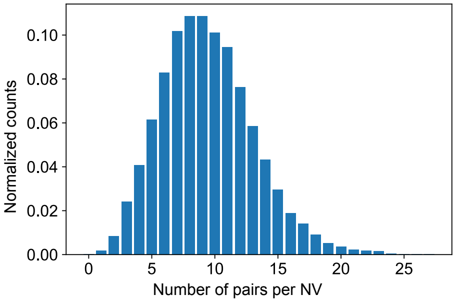

Figure 3.9: **Statistics for the number of ^{13}C pairs per NV center with coupling parameters in the range of the experimentally observed pairs.** To estimate if the observed number of pairs is consistent with the ^{13}C concentration (1.1%), we generate 10000 NV centers with random nuclear spin baths. For each NV, all pairs with coupling strength in the range $X = 2\pi \cdot 75$ Hz to $X = 2\pi \cdot 2061$ Hz are identified. For the range $2\pi \cdot 75$ Hz $\leqslant X \leqslant 2\pi \cdot 687$ Hz, we count the pairs for which the first resonance lies within our experimental window: $\tau_r = \frac{\pi}{2\omega_r} < 300$ μs, with $\omega_r = \sqrt{X^2 + (Z/2)^2}$. This lead to the condition: $\sqrt{X^2 + (Z/2)^2} > 2\pi \cdot 833$ Hz. For pairs with $X = 2\pi \cdot 2.061$ kHz the signal always lies within the 300 μs window, however for the signal strength to be significant Z must be sufficiently large. We count all such pairs with $Z > 50$ Hz. The resulting statistics for the total number of pairs per NV gives an average of 9.4 with a standard deviation of 3.7. Although this estimate doesn't take into account the all the subtleties of the possible dynamics of the pairs, it indicates that the number of observed pairs is consistent with the ^{13}C concentration.

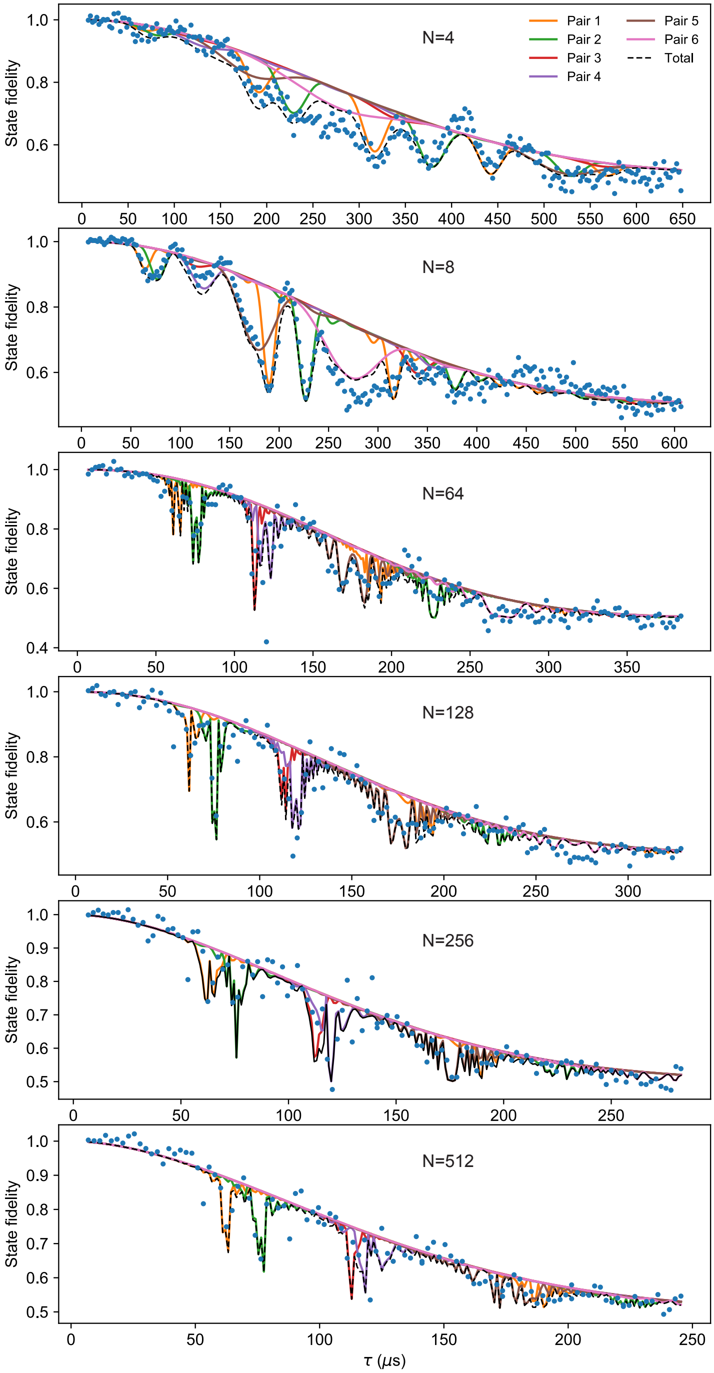

Figure 3.10: **Comparison of the calculated signal for the six $^{13}C-^{13}C$ pairs to the decoupling data.** Similar to the examples in Fig. 3.4 for N = 16 and 32, here we show extra examples for different N to confirm that the six identified $^{13}C-^{13}C$ pairs provide a good description of the dynamical decoupling data. $\tau = m \cdot \frac{2\pi}{\omega_L}$ to avoid effects of coupling to individual ^{13}C spins.

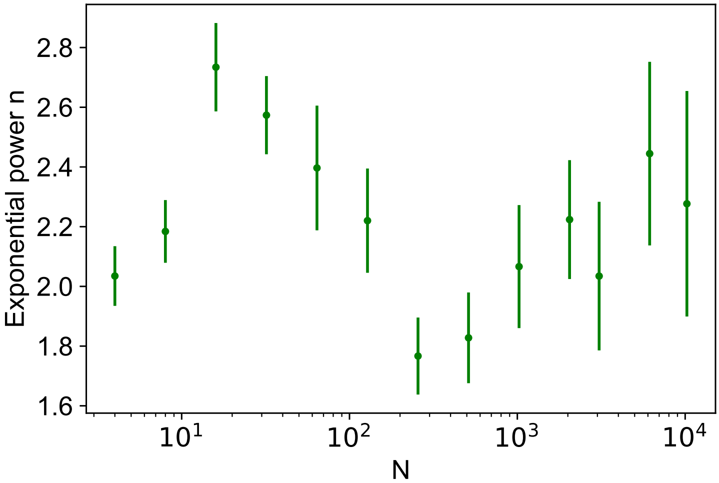

Figure 3.11: **Extracted exponent of the coherence decay.** Fitted values of n for the $e^{-(\tau/T)^n}$ envelop decay for the different numbers of pulses N in Fig. 3.5a. The fact that the value is around 2 even for $N = 10^4$ pulses confirms that coherence times are not yet limited by T_1 (expected $n = 1$ for T_1-limited case).

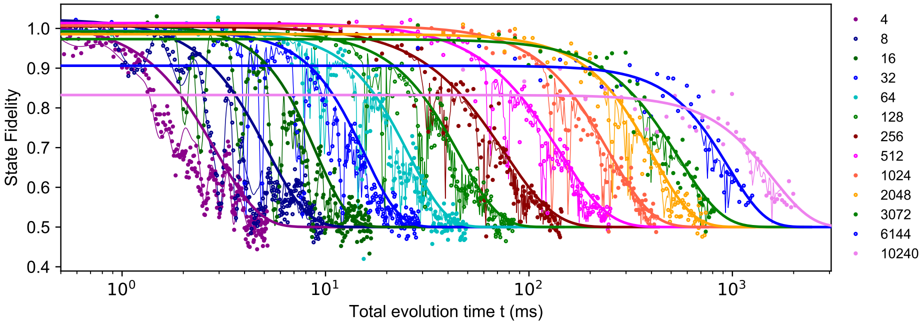

Figure 3.12: **Dynamical decoupling data of Fig. 3.5a without normalization.** Measured state fidelities under dynamical decoupling with the number of pulses varying from $N = 4$ to $N = 10240$. Pulse errors become significant for higher number of pulses causing a decrease in the initial amplitude A (see also Fig. 3.13).

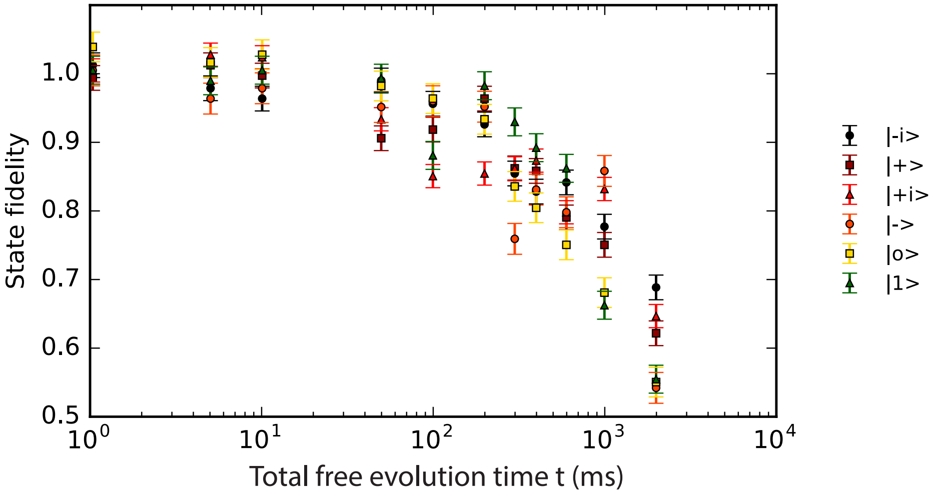

Figure 3.13: **State fidelity for the six states used in Fig. 3.5c.** We prepare the six states: $|0\rangle = |m_s = 0\rangle$, $|1\rangle = |m_s = -1\rangle$, $|\pm\rangle = (|0\rangle \pm |1\rangle)$, $|\pm i\rangle = (|0\rangle \pm i|1\rangle)$ and measure the fidelity of the final state with the ideal initial state. The curve in Fig. 3.5c in the main text is the average of these six state fidelities. The spin eigenstates $|0\rangle$ and $|1\rangle$ show a similar decay to the superposition states, indicating that the fidelities are likely limited by pulse errors.

$m_s = -1$ transition (f_{-1})	1.746666(3) GHz
$m_s = +1$ transition (f_{+1})	4.008580(3) GHz
Zero field splitting (Δ)	2.877623 GHz
Magnetic field B_z	403.553 G
Magnetic field stability	$3 \cdot 10^{-3}$ G
Magnetic field alignment	< 0.35 degrees
Electron T_2^*	4.9(2) μs
Electron T_2	1.182(5) ms
Electron T_1	$3.6(3) \cdot 10^3$ s
Frequency for pulse spacing $\omega_L/2\pi$	432.004 kHz
Period for pulse spacing τ_L	2.3147 μs
Electron Rabi freq.	14.31(3) MHz
NV strain	4.0 GHz

Table 3.1: **Experimental parameters.** $m_s = -1$ and $m_s = +1$ transitions are the obtained frequencies from electron spin resonance (ESR) measurements for the two spin transitions $0 \rightarrow -1$ and $0 \rightarrow +1$. Assuming a well-aligned field with the NV axis, the zero field splitting (ZFS) is the average of the two frequencies. The magnetic field B_z is the estimated field strength from $m_s = -1$ and $m_s = +1$ frequencies ($B_z = \frac{f_{+1}-f_{-1}}{2\gamma_e}$, $\gamma_e = 2.8024$ MHz/Gauss). The magnetic field stability is the standard deviation of the magnetic field measured continuously (typical measurement time is 80 s) for 5 hours, during which the magnetic field is re-calibrated every 30 minutes, just as during the actual measurements. The magnetic field is aligned with the NV axis by sweeping the magnet position in the transversal directions and minimizing $\frac{f_{+1}+f_{-1}}{2}$. The maximum deviation from the minimum is estimated to be 10 kHz. This implies a maximum perpendicular field $B_\perp$ of 2.5 G, equivalent to a maximum misalignment angle of 0.35 degrees. Electron T_2^* is the free induction decay of the electron spin measured in a Ramsey interference experiment. Electron T_2 is the 1/e decay time of a spin echo measurement. Electron T_1 is the electron relaxation time shown in Fig. 3.1. $\omega_L/2\pi$ is the ^{13}C Larmor frequency for $m_s = 0$ estimated from the ESR measurements ($\omega_L = 2\pi\gamma_c \cdot B_z$, $\gamma_c = 1.0705$ kHz/Gauss). τ_L is the estimated ^{13}C Larmor period ($\frac{2\pi}{\omega_L}$) as used for setting the half interpulse delay ($\tau = m \cdot \tau_L$) in the dynamical decoupling sequences. NV strain is the splitting of the excited states E_x and E_y due to strain perpendicular to the NV axis, measured by a resonant excitation spectroscopy at a temperature of 3.7 K.

	$\omega_0/2\pi$ (kHz)	$\omega_1/2\pi$ (kHz)	T_2^* (ms)	$A_\parallel/2\pi$ (kHz)	$A_\perp/2\pi$(kHz)
C1	431.994(3)	469.320(5)	10.2(4)	-36.4	25
C2	431.874(3)	413.739(1)	12.5(5)	20.6	43
C3	431.891(2)	447.209(2)	6.6(3)	-11.4	59
C4	431.947(3)	440.740(2)	8.3 (6)	8.1	21
C5	431.934(3)	408.303(3)	20.8(7)	24.4	26
C6	431.960(1)	480.607(4)	4.0(2)	-48.7	12
C7	431.95(1)	446.63(1)	5.0(7)	14.5	11

Table 3.2: **Spectroscopy of isolated ^{13}C.** ω_0 and ω_1 are the measured nuclear precession frequencies for $m_s = 0$ and $m_s = -1$ ($m_s = +1$ for C4 and C7), obtained from least-squares fits of the Ramsey signals (e.g. Fig. 3.6) to sinusoidal functions with Gaussian decays. T_2^* is the dephasing time for $m_s = -1$ ($m_s = +1$ for C4 and C7) obtained from the same fit. We use the variation in ω_0 for these spins as an estimate of how much ω_0 varies between spins. This variation can be explained by an effective g-tensor for ^{13}C nuclear spins, due to a slightly misaligned field (see section 3.10.3). We study how these variations can affect the dynamical decoupling signal in Fig. 3.7. $A_\parallel$ and $A_\perp$ are estimates for the hyperfine interaction components parallel and perpendicular to the applied magnetic field, obtained by matching theoretical signal (e.g. Fig. 3.2a, b) to the observed electron spin coherence. Uncertainties are estimated to be of the order of the last digit.

$\vec{r}$	r	θ (degrees)	$\lvert X\rvert/2\pi$ (Hz)
$\frac{a_0}{4}[1,1,1]$	$0.433a_0$	0	2061.0
$\frac{a_0}{4}[1,-1,1]$	$0.433a_0$	70.5	687.0
$\frac{a_0}{4}[\pm2,2,0]$	$0.707a_0$	35.3/90	236.7
$\frac{a_0}{4}[1,1,3]$	$0.829a_0$	29.5	186.8
$\frac{a_0}{4}[1,-3,1]$	$0.829a_0$	80.0	133.4
$\frac{a_0}{4}[3,1,3]$	$1.089a_0$	22.0	102.1
$\frac{a_0}{4}[3,3,3]$	$1.299a_0$	0	76.3
$\frac{a_0}{4}[2,2,4]$	$1.225a_0$	19.5	75.9
$\frac{a_0}{4}[3,-1,-3]$	$1.089a_0$	82.4	61.3

Table 3.3: **Main $^{13}C-^{13}C$ pairs in the diamond lattice and their calculated coupling strengths.** The coupling strength X is given by equation (3.13). $\vec{r}$ is the vector connecting the $^{13}C-^{13}C$ pair; θ is the angle between the pair axis and the external magnetic field which is along [1,1,1]. The distance between the two carbons forming the pair is r. The diamond lattice constant is taken to be $a_0 = 3.5668$ Å at 3.7 K [68]. This table shows pairs with coupling strength down to 61 Hz which covers the range of pairs that we observed in this work. For the pairs with $X = 236.7$ Hz two different angles with respect to the magnetic field are possible.

	τ (μs)	N	$\omega_0/2\pi$ (kHz)	$X_{theory}/2\pi$ (kHz)	$\omega_{-1}/2\pi$ (kHz)	$Z/2\pi$ (kHz)
Pair 1	63	14	0.244(3)	0.2367	7.894(9)	7.890(9)
Pair 2	76	10	0.247(6)	0.2367	6.587(7)	6.582(6)
Pair 3	111	26	0.083(2)	0.0759/0.0763	4.42(2)	4.42(2)
Pair 4	120	24	2.0827(7)	2.061	2.0843(2)	0.230
Pair 5	172	8	0.1868(6)	0.1868	2.807(4)	2.801(4)
Pair 6	277	8	0.1338(1)	0.1334	1.831(3)	1.826(3)

Table 3.4: **Parameters for the six $^{13}C-^{13}C$ pairs.** τ is half of the interpulse delay and N is the number of pulses in the decoupling sequence used to perform the conditional gates in the Ramsey measurement sequences shown in Fig. 3.3. ω_0 and ω_{-1} are the measured pseudo-spin precession frequencies for $m_s = 0$ and $m_s = -1$ respectively. $\omega_0/2\pi$ is a direct measurement of the coupling strength X and X_{theory} is the closest theoretical dipolar coupling strength to this value. This can be used to determine the atomic structure of the pair as shown in Table 3.3. Z is due to the hyperfine field gradient and is calculated from the measured ω_0 and ω_{-1}: $Z = \sqrt{\omega_{-1}^2 - \omega_0^2}$. Note that for pair 4 we have $X >> Z$, so the resonance condition is mainly governed by the coupling strength X (resonant $\tau \sim 120$ μs). Therefore, it is likely that additional pairs with the same X — but smaller Z values — contribute to the observed signal at 120 μs. Here we match the measured dynamical decoupling data for different values of N (see e.g. Fig. 3.4b) to the calculated signal for a single pair, and find that the results are accurately reproduced for $Z/2\pi = 0.230$ kHz. Note that for pair 3, there are two possible configurations with theoretical coupling strength close to the measured value.

REFERENCES

[1] W. Pfaff, T. H. Taminiau, L. Robledo, H. Bernien, M. Markham, D. J. Twitchen, and R. Hanson, *Demonstration of entanglement-by-measurement of solid-state qubits,* Nat. Phys. **9**, 29 (2013).

[2] G. Waldherr, Y. Wang, S. Zaiser, M. Jamali, T. Schulte-Herbruggen, H. Abe, T. Ohshima, J. Isoya, J. F. Du, P. Neumann, and J. Wrachtrup, *Quantum error correction in a solid-state hybrid spin register,* Nature **506**, 204 (2014).

[3] J. Cramer, N. Kalb, M. A. Rol, B. Hensen, M. S. Blok, M. Markham, D. J. Twitchen, R. Hanson, and T. H. Taminiau, *Repeated quantum error correction on a continuously encoded qubit by real-time feedback,* Nat. Commun. **7**, 11526 (2016).

[4] G. Wolfowicz, P.-A. Mortemousque, R. Guichard, S. Simmons, M. L. W. Thewalt, K. M. Itoh, and S. J. J. L. Morton, ^{29}*Si nuclear spins as a resource for donor spin qubits in silicon,* New J. Phys. **18**, 023021 (2016).

[5] J. T. Muhonen, J. P. Dehollain, A. Laucht, F. E. Hudson, R. Kalra, T. Sekiguchi, K. M. Itoh, D. N. Jamieson, J. C. McCallum, A. S. Dzurak, and A. Morello, *Storing quantum information for 30 seconds in a nanoelectronic device,* Nat. Nanotech. **9**, 986 (2014).

[6] J. P. Dehollain, S. Simmons, J. T. Muhonen, R. Kalra, A. Laucht, F. Hudson, K. M. Itoh, D. N. Jamieson, J. C. McCallum, A. S. Dzurak, *et al.*, *Bell's inequality violation with spins in silicon,* Nat. Nanotech. **11**, 242 (2016).

[7] S. Zaiser, T. Rendler, I. Jakobi, T. Wolf, S.-Y. Lee, S. Wagner, V. Bergholm, T. Schulte-Herbrüggen, P. Neumann, and J. Wrachtrup, *Enhancing quantum sensing sensitivity by a quantum memory,* Nat. Commun. **7**, 12279 (2016).

[8] M. Pfender, N. Aslam, H. Sumiya, S. Onoda, P. Neumann, J. Isoya, C. A. Meriles, and J. Wrachtrup, *Nonvolatile nuclear spin memory enables sensor-unlimited nanoscale spectroscopy of small spin clusters,* Nat. Commun. **8**, 834 (2017).

[9] T. Rosskopf, J. Zopes, J. M. Boss, and C. L. Degen, *A quantum spectrum analyzer enhanced by a nuclear spin memory,* NPJ Quantum Inf. **3**, 33 (2017).

[10] I. Lovchinsky, A. O. Sushkov, E. Urbach, N. P. de Leon, S. Choi, K. De Greve, R. Evans, R. Gertner, E. Bersin, Müller, *et al.*, *Nuclear magnetic resonance detection and spectroscopy of single proteins using quantum logic,* Science **351**, 836 (2016).

[11] T. Unden, P. Balasubramanian, D. Louzon, Y. Vinkler, M. B. Plenio, M. Markham, D. Twitchen, A. Stacey, I. Lovchinsky, A. O. Sushkov, M. D. Lukin, A. Retzker, B. Naydenov, L. P. McGuinness, and F. Jelezko, *Quantum metrology enhanced by repetitive quantum error correction,* Phys. Rev. Lett. **116**, 230502 (2016).

[12] S. Kolkowitz, Q. P. Unterreithmeier, S. D. Bennett, and M. D. Lukin, *Sensing distant nuclear spins with a single electron spin,* Phys. Rev. Lett. **109**, 137601 (2012).

[13] T. H. Taminiau, J. J. T. Wagenaar, T. van der Sar, F. Jelezko, V. V. Dobrovitski, and R. Hanson, *Detection and control of individual nuclear spins using a weakly coupled electron spin,* Phys. Rev. Lett. **109**, 137602 (2012).

[14] N. Zhao, J. Honert, B. Schmid, M. Klas, J. Isoya, M. Markham, D. Twitchen, F. Jelezko, R.-B. Liu, H. Fedder, and J. Wrachtrup, *Sensing single remote nuclear spins,* Nat. Nanotech. **7**, 657 (2012).

[15] C. Müller, X. Kong, J. M. Cai, K. Melentijević, A. Stacey, M. Markham, D. Twitchen, J. Isoya, S. Pezzagna, J. Meijer, J. F. Du, M. B. Plenio, B. Naydenov, L. P. McGuinness, and F. Jelezko, *Nuclear magnetic resonance spectroscopy with single spin sensitivity,* Nat. Commun. **5**, 4703 (2014).

[16] F. Shi, X. Kong, P. Wang, F. Kong, N. Zhao, R.-B. Liu, and J. Du, *Sensing and atomic-scale structure analysis of single nuclear-spin clusters in diamond,* Nat. Phys. **10**, 21 (2014).

[17] S.-Y. Lee, M. Widmann, T. Rendler, M. W. Doherty, T. M. Babinec, S. Yang, M. Eyer, P. Siyushev, B. J. Hausmann, M. Loncar, *et al.*, *Readout and control of a single nuclear spin with a metastable electron spin ancilla,* Nat. Nanotech. **8**, 487 (2013).

[18] N. Kalb, J. Cramer, D. J. Twitchen, M. Markham, R. Hanson, and T. H. Taminiau, *Experimental creation of quantum zeno subspaces by repeated multi-spin projections in diamond,* Nat. Commun. **7**, 13111 (2016).

[19] B. Hensen, H. Bernien, A. E. Dreau, A. Reiserer, N. Kalb, M. S. Blok, J. Ruitenberg, R. F. L. Vermeulen, R. N. Schouten, C. Abellan, W. Amaya, V. Pruneri, M. W. Mitchell, M. Markham, D. J. Twitchen, D. Elkouss, S. Wehner, T. H. Taminiau, and R. Hanson, *Loophole-free bell inequality violation using electron spins separated by 1.3 kilometres,* Nature **526**, 682 (2015).

[20] S. Yang, Y. Wang, D. D. B. Rao, T. Hien Tran, A. S. Momenzadeh, MarkhamM, D. J. Twitchen, P. Wang, W. Yang, R. Stöhr, P. Neumann, H. Kosaka, and J. Wrachtrup, *High-fidelity transfer and storage of photon states in a single nuclear spin,* Nat. Photon. **10**, 507 (2016).

[21] A. Reiserer, N. Kalb, M. S. Blok, K. J. M. van Bemmelen, T. H. Taminiau, R. Hanson, D. J. Twitchen, and M. Markham, *Robust quantum-network memory using decoherence-protected subspaces of nuclear spins,* Phys. Rev. X **6**, 021040 (2016).

[22] N. Kalb, A. A. Reiserer, P. C. Humphreys, J. J. W. Bakermans, S. J. Kamerling, N. H. Nickerson, S. C. Benjamin, D. J. Twitchen, M. Markham, and R. Hanson, *Entanglement distillation between solid-state quantum network nodes,* Science **356**, 928 (2017).

[23] N. Bar-Gill, L. M. Pham, A. Jarmola, D. Budker, and R. L. Walsworth, *Solid-state electronic spin coherence time approaching one second,* Nat. Commun. **4**, 1743 (2013).

[24] A. M. Tyryshkin, S. Tojo, J. J. L. Morton, H. Riemann, N. V. Abrosimov, P. Becker, H.-J. Pohl, T. Schenkel, M. L. W. Thewalt, K. M. Itoh, and S. A. Lyon, *Electron spin coherence exceeding seconds in high-purity silicon,* Nat. Mater. **11**, 143 (2012).

[25] G. Wolfowicz, S. Simmons, A. M. Tyryshkin, R. E. George, H. Riemann, N. V. Abrosimov, P. Becker, H.-J. Pohl, S. A. Lyon, M. L. W. Thewalt, and J. J. L. Morton, *Decoherence mechanisms of* ^{209}*bi donor electron spins in isotopically pure* ^{28}*si,* Phys. Rev. B **86**, 245301 (2012).

[26] G. Wolfowicz, A. M. Tyryshkin, R. E. George, H. Riemann, N. V. Abrosimov, P. Becker, H.-J. Pohl, M. L. W. Thewalt, S. A. Lyon, and J. J. L. Morton, *Atomic clock transitions in silicon-based spin qubits,* Nat. Nanotech. **8**, 561 (2013).

[27] L. Robledo, L. Childress, H. Bernien, B. Hensen, P. F. A. Alkemade, and R. Hanson, *High-fidelity projective read-out of a solid-state spin quantum register,* Nature **477**, 574 (2011).

[28] S. Takahashi, R. Hanson, J. van Tol, M. S. Sherwin, and D. D. Awschalom, *Quenching spin decoherence in diamond through spin bath polarization,* Phys. Rev. Lett. **101**, 047601 (2008).

[29] A. Jarmola, V. M. Acosta, K. Jensen, S. Chemerisov, and D. Budker, *Temperature- and magnetic-field-dependent longitudinal spin relaxation in nitrogen-vacancy ensembles in diamond,* Phys. Rev. Lett. **108**, 197601 (2012).

[30] T. Astner, J. Gugler, A. Angerer, S. Wald, S. Putz, N. J. Mauser, M. Trupke, H. Sumiya, S. Onoda, J. Isoya, *et al., Solid-state electron spin lifetime limited by phononic vacuum modes,* Nature materials **17**, 313 (2018).

[31] A. Norambuena, E. Muñoz, H. T. Dinani, A. Jarmola, P. Maletinsky, D. Budker, and J. R. Maze, *Spin-lattice relaxation of individual solid-state spins,* Phys. Rev. B **97**, 094304 (2018).

[32] N. Zhao, J.-L. Hu, S.-W. Ho, J. T. K. Wan, and R. B. Liu, *Atomic-scale magnetometry of distant nuclear spin clusters via nitrogen-vacancy spin in diamond,* Nat. Nanotech. **6**, 242 (2011).

[33] L. Childress, M. V. Gurudev Dutt, J. M. Taylor, A. S. Zibrov, F. Jelezko, J. Wrachtrup, P. R. Hemmer, and M. D. Lukin, *Coherent dynamics of coupled electron and nuclear spin qubits in diamond,* Science **314**, 281 (2006).

[34] J. Maze, J. Taylor, and M. Lukin, *Electron spin decoherence of single nitrogen-vacancy defects in diamond,* Physical Review B **78**, 094303 (2008).

[35] P. L. Stanwix, L. M. Pham, J. R. Maze, D. Le Sage, T. K. Yeung, P. Cappellaro, P. R. Hemmer, A. Yacoby, M. D. Lukin, and R. L. Walsworth, *Coherence of nitrogen-vacancy electronic spin ensembles in diamond,* Physical Review B **82**, 201201 (2010).

[36] Z.-Y. Wang, J. Casanova, and M. B. Plenio, *Delayed entanglement echo for individual control of a large number of nuclear spins,* Nat. Commun. **8**, 14660 (2017).

[37] T. van der Sar, Z. H. Wang, M. S. Blok, H. Bernien, T. H. Taminiau, D. M. Toyli, D. A. Lidar, D. D. Awschalom, R. Hanson, and V. V. Dobrovitski, *Decoherence-protected quantum gates for a hybrid solid-state spin register,* Nature **484**, 82 (2012).

[38] T. H. Taminiau, J. Cramer, T. van der Sar, V. V. Dobrovitski, and R. Hanson, *Universal control and error correction in multi-qubit spin registers in diamond,* Nat. Nanotech. **9**, 171 (2014).

[39] M. Loretz, J. M. Boss, T. Rosskopf, H. J. Mamin, D. Rugar, and C. L. Degen, *Spurious harmonic response of multipulse quantum sensing sequences,* Phys. Rev. X **5**, 021009 (2015).

[40] J. E. Lang, J. Casanova, Z.-Y. Wang, M. B. Plenio, and T. S. Monteiro, *Enhanced resolution in nanoscale NMR via quantum sensing with pulses of finite duration,* Phys. Rev. Applied **7**, 054009 (2017).

[41] A. Ajoy, Y. Liu, and P. Cappellaro, *Dc magnetometry at the T_2 limit,* ArXiv , 1611.04691 (2016).

[42] G. de Lange, Z. H. Wang, D. Ristè, V. V. Dobrovitski, and R. Hanson, *Universal dynamical decoupling of a single solid-state spin from a spin bath,* Science **330**, 60 (2010).

[43] C. A. Ryan, J. S. Hodges, and D. G. Cory, *Robust decoupling techniques to extend quantum coherence in diamond,* Phys. Rev. Lett. **105**, 200402 (2010).

[44] B. Naydenov, F. Dolde, L. T. Hall, C. Shin, H. Fedder, L. C. Hollenberg, F. Jelezko, and J. Wrachtrup, *Dynamical decoupling of a single-electron spin at room temperature,* Phys. Rev. B **83**, 081201 (2011).

[45] J. Medford, L. Cywiński, C. Barthel, C. M. Marcus, M. P. Hanson, and A. C. Gossard, *Scaling of dynamical decoupling for spin qubits,* Phys. Rev. Lett. **108**, 086802 (2012).

[46] H. Seo, A. L. Falk, P. V. Klimov, K. C. Miao, G. Galli, and D. D. Awschalom, *Quantum decoherence dynamics of divacancy spins in silicon carbide,* Nat. Commun. **7**, 12935 (2016).

[47] M. Widmann, S.-Y. Lee, T. Rendler, N. Tien Son, H. Fedder, S. Paik, L.-P. Yang, N. Zhao, S. Yang, I. Booker, A. Denisenko, M. Jamali, S. A. Momenzadeh, I. Gerhardt, T. Ohshima, A. Gali, E. Janzén, and J. Wrachtrup, *Coherent control of single spins in silicon carbide at room temperature,* Nat. Mater. **14**, 164–168 (2014).

[48] A. L. Falk, P. V. Klimov, V. Ivády, K. Szász, D. J. Christle, W. F. Koehl, A. Gali, and D. D. Awschalom, *Optical polarization of nuclear spins in silicon carbide,* Phys. Rev. Lett. **114**, 247603 (2015).

[49] L.-P. Yang, C. Burk, M. Widmann, S.-Y. Lee, J. Wrachtrup, and N. Zhao, *Electron spin decoherence in silicon carbide nuclear spin bath,* Phys. Rev. B **90**, 241203 (2014).

[50] L. J. Rogers, K. D. Jahnke, M. H. Metsch, A. Sipahigil, J. M. Binder, T. Teraji, H. Sumiya, J. Isoya, M. D. Lukin, P. Hemmer, and F. Jelezko, *All-optical initialization, readout, and coherent preparation of single silicon-vacancy spins in diamond,* Phys. Rev. Lett. **113**, 263602 (2014).

[51] D. D. Sukachev, A. Sipahigil, C. T. Nguyen, M. K. Bhaskar, R. E. Evans, F. Jelezko, and M. D. Lukin, *Silicon-vacancy spin qubit in diamond: A quantum memory exceeding 10 ms with single-shot state readout,* Phys. Rev. Lett. **119**, 223602 (2017).

[52] J. N. Becker, B. Pingault, D. Groß, M. Gündoğan, N. Kukharchyk, M. Markham, A. Edmonds, M. Atatüre, P. Bushev, and C. Becher, *All-optical control of the silicon-vacancy spin in diamond at millikelvin temperatures,* Phys. Rev. Lett. **120**, 053603 (2018).

[53] B. C. Rose, D. Huang, Z.-H. Zhang, P. Stevenson, A. M. Tyryshkin, S. Sangtawesin, S. Srinivasan, L. Loudin, M. L. Markham, A. M. Edmonds, *et al.*, *Observation of an environmentally insensitive solid-state spin defect in diamond,* Science **361**, 60 (2018).

[54] P. Siyushev, M. H. Metsch, A. Ijaz, J. M. Binder, M. K. Bhaskar, D. D. Sukachev, A. Sipahigil, R. E. Evans, C. T. Nguyen, M. D. Lukin, P. R. Hemmer, Y. N. Palyanov, I. N. Kupriyanov, Y. M. Borzdov, L. J. Rogers, and F. Jelezko, *Optical and microwave control of germanium-vacancy center spins in diamond,* Phys. Rev. B **96**, 081201 (2017).

[55] J. J. Pla, F. A. Mohiyaddin, K. Y. Tan, J. P. Dehollain, R. Rahman, G. Klimeck, D. N. Jamieson, A. S. Dzurak, and A. Morello, *Coherent control of a single* ^{29}Si *nuclear spin qubit,* Phys. Rev. Lett. **113**, 246801 (2014).

[56] T. Iwasaki, Y. Miyamoto, T. Taniguchi, P. Siyushev, M. H. Metsch, F. Jelezko, and M. Hatano, *Tin-vacancy quantum emitters in diamond,* Phys. Rev. Lett. **119**, 253601 (2017).

[57] G. Kucsko, P. Maurer, N. Y. Yao, M. Kubo, H. Noh, P. Lo, H. Park, and M. D. Lukin, *Nanometer scale thermometry in a living cell,* Nature **500**, 54 (2013).

[58] F. Shi, Q. Zhang, P. Wang, H. Sun, J. Wang, X. Rong, M. Chen, C. Ju, F. Reinhard, H. Chen, *et al.*, *Single-protein spin resonance spectroscopy under ambient conditions,* Science **347**, 1135 (2015).

[59] J.-P. Tetienne, T. Hingant, J.-V. Kim, L. H. Diez, J.-P. Adam, K. Garcia, J.-F. Roch, S. Rohart, A. Thiaville, D. Ravelosona, *et al.*, *Nanoscale imaging and control of domain-wall hopping with a nitrogen-vacancy center microscope,* Science **344**, 1366 (2014).

[60] P. C. Humphreys, N. Kalb, J. P. Morits, R. N. Schouten, R. F. Vermeulen, D. J. Twitchen, M. Markham, and R. Hanson, *Deterministic delivery of remote entanglement on a quantum network,* Nature **558**, 268 (2018).

[61] D. A. Lidar, I. L. Chuang, and K. B. Whaley, *Decoherence-free subspaces for quantum computation,* Phys. Rev. Lett. **81**, 2594 (1998).

[62] L. M. K. Vandersypen and I. L. Chuang, *NMR techniques for quantum control and computation,* Rev. Mod. Phys. **76**, 1037 (2005).

[63] W. S. Warren, *Effects of arbitrary laser or NMR pulse shapes on population inversion and coherence,* J. Chem. Phys. **81**, 5437 (1984).

[64] T. Gullion, D. B. Baker, and M. S. Conradi, *New, compensated Carr-Purcell sequences,* Journal of Magnetic Resonance **89**, 479 (1990).

[65] J. P. Hadden, J. P. Harrison, A. C. Stanley-Clarke, L. Marseglia, Y.-L. D. Ho, B. R. Patton, J. L. O'Brien, and J. G. Rarity, *Strongly enhanced photon collection from diamond defect centers under microfabricated integrated solid immersion lenses,* App. Phys. Lett. **97**, 241901 (2010).

[66] W. Pfaff, B. J. Hensen, H. Bernien, S. B. v. Dam, M. S. Blok, T. H. Taminiau, M. J. Tiggelman, R. N. Schouten, M. Markham, D. J. Twitchen, and R. Hanson, *Unconditional quantum teleportation between distant solid-state quantum bits,* Science **345**, 532 (2014).

[67] T. K. Yeung, D. L. Sage, L. M. Pham, P. L. Stanwix, and R. L. Walsworth, *Anti-reflection coating for nitrogen-vacancy optical measurements in diamond,* App. Phys. Lett. **100**, 251111 (2012).

[68] S. Stoupin and Y. V. Shvyd'ko, *Thermal expansion of diamond at low temperatures,* Phys. Rev. Lett. **104**, 085901 (2010).

4

ATOMIC-SCALE MAGNETIC RESONANCE IMAGING USING A QUANTUM SENSOR

**M. H. Abobeih, J. Randall, C. E. Bradley, H. P. Bartling, M. A. Bakker, M. J. Degen,
M. Markham, D. J. Twitchen, T. H. Taminiau**

Nuclear magnetic resonance (NMR) is a powerful method for determining the structure of molecules and proteins [1]. Whereas conventional NMR requires averaging over large ensembles, recent progress with single-spin quantum sensors [2–9] has created the prospect of magnetic imaging of individual molecules [10–13]. As an initial step towards this goal, isolated nuclear spins and spin pairs have been mapped [14–21]. However, large clusters of interacting spins—such as those found in molecules—result in highly complex spectra. Imaging these complex systems is an outstanding challenge because it requires high spectral resolution and efficient spatial reconstruction with sub-angstrom precision. Here we realize such atomic-scale imaging using a single nitrogen-vacancy (NV) center as a quantum sensor, and demonstrate it on a model system of 27 *coupled* ^{13}C *nuclear spins in a diamond. We present a multidimensional spectroscopy method that isolates individual nuclear-nuclear spin interactions with high spectral resolution (*< 80 *mHz) and high accuracy (*2 *mHz). We show that these interactions encode the composition and interconnectivity of the cluster, and develop methods to extract the 3D structure of the cluster with sub-angstrom resolution. Our results demonstrate a key capability towards magnetic imaging of individual molecules and other complex spin systems [9–13].*

The results of this chapter have been published in Nature **576**,7787 (2019).

4.1. INTRODUCTION

The nitrogen-vacancy (NV) center in diamond has emerged as a powerful quantum sensor [2–13, 22, 23]. The NV electron spin provides long coherence times [5, 6, 20] and high-contrast optical readout [5, 24, 25], enabling high sensitivity over a large range of temperatures [5, 6, 20, 25, 26]. Pioneering experiments with near-surface NV centers have demonstrated spectroscopy of small ensembles of nuclear spins in nano-scale volumes [2, 3, 5–8], and electron-spin labelled proteins [4]. Furthermore, single nuclear spin sensitivity has been demonstrated and isolated individual nuclear spins and spin pairs have been mapped [14–21]. Together, these results have established the NV center as a promising platform for magnetic imaging of complex spin systems and single molecules [10–13].

In this work, we realise a key ability towards that goal: the 3D imaging of large nuclear-spin structures with atomic resolution. The main idea of our method is to obtain structural information by accessing the couplings between individual nuclear spins. Three key elements are: (1) realising high spectral resolution so that small couplings can be accessed, (2) isolating such couplings from complex spectra, and (3) transforming the revealed connectivity into the 3D spatial structure with sub-angstrom precision.

The basic elements of our experiment are illustrated in Fig. 4.1a. We consider a cluster of ^{13}C nuclear spins in the vicinity of a single NV center in diamond at 4 Kelvin. This cluster provides a model system for the magnetic imaging of single molecules and spin structures external to the diamond. Each ^{13}C spin precesses at a shifted frequency due to the hyperfine interaction with the electron spin, resembling a chemical shift in traditional NMR [1, 27]. These shifts enable different nuclear spins in the cluster to be distinguished.

4.2. MULTIDIMENSIONAL SPECTROSCOPY

We use the NV electron spin as a sensor to probe the nuclear-nuclear interactions (Fig. 4.1b). Inspired by NMR spectroscopy [1, 27], we develop sequences that employ spin-echo double-resonance (SEDOR) techniques to isolate and measure individual couplings with high spectral resolution. First, we polarise a nuclear “probe" spin (frequency $RF1$) using recently developed quantum sensing sequences that can detect spins in any direction from the NV, enabling access to a large number of spins (see section 4.7) [28]. Second, we let this probe spin evolve for a time t and apply N echo pulses that decouple it from the other spins and environmental noise. Simultaneously, pulses on a “target" spin in the cluster (frequency $RF2$) re-couple it to the probe spin, selecting the interaction between these two spins. Finally, a second sensing sequence detects the resulting polarisation of the probe spin through a high-contrast readout of the electron spin (see section 4.7), which enables fast data collection. This double-resonance sequence provides a high spectral resolution through a long nuclear phase accumulation time. Importantly, the resolution is not limited by the relatively short coherence time of the electron spin sensor (see section 4.7) [24, 29].

It is instructive to first consider the case without echo pulses ($N = 0$). In such a Ramsey-type measurement [24–26, 29, 30], all couplings act simultaneously. This results in complex spectra that indicate the presence of multiple spins and many nuclear-

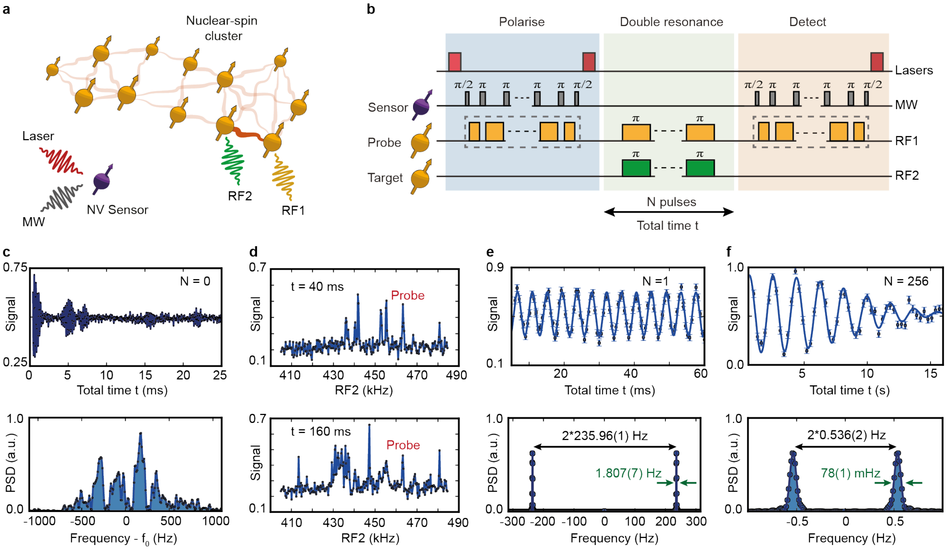

Figure 4.1: **Basic concepts of the experiment. a,** We consider an individual cluster of ^{13}C nuclear spins near a single NV center in diamond. To obtain the 3D structure of the cluster we use the NV electron spin as a quantum sensor to measure nuclear-nuclear spin couplings. **b,** Experimental sequence. The NV sensor is used to polarise and detect the “probe” spin(s) at frequency $RF1$ (see section 4.7). A double-resonance sequence of N echo pulses is applied simultaneously on the probe spin(s) ($RF1$) and the “target” spin(s) ($RF2$), so that the coupling between these spins is selectively detected. See Fig. 4.5 for the detailed sequence. **c,** A Ramsey signal ($N = 0$) for a nuclear spin in the cluster (detuning $f_0 = 5$ kHz relative to $RF1 = 455.37$ kHz). Because all couplings are probed simultaneously, the power spectral density (PSD) yields a complex non-resolvable spectrum. See Fig. 4.6 for more examples. **d,** Double-resonance spectroscopy ($N = 1$). Sweeping the target frequency ($RF2$) reveals all spins that couple to the probe spin(s). For larger t, more peaks appear as weaker couplings become visible. $RF1 = 463.27$ kHz. **e,** Sweeping the evolution time t for a fixed $RF1$ and $RF2$ reveals the coupling strength between spins. This example reveals a 235.96(1) Hz coupling between two spins with a spectral resolution of 1.807(7) Hz FWHM. $RF1 = 463.27$ kHz and $RF2 = 455.37$ kHz. **f,** An example with $N = 256$ echo pulses showing an extended coherence time to 10.9(5) seconds, which enables selective measurements of sub-Hz couplings with high spectral resolution (78(1) mHz) and precision (2 mHz). $RF1 = 408.32$ kHz and $RF2 = 413.48$ kHz. All graphs: see section 4.7 for fit functions. Error bars are one standard deviation, a.u. indicates arbitrary units.

nuclear spin interactions in the cluster (Fig. 4.1c). However, this 1D measurement gives no direct information on the connectivity between spins. Additionally, the underlying structure of individual spins and couplings is obscured by the many frequencies (2^j for coupling to j spins) and the low spectral resolution of >30 Hz FWHM (set by the dipolar-broadened linewidth of the nuclear spins and inversely proportional to the dephasing time T_2^*).

In contrast, our double-resonance sequence enables couplings between specific spins to be isolated and measured with high resolution. We first scan the target frequency $RF2$ for a fixed probe frequency $RF1$ (Fig. 4.1d). This reveals the spectral positions of nuclear spins coupled to the probe spin. We then sweep the evolution time t and Fourier transform the signal to quantify the coupling strengths (Fig. 4.1e). For a single pulse ($N = 1$), the nuclear spin coherence time is $T_2 = 0.58(2)$ s, yielding a spectral resolution of 1.807(7) Hz and a center frequency accuracy of 10 mHz. The spectral resolution is set by the coherence of the sample spins and can be further enhanced by applying more echo pulses. For $N = 256$, a resolution of 78(1) mHz and an accuracy of 2 mHz are obtained, making it possible to detect sub-Hertz interactions (Fig. 4.1f). The obtained resolution is an improvement by a factor $\sim 10^3$ over Ramsey-type spectroscopy on the same type of sample (Fig. 4.1c) [18–21, 24, 26, 29], and is an order of magnitude higher than in previous experiments on other spin samples [6–8, 25, 30, 31].

To characterise the complete cluster, we perform 3D spectroscopy by varying the probe frequency $RF1$, the target frequency $RF2$, and the evolution time t. The combinations of $RF1$ and $RF2$ reveal the spectral positions of the spins in the cluster. The coupling between spins is retrieved from the Fourier transform along the time dimension t. This yields a 3D data set that in principle encodes the composition and connectivity of the spin cluster (Fig. 4.2).

4.3. RESOLVING SPECTRALLY OVERLAPPING SPINS

In general, multiple spins can have (near-)identical precession frequencies. This has two consequences. First, the echo pulses will invert these spins simultaneously, so that multiple couplings are probed at the same time. Figure 4.3a shows an example with one probe spin and three target spins. This example illustrates that, while the resulting spectra are more complex, the high spectral resolution of our method enables retrieval of the underlying nuclear-nuclear couplings even when several spins overlap spectrally.

Second, to determine the number of spins in the cluster, and to assign the measured couplings to them, we need to resolve the ambiguity introduced by the fact that multiple spins can overlap spectrally. For example, the observation of a coupling between frequencies $\{RF1, RF2\} = \{A, C\}$ and a coupling between frequencies $\{B, C\}$ is by itself not enough to determine if there are one or two spins with frequency C. Our method resolves such ambiguities by extracting an over-determined data set with many couplings that together constrain the problem. This enables individual spins to be uniquely identified from their connections to the rest of the cluster (see Fig. 4.3b for an example).

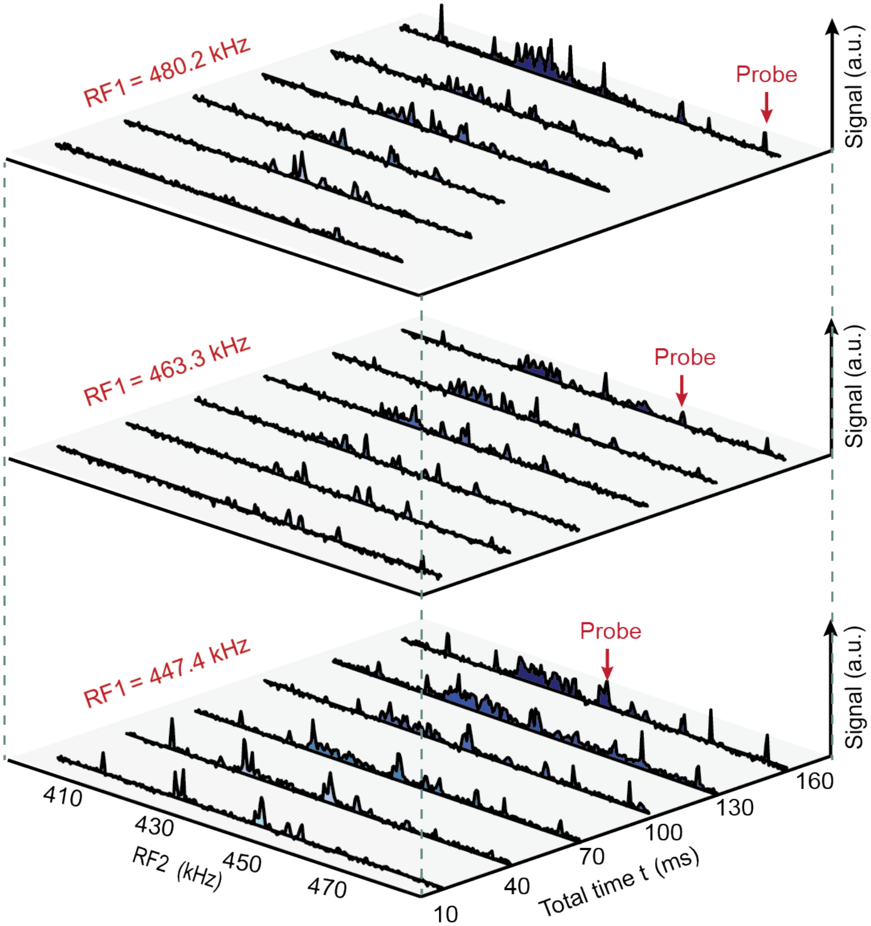

Figure 4.2: **Three-dimensional spectroscopy.** By varying the probe frequency $RF1$, the target frequency $RF2$, and the evolution time t, we obtain a three-dimensional data set that encodes the composition of the spins in the cluster and their couplings. The observation of a signal at $\{RF1, RF2\}$ indicates the presence of one or more spins at both frequencies and a coupling between them. The Fourier transform along the time dimension t reveals the spin-spin coupling strengths. Examples for three different $RF1$ values are shown.

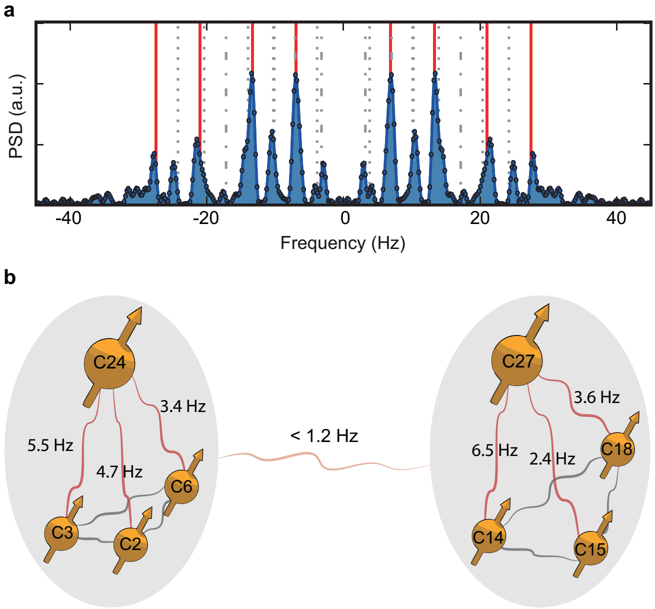

Figure 4.3: **Spectrally overlapping spins. a,** Retrieving couplings when multiple spins are re-coupled simultaneously. Example in which the echo pulses invert three target spins (quadruple resonance). The PSD reveals a complex, yet resolvable, spectrum. Red lines indicate the 8 frequencies $f = \pm f_1 \pm f_2 \pm f_3$, where $f_1 = 17.17(2)$ Hz, $f_2 = 7.05(3)$ Hz and $f_3 = 3.21(4)$ Hz are the extracted couplings of the probe spin to three target spins. Grey dashed lines mark additional frequency components that appear due to failures to invert one or two of the target spins (see Fig. 4.11 for detailed analysis). **b,** Overcoming ambiguity in identifying spins and assigning couplings. Example from the data. Spins C2, C3, C6, C14, C15 and C18 all yield a coupling signal to the same RF2 frequency. Because the couplings between these 6 spins reveal that they are part of two spatially separated sub-clusters, it follows that the signals at RF2 must originate from two distinct spins (C24 and C27).

4.4. CORRECTIONS FOR ELECTRON MEDIATED INTERACTIONS

Transforming the 3D spectra into a spatial structure requires a precise relation between the measured couplings and the relative positions of the spins. A complication is that the presence of electronic spins can modify the nuclear couplings [32], causing the measured value to deviate from a basic dipole-dipole coupling. We use perturbation theory to derive a set of many-body corrections that depend on the electron-nuclear and nuclear-nuclear couplings, and the magnetic field direction (see section 4.7). For the type of cluster considered here, the corrections could be significant. However, the signs of the leading terms depend on the electron spin state. By averaging the measured couplings for the $m_s = +1$ and $m_s = -1$ states, the deviations are strongly reduced. Together with a novel method to align the magnetic field to within 0.07 degrees (see section 4.7), this enables us to approximate the nuclear-nuclear couplings as dipolar.

4.5. ATOMIC-SCALE IMAGING OF THE CLUSTER

Finally, we determine the structure of the spin cluster. Figure 4.4a summarises all extracted couplings. We identify $M = 27$ nuclear spins and retrieve a total of 171 pairwise couplings, out of the total of $M(M-1)/2 = 351$ couplings. The structure of the cluster is completely described by $3M - 4 = 77$ spatial coordinates (see section 4.7), so that the problem is over-determined. However, due to the large number of parameters and local minima, a direct least-squares minimisation [10] is challenging. Instead, we sequentially build the structure by progressively adding spins, while keeping track of all possible structures that match the measured couplings within a certain tolerance.

We use two different methods. The first method constrains the spin coordinates to the diamond lattice. The second method discretises space in a general cubic lattice, with voxel spacing down to 5×10^{-3} nm (~ 1/70th of the lattice constant, see section 4.7). While this second method is more computationally intensive, it uses minimum a priori knowledge and can be applied on arbitrary spin systems. We run these analyses in parallel with the measurements, so that sets of the most promising spin assignments and structures are regularly created. These yield predictions for which unmeasured couplings (combinations of $RF1$ and $RF2$) are required to decide between different assignments and structures, which we use to guide the experiments and reduce the total measurement time (see section 4.7).

Figure 4.4b shows the structure obtained for the 27 spins using the diamond-lattice. The blue connections show the strongest couplings (> 3 Hz) and visualise the interconnectivity of the cluster. The cubic-lattice method yields a nearly identical structure (see section 4.7); the average distance between the spin positions for the two solutions is 0.58Å, a fraction of the bond length of ~ 1.54Å. As a final step, we use these structures as inputs for least-squares minimisation, where the x, y, z coordinates are allowed to relax to any value. The solution obtained lies close to the initial guess with an average distance of 0.46 Å. The uncertainties for the spatial coordinates (δx, δy, δz) are below a diamond bond length for all 27 spins (Fig. 4.4c,d), indicating atomic-scale imaging of the complete 27-spin cluster.

Additionally, we determine the position of the NV sensor relative to the cluster. Although not required to reconstruct the cluster, this provides a control experiment. We

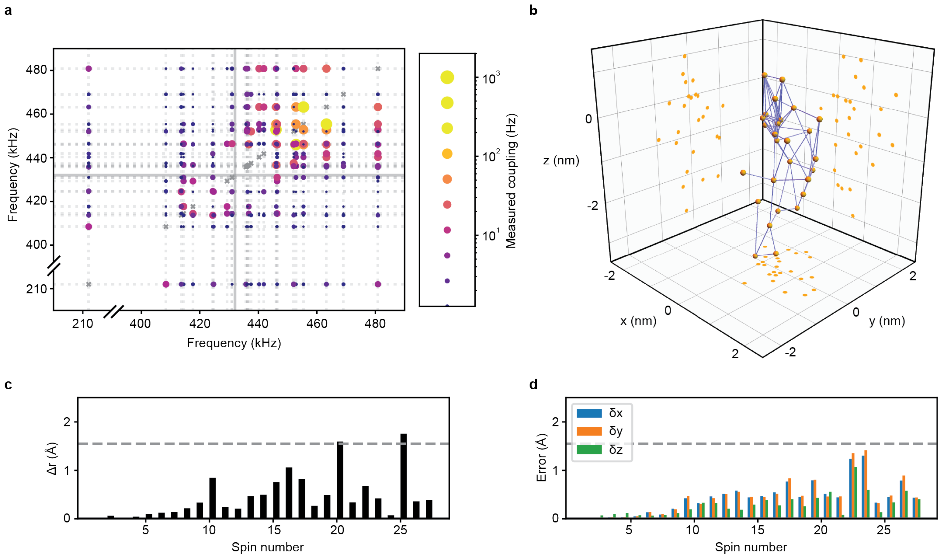

Figure 4.4: **Atomic-scale imaging of the 27-nuclear-spin cluster.** **a,** 2D plot summarising all couplings between the 27 spins identified from the 3D spectroscopy (Fig. 4.2). Includes identification of spins with overlapping frequencies. The size and colour of each point indicates the strength of the measured coupling averaged over the electron $m_s = +1$ and $m_s = -1$ states. Dashed grey lines indicate the nuclear spin frequencies ($m_s = -1$ state). Solid grey lines indicate the bare ^{13}C Larmor frequency. Total measurement time: ~ 400 hours. See Tables 4.2,4.3,4.4 for numerical values and uncertainties. **b,** 3D structure of the nuclear spins obtained using the diamond-lattice method (see text). Blue lines indicate couplings greater than 3 Hz and illustrate the connectivity of the cluster. See Fig. 4.7 for zoom-ins of strongly coupled subclusters. **c,** Distance Δr between the obtained spin positions from the diamond-lattice method (see text) and from a least-squares optimisation. Deviations are generally below one diamond bond length (dashed line, ~ 1.54 Å). **d,** The uncertainties for the 77 spatial coordinates of the cluster from a least-squares optimisation are less than the bond length, indicating atomic-scale resolution. See Figs 4.13,4.14,4.15 and Table 4.5 for in depth comparisons between the structures and uncertainties obtained with the different methods.

measure the coupling of the ^{14}N nuclear spin to 12 of the ^{13}C spins (Fig. 4.8). This unambiguously determines the location of both the ^{14}N atom and the vacancy (fit uncertainties < 0.3Å). We can now compare the electron-^{13}C hyperfine couplings to previous density functional theory (DFT) calculations for 5 of our spins [33]. All 5 couplings agree with the DFT calculations (Fig. 4.8), providing an independent corroboration of the extracted structure, as well as a direct test of the DFT calculations. Looking beyond quantum sensing, this precise microscopic characterisation of the NV environment provides new opportunities for improved control of quantum bits for quantum information [20, 24, 28, 31, 32], and for investigating many-body physics in coupled spin systems.

In our method, the NV sensor spin is exclusively used to create and detect polarisation (Fig. 4.1b). Therefore, the two main requirements for the sensor spin are (1) a high-contrast readout to keep measurement times manageable, and (2) that it does not limit the spectral resolution by disturbing the evolution of the nuclear spins through relaxation [25, 30, 31]. We satisfy these requirements by working at 4 Kelvin, so that the electron relaxation is negligible ($T_1 = 3.6(3) \times 10^3$ s [20]), and high-fidelity readout through resonant optical excitation is available (see section 4.7). Recent experiments have demonstrated both these requirements up to room temperature [5, 25, 26, 30, 31]. The electron spin relaxation—milliseconds at room temperature—can be decoupled from the sample spins through laser illumination [30, 31] or sequential weak measurements [25, 26]. High-contrast readout has been demonstrated by using a nuclear spin as a memory that can be read out repeatedly [5, 30]. Nuclear spins themselves are well-isolated from temperature [31]. Therefore, when combined with those methods, the ideas presented here could be extended to ambient conditions.

4.6. CONCLUSION

In conclusion, we have developed and demonstrated 3D atomic-scale imaging of large clusters of nuclear spins using a single-spin quantum sensor. Our approach is compatible with room temperature operation [25, 26, 30, 31] and could be extended to larger structures, as the number of required measurements scales linearly with the number of spins. Future improvements in the data acquisition and the computation of 3D structures can further reduce time requirements. In particular, recent methods to polarise and measure nuclear spins are expected to improve sensitivity [25, 26], especially for samples with weak couplings to the NV sensor. Optimised sampling of the measurements and adaptive algorithms based on a real-time structure analysis can further reduce the total number of required measurements. Therefore, when combined with recent progress in nanoscale NMR with near-surface NV centers [2–8], our results provide a path towards the magnetic imaging of individual molecules and complex spin structures external to diamond [10–13].

4.7. METHODS

4.7.1. SAMPLE AND NV CENTER SENSOR

We use a naturally occurring NV center in a homoepitaxially chemical-vapor-deposition (CVD) grown diamond with a 1.1% natural abundance of ^{13}C and a $\langle 111 \rangle$ crystal orientation (Element Six). The NV is placed in a solid-immersion lens to enhance photon collection efficiency [34]. The NV center has been selected for the absence of ^{13}C spins with hyperfine couplings > 500 kHz. The NV electron spin coherence times are $T_2^* = 4.9(2)\,\mu$s and $T_2 = 1.182(5)$ ms. We work at 4 Kelvin, so that the electron relaxation is negligible ($T_1 = 3.6(3) \times 10^3$ s [20]), and use high-fidelity readout through resonant optical excitation (average $F = 94.5\%$) [34].

The nuclear-spin dephasing times observed range from $T_2^* = 3$ ms to 17 ms, corresponding to a inhomogeneous linewidth of ~ 30 – 150 Hz. Due to the frequency differences between nuclear spins in $m_s = \pm 1$ (Table 4.1), spin diffusion is strongly suppressed and the longitudinal relaxation of the nuclear spins is $T_1 > 6$ minutes [28].

4.7.2. MAGNETIC FIELD ALIGNMENT

A magnetic field of ~ 403 G is applied using a room-temperature permanent magnet which is installed on a XYZ translation stage to control the strength and the direction of the magnetic field. Our methods are based on echoes and are therefore robust against slow fluctuations in the magnetic field strength. Although magnetic field drift has no significant effect on the measured nuclear-nuclear couplings, we stabilise the magnetic field to < 3 mG using temperature stabilisation of the magnet and an automatic recalibration procedure (every few hours).

We align the magnetic field along the NV axis to avoid electron-mediated shifts that cause the measured couplings to deviate from nuclear-nuclear dipolar coupling (see section 4.8.3). We use a "thermal" echo sequence—previously introduced to measure temperature [35] (see Fig. 4.9). In this sequence, the electron evolves half of the time in a superposition of the states $m_s = 0$ and $m_s = -1$, and half of the time in a superposition of $m_s = 0$ and $m_s = +1$. Since the energies of the states $m_s = \pm 1$ are shifted by equal and opposite amounts by Hamiltonian terms proportional to S_z, the effects of such terms are cancelled. However, Hamiltonian terms that shift the energies of $m_s = \pm 1$ in the same way, such as the magnetic field perpendicular to z, do not cancel. Therefore, the sequence decouples the main source of noise (the magnetic field fluctuations along z from the surrounding spin bath), while remaining sensitive to shifts caused by a non-zero magnetic field in the x, y directions. This sequence extends the sensing time from $T_2^* \approx 5\,\mu$s to $T_2 \approx 1$ ms, resulting in an uncertainty in the alignment of 0.07 degrees (Fig. 4.9).

4.7.3. QUANTUM SENSING SEQUENCES

We employ two different sensing sequences (see the polarise and detect blocks in Fig. 4.1b). Sequence A consists of dynamical decoupling sequences of N' equally spaced π-pulses on the electron spin of the form $(\tau_r - \pi - \tau_r)^{N'}$ [36–38]. This sequence is only sensitive to nuclear spins with a significant electron-nuclear hyperfine component perpendicular to the applied magnetic field [36]. The inter-pulse spacing $2\tau_r$ determines the spin frequency that is being probed.

Sequence B is a recently developed method, described in detail in Bradley et al. [28], that interleaves the dynamical decoupling sequence with RF pulses. This method enables the detection of spins with a weak or negligible perpendicular hyperfine component [28, 30]. For this sequence, the frequency of the RF pulse sets the targeted spin frequency, while τ_r can be freely chosen [28]. Importantly, the amplitudes and phases of the RF pulses are set so that they together build up to the desired evolution [28]. The added RF field imprints a deterministic phase on the electron spin sensor [28], which we compensate by calibrating the phase of the electron $\pi/2$-pulses.

4.7.4. ELECTRON-NUCLEAR SPECTROSCOPY

As a starting point, we use the electron spin as a sensor to roughly characterise some of the nuclear spins in the cluster. We perform spectroscopy by sweeping the interpulse delay τ_r in sequence A (see for example Abobeih et al. [20]) and the RF frequency for sequence B [28]. This identifies the frequency range at which spins are present in the cluster and provides the parameters to polarise and detect several spins [24]. Note that the resolution of this spectroscopy technique is limited by the electron spin T_2 and the nuclear spin T_2^*.

4.7.5. NUCLEAR-NUCLEAR DOUBLE-RESONANCE SPECTROSCOPY

The sequence for the double-resonance experiments is shown in Fig. 4.1b and Fig. 4.5. To polarise and detect the probe spin, we either use sequence A (without the RF1 pulses in the dashed box) or sequence B (with the RF1 pulses), depending on whether the perpendicular hyperfine coupling to the electron spin is significant or not. For sequence A, we set the interpulse delay as $\tau_r = (2k-1)\pi/(\omega_0 + RF1)$, with k an integer and ω_0 the ^{13}C Larmor frequency for the electron $m_s = 0$ state, and calibrate the number of pulses N' to maximise the signal [36]. For sequence B we calibrate the RF power to maximise the signal.

We create nuclear polarisation by projective measurements [24]. First the electron is prepared in a superposition state through resonant excitation [34] and a $\pi/2$ pulse. Second, the sensing sequence correlates the phase of the electron with the nuclear spin state. Finally, the electron is read out so that the nuclear spin is projected into a polarised state [24]. To enhance the signal-to-noise ratio and to ensure that the electron measurement does not disturb the nuclear spin evolution, we only perform the double-resonance sequence if a photon was detected during the electron readout [24]. The resulting signal contrast for different spins varies from 20% to 96%.

Because the correlation data is read out and stored in the electronics, the ultimate limit for the spectral resolution of our method - i.e. when applied on hypothetical signals with infinitesimal spectral width - is set by the precision of the 10 MHz reference clock used for the timing of the waveform generator [7, 39, 40]. For the double-resonance sequence, the phases of the RF1 echo pulses are calibrated so that their phase difference is 0 or $\pi/2$ with respect to the polarisation axis, which is determined by the direction of the hyperfine interaction [18, 19, 41]. For the target spins, the phase of the RF2 pulse does not affect the signal and is arbitrarily set.

To mitigate pulse errors we alternate the phases of the pulses following the XY8 scheme [42], both for the electron and nuclear spins. For the electron spin, we use Hermite pulse envelopes [43] with Rabi frequency $\sim 14\,\mathrm{MHz}$ to obtain effective microwave pulses without initialisation of the intrinsic ^{14}N nuclear spin. The nuclear-spin Rabi frequencies are in the range $0.3-0.7\,\mathrm{kHz}$.

4.7.6. DATA ANALYSIS

We extract the spin-spin couplings f and their uncertainties from fitting the time-domain double-resonance signals (e.g. Fig. 4.1e-f, top) to $S = a + A\cdot e^{-(t/T_2)^n}\cos(2\pi f t + \phi)$, where T_2 is the coherence time (also a fit parameter). The PSD is obtained from a Fourier transform of the time domain signal with zero filling [1] and the D.C. component filtered out (e.g. Fig. 4.1e-f, bottom). The spectral resolution (FWHM) is obtained from a Gaussian fit of the PSD. Alternatively we can define the spectral resolution (FWHM) directly from the time domain signal as $\frac{2\sqrt{ln2}}{\pi T_2}$. This yields a spectral resolution of 0.91(3) Hz for Fig. 4.1e. For the spin in Fig. 4.1f, using $N = 1$ yields a spectral resolution of 0.8(1) Hz and using $N = 256$ yields 49(2) mHz. Note that no saturation of the improvement of spectral resolution with the number of pulses is yet observed. Therefore, with more pulses (and longer measurement times) higher spectral resolutions and more precise measurements are feasible.

4.7.7. ELECTRON-MEDIATED INTERACTIONS

We calculate corrections to the nuclear-nuclear couplings due to the presence of the electron spin using perturbation theory up to second order. The effect of other nuclear spins on nuclear-nuclear couplings was found by numerical simulations to be negligible (~ mHz). In contrast to previous results for strong electron-nuclear couplings [32, 44], here many-body interactions due to the non-secular nuclear-nuclear couplings must be taken into account. The resulting frequency in a double-resonance experiment is of the form (see section 4.8.1)

$$\begin{aligned} f_{\mathrm{DR}}(m_s = \pm 1) \approx \frac{1}{4\pi}|C +& \\ + \Delta\lambda_1(m_s) + \Delta\lambda_2(m_s) + \Delta\lambda_3(m_s)|,& \end{aligned} \tag{4.1}$$

where C is the parallel (zz) component of the dipole-dipole interaction between the nuclear spins and $\Delta\lambda_i$ are correction terms due to the presence of the electron spin. See section 4.8 for the full analysis of all terms.

The dominant correction for our parameter regime is $\Delta\lambda_2$, which depends on both the electron-nuclear and nuclear-nuclear interactions. We make a Taylor expansion up to first order in $A_{zz}^{(j)}/\gamma_c B_z$, where $A_{zz}^{(j)}$ is the parallel electron-nuclear hyperfine coupling for spin j, γ_c is the nuclear gyromagnetic ratio and B_z is the component of the magnetic field along the NV axis. This yields an expression of the form $\Delta\lambda_2(m_s) \approx m_s\Delta\lambda_2^{(0)} + \Delta\lambda_2^{(1)}$, where the leading, zeroth-order, correction $m_s\Delta\lambda_2^{(0)}$ is given by

$$\Delta\lambda_2^{(0)} = \frac{(A_{zx}^{(1)} + A_{zx}^{(2)})C_{zx} + (A_{zy}^{(1)} + A_{zy}^{(2)})C_{zy}}{\gamma_c B_z}, \tag{4.2}$$

where $A_{zx}^{(j)}$ (C_{zx}) and $A_{zy}^{(j)}$ (C_{zy}) are the perpendicular electron-nuclear (nuclear-nuclear) coupling components. We cancel this term by averaging the double-resonance frequencies measured for the $m_s = \pm 1$ electron spin projections.

The remaining electron-mediated corrections depend on the angles of the electron-nuclear hyperfine interactions. Because these angles are unknown, we estimate the maximum possible shift for each spin-spin interaction by maximising over all angles. For our cluster (Fig. 4.4), most of these maximum possible shifts are small (their average value is $\sim 0.03\,\text{Hz}$). In rare cases, the maximum possible correction runs up to 0.6 Hz (see section 4.8.3), but as the locations of the involved spins are already precisely fixed through strong ($> 20\,\text{Hz}$) interactions with several other spins, this would have a negligible effect on the obtained structure. Therefore, we can base the structural analysis on dipole-dipole interactions.

4.7.8. 3D STRUCTURE ANALYSIS

The 3D structure of the nuclear spins is obtained using the dipole-dipole coupling formula, which relates the zz couplings C_{ij} to the spatial x, y, z coordinates of spins i and j as

$$C_{ij} = \frac{\alpha_{ij}}{\Delta r_{ij}^3}\left(\frac{3(z_j - z_i)^2}{\Delta r_{ij}^2} - 1\right), \tag{4.3}$$

where $\Delta r_{ij} = \sqrt{(x_j - x_i)^2 + (y_j - y_i)^2 + (z_j - z_i)^2}$, $\alpha_{ij} = \mu_0 \gamma_i \gamma_j \hbar / 4\pi$, μ_0 is the permeability of free space, γ_i is the gyromagnetic ratio of nuclear spin i and $\hbar$ is the reduced Planck constant.

The goal is to minimise the sum of squares $\xi = \sum_{i<j} |\Delta f_{ij}|^2$, where $\Delta f_{ij} = f_{ij} - |C_{ij}|/4\pi$ are the residuals and f_{ij} are the measured coupling frequencies. For $M = 27$ spins, there are $3M - 4 = 77$ free coordinates and $M(M-1)/2 = 351$ pairwise couplings, of which 171 were determined in this work. ξ can in principle be minimised using standard fitting methods, however tests with randomly generated spin clusters indicate that the initial guess for the coordinates should be within $\sim 0.5\,\text{Å}$ in order for the fit to converge to the correct solution. For 27 spins, this corresponds to an intractable $\sim 10^{100}$ possible initial guesses. Instead we sequentially build the structure by adding spins one-by-one.

For the diamond lattice positioning method, we first use the strongest measured coupling to any spin that is already positioned to reduce the position of a new spin to a number of possible lattice coordinates. For each possible coordinate, we then check if the predicted couplings to all other spins satisfy $\Delta f_{ij} < \mathscr{T}$, where $\mathscr{T} = 1.1\,\text{Hz}$ is a tolerance that is chosen to ensure that all promising configurations are included while maintaining reasonable computation time. Configurations are discarded if they do not satisfy this requirement for one or more of the pairwise couplings. If more than $X_{\text{cutoff}} = 5000$ possible configurations are identified, only the best X_{cutoff} solutions are kept, according to their ξ values.

For the cubic lattice positioning method, the same procedure is followed, with the key difference being that the lattice is adaptively generated depending on the strongest coupling to an already positioned spin in the cluster (see section 4.8.4). This ensures that in each case the lattice spacing is fine enough to appropriately sample the volume associated with the dipole-dipole coupling between the nuclear spins.

4.7.9. ROBUSTNESS OF THE ANALYSIS

The method is robust to failure. The problem is generally highly over-determined, so that discarding the correct configuration due to X_{cutoff} will lead to no solution at all, rather than an erroneous solution. Given enough computational resources, a correct solution is always expected to be found. As a test, we used the cubic lattice reconstruction method on 17 randomly generated 30-spin clusters spins with added noise and no erroneous structures were returned (see section 4.8.4).

4.7.10. COMPARISON TO 1D RAMSEY SPECTROSCOPY

Fig. 4.6 compares the 1D Ramsey signal with reconstructed spectra from our 3D spectroscopy. This comparison illustrates the effective improvement in resolution, and the ability to resolve dense spectra, of our method. Note that, apart from the spectral resolution, the signals should not be compared directly, because the Ramsey experiment is difficult to interpret quantitatively. First, the Ramsey signals likely contain contributions from multiple spins, both due to spectral overlap and higher-order contributions [36–38]. Second, any inadvertent polarisation of other spins in the cluster or the environment modifies the spectrum. These effects are difficult to separate from actual nuclear-nuclear couplings, and the fact that the spectra are asymmetric indicates that they play a significant role. Our 3D spectroscopy method resolves these issues.

4.7.11. FINDING THE POSITION OF THE NV CENTER

Because the NV electron wavefunction is not known a-priori, we cannot use the electron-nuclear couplings to find the NV position. In particular, density functional theory (DFT) calculations [33] indicate that, for electron-nuclear couplings in the range observed here, assuming a point-dipole model for the electron spin can lead to large discrepancies, and is therefore not justified.

Our approach is to measure the couplings between the ^{13}C spins and the NV nitrogen nuclear spin, for which the point-dipole approximation is accurate. The nitrogen-^{13}C couplings can be measured using a similar double-resonance procedure as for measuring ^{13}C-^{13}C couplings. We use the nitrogen spin as the probe spin: this gives better spectral resolution, due to its longer coherence time ($T_2 = 2.3(2)\,\mathrm{s}$ [28]). We initialise the nitrogen spin in $m_I = 0$ using measurement-based initialisation [34] and manipulate the spin state using RF pulses. Fig. 4.8b shows the measured couplings between the nitrogen and ^{13}C spins.

Using the couplings, the nitrogen spin is added to the ^{13}C nuclear spin cluster using the diamond lattice positioning method, where $\gamma_j \to \gamma_n = 2\pi \times 0.3077\,\mathrm{kHz/G}$, the nitrogen gyromagnetic ratio, in equation 4.19. Determining the nitrogen lattice site also allows the vacancy site to be determined due to the known N-V distance and the alignment with the magnetic field along z, thereby giving the location and the orientation of the NV center with respect to the ^{13}C nuclear spin cluster. The resulting 3D plot showing the best solution is shown in Fig. 4.8a. The nitrogen spin coordinate is the same for all 5000 configurations identified. Fig. 4.8c gives the results of a least-squares fit.

4.7.12. COMPARISON TO DFT

Now that we independently determined the position of the ^{13}C spins relative to the NV center, we can compare the hyperfine couplings to DFT calculations, without any prior assumptions. In Nizovtsev et al. [33], hyperfine couplings are calculated for 510 lattice sites surrounding the NV center. Fig. 4.8d shows the lattice positions given in Nizovtsev et al. along with the coordinates of the ^{13}C spins found in this work. The ^{13}C spin coordinates are transformed so that the nitrogen spin is at the origin, and mirrored such that $z \rightarrow -z$, in order to be in the correct coordinate frame. Additionally a scaling factor of 1.02 was applied, which was found by comparing the 510 lattice sites from Nizovtsev et al. with the same sites in our work. 5 of the 27 spins identified in this work were calculated in Nizovtsev et al. The remaining spins cannot yet be compared with DFT calculations. Fig. 4.8e shows the measured electron-^{13}C hyperfine couplings (see Table 4.1), as well as those predicted in Nizovtsev et al., for the 5 spins. For the DFT results, we take the average of the predicted couplings for the possible C_{3v} symmetric lattice sites. Additionally, we take the negative of the predicted $A_{\parallel}$ for all spins (a global minus sign is possible due to the unknown orientation of the magnetic field along z).

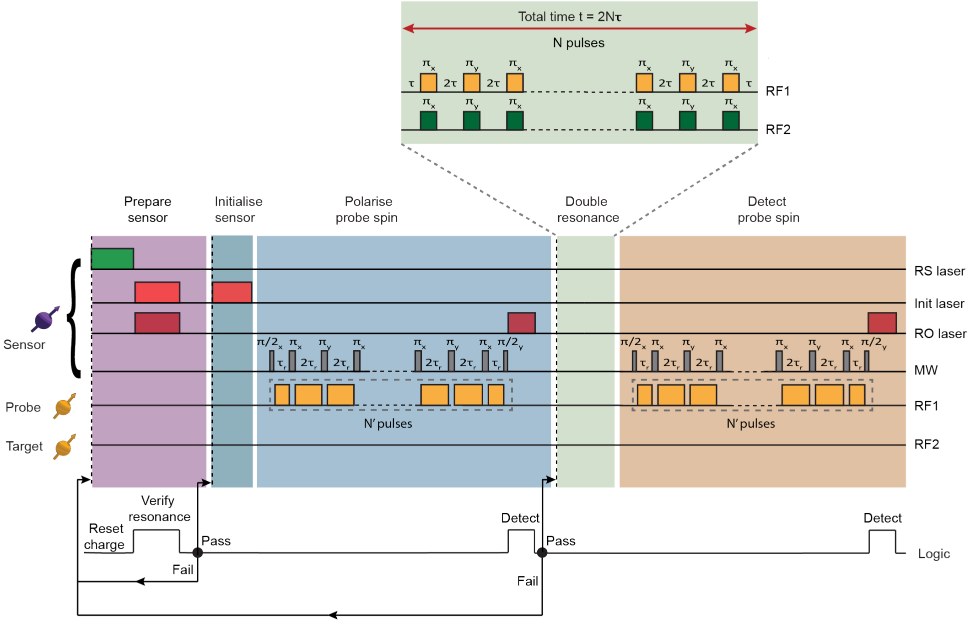

Figure 4.5: **Experimental sequence.** The pulse sequence consists of five parts: sensor preparation, sensor initialisation, polarisation of the probe spin, double resonance, and detection of the probe spin. Sensor preparation: The NV center is prepared by excitation with two 637 nm lasers for 150 μs and counting the detected photons (RO laser resonant with the E_x transition and Init laser with the $E^{'}$ transition) [24, 34]. If the number of photons exceeds a certain threshold, the NV is in the negative charge state and resonant with both lasers, and we proceed to the next step. If not, we apply a 515 nm laser (charge reset (RS) laser, 1 ms) and repeat the process [24, 34]. Sensor initialisation: The NV electron spin is initialised into the $m_s = 0$ state through spin pumping (Init laser, 100 μs) [34]. Polarising probe spin: First, the NV sensor is brought into a superposition state using a $\pi/2$ pulse. Then, a dynamical decoupling sequence of N' equally spaced π-pulses on the electron spin of the form $(\tau_r - \pi - \tau_r)^{N'}$ is applied. This sequence correlates the state of the nuclear spin(s) with the phase of the electron spin. We use two different sequences (see section 4.7). For sequence B, the MW π-pulses are interleaved with radio-frequency pulses ($RF1$) that resonantly drive the probe spin(s) (dashed box), see Bradley et al. for details [45]. A second $\pi/2$ pulse maps the electron phase to population and the electron spin is read out (RO laser). Double resonance: N echo pulses are applied simultaneously on the probe spin(s) ($RF1$) and the target spin(s) ($RF2$), so that the coupling between these spins is isolated. To mitigate pulse errors we alternate the phases of the pulses following the XY8 scheme [42]. Detecting probe spin: The detection sequence is the same as the polarisation sequence except for the final RO laser pulse which is applied for 10 μs and with higher power.

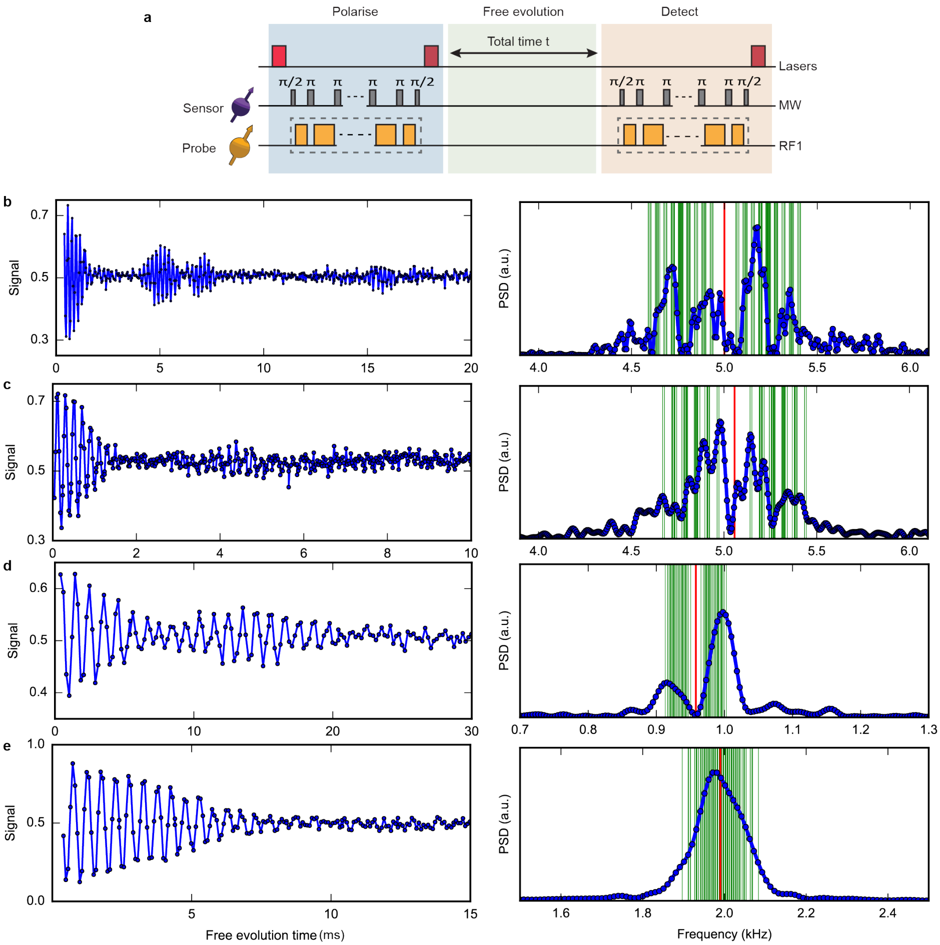

Figure 4.6: **Ramsey experiments and reconstructed underlying spectra. a**, Schematic of the pulse sequence used to perform the Ramsey experiment (equivalent to correlation spectroscopy). See section 4.7 and Fig. 4.5 for details. **b**, Ramsey signal for C2 and the corresponding power spectral density (5 kHz detuning). The red line represents the central frequency f_0. Green lines are the 2^7 frequencies based on the 7 strongest coupling strengths extracted from our high resolution double-resonance spectroscopy (Table 4.4). These frequencies are given by $f_0 \pm f_1 \pm f_2 \pm f_3 \pm f_4 \pm f_5 \pm f_6 \pm f_7$, where f_1 to f_7 are the 7 largest measured coupling strengths for C2. **c**, The same experiment for C3 (~ 5 kHz detuning), **d**, for C15 (~ 1 kHz detuning) and **e**, for C5 (~ 2 kHz detuning).

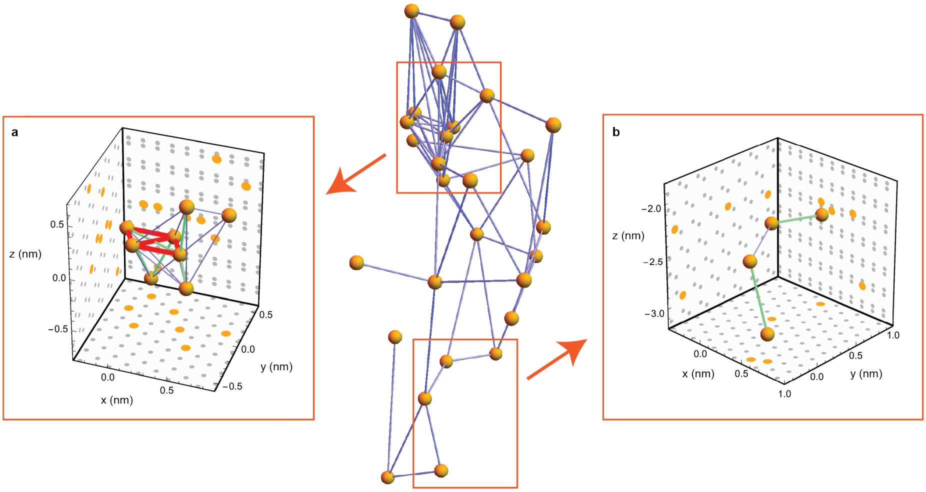

Figure 4.7: **Strongly coupled subclusters.** 3D plots showing the structure of two strongly coupled subclusters (orange panels) within the larger cluster (shown in the center). The positions of the subclusters within the larger cluster are marked by the orange boxes and arrows. Ramsey measurements performed on spins within these subclusters show clear beating signals within their T_2^* dephasing time (see for example Fig. 4.6). Panel a) shows an 8 spin subcluster, while panel b) shows a 4 spin subcluster. Couplings above 3 Hz are marked blue, above 20 Hz green and above 50 Hz red. Grey points show the 2D projections of the diamond lattice coordinates.

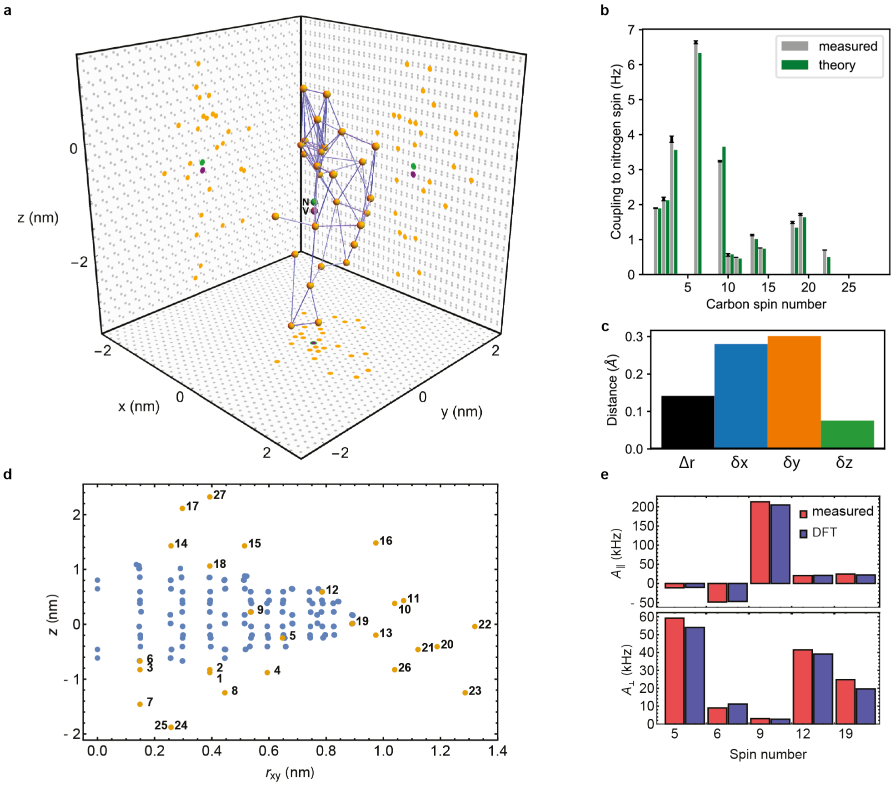

Figure 4.8: **Finding the position of the NV center. a,** 3D plot showing the 27 nuclear spin cluster as shown in Fig. 4.4, with the position of the nitrogen spin (green) and vacancy (purple) lattice sites calculated from the measured nitrogen-^{13}C couplings. The grey dots show the 2D projections of the diamond lattice coordinates. **b,** Bar plot showing the measured couplings f_{iN} between ^{13}C spin i and the nitrogen spin (grey), as well as the theoretically calculated couplings $|C_{iN}|/4\pi$ (green). Error bars are one standard deviation. See Table 4.4 for the numerical values. **c,** Bar plots of Δr for the fitted position for the nitrogen spin (black), as well as fit errors δx (blue), δy (orange) and δz (green), where the ^{13}C spins are fixed at the diamond lattice solution. **d,** Plot of z vs. $r_{xy} = \sqrt{x^2 + y^2}$ for all lattice positions used in the DFT calculation from Nizovtsev et al. [33] (blue) and for the appropriately transformed ^{13}C coordinates found in this work (orange). Spins 5, 6, 9, 12 and 19 match a DFT lattice position, while the rest of the spins identified are outside of the 510 lattice sites simulated. **e,** Measured electron-^{13}C parallel (top) and perpendicular (bottom) hyperfine couplings for the 5 spins that are within the DFT calculation volume (red, taken from Table 4.1), compared with the DFT results from Nizovtsev et al. (blue).

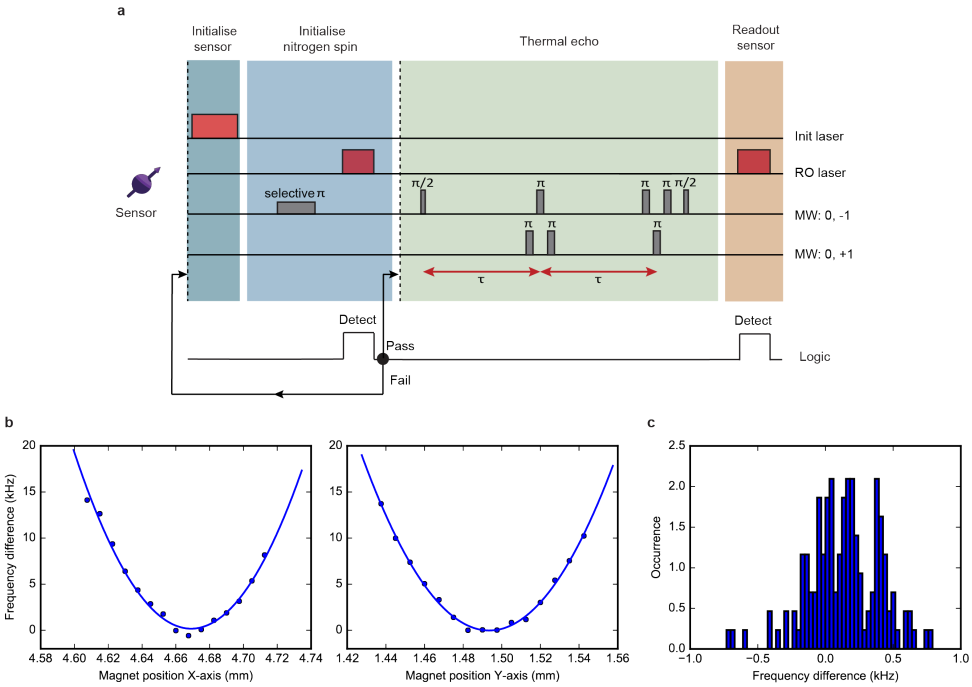

Figure 4.9: **Aligning the magnetic field using a thermal echo sequence.** **a,** Pulse sequence for the thermal echo measurement [35]. The electron spin is prepared in a superposition of the states $m_s = 0$ and $m_s = -1$ in the first half of the sequence, and then swapped to a superposition of $m_s = 0$ and $m_s = +1$ for the second half, using a sequence of three closely spaced π pulses. By sweeping τ, the average frequency $f_{\mathrm{TE}} = (f_{+1} + f_{-1})/2$ is obtained, which is minimised when $B_\perp = 0$. $f_{\pm 1}$ are the $m_s = 0 \leftrightarrow m_s = \pm 1$ transition frequencies. The NV nitrogen spin is initialised in $m_I = 0$ [34]. **b,** Magnetic field alignment by scanning the magnet position in two orthogonal directions. The obtained thermal echo frequencies are fitted to a parabolic function to find the optimum position (i.e. minimal f_{TE}). The plots show the frequency difference $f_{\mathrm{TE}} - 2.877652\,\mathrm{GHz}$. **c,** Placing the magnet at the optimum position and repeating the measurement 200 times (over a 10-hour period). The obtained average frequency difference is 0.13 kHz, with a standard deviation of 0.27 kHz, which is consistent with the statistical measurement error. Therefore, the total uncertainty for the magnet alignment is ~ 0.4 kHz which corresponds to a perpendicular field of 0.5 Gauss or a misalignment angle of 0.07 degrees.

4.8. SUPPLEMENTARY INFORMATION

4.8.1. PROPERTIES OF THE NUCLEAR SPIN CLUSTER

This section summarises the properties of the nuclear spin cluster that we retrieved from the 3D spectroscopy. Table 4.1 gives the precession frequencies of the 27 spins that compose the cluster. Tables 4.2-4.4 summarise the retrieved couplings between these spins. Table 4.5 gives the obtained spatial coordinates for the spins in the cluster.

Additionally, Table 4.1 gives estimates for the hyperfine couplings of the nuclear spins to the electron spin. These electron-nuclear couplings play no role in retrieving the structure of the cluster as our imaging method solely relies on the internal nuclear-nuclear couplings. Instead, these couplings are used to estimate realistic bounds on electron-mediated interactions (section 4.8.3) and to provide an independent comparison to DFT calculations (see section 4.7).

The hyperfine couplings are estimated as follows. Under the secular approximation and assuming a perfectly aligned magnetic field, the nuclear spin precession frequencies ω_{m_s} for electron spin state m_s are given by [36]

$$\begin{aligned} \omega_0 &= \omega_L, \\ \omega_{\pm 1} &= \sqrt{(\omega_L \pm A_\parallel)^2 + A_\perp^2}, \end{aligned} \tag{4.4}$$

where $\omega_L = \gamma_c B_z$ is the Larmor frequency, γ_c is the ^{13}C gyromagnetic ratio and B_z is the $\hat{z}$ component of the externally applied magnetic field. Rearranging equations 4.4, we obtain expressions for the electron-^{13}C hyperfine parameters, given by

$$\begin{aligned} A_\parallel &= \frac{\omega_{+1}^2 - \omega_{-1}^2}{4\omega_0}, \\ A_\perp &= \sqrt{\frac{\omega_{+1}^2 + \omega_{-1}^2 - 2\omega_0^2 - 2A_\parallel^2}{2}}. \end{aligned} \tag{4.5}$$

For spins C5, C6, C9, C10, C12, C14, C18 and C19, we measure the $m_s = 0$ precession frequency ω_0, while for the rest of the spins we use the average of these measured values ($= 2\pi \cdot 431.960$ kHz). We observe a standard deviation of 6 Hz in the measured values of ω_0, which can be attributed to non-secular terms in the Hamiltonian in conjunction with a slightly misaligned magnetic field (< 0.1 deg, see Fig. 4.9). For spins C24 to C27, equations 4.5 give imaginary values for $A_\perp$, which we attribute to shifts in ω_0 that are not captured in this approximate model. For these spins we set $A_\perp = 0$ in the table.

	$\omega_{-1}/2\pi$ (kHz)	$\omega_{+1}/2\pi$ (kHz)	$A_{\parallel}/2\pi$ (kHz)	$A_{\perp}/2\pi$(kHz)	$\tau_r(\mu s)$	$N^{'}$	Sequence
C1	452.83(2)	411.40(2)	-20.72(1)	12(1)	7.435	64	A
C2	455.37(2)	408.956(9)	-23.22(1)	13(1)	8.92	62	A
C3	463.27(2)	400.79(2)	-31.25(1)	8(2)	18.522	48	B
C4	446.23(4)	418.10(1)	-14.07(2)	13(1)	-	-	-
C5	447.234(1)	424.752(3)	-11.346(2)	59.21(3)	16.480	20	A
C6	480.625(1)	383.48(4)	-48.58(2)	9(2)	4.932	90	A
C7	440.288(6)	423.65(2)	-8.32(1)	3(5)	-	-	-
C8	441.77(1)	422.20(4)	-9.79(2)	5(4)	-	-	-
C9	218.828(1)	645.123(1)	213.154(1)	3.0(4)	16.204	48	B
C10	414.407(1)	449.687(2)	17.643(1)	8.6(2)	23.152	48	B
C11	417.523(4)	446.612(3)	14.548(3)	10(1)	10.812	58	A
C12	413.477(1)	454.427(1)	20.569(1)	41.51(3)	11.25	22	A
C13	424.449(1)	440.490(1)	8.029(1)	21.0(4)	10.682	36	A
C14	451.802(1)	412.175(5)	-19.815(3)	5.3(5)	18.522	64	B
C15	446.010(5)	418.093(3)	-13.961(3)	9(1)	8.444	72	A
C16	436.67(5)	427.35(3)	-4.66(3)	7(4)	-	-	-
C17	437.61(1)	426.38(2)	-5.62(1)	5(2)	-	-	-
C18	469.020(1)	396.542(1)	-36.308(1)	26.62(4)	7.218	44	A
C19	408.317(1)	457.035(1)	24.399(1)	24.81(4)	6.540	32	A
C20	429.403(4)	434.782(6)	2.690(4)	11(1)	-	-	-
C21	430.937(3)	433.36(1)	1.212(5)	13(1)	-	-	-
C22	424.289(3)	439.655(7)	7.683(4)	4(3)	-	-	-
C23	435.143(7)	428.789(5)	-3.177(5)	2(4)	-	-	-
C24	436.183(3)	427.732(7)	-4.225(4)	0(6)	-	-	-
C25	435.827(5)	428.079(9)	-3.873(5)	0(4)	-	-	-
C26	435.547(2)	428.31(1)	-3.618(5)	0(2)	-	-	-
C27	435.990(3)	427.910(9)	-4.039(5)	0(3)	-	-	-

Table 4.1: **The 27 nuclear spins.** Retrieved ^{13}C spin precession frequencies ω_{-1}, ω_{+1} for the $m_s = -1$ and $m_s = +1$ electron spin projections respectively. Obtained by least-squares fitting the frequency scan signal in double resonance experiments to a Gaussian function (e.g. Fig. 4.11) or from fits of Ramsey signals to sinusoidal functions with Gaussian decays. $A_{\parallel}$ and $A_{\perp}$ are estimates for the parallel and perpendicular components of the electron-^{13}C hyperfine interaction respectively, obtained from the measured frequencies ω_{-1}, ω_{+1} and ω_0 (see equations 4.5). τ_r and $N^{'}$ are the half pulse delay and the total number of pulses used in the polarisation and detection sequences (Fig. 4.5). The sequence column identifies whether sequence A or B was used to polarise/detect the spin. The spins marked with “-" were detected as target spins (no initialisation or direct detection with the electron spin required). The dephasing time, T_2^*, for the spins in the cluster varies from 3 ms to 17 ms. The measured coherence time (T_2) using a single refocusing pulse is typically ~ 0.5 seconds, corresponding to a FWHM spectral resolution of ~ 1 Hz in the double resonance experiments.

	C1	C2	C3	C4	C5	C6	C7	C8	C9	C10	C11	C12	C13	C14	C15	C16	C17	C18	C19	C20	C21	C22	C23	C24	C25	C26	C27	N
C1	-	61.88(9)	61.49(6)	236.0(2)	7.05(3)	12.66(6)	4.8(1)	2.9(2)	1.07(7)	<1	-	<1	<1	<1	-	-	-	1.0(1)	<1	-	2.3(2)	-	-	7.8(2)	2.2(2)	-	-	1.95(1)
C2	61.88(9)	-	235.95(1)	61.40(8)	17.17(2)	19.1(1)	5.61(6)	1.6(1)	1.11(6)	2.1(1)	1.4(1)	0.97(9)	<1	<1	<1	-	-	1.07(7)	<1	-	3.14(7)	-	-	4.6(1)	4.1(2)	<1	-	2.25(5)
C3	61.49(6)	235.95(1)	-	24.9(1)	3.21(4)	28.99(7)	20.2(4)	13.1(1)	2.53(7)	<1	<1	1.37(7)	<1	<1	-	-	-	1.01(7)	<1	-	2.3(1)	-	-	5.5(1)	5.0(3)	3.1(2)	-	3.87(9)
C4	236.0(2)	61.40(8)	24.9(1)	-	19.0(1)	7.0(1)	-	-	-	-	-	<1	<1	<1	<1	-	-	-	-	-	-	-	-	-	-	-	-	-
C5	7.05(3)	17.17(2)	3.21(4)	19.0(1)	-	2.5(9)	1.1(2)	0.9(2)	0.96(4)	7.75(3)	<1	<1	-	-	1.9(1)	-	-	2.33(5)	0.6(2)	7.1(1)	9.90(7)	-	-	-	-	-	-	-
C6	12.66(6)	19.1(1)	28.99(7)	7.0(1)	2.5(9)	-	16.50(9)	12.64(5)	6.48(2)	<1	<1	2.01(5)	<1	0.8(2)	-	-	-	1.28(6)	<1	1.1(3)	1.96(9)	-	0.8(2)	3.4(1)	5.6(2)	4.89(9)	-	6.69(4)
C7	4.8(1)	5.61(6)	20.2(4)	-	1.1(2)	16.50(9)	-	-	1.45(7)	<1	-	0.4(2)	<1	<1	-	-	-	<1	-	-	-	-	-	-	-	-	-	-
C8	2.9(2)	1.6(1)	13.1(1)	-	0.9(2)	12.64(5)	-	-	1.53(5)	<1	-	1.15(9)	3.11(8)	<1	<1	-	-	<1	-	-	-	-	-	-	-	-	-	-
C9	1.07(7)	1.11(6)	2.53(7)	-	0.96(4)	6.48(2)	1.45(7)	1.53(5)	-	1.12(7)	1.26(3)	1.56(4)	1.8(2)	3.77(3)	-	<1	1.1(1)	1.39(1)	8.45(2)	-	-	3.70(7)	0.7(1)	-	-	3.5(1)	0.89(4)	3.25(2)
C10	<1	2.1(1)	<1	-	7.75(3)	<1	<1	<1	1.12(7)	-	14.51(7)	1.2(1)	<1	<1	3.7(5)	5.0(1)	-	<1	<1	6.9(2)	3.8(2)	-	-	-	-	-	-	0.56(3)
C11	-	1.4(1)	<1	-	<1	<1	-	-	1.26(3)	14.51(7)	-	3.35(3)	<1	<1	2.1(3)	4.7(1)	-	0.5(3)	<1	9.5(2)	-	-	-	-	<1	-	-	0.49(2)
C12	<1	0.97(9)	1.37(7)	<1	<1	2.01(5)	0.4(2)	1.15(9)	1.56(4)	1.2(1)	3.35(3)	-	12.17(6)	1.46(9)	-	<1	1.26(8)	1.1(2)	0.536(2)	-	-	1.7(2)	1.1(1)	-	-	-	-	-
C13	<1	<1	<1	<1	-	<1	<1	3.11(8)	1.8(2)	<1	<1	12.17(6)	-	<1	<1	<1	<1	-	1.3(2)	-	-	7.3(1)	3.5(1)	-	-	-	-	1.2(1)
C14	<1	<1	<1	<1	-	0.8(2)	<1	<1	3.77(3)	<1	<1	1.46(9)	<1	-	8.89(7)	2.1(2)	21.7(3)	1.39(6)	1.6(1)	-	-	-	-	-	-	-	6.3(2)	0.76(3)
C15	-	<1	-	<1	1.9(1)	-	-	<1	-	3.7(5)	2.1(3)	-	<1	8.89(7)	-	24.6(3)	-	<1	<1	-	-	-	-	-	-	-	2.2(6)	-
C16	-	-	-	-	-	-	-	-	<1	5.0(1)	4.7(1)	<1	<1	2.1(2)	24.6(3)	-	-	1.5(1)	<1	-	-	-	-	-	-	-	-	-
C17	-	-	-	-	-	-	-	-	1.1(1)	-	-	1.26(8)	<1	21.7(3)	-	-	-	2.42(5)	0.9(1)	-	-	-	-	-	-	-	-	-
C18	1.0(1)	1.07(7)	1.01(7)	-	2.33(5)	1.28(6)	<1	<1	1.39(1)	<1	0.5(3)	1.1(2)	-	1.39(6)	<1	1.5(1)	2.42(5)	-	1.32(4)	-	1.50(7)	-	-	-	-	-	3.60(6)	1.49(4)
C19	<1	<1	<1	-	0.6(2)	<1	-	-	8.45(2)	<1	<1	0.536(2)	1.3(2)	1.6(1)	<1	<1	0.9(1)	1.32(4)	-	1.7(3)	-	1.4(1)	-	-	-	0.4(3)	0.65(5)	1.72(3)
C20	-	-	-	-	7.1(1)	1.1(3)	-	-	-	6.9(2)	9.5(2)	-	-	-	-	-	-	-	1.7(3)	-	-	-	-	-	-	-	-	-
C21	2.3(2)	3.14(7)	2.3(1)	-	9.90(7)	1.96(9)	-	-	-	3.8(2)	-	-	-	-	-	-	-	1.50(7)	-	-	-	-	-	-	-	-	-	-
C22	-	-	-	-	-	-	-	-	3.70(7)	-	-	1.7(2)	7.3(1)	-	-	-	-	-	1.4(1)	-	-	-	-	-	-	-	-	0.70(7)
C23	-	-	-	-	-	0.8(2)	-	-	0.7(1)	-	-	1.1(1)	3.5(1)	-	-	-	-	-	-	-	-	-	-	-	-	-	-	-
C24	7.8(2)	4.6(1)	5.5(1)	-	-	3.4(1)	-	-	-	-	-	-	-	-	-	-	-	-	-	-	-	-	-	-	-	-	-	-
C25	2.2(2)	4.1(2)	5.0(3)	-	-	5.6(2)	-	-	-	-	<1	-	-	-	-	-	-	-	-	-	-	-	-	-	-	-	-	-
C26	-	<1	3.1(2)	-	-	4.89(9)	-	-	3.5(1)	-	-	-	-	-	-	-	-	-	0.4(3)	-	-	-	-	-	-	-	-	-
C27	-	-	-	-	-	-	-	-	0.89(4)	-	-	-	-	6.3(2)	2.2(6)	-	-	3.60(6)	0.65(5)	-	-	-	-	-	-	-	-	-
N	1.95(1)	2.25(5)	3.87(9)	-	-	6.69(4)	-	-	3.25(2)	0.56(3)	0.49(2)	-	1.2(1)	0.76(3)	-	-	-	1.49(4)	1.72(3)	-	-	0.70(7)	-	-	-	-	-	-

Table 4.2: All measured coupling frequencies in Hz for the $m_s = -1$ electron spin projection. To account for the cases where pulse errors cannot be neglected, the coupling frequencies are extracted by fitting the time-domain double resonance signals to $S = a + A \cdot e^{-(t/T_2)^n} \cos(2\pi f t + \phi) + B \cdot e^{-(t/T_2)^n}$, where T_2 is the coherence time and n, A and B are fit parameters that account for the signal decay shape, contrast and pulse errors. For the couplings marked as < 1 Hz in the tables, no oscillation was observed within the decay time. All couplings in the table are measured using $N = 1$ ($T_2 \sim 0.5$ s) except for C19 - C12 ($N = 256$) and C9 - C18 ($N = 32$).

	C1	C2	C3	C4	C5	C6	C7	C8	C9	C10	C11	C12	C13	C14	C15	C16	C17	C18	C19	C20	C21	C22	C23	C24	C25	C26	C27	N
C1	-	61.93(7)	62.87(9)	235.8(2)	10.1(1)	12.70(7)	5.9(2)	2.6(2)	1.1(2)	-	-	-	-	-	-	-	-	1.1(3)	-	-	2.7(5)	-	-	7.5(3)	1.8(3)	-	-	1.86(3)
C2	61.93(7)	-	235.6(1)	62.7(2)	22.7(2)	19.33(3)	6.3(3)	2.2(3)	1.00(9)	-	1.40(9)	<1	-	-	-	-	-	1.0(2)	-	-	2.6(1)	-	-	4.8(1)	3.35(9)	1.2(6)	-	2.06(4)
C3	62.87(9)	235.6(1)	-	25.2(1)	7.1(2)	24.8(1)	20.07(6)	12.25(5)	2.46(5)	-	-	1.14(8)	-	-	-	-	-	0.97(7)	-	-	1.8(3)	-	-	5.43(6)	4.6(1)	3.1(2)	-	-
C4	235.8(2)	62.7(2)	25.2(1)	-	20.2(4)	7.2(2)	-	-	-	-	-	-	-	-	-	-	-	-	-	-	-	-	-	-	-	-	-	-
C5	10.1(1)	22.7(2)	7.1(2)	20.2(4)	-	1.1(3)	1.4(8)	1.7(1)	1.35(9)	9.9(1)	-	-	1.86(9)	-	-	-	-	1.3(2)	1.05(8)	7.9(2)	15.3(1)	-	-	-	-	-	-	-
C6	12.70(7)	19.33(3)	24.8(1)	7.2(2)	1.1(3)	-	16.68(4)	12.1(1)	6.74(4)	-	-	1.74(6)	-	1.04(7)	-	-	-	1.07(6)	0.7(1)	<1	1.6(2)	-	0.78(8)	3.36(6)	3.37(7)	5.09(6)	-	6.60(7)
C7	5.9(2)	6.3(3)	20.07(6)	-	1.4(8)	16.68(4)	-	-	1.41(6)	-	-	0.4(2)	-	-	-	-	-	-	-	-	-	-	-	-	-	-	-	-
C8	2.6(2)	2.2(3)	12.25(5)	-	1.7(1)	12.1(1)	-	-	1.65(5)	-	-	1.10(7)	3.61(6)	-	-	-	-	-	-	-	-	-	-	-	-	-	-	-
C9	1.1(2)	1.00(9)	2.46(5)	-	1.35(9)	6.74(4)	1.41(6)	1.65(5)	-	1.2(2)	1.23(6)	3.48(7)	1.96(7)	3.80(6)	-	-	0.9(1)	1.16(6)	9.57(2)	-	-	3.82(6)	0.8(2)	-	-	3.1(1)	0.94(4)	3.24(3)
C10	-	-	-	-	9.9(1)	-	-	-	1.2(2)	-	14.45(6)	1.2(1)	-	-	3.7(1)	-	-	-	0.7(2)	6.9(3)	-	-	-	-	-	-	-	-
C11	-	1.40(9)	-	-	-	-	-	-	1.23(6)	14.45(6)	-	3.38(6)	-	-	1.7(5)	-	-	0.5(3)	-	-	-	-	-	-	-	-	-	-
C12	-	<1	1.14(8)	-	-	1.74(6)	0.4(2)	1.10(7)	3.48(7)	1.2(1)	3.38(6)	-	12.23(3)	2.48(9)	-	-	1.42(9)	1.1(5)	0.81(7)	-	-	2.35(4)	1.1(2)	-	-	-	-	-
C13	-	-	-	-	1.86(9)	-	-	3.61(6)	1.96(7)	-	-	12.23(3)	-	-	-	-	-	-	0.83(8)	-	-	7.21(4)	3.5(1)	-	1.5(1)	-	-	1.06(2)
C14	-	-	-	-	-	1.04(7)	-	-	3.80(6)	-	-	2.48(9)	-	-	8.86(1)	2.13(9)	22.02(6)	1.0(2)	1.61(7)	-	-	-	-	-	-	-	6.6(1)	-
C15	-	-	-	-	-	-	-	-	-	3.7(1)	1.7(5)	-	-	8.86(1)	-	26.2(5)	1.7(2)	-	-	-	-	-	-	-	-	-	2.7(2)	-
C16	-	-	-	-	-	-	-	-	-	-	-	-	-	2.13(9)	26.2(5)	-	-	1.39(7)	-	-	-	-	-	-	-	-	-	-
C17	-	-	-	-	-	-	-	-	0.9(1)	-	-	1.42(9)	-	22.02(6)	1.7(2)	-	-	2.70(8)	1.0(1)	-	-	-	-	-	-	-	-	-
C18	1.1(3)	1.0(2)	0.97(7)	-	1.3(2)	1.07(6)	-	-	1.16(6)	-	0.5(3)	1.1(5)	-	1.0(2)	-	1.39(7)	2.70(8)	-	0.95(6)	-	1.3(1)	-	-	-	-	-	3.56(9)	-
C19	-	-	-	-	1.05(8)	0.7(1)	-	-	9.57(2)	0.7(2)	-	0.81(7)	0.83(8)	1.61(7)	-	-	1.0(1)	0.95(6)	-	<1	-	1.3(1)	-	-	-	<1	0.88(4)	-
C20	-	-	-	-	7.9(2)	<1	-	-	-	6.9(3)	-	-	-	-	-	-	-	-	<1	-	-	-	-	-	-	-	-	-
C21	2.7(5)	2.6(1)	1.8(3)	-	15.3(1)	1.6(2)	-	-	-	-	-	-	-	-	-	-	-	1.3(1)	-	-	-	-	-	-	-	-	-	-
C22	-	-	-	-	-	-	-	-	3.82(6)	-	-	2.35(4)	7.21(4)	-	-	-	-	-	1.3(1)	-	-	-	-	-	-	-	-	-
C23	-	-	-	-	-	0.78(8)	-	-	0.8(2)	-	-	1.1(2)	3.5(1)	-	-	-	-	-	-	-	-	-	-	-	-	-	-	-
C24	7.5(3)	4.8(1)	5.43(6)	-	-	3.36(6)	-	-	-	-	-	-	-	-	-	-	-	-	-	-	-	-	-	-	-	-	-	-
C25	1.8(3)	3.35(9)	4.6(1)	-	-	3.37(7)	-	-	-	-	-	-	1.5(1)	-	-	-	-	-	-	-	-	-	-	-	-	-	-	-
C26	-	1.2(6)	3.1(2)	-	-	5.09(6)	-	-	3.1(1)	-	-	-	-	-	-	-	-	-	<1	-	-	-	-	-	-	-	-	-
C27	-	-	-	-	-	-	-	-	0.94(4)	-	-	-	-	6.6(1)	2.7(2)	-	-	3.56(9)	0.88(4)	-	-	-	-	-	-	-	-	-
N	1.86(3)	2.06(4)	-	-	-	6.60(7)	-	-	3.24(3)	-	-	-	1.06(2)	-	-	-	-	-	-	-	-	-	-	-	-	-	-	-

Table 4.3: All measured coupling frequencies in Hz for the $m_s = +1$ electron spin projection. All couplings in the table are measured using $N = 1$.

	C1	C2	C3	C4	C5	C6	C7	C8	C9	C10	C11	C12	C13	C14	C15	C16	C17	C18	C19	C20	C21	C22	C23	C24	C25	C26	C27	N
C1	-	61.90(8)	62.18(8)	235.9(2)	8.57(7)	12.68(7)	5.4(2)	2.8(2)	1.1(2)	<1	-	<1	<1	<1	-	-	-	1.1(2)	<1	-	2.5(4)	-	-	7.7(2)	2.0(2)	-	-	1.90(2)
C2	61.90(8)	-	235.77(7)	62.1(2)	19.9(1)	19.22(7)	5.9(2)	1.9(2)	1.06(8)	2.1(1)	1.4(1)	0.97(9)	<1	<1	<1	-	-	1.0(2)	<1	-	2.87(9)	-	-	4.7(1)	3.7(2)	1.2(6)	-	2.16(5)
C3	62.18(8)	235.77(7)	-	25.1(1)	5.2(1)	26.90(9)	20.1(3)	12.68(8)	2.50(6)	<1	<1	1.25(8)	<1	<1	-	-	-	0.99(5)	<1	-	2.0(2)	-	-	5.46(8)	4.8(2)	3.1(2)	-	3.87(9)
C4	235.9(2)	62.1(2)	25.1(1)	-	19.6(3)	7.1(2)	-	-	-	-	-	<1	<1	<1	<1	-	-	-	-	-	-	-	-	-	-	-	-	-
C5	8.57(7)	19.9(1)	5.2(1)	19.6(3)	-	1.8(7)	1.3(6)	1.3(2)	1.16(7)	8.82(7)	<1	<1	1.86(9)	-	1.9(1)	-	-	1.8(2)	0.8(2)	7.5(2)	12.60(9)	-	-	-	-	-	-	-
C6	12.68(7)	19.22(7)	26.90(9)	7.1(2)	1.8(7)	-	16.59(7)	12.37(8)	6.61(3)	<1	<1	1.88(6)	<1	0.9(2)	-	-	-	1.18(6)	0.7(1)	1.1(3)	1.8(2)	-	0.8(2)	3.38(8)	4.5(2)	4.99(8)	-	6.64(6)
C7	5.4(2)	5.9(2)	20.1(3)	-	1.3(6)	16.59(7)	-	-	1.43(7)	<1	-	0.4(2)	<1	<1	-	-	-	<1	-	-	-	-	-	-	-	-	-	-
C8	2.8(2)	1.9(2)	12.68(8)	-	1.3(2)	12.37(8)	-	-	1.59(5)	<1	-	1.12(8)	3.36(7)	<1	<1	-	-	<1	-	-	-	-	-	-	-	-	-	-
C9	1.1(2)	1.06(8)	2.50(6)	-	1.16(7)	6.61(3)	1.43(7)	1.59(5)	-	1.2(2)	1.25(5)	2.52(6)	1.9(2)	3.78(5)	-	<1	1.0(1)	1.27(4)	9.01(2)	-	-	3.76(7)	0.8(2)	-	-	3.3(1)	0.92(4)	3.24(3)
C10	<1	2.1(1)	<1	-	8.82(7)	<1	<1	<1	1.2(2)	-	14.48(7)	1.2(1)	<1	<1	3.7(4)	5.0(1)	-	<1	0.7(2)	6.9(2)	3.8(2)	-	-	-	-	-	-	0.56(3)
C11	-	1.4(1)	<1	-	<1	<1	-	-	1.25(5)	14.48(7)	-	3.36(5)	<1	<1	1.9(4)	4.7(1)	-	0.5(3)	<1	9.5(2)	-	-	-	-	<1	-	-	0.49(2)
C12	<1	0.97(9)	1.25(8)	<1	<1	1.88(6)	0.4(2)	1.12(8)	2.52(6)	1.2(1)	3.36(5)	-	12.20(5)	1.97(9)	-	<1	1.34(9)	1.1(4)	0.67(5)	-	-	2.0(1)	1.1(2)	-	-	-	-	-
C13	<1	<1	<1	<1	1.86(9)	<1	<1	3.36(7)	1.9(2)	<1	<1	12.20(5)	-	<1	<1	<1	<1	-	1.1(2)	-	-	7.26(8)	3.5(1)	-	1.5(1)	-	-	1.13(7)
C14	<1	<1	<1	<1	-	0.9(2)	<1	<1	3.78(5)	<1	<1	1.97(9)	<1	-	8.88(5)	2.1(2)	21.9(2)	1.2(2)	1.60(9)	-	-	-	-	-	-	-	6.5(2)	0.76(3)
C15	-	<1	-	<1	1.9(1)	-	-	<1	-	3.7(4)	1.9(4)	-	<1	8.88(5)	-	25.4(4)	1.7(2)	<1	<1	-	-	-	-	-	-	-	2.4(4)	-
C16	-	-	-	-	-	-	-	-	<1	5.0(1)	4.7(1)	<1	<1	2.1(2)	25.4(4)	-	-	1.44(9)	<1	-	-	-	-	-	-	-	-	-
C17	-	-	-	-	-	-	-	-	1.0(1)	-	-	1.34(9)	<1	21.9(2)	1.7(2)	-	-	2.56(7)	1.0(1)	-	-	-	-	-	-	-	-	-
C18	1.1(2)	1.0(2)	0.99(5)	-	1.8(2)	1.18(6)	<1	<1	1.27(4)	<1	0.5(3)	1.1(4)	-	1.2(2)	<1	1.44(9)	2.56(7)	-	1.14(5)	-	1.40(9)	-	-	-	-	-	3.58(8)	1.49(4)
C19	<1	<1	<1	-	0.8(2)	0.7(1)	-	-	9.01(2)	0.7(2)	<1	0.67(5)	1.1(2)	1.60(9)	<1	<1	1.0(1)	1.14(5)	-	1.7(3)	-	1.4(1)	-	-	-	0.4(3)	0.76(5)	1.72(3)
C20	-	-	-	-	7.5(2)	1.1(3)	-	-	-	6.9(2)	9.5(2)	-	-	-	-	-	-	-	1.7(3)	-	-	-	-	-	-	-	-	-
C21	2.5(4)	2.87(9)	2.0(2)	-	12.60(9)	1.8(2)	-	-	-	3.8(2)	-	-	-	-	-	-	-	1.40(9)	-	-	-	-	-	-	-	-	-	-
C22	-	-	-	-	-	-	-	-	3.76(7)	-	-	2.0(1)	7.26(8)	-	-	-	-	-	1.4(1)	-	-	-	-	-	-	-	-	0.70(7)
C23	-	-	-	-	-	0.8(2)	-	-	0.8(2)	-	-	1.1(2)	3.5(1)	-	-	-	-	-	-	-	-	-	-	-	-	-	-	-
C24	7.7(2)	4.7(1)	5.46(8)	-	-	3.38(8)	-	-	-	-	-	-	-	-	-	-	-	-	-	-	-	-	-	-	-	-	-	-
C25	2.0(2)	3.7(2)	4.8(2)	-	-	4.5(2)	-	-	-	-	<1	-	1.5(1)	-	-	-	-	-	-	-	-	-	-	-	-	-	-	-
C26	-	1.2(6)	3.1(2)	-	-	4.99(8)	-	-	3.3(1)	-	-	-	-	-	-	-	-	-	0.4(3)	-	-	-	-	-	-	-	-	-
C27	-	-	-	-	-	-	-	-	0.92(4)	-	-	-	-	6.5(2)	2.4(4)	-	-	3.58(8)	0.76(5)	-	-	-	-	-	-	-	-	-
N	1.90(2)	2.16(5)	3.87(9)	-	-	6.64(6)	-	-	3.24(3)	0.56(3)	0.49(2)	-	1.13(7)	0.76(3)	-	-	-	1.49(4)	1.72(3)	-	-	0.70(7)	-	-	-	-	-	-

Table 4.4: All measured coupling frequencies in Hz averaged over the $m_s = +1$ and $m_s = -1$ electron spin projections. A total of 171 couplings are measured, including the couplings marked < 1 Hz.

Spin	Diamond			Diamond Fit			Cubic			Cubic Fit		
	x (Å)	y (Å)	z (Å)	x (Å)	y (Å)	z (Å)	x (Å)	y (Å)	z (Å)	x (Å)	y (Å)	z (Å)
1	0.00	0.00	0.00	$0.00^{\dagger}$	$0.00^{\dagger}$	$0.00^{\dagger}$	0.00	0.00	0.00	$0.00^{\dagger}$	$0.00^{\dagger}$	$0.00^{\dagger}$
2	2.52	2.91	-0.51	$2.53(2)^{\ddagger}$	$2.92(2)^{\ddagger}$	-0.45(7)	2.52	2.91	-0.50	$2.52(2)^{\ddagger}$	$2.91(2)^{\ddagger}$	-0.47(7)
3	3.78	0.73	-0.51	3.77(3)	0.72(3)	-0.50(9)	3.75	0.71	-0.55	3.78(3)	0.72(3)	-0.48(9)
4	-1.26	2.18	0.00	-1.28(3)	2.18(3)	- 0.0(1)	-1.23	2.20	0.05	-1.28(3)	2.17(4)	- 0.1(1)
5	0.00	4.37	-6.18	0.06(5)	4.45(5)	-6.17(7)	0.03	4.38	-6.19	0.05(5)	4.45(5)	-6.18(7)
6	5.04	-1.46	-2.06	5.1(1)	- 1.4(1)	-2.03(6)	5.14	-1.36	-2.08	5.1(1)	- 1.4(1)	-2.02(6)
7	5.04	-1.46	5.66	4.93(9)	- 1.5(1)	5.67(8)	4.83	-1.59	5.65	4.92(9)	- 1.6(1)	5.67(8)
8	7.57	1.46	3.60	7.5(2)	1.7(2)	3.6(1)	7.42	1.72	3.32	7.5(2)	1.6(2)	3.6(1)
9	7.57	-4.37	-10.81	7.3(4)	- 4.6(5)	-10.7(2)	7.70	-4.31	-10.90	7.2(4)	- 4.5(4)	-11.0(2)
10	0.00	8.74	-12.36	0.0(3)	8.5(3)	-13.2(3)	0.05	8.56	-12.99	- 0.1(3)	8.6(3)	-13.1(3)
11	6.31	9.46	-12.87	6.3(5)	9.5(4)	-12.6(3)	6.39	9.47	-12.67	6.2(4)	9.6(4)	-12.7(3)
12	11.35	0.73	-14.42	11.4(5)	0.9(5)	-14.5(2)	11.37	0.54	-14.42	11.0(5)	1.0(5)	-14.7(2)
13	12.61	2.91	-6.69	12.7(6)	3.3(6)	- 6.9(2)	12.23	3.23	-6.99	12.3(6)	3.3(5)	- 7.1(2)
14	5.04	-2.91	-22.65	5.4(4)	- 3.2(4)	-22.9(3)	5.40	-3.35	-22.72	4.9(4)	- 3.2(4)	-23.2(3)
15	1.26	3.64	-22.65	2.0(5)	3.5(4)	-22.7(4)	2.34	3.48	-22.27	1.8(5)	3.6(4)	-22.7(4)
16	2.52	8.74	-23.17	3.5(6)	8.4(5)	-23.5(3)	3.26	8.28	-23.38	3.3(5)	8.5(5)	-23.5(3)
17	6.31	-2.18	-29.34	5.8(8)	- 2.6(8)	-29.8(4)	5.40	-3.35	-29.75	5.7(7)	- 2.7(8)	-30.1(4)
18	0.00	-1.46	-19.05	- 0.2(4)	- 1.2(5)	-19.1(3)	0.17	-1.55	-18.46	- 0.2(4)	- 1.3(4)	-19.0(3)
19	3.78	-9.46	-8.75	3.8(8)	- 9.1(8)	- 8.4(4)	4.55	-9.32	-8.65	3.3(8)	- 9.4(8)	- 8.8(5)
20	3.78	10.92	-4.63	3.1(5)	11.8(5)	- 5.7(6)	3.24	11.64	-5.49	3.0(5)	11.9(4)	- 5.7(6)
21	-5.04	5.82	-4.12	- 4.7(4)	5.8(5)	-4.02(8)	-4.81	5.78	-4.08	- 4.8(4)	5.7(4)	-4.03(8)
22	16.39	-3.64	-8.24	16(1)	-3(1)	-8(1)	16.94	-2.19	-9.02	15(1)	-3(1)	- 8.4(7)
23	16.39	-0.73	3.60	16(1)	0(1)	3.5(6)	16.14	-0.16	3.37	15(1)	0(1)	3.5(5)
24	1.26	-0.73	9.78	1.2(3)	- 0.8(3)	9.8(1)	1.08	-0.28	9.98	1.2(3)	- 0.8(3)	9.8(1)
25	6.31	-0.73	9.78	7.5(4)	0.5(5)	9.4(3)	7.17	0.47	9.74	7.5(4)	0.5(5)	9.4(3)
26	12.61	-5.82	-0.51	12.6(8)	- 6.1(9)	- 0.7(6)	13.12	-5.59	-1.40	12.3(8)	- 6.6(9)	- 0.8(6)
27	1.26	-3.64	-31.40	1.3(4)	- 3.3(4)	-31.4(4)	1.06	-3.27	-31.06	0.7(4)	- 3.1(4)	-31.5(4)
N	3.78	-0.73	-8.75	3.8(3)*	- 0.7(3)*	-8.61(8)*	-	-	-	-	-	-

Table 4.5: **Structure of the cluster.** Coordinates obtained from the measured couplings using the diamond lattice positioning method (section 4.8.4), the cubic lattice method (section 4.8.4) and from using least-squares minimisation using the diamond and cubic solutions as an initial guess (section 4.8.4). †Coordinate fixed to zero in the fitting routine. ‡Rotational symmetry fixed by rotating the initial guess solution by -49.1 deg and fixing the rotated coordinate y'_2 to zero. *Nitrogen spin fitted coordinates when the ^{13}C coordinates are fixed to the diamond lattice solution (see section 4.7).

4.8.2. MULTI-RESONANCE EXPERIMENTS AND RESOLVING SPECTRALLY OVERLAPPING SPINS

As discussed in the main text, resolving ambiguities due to overlapping signals from multiple spins at (near-)identical frequencies is a key component for determining the composition of the cluster and how the spins couple to each other. To resolve such ambiguities, there are two main challenges: first, how to extract the underlying coupling frequencies from the complex signals in the case of multiple overlapping spins; second, how to determine the number of spins in the cluster and to assign the measured couplings to specific spins.

To address the first challenge we use two examples from our data to demonstrate that our method can extract the coupling frequencies from the complex signals in the case of multiple overlapping spins (Fig. 4.10). In this scenario, our pulse sequence would essentially perform a spin echo multi-resonance experiment as multiple overlapping target spins will be flipped simultaneously with the probe spin. Correspondingly, the couplings between the probe spin and the target spins will be isolated. Whilst this case naturally arises when the NMR lines of multiple spins overlap, we note that the effect might more generally allow for the extraction of multiple couplings simultaneously by the application of several resonant RF pulses (Fig. 4.10a) or a single spectrally broad pulse. This is a potential technique for parallelised data acquisition.

Fig. 4.10b shows the obtained signal for a spin echo triple-resonance experiment between a probe spin (C5) and two spectrally overlapping target spins (C4, C15). The two spins have similar resonance frequencies within 200 Hz, and their spectra strongly overlap (Fig. 4.11b). The Rabi frequency of the RF pulses is ~ 500 Hz. Therefore a single resonant RF pulse on one of the target spins would flip the other target spin simultaneously.

While the obtained spectra for multi-resonance experiments are generally more complex (Fig. 4.10b), the high spectral resolution in our case enables the coupling frequencies to be resolved. For the triple-resonance experiment, and assuming ideal inversion pulses, the expected frequencies are $f = \pm f_1 \pm f_2$ where $f_1 = 19.0(1)$ Hz and $f_2 = 1.9(1)$ Hz are the extracted couplings between the probe spin and the two target spins (red lines). Due to pulse imperfections, additional frequencies also emerge (grey lines). For example, a failure in the inversion of the second target spin will create the frequency components $\pm f_1$ that originate from a double resonance signal between the probe and the first target spin. Similarly a failure on the inversion of the first target spin will lead to $\pm f_2$. We perform numerical simulations of this experiment taking into account the pulse errors (Fig. 4.10c). The inversion probability of the pulses in this simulation is set to 80%. The large infidelity in the pulses in this case is due to strong couplings of the target spins to other nearby nuclear spins, which leads to a spectrally broad signal compared to the Rabi frequency. The result of this simulation shows that pulse errors can indeed explain the emergence of the extra observed frequencies.

Fig. 4.10d shows another example of a quadruple resonance experiment (Probe spin: C5, Target spins: C2, C1, C3). In this case we use 3 separate RF pulses to invert the three target spins as they have different resonance frequencies. The obtained spectrum of this measurement is even more complex, yet nevertheless the high spectral resolution makes it possible to resolve the couplings. For ideal inversion pulses, the eight theoretically expected frequencies are given by $f = \pm f_1 \pm f_2 \pm f_3$, where $f_1 = 17.17(2)$ Hz, $f_2 = 7.05(3)$ Hz and $f_3 = 3.21(4)$ Hz are the extracted couplings between the probe spin and the three target spins respectively. Additional frequencies emerge due to pulse imperfections (grey lines) as described above and confirmed by numerical simulations (Fig. 4.10e).

While our scheme allows multiple couplings to be extracted from the complex obtained signal due to the high spectral resolution, this measurement alone does not yet enable the obtained couplings to be assigned to certain spins. To overcome this, we utilise the inter-connectivity between the spins in the cluster which provides enough redundancy to constrain the problem. The key idea is that each spin couples predominantly to other spins in its vicinity, and so provides a different vantage point of the cluster. So by repeating the previous measurement using different probe spins we can obtain more information to resolve these ambiguities. Fig. 4.11a,b show how we can resolve and identify the two overlapping spins, C4 and C15 shown in Fig. 4.10b.

The same idea—nuclear spins predominantly couple to other spins in their vicinity—enables the detection and imaging of nuclear spins with small hyperfine couplings to the electron spin (< 5kHz). In the system considered here, spins with small hyperfine couplings are challenging to resolve directly using the electron spin, because of a multitude of overlapping signals from spins with very similar frequencies [36]. By using multiple spatially close nuclear spins (i.e., a sub-cluster) as probes, we can filter out the signals from remote nuclear spins at the target frequency, as we predominantly probe a certain region of the space. This allows our method to also isolate and detect, and therefore position, spins with small couplings to the electron. Fig. 4.11c,d,e illustrate this concept.

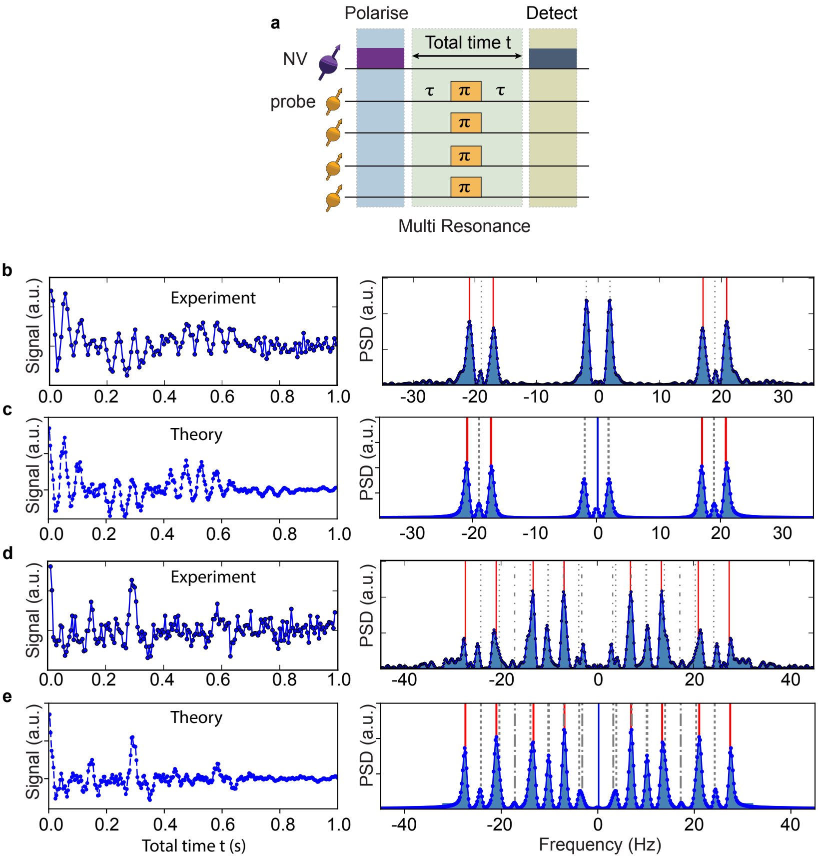

Figure 4.10: **Multi-resonance experiments: probing multiple couplings simultaneously.** **a**, A pulse sequence describing a multi-resonance experiment that causes multiple couplings to be accessed simultaneously. The echos are performed simultaneously on the probe and the target spins. This can be realised using multiple resonant RF pulses or a single spectrally broad pulse. When the NMR lines of multiple spins overlap, the last situation naturally and inevitably occurs . **b**, In this case two spectrally overlapping spins in the cluster are flipped simultaneously using a single RF pulse (i.e., a triple resonance experiment). For ideal inversion pulses the expected frequencies are $f = \pm f_1 \pm f_2$, where $f_1 = 19.0(1)$ Hz and $f_2 = 1.9(1)$ Hz are the extracted couplings between the probe spin and the two target spins (red lines). Additional frequencies emerge due to non-ideal inversion pulses (grey lines). **c**, Numerical simulation of the experiment in b) taking into account the non-ideal pulses. The obtained result matches well the experimental data and confirms that pulse errors can indeed explain the emergence of the extra observed frequencies. **d**, A quadruple-resonance experiment between a probe spin (C5) and three spectrally resolvable target spins (C2, C1, C3). See also main text Figure 4.3. Red lines are the theoretically expected frequencies for ideal π- pulses on the target spins, $f = \pm f_1 \pm f_2 \pm f_3$, where $f_1 = 17.17(2)$ Hz, $f_2 = 7.05(3)$ Hz and $f_3 = 3.21(4)$ Hz are the extracted couplings between the probe spin and the three target spins respectively. Grey dashed lines correspond to additional frequencies due to a failure to invert one or two of the target spins. **e**, Numerical simulation taking into account the pulse errors.

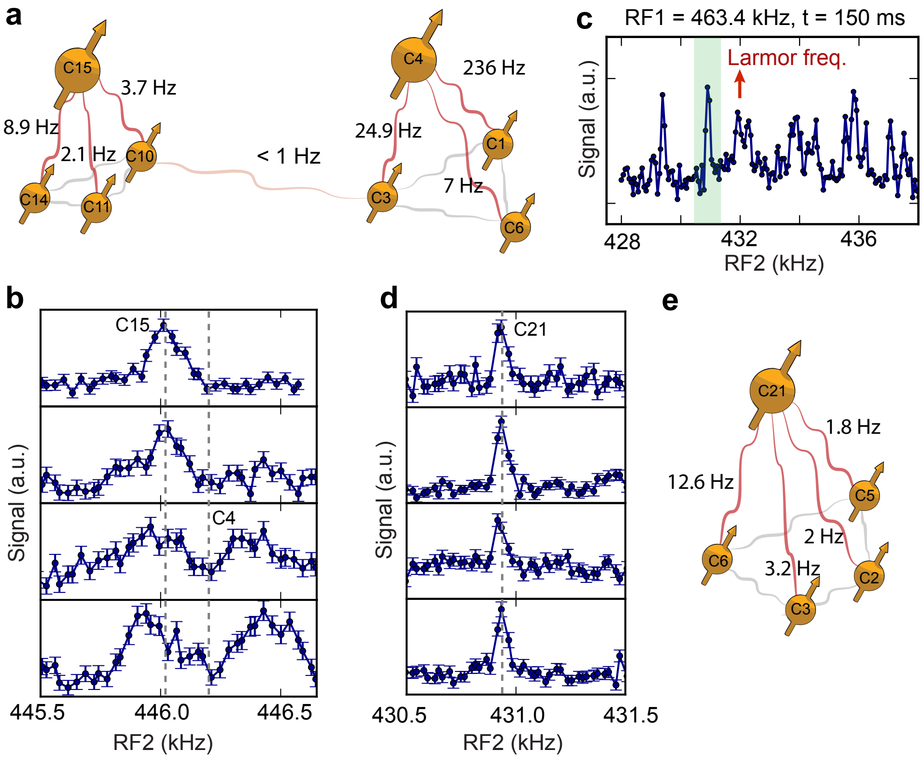

Figure 4.11: **Identifying spectrally overlapping nuclear spins.** **a**, Illustration of the basic idea: C15 and C4 are two nuclear spins with similar precession frequencies due to their similar coupling to the electron spin, yet we can identify and position them through their coupling to other nuclear spins. Each of these spins couples strongly to other nuclear spins in their vicinity. This connectivity reveals that there are two spins (C15 and C4) that are far apart. **b**, Double resonance frequency scan using four different probe spins (top to bottom: C14, C10, C6, C3) around a target frequency of 446 kHz. C10 and C14 are more strongly coupled to C15, while C6 and C3 are more strongly coupled to C4. The scans for C14 and C10 show a peak at a target frequency of 446 kHz due to coupling to C15, while scans for C6 and C3 show two peaks due to a coupling to C4 (in this case C4 also strongly couples to another spin with 236 Hz which causes this splitting in its spectrum). The spectra of C15 and C4 are thus overlapping but each of them couples very differently to the 4 probe spins, revealing that there are two distinct spins. The dashed grey lines mark the center frequencies of C15 and C4. **c**, The same idea—i.e., nuclear spins predominantly couple to other nuclear spins in their vicinity—can be used to uniquely identify and position nuclear spins with small couplings to the electron spin (< 1kHz), even though, in our system, there will generally be multiple other spins with near-identical frequencies at other locations. The shown data is a double resonance frequency scan near the bare nuclear spin Larmor frequency using C6 as a probe spin. We observe well resolved peaks potentially due to nuclear spins with relatively strong couplings to this probe spin. **d**, Double resonance scan around the shaded area in **c** (~ 1 kHz from the Larmor frequency) using 4 probe spins (top to bottom: C6, C3, C2, C5) that are spatially close to each other. **e**, The measured couplings between this target spin (C21) and the four probe spins. These measured couplings provide sufficient information to identify C21 and position it with respect to the four probe spins. The error bars represent one statistical standard deviation.

4.8.3. ACCOUNTING FOR ELECTRON-MEDIATED COUPLINGS

The nuclear-nuclear couplings measured by a double-echo sequence can be modified due to the presence of the electron spin and a misaligned magnetic field. To understand these effects, we can use perturbation theory. In refs. [44, 46], shifts in the nuclear-nuclear couplings are calculated by only considering the interaction between the electron and ^{13}C spins in the perturbation. However, for the weak electron-nuclear couplings considered in this work, modifications due to the non-secular nuclear-nuclear interactions combined with the electron-nuclear interactions can also give a significant correction, and should therefore also be included in the perturbation. We will consider the Hamiltonian describing the spin-1 electron plus two spin-1/2 ^{13}C spins, given by

$$\begin{aligned} H &= H_e + H_c + H_{ec} + H_{cc}, \\ H_e &= \Delta_{\mathrm{ZFS}} S_z^2 + \gamma_e (B_x S_x + B_y S_y + B_z S_z), \\ H_c &= \gamma_c \mathbf{B} \cdot (\mathbf{I}^{(1)} + \mathbf{I}^{(2)}), \\ H_{ec} &= \mathbf{S} \cdot \mathbf{A}^{(1)} \cdot \mathbf{I}^{(1)} + \mathbf{S} \cdot \mathbf{A}^{(2)} \cdot \mathbf{I}^{(2)}, \\ H_{cc} &= \mathbf{I}^{(1)} \cdot \mathbf{C} \cdot \mathbf{I}^{(2)}, \end{aligned} \tag{4.6}$$

where Δ_{ZFS} is the electron zero field splitting, γ_e (γ_c) is the electron (^{13}C) gyromagnetic ratio, $\mathbf{B} = (B_x, B_y, B_z)$ is the magnetic field vector, $\mathbf{S} = (S_x, S_y, S_z)$ are the electron spin operators, $\mathbf{I}^{(j)} = (I_x^{(j)}, I_y^{(j)}, I_z^{(j)})$ are the ^{13}C spin operators for spin j, and $\mathbf{A}^{(j)}$ and $\mathbf{C}$ are the hyperfine tensors describing the electron-nuclear and nuclear-nuclear interactions respectively, with components $A_{\alpha\beta}^{(j)}$ and $C_{\alpha\beta}$ for $\alpha, \beta \in \{x, y, z\}$.

In our experiments we apply a strong magnetic field along the z-axis ($B_z \sim 403\,\mathrm{G}$), and align the field such that $B_x, B_y \approx 0$. The dominant energy scales are then given by the terms $\Delta_{\mathrm{ZFS}} S_z^2$, $\gamma_e B_z S_z$ and $\gamma_c B_z I_z^{(j)}$. Therefore, we will take terms that commute with S_z^2, S_z, $I_z^{(1)}$ and $I_z^{(2)}$ as the unperturbed Hamiltonian H_0. This gives

$$H_0 = \Delta_{\mathrm{ZFS}} S_z^2 + \gamma_e B_z S_z + \gamma_c B_z (I_z^{(1)} + I_z^{(2)}) + A_{zz}^{(1)} S_z I_z^{(1)} + A_{zz}^{(2)} S_z I_z^{(2)} + C_{zz} I_z^{(1)} I_z^{(2)}. \tag{4.7}$$

The eigenstates of H_0 are $|m_s, m_I^{(1)}, m_I^{(2)}\rangle$, where $m_s \in \{+1, 0, -1\}$ are the eigenvalues of S_z and $m_I^{(j)} \in \{+\frac{1}{2}, -\frac{1}{2}\}$ are the eigenvalues of $I_z^{(j)}$. The eigenvalues of H_0 are then

$$\begin{aligned} \lambda_0(m_s, m_I^{(1)}, m_I^{(2)}) = {} & m_s^2 \Delta_{\mathrm{ZFS}} + m_s \gamma_e B_z + (m_I^{(1)} + m_I^{(2)}) \gamma_c B_z \\ & + m_s m_I^{(1)} A_{zz}^{(1)} + m_s m_I^{(2)} A_{zz}^{(2)} + m_I^{(1)} m_I^{(2)} C_{zz}. \end{aligned} \tag{4.8}$$

A double-resonance measurement gives an oscillating signal at frequency [27]

$$f_{\mathrm{DR}}(m_s) = \frac{1}{4\pi} \left| \lambda\left(m_s, +\frac{1}{2}, +\frac{1}{2}\right) + \lambda\left(m_s, -\frac{1}{2}, -\frac{1}{2}\right) - \lambda\left(m_s, +\frac{1}{2}, -\frac{1}{2}\right) - \lambda\left(m_s, -\frac{1}{2}, +\frac{1}{2}\right) \right|. \tag{4.9}$$

If we take the zeroth order approximation, such that $\lambda(m_s, m_I^{(1)}, m_I^{(2)}) \approx \lambda_0(m_s, m_I^{(1)}, m_I^{(2)})$, we obtain

$$f_{\mathrm{DR}} \approx \frac{1}{4\pi}|C_{zz}|, \tag{4.10}$$

which holds for all electron spin projections. To zeroth order, the double resonance measurement gives the zz dipolar coupling between the two ^{13}C spins, as expected.

We can now calculate corrections to the nuclear-nuclear couplings due to the other Hamiltonian terms using perturbation theory. Defining the remaining terms in the Hamiltonian as $V = H - H_0$, up to second order the corrected eigenvalues are given by [47]

$$\lambda(\psi_n) \approx \lambda_0(\psi_n) + \langle\psi_n|V|\psi_n\rangle + \sum_{k\neq n}\frac{|\langle\psi_k|V|\psi_n\rangle|^2}{\lambda_0(\psi_n) - \lambda_0(\psi_k)}, \tag{4.11}$$

where $|\psi_n\rangle$ are the eigenstates of H_0. Since V contains no diagonal matrix elements, $\langle\psi_n|V|\psi_n\rangle = 0$ for all $|\psi_n\rangle$. We will restrict our analysis to the $m_s = \pm1$ subspace, as only transitions within this subspace are measured for the experiments described in this manuscript and for the $m_s = 0$ subspace some eigenstates are degenerate, making the analysis more complex. We find three sets of correction terms, allowing us to write the corrected double resonance frequency up to second order as

$$f_{\mathrm{DR}}(m_s = \pm1) \approx \frac{1}{4\pi}|C_{zz} + \Delta\lambda_1(m_s) + \Delta\lambda_2(m_s) + \Delta\lambda_3(m_s)|. \tag{4.12}$$

The first correction term $\Delta\lambda_1$ describes a correction to the nuclear-nuclear coupling that is only dependent on the interaction between each ^{13}C spin and the electron spin. This term is equal to the correction term derived in refs. [44, 46]. With the approximation that $|\gamma_c B_z|, |A_{zz}^{(j)}|, |C_{zz}| \ll |\Delta_{\mathrm{ZFS}} + m_s\gamma_e B_z|$, we obtain

$$\Delta\lambda_1(m_s = \pm1) \approx \frac{A_{zx}^{(1)}A_{zx}^{(2)} + A_{zy}^{(1)}A_{zy}^{(2)}}{\Delta_{\mathrm{ZFS}} + m_s\gamma_e B_z}. \tag{4.13}$$

The second correction term $\Delta\lambda_2$ describes a correction that depends on both the nuclear-electron and the nuclear-nuclear interactions. With the approximation that $|C_{zz}| \ll |\gamma_c B_z|$, and making a Taylor expansion up to first order in $A_{zz}^{(j)}/\gamma_c B_z$, we find

$$\Delta\lambda_2(m_s = \pm1) \approx m_s\Delta\lambda_2^{(0)} + \Delta\lambda_2^{(1)} \tag{4.14}$$

where $m_s\Delta\lambda_2^{(0)}$ and $\Delta\lambda_2^{(1)}$ are the zeroth and first order terms in the Taylor expansion respectively, given by

$$\begin{aligned} \Delta\lambda_2^{(0)} &= \frac{(A_{zx}^{(1)} + A_{zx}^{(2)})C_{zx} + (A_{zy}^{(1)} + A_{zy}^{(2)})C_{zy}}{\gamma_c B_z} \\ \Delta\lambda_2^{(1)} &= -\sum_{j=1}^{2}\frac{(A_{zx}^{(j)}C_{zx} + A_{zy}^{(j)}C_{zy})A_{zz}^{(j)}}{\gamma_c^2 B_z^2}. \end{aligned} \tag{4.15}$$

Lastly, there is a correction that depends on the perpendicular magnetic field. With the approximation that $|C_{zz}| \ll |\gamma_c B_z|$, and making a Taylor expansion up to first order in $A_{zz}^{(j)}/\gamma_c B_z$, we obtain

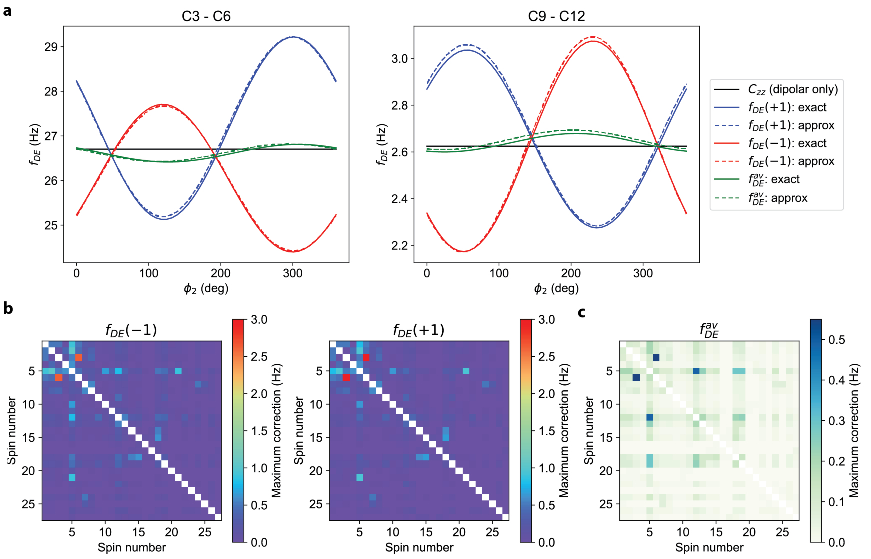

Figure 4.12: **Corrections to the measured couplings a,** Two examples of modified nuclear-nuclear couplings due to electron mediated effects for exact numerical solutions (solid lines) and approximate solutions using equations 4.12 and 4.18 (dashed lines). The hyperfine parameters are taken from Table 4.4. The radial magnetic field component $B_\perp$ is set to zero in these examples, but similar results are seen for small values $< 1\,\mathrm{G}$ as measured experimentally (see Fig. 4.9). The nuclear-nuclear hyperfine tensors are calculated from the coordinates given in Table 4.5 and the unknown angles φ_j are set to 0 for the first spin and varied for the second spin (other values for the first spin also give similar agreement). **b,** Maximum corrections to the measured nuclear-nuclear couplings between each of the 27 spins for the $m_s = \pm 1$ spin projections, $f_{\mathrm{DR}}(\pm 1)$, calculated from equation 4.12. For each coupling the correction is maximised over the unknown parameters $0 < \varphi_j < 2\pi$, $0 < B_\perp < 1\,\mathrm{G}$ and $0 < \theta < 2\pi$. **c,** The same correction matrix as in (b) for the averaged coupling $f^{\mathrm{av}}_{\mathrm{DR}}$ (equation 4.18).

$$\Delta\lambda_3(m_s = \pm 1) \approx \Delta\lambda_3^{(0)} + m_s \Delta\lambda_3^{(1)} \tag{4.16}$$

where $\Delta\lambda_3^{(0)}$ and $m_s\Delta\lambda_3^{(1)}$ are the zeroth and first order terms in the Taylor expansion respectively, given by

$$\begin{aligned} \Delta\lambda_3^{(0)} &= \frac{2(B_x C_{zx} + B_y C_{zy})}{B_z} \\ \Delta\lambda_3^{(1)} &= \frac{(A_{zz}^{(1)} + A_{zz}^{(2)})(B_x C_{zx} + B_y C_{zy})}{\gamma_c B_z^2}. \end{aligned} \tag{4.17}$$

We can now calculate the average frequency for a double resonance measurement on both $m_s = \pm 1$ transitions. We find

$$\begin{aligned} f_{\mathrm{DR}}^{\mathrm{av}} &= \frac{1}{2}\big(f_{\mathrm{DR}}(+1) + f_{\mathrm{DR}}(-1)\big) \\ &= \frac{1}{4\pi}\left| C_{zz} + \frac{\Delta\lambda_1(+1) + \Delta\lambda_1(-1)}{2} + \Delta\lambda_2^{(1)} + \Delta\lambda_3^{(0)} \right|, \end{aligned} \tag{4.18}$$

where in the last line we have assumed that $|\Delta\lambda_1(m_s) + \Delta\lambda_2(m_s) + \Delta\lambda_3(m_s)| < |C_{zz}|$. It can be seen that the terms $m_s\Delta\lambda_2^{(0)}$ and $m_s\Delta\lambda_3^{(1)}$ cancel when taking the average double resonance frequency.

To check the validity of the approximate solutions, we can compare to exact numerical solutions of the full Hamiltonian (equation 4.6) for some example cases. Since we only measure the magnitude of the perpendicular couplings $A_\perp^{(j)} = \sqrt{\left(A_{zx}^{(j)}\right)^2 + \left(A_{zy}^{(j)}\right)^2}$, we will parameterise the couplings as $A_{zx}^{(j)} = A_\perp^{(j)}\cos(\varphi_j)$ and $A_{zy}^{(j)} = A_\perp^{(j)}\sin(\varphi_j)$, where φ_j is the unknown azimuthal angle of the electron-nuclear hyperfine coupling for spin j. Additionally, we can parameterise the magnetic field in the $x - y$ plane as $B_x = B_\perp\cos(\theta)$ and $B_y = B_\perp\sin(\theta)$. We can infer that $B_\perp < 1\,\mathrm{G}$ (see Fig. 4.9), while no information about θ is known. Fig. 4.12(a) shows a comparison between the approximate and exact solutions for two example cases based on parameters measured in this experiment. We can also estimate the magnitude of each correction term using the values for the parameters used in the experiment. Taking the coordinates of the 27 spin cluster (Table 4.5), for each possible spin pair we can maximise equations 4.12 and 4.18 over the unknown angles φ_j and the magnetic field parameters $B_\perp$ and θ. Matrix plots of estimated maximum values are shown in Fig. 4.12(b,c). Averaging over the unknown angles φ_j, the average correction over all spins is 0.04 Hz for $m_s = \pm 1$ and 0.01 Hz for the average, while the maximum over all φ_j and spins is 2.6 Hz (3.1 Hz) for $m_s = -1$ ($m_s = +1$) and 0.55 Hz for the average. The corrections for $m_s = \pm 1$ are therefore much greater than the averaged values, thereby showing that the measured couplings are closer to the dipolar values when taking the average of the $m_s = \pm 1$ measurements.

4.8.4. OBTAINING THE STRUCTURE OF THE NUCLEAR SPIN CLUSTER

We would like to find the relative coordinates of M nuclear spins: $\{x_i, y_i, z_i\}$, $i = 1, \ldots, M$. Each nuclear spin is pairwise coupled to every other spin with zz coupling constants

$C_{ij}(x_i, y_i, z_i, x_j, y_j, z_j)$, which, assuming point-dipole coupling, are related to the coordinates by the set of equations

$$C_{ij} = \frac{\alpha_{ij}}{\Delta r_{ij}^3}\left(\frac{3(z_j - z_i)^2}{\Delta r_{ij}^2} - 1\right), \tag{4.19}$$

where $\Delta r_{ij} = \sqrt{(x_j - x_i)^2 + (y_j - y_i)^2 + (z_j - z_i)^2}$, $\alpha_{ij} = \mu_0 \gamma_i \gamma_j \hbar/4\pi$, μ_0 is the permeability of free space, γ_i is the gyromagnetic ratio of nuclear spin i and $\hbar$ is the reduced Planck constant. A double resonance measurement performed on two spins i and j gives a signal oscillating at frequency f_{ij}, which is approximately related to the magnitude of the coupling as $f_{ij} \approx |C_{ij}|/4\pi$. Therefore, we define the residual for each coupling as $\Delta f_{ij} \equiv f_{ij} - |C_{ij}|/4\pi$. There are $3M$ coordinates and $M(M-1)/2$ coupling constants. Since we are interested in only the relative coordinates, we can fix the first spin to be at the origin: $\{x_1, y_1, z_1\} = \{0, 0, 0\}$. Additionally, since there is a rotational symmetry in the $x - y$ plane, we can also set one of the x, y coordinates of the second spin to zero. The number of free coordinates is therefore $3M - 4$, and consequently to achieve more measurements than free parameters, as required for the problem to be overdetermined, we require $M \geq 6$ (for $M = 6$: $3M - 4 = 14$, $M(M-1)/2 = 15$). The best fit solution is then given by a set of parameters $\{x_i, y_i, z_i\}$ that minimise the sum of squares, defined as

$$\xi \equiv \sum_{i=1}^{M} \sum_{j=1}^{i} |\Delta f_{ij}|^2. \tag{4.20}$$

As described in section 4.8.3, the largest of the corrections to the couplings (due to the presence of the electron spin) are cancelled when taking the average of the frequencies measured for the $m_s = \pm 1$ electron spin projections. Despite this, the measurement uncertainties can be smaller than the corrections (measurement uncertainties are typically < 0.1 Hz, while the corrections could be up to ~ 0.6 Hz in the worst case). Since the corrections depend on unknown parameters (such as the azimuthal angles between the electron wavefunction and the ^{13}C spins), we consider them as an additional source of uncertainty in this work. Techniques to measure these unknown parameters have been developed in refs. [17, 18]. Combining our methods with those techniques could in the future be used for precision spectroscopy on these coupled electron-nuclear-nuclear systems.

A common method to minimise ξ is to use a fitting algorithm such as least-squares minimisation. However, with no a priori information regarding the structure, finding an initial guess where the fit will converge to the global minimum becomes difficult. By testing with randomly generated clusters within a 1 nm^3 volume, we found that the initial guess should be within approximately 0.5Å for each x, y, z component for each spin in order for the fit to converge to the true solution. For 27 spins, this corresponds to an intractable $\sim 10^{100}$ required initial guesses to cover the entire search space.

A solution is to build up the configuration on a three-dimensional grid by adding spins one-by-one, while tracking all solutions within an error tolerance. We do this using two different methods. In the first method, we use a priori knowledge of the diamond lattice to constrain the possible spin positions (section 4.8.4). This is efficient for nuclear spins in diamond, but cannot be used for an arbitrary spin system. The second method uses a finer cubic lattice (section 4.8.4), which is more computationally intensive, but is general to any spin system measured using the methods described in this work. We can also use these solutions as an initial guess for a fit of the spatial coordinates to the measured couplings.

POSITIONING SPINS USING THE DIAMOND LATTICE

Since we know that the ^{13}C spins identified in this work are located at points on the diamond lattice, it is efficient to constrain the spatial coordinates to possible lattice sites. The procedure used to find the configuration is as follows. Firstly, the coordinates of a diamond lattice are generated with $2N_L+1$ points along each of the $[0,1,1]$, $[1,0,1]$ and $[1,1,0]$ crystal axes, where N_L is an integer, spaced by $a_0/\sqrt{2}$, where $a_0 = 3.5668\,\text{Å}$ is the diamond lattice constant [48]. An additional lattice site for each point is then added at a displacement $\frac{a_0}{4}[1,1,1]$, and the lattice is oriented such that the $[1,1,1]$ direction is parallel to the z-axis with the origin at the center. The total number of lattice sites is therefore $2(2N_L+1)^3$. For each lattice site, the coupling to a spin at the origin is calculated using equation 4.19 and stored in a lookup table along with the corresponding spatial vector between the two coordinates. Starting from an initial spin placed at the origin, each spin is placed in turn at a lattice site by choosing the strongest measured coupling to any spin that has already been placed and finding all corresponding possible vectors from the lookup table. Vectors from the lookup table are selected if the theoretically calculated coupling satisfies $\Delta f_{ij} < \mathcal{T}$, where $\mathcal{T}$ is a tolerance that is chosen to ensure that all promising configurations are included while maintaining reasonable computation time.

Next, for each possible configuration all theoretically calculated pairwise couplings are compared with the experimentally measured values and are also required to satisfy $\Delta f_{ij} < \mathcal{T}$. Configurations that meet the criteria for all couplings are kept and the procedure is then repeated for the next spin. For the second spin added only one of the six possible C_{3v}-symmetric configurations is kept. Once this procedure has been performed for all spins in the measured cluster, if multiple configurations have been found, the best solution can be determined by minimising the sum of squares ξ (equation 4.20). We use $N = 1$ echo pulses for most coupling measurements in Table 4.4. For some weak couplings, no oscillation could be observed within the decay time for $N = 1$. Such weak couplings can be measured more accurately using multiple pulses (e.g. Fig. 4.1f) or by a low-noise comparison to the Hahn echo. However, since the precise values of such weak couplings have a small effect on the obtained solution and due to time constraints, we did not perform such measurements for all couplings. Couplings that have been determined to be weak, but for which no precise value was established, are marked as $< 1\,\text{Hz}$ (Tables 4.2-4.4). For these measurements, we use a value of $0.5\,\text{Hz}$ in the analysis.

For the solution presented in Fig. 4.4 of the main text and also in Fig. 4.13, the diamond lattice coordinates were generated using $N_L = 11$, corresponding to approximately 24×10^3 lattice sites and a volume of around $120\,\text{nm}^3$. The tolerance was chosen to be $\mathcal{T} = 1.1\,\text{Hz}$, so that the best solution is among the configurations identified with a high probability. For a small number of measured couplings, the double resonance measurement was only performed for one of the $m_s = \pm1$ electron spin projections, and therefore the higher order corrections (section 4.8.3) can be larger. For these couplings we allowed a higher tolerance of $\mathcal{T}_{\text{single}} = 3\,\text{Hz}$. In addition, a cutoff limit of $X_{\text{cutoff}} = 5000$ was set for the maximum number of solutions that are carried over to the next spin. If the number

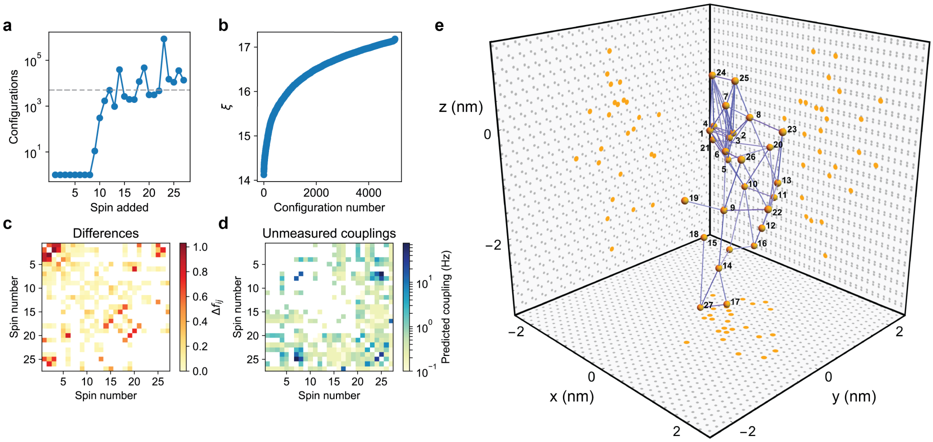

Figure 4.13: **Obtaining the structure using the diamond lattice. a,** Total number of configurations found after each spin added (log scale). The dashed grey line indicates the cutoff point set at $X_{\text{cutoff}} = 5000$. If more than X_{cutoff} solutions are found for a given spin (the point is above the dashed line), only the best X_{cutoff} solutions are kept for the next spin. **b,** Sum of squares ξ calculated from equation 4.20 for all configurations found for 27 spins, arranged in order from best to worst. **c,** Matrix plot showing the residuals Δf_{ij} for the configuration with the lowest ξ. White squares indicate unmeasured couplings. **d,** Matrix plot showing the predicted values of $|C_{ij}|/4\pi$ for couplings that were not measured. White squares indicate measured couplings. **e,** 3D plot of the 27 spin configuration with the lowest ξ value. The three sides show the $x-y$, $x-z$ and $y-z$ projections of the spins (yellow points) and the diamond lattice coordinates (grey points). Blue lines represent couplings greater than 3 Hz.

of solutions found exceeds X_{cutoff}, the solutions are ordered from best to worst according to their ξ value and only the first X_{cutoff} are saved.

For the first 8 spins, which form a strongly coupled sub-cluster, only one solution is found for each spin added (Fig. 4.13a). After this, more weakly coupled spins are added, which can give multiple configurations that satisfy the criteria. The final 27 spin solution is given by the solution with the lowest ξ (Fig. 4.13b). Coordinates for this configuration are given in Table 4.5 and the matrix of differences Δf_{ij}, the unmeasured couplings and a 3D plot are shown in Fig. 4.13c,d,e. Two identified sub-clusters are shown in greater detail in Fig. 4.7. 19 spins have the same coordinates in all 5000 configurations found, while the remaining 8 spins (18, 19, 20, 23, 24, 25, 26 and 27) have multiple positions within the range of identified solutions. The routine took approximately 6 hours on a desktop PC.

Using the solution found for the spatial coordinates of the 27 spin cluster, we can calculate the number of expected spins in the total volume to estimate the fraction of spins in this region we have identified. Defining a rectangular box around the cluster defined by the minimum and maximum x, y and z coordinates over all spins, we get a volume of $2 \times 2 \times 4 = 16\,\text{nm}^3$. This volume contains approximately 2900 lattice sites. With a natural ^{13}C concentration of 1.1%, we therefore expect approximately 32 spins in this volume, consistent with the 27 spins identified.

LEAST-SQUARES MINIMISATION

In addition to finding to structure of the cluster using the diamond lattice, we can further use the obtained solution as an initial guess for a least-squares minimisation routine. To properly constrain the fit, all three coordinates of spin 1 and additionally the y coordinate of spin 2 are fixed to zero in order to constrain to only relative positions and to break the rotational symmetry in the $x-y$ plane. The solution used for the initial guess is therefore rotated around the z-axis by an angle $\phi = -49.1\,\text{deg}$ so that the rotated coordinate $y'_2 = 0$. To quantify the difference between the initial and fitted solutions, we can define the distance from the initial guess for each spin as $\Delta r_i = \sqrt{\Delta x_i^2 + \Delta y_i^2 + \Delta z_i^2}$, where $\{\Delta x_i, \Delta y_i, \Delta z_i\}$ are the differences between the fitted coordinates and the initial guess coordinates (from the diamond lattice solution) for spin i. A bar plot of Δr_i for each spin in the fitted 27 spin solution, along with the associated fit uncertainties, is shown in Fig. 4.14a. The average distance between the solutions is $\frac{1}{M}\sum_i^M \Delta r_i = 0.46$Å. Since the measurement uncertainties are not well known due to the electron-mediated coupling corrections (section 4.8.3), we calculate the fit parameter errors based only on the variance of the residuals. It can be seen that for the majority of spins, the fitted coordinates and uncertainties are within one diamond bond length from the configuration entered as the initial guess.

The uncertainty of the fit for a given spin is dependent on its distance to the origin, which is set by the spin whose coordinates are fixed. This can hide information about the internal structure of a sub-cluster of strongly coupled spins that is far from the origin. In particular, the internal structure of sub-clusters might be tightly defined, while the position of the subcluster respectively to the origin is more uncertain. As an example, in Fig. 4.14a, the origin is fixed at the position of spin 1, which is situated in a strongly coupled 8 spin sub-cluster. The uncertainties in the fitted positions for spins within this

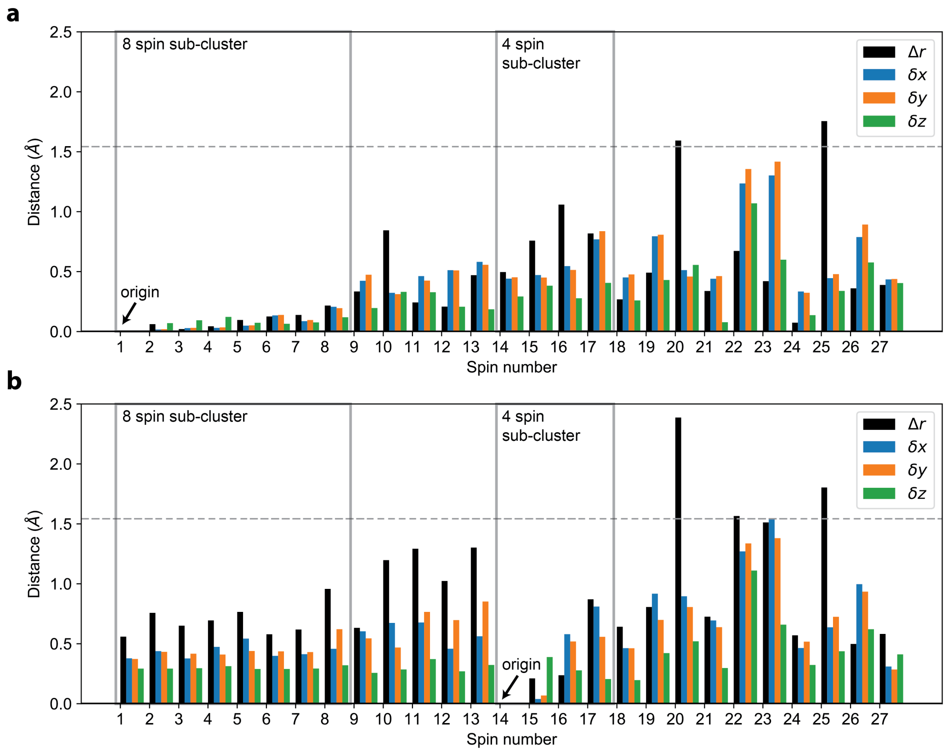

Figure 4.14: **Fitted solution for 27 spins.** Bar plots of Δr for each spin (black), defined as the magnitude of the distance between the fitted coordinates and the initial guess, as well as fit errors δx (blue), δy (orange) and δz (green). The initial guess was found using the diamond lattice method (see text). The dashed grey line indicates the diamond bond length. **a**, Fit result if spin 1 is fixed at the origin. **b**, Fit result if spin 14 is fixed at the origin.

sub-cluster are therefore low, whereas the uncertainties in the fitted positions for spins 14 - 17, which are in a separate 4 spin sub-cluster, are higher. In Fig. 4.14b, the origin is instead fixed at the position of spin 14, and consequently the uncertainties for the spins in the 4 spin sub-cluster are reduced, while for the 8 spin sub-cluster they are increased.

POSITIONING SPINS USING A CUBIC LATTICE

The method outlined in section 4.8.4 is well suited for obtaining the structure of a ^{13}C nuclear spin cluster in diamond. However, this method could not be used to find the structure of a spin cluster that is placed on the surface of the diamond, as the spins in this case are not confined to lie at diamond lattice points (although other a priori knowledge might be exploited). It is desirable to develop a method to find the structure of an arbitrary nuclear spin cluster. One option is to follow a similar method, but instead use a cubic lattice, which uses no pre-knowledge of the spin structure. In this case, the lattice spacing should be made much finer than in the diamond lattice case, so as to appropriately sample the entire volume given by the hyperfine coupling to the previous spin. The number of possible solutions per spin is consequently much larger, making the problem more computationally intensive. By using a cutoff for the number of solutions as introduced in section 4.8.4, the computation time can be reduced. However, this gives a risk that the optimum solution for the entire spin cluster will be discarded if a different solution is optimum for a subset of spins.

Despite these computational challenges, it was found that a similar solution to the one found in section 4.8.4 is obtained using this method. The cubic lattice was created with $2N_L+1$ lattice points per edge of length L, where N_L is an integer. This gives $(2N_L+1)^3$ points in total in a volume of L^3, with lattice spacing $\Delta L = L/2N_L$. To further constrain the number of solutions obtained for each spin, N_L and L were varied depending on the coupling being used. By inverting equation 4.19, we can find the maximum distance between two spins for a given coupling to be

$$\Delta r_{ij}^{\max} = \left(\frac{2\alpha_{ij}}{C_{ij}}\right)^{1/3}, \tag{4.21}$$

from which we can set $L_{ij} = 2\Delta r_{ij}^{\max}$, with spin i at the origin (see Fig. 4.15a). We then set $N_L^{ij} = \tilde{N}_L/\Delta r_{ij}^{\max}$, where $\tilde{N}_L = 2\times 10^{-8}$ is a scaling factor chosen to give a fine enough lattice while also keeping the computation time within reasonable limits. Due to the rotational symmetry in the $x-y$ plane and inversion symmetry in z, for the second spin added the position is confined to the $x-z$ plane and for the third spin only solutions with positive y values are taken.

Fig. 4.15b-e show the result of this method. The routine took approximately 14 hours on a desktop PC parallelised over 8 cores. It can be seen that the best solution obtained is close to the diamond lattice solution, both in the predicted couplings (b,c) and the coordinates of the spins (d,e). The average distance between the diamond lattice positions and the cubic lattice positions is 0.58Å. We can also use this solution as an initial guess for least-squares minimisation, which returns a similar solution as that obtained by using the diamond lattice configuration as an initial guess (Fig. 4.15e).

As a test, we ran the cubic lattice reconstruction method on randomly generated 30-spin clusters in a volume of 2x2x4 nm. For each cluster, the coupling matrix was calculated using equation 3 in the methods and random Gaussian noise was added to each coupling with a 10 mHz standard deviation to emulate measurement uncertainties. To make the analysis run faster in order to get better statistics, we used a variable cutoff point (defined in section IVA) which reduced the number of solutions kept to 10 after 8 spins were positioned. This was based on observations that often many similar solutions were being kept from 8 spins onward causing unnecessary additional computation time. We analysed 17 clusters over ~ 300 hours, and in 16 cases found the correct solution (defined as an average error in position of < 1.5 Å). In 10 cases, the analysis first returned “no solution”, before finding the correct structure in 9 out of those 10 cases by increasing the number of solutions tracked and/or attempting different orderings. The case where no solution was returned ran into the memory limits of the PCs used to run the analysis (~ 2 GB). It is expected that, given more computational power or time, also this solution will be found. Crucially, no erroneous structures were returned in any of the cases, illustrating the robustness of the method.

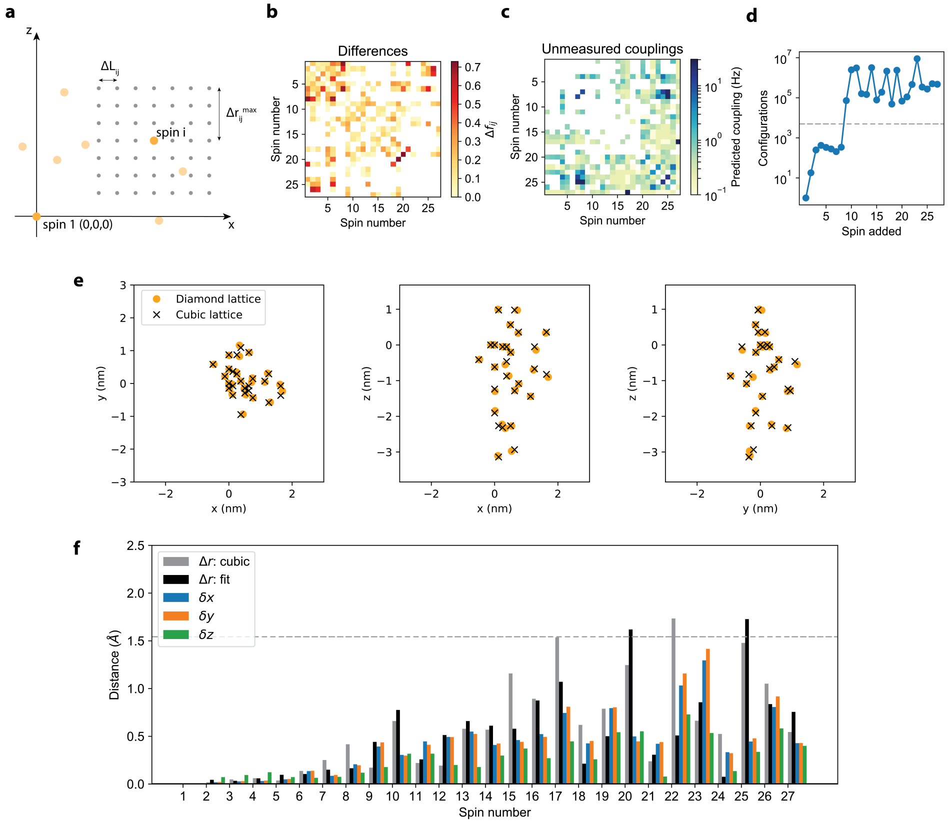

Figure 4.15: **Obtaining the structure using a cubic lattice.** **a,** Illustration of the lattice generation method, shown in 2D for clarity. Parameters are defined in the text. **b,** Matrix plot showing the residuals Δf_{ij} for the configuration with the lowest ξ. White squares indicate unmeasured couplings. **c,** Matrix plot showing the predicted values of $|C_{ij}|/4\pi$ for couplings that were not measured. White squares indicate measured couplings. **d,** Total number of configurations found after each spin added (log scale). The dashed grey line indicates the cutoff point set at $X_{\text{cutoff}} = 5200$. **e,** 2D projections showing a comparison between the nuclear spin structure obtained using the diamond and cubic lattice methods. The cubic lattice solution has undergone the transformation $y \rightarrow -y$, $z \rightarrow -z$ plus a rotation around z by 49.1 deg in order to align the two solutions. **f,** Distance between the diamond and cubic lattice solutions for each spin (grey), and fit result using the cubic lattice as an initial guess with spin 1 fixed, relative to the diamond solution (black). The associated fit errors δx (blue), δy (orange) and δz (green) are also shown. The average distance between the cubic and diamond solutions is 0.58 Å.

REFERENCES

[1] G. S. Rule and T. K. Hitchens, *Fundamentals of protein NMR spectroscopy*, Vol. 5 (Springer Science & Business Media, 2006).

[2] H. Mamin, M. Kim, M. Sherwood, C. Rettner, K. Ohno, D. Awschalom, and D. Rugar, *Nanoscale nuclear magnetic resonance with a nitrogen-vacancy spin sensor,* Science **339**, 557 (2013).

[3] T. Staudacher, F. Shi, S. Pezzagna, J. Meijer, J. Du, C. A. Meriles, F. Reinhard, and J. Wrachtrup, *Nuclear magnetic resonance spectroscopy on a (5-nanometer) 3 sample volume,* Science **339**, 561 (2013).

[4] F. Shi, Q. Zhang, P. Wang, H. Sun, J. Wang, X. Rong, M. Chen, C. Ju, F. Reinhard, H. Chen, *et al.*, *Single-protein spin resonance spectroscopy under ambient conditions,* Science **347**, 1135 (2015).

[5] I. Lovchinsky, A. O. Sushkov, E. Urbach, N. P. de Leon, S. Choi, K. De Greve, R. Evans, R. Gertner, E. Bersin, Müller, *et al.*, *Nuclear magnetic resonance detection and spectroscopy of single proteins using quantum logic,* Science **351**, 836 (2016).

[6] N. Aslam, M. Pfender, P. Neumann, R. Reuter, A. Zappe, F. Fávaro de Oliveira, A. Denisenko, H. Sumiya, S. Onoda, J. Isoya, and J. Wrachtrup, *Nanoscale nuclear magnetic resonance with chemical resolution,* Science **357**, 67 (2017).

[7] D. R. Glenn, D. B. Bucher, J. Lee, M. D. Lukin, H. Park, and R. L. Walsworth, *High-resolution magnetic resonance spectroscopy using a solid-state spin sensor,* Nature **555**, 351 (2018).

[8] J. Smits, J. T. Damron, P. Kehayias, A. F. McDowell, N. Mosavian, I. Fescenko, N. Ristoff, A. Laraoui, A. Jarmola, and V. M. Acosta, *Two-dimensional nuclear magnetic resonance spectroscopy with a microfluidic diamond quantum sensor,* Sci. Adv. **5**, eaaw7895 (2019).

[9] I. Lovchinsky, J. Sanchez-Yamagishi, E. Urbach, S. Choi, S. Fang, T. Andersen, K. Watanabe, T. Taniguchi, A. Bylinskii, E. Kaxiras, *et al.*, *Magnetic resonance spectroscopy of an atomically thin material using a single-spin qubit,* Science **355**, 503 (2017).

[10] A. Ajoy, U. Bissbort, M. D. Lukin, R. L. Walsworth, and P. Cappellaro, *Atomic-scale nuclear spin imaging using quantum-assisted sensors in diamond,* Phys. Rev. X **5**, 011001 (2015).

[11] M. Kost, J. Cai, and M. B. Plenio, *Resolving single molecule structures with nitrogen-vacancy centers in diamond,* Sci. Rep. **5**, 11007 (2015).

[12] V. Perunicic, C. Hill, L. Hall, and L. Hollenberg, *A quantum spin-probe molecular microscope,* Nat. Commun. **7**, 12667 (2016).

[13] Z.-Y. Wang, J. F. Haase, J. Casanova, and M. B. Plenio, *Positioning nuclear spins in interacting clusters for quantum technologies and bioimaging,* Phys. Rev. B **93**, 174104 (2016).

[14] A. Sushkov, I. Lovchinsky, N. Chisholm, R. L. Walsworth, H. Park, and M. D. Lukin, *Magnetic resonance detection of individual proton spins using quantum reporters,* Phys. Rev. Lett. **113**, 197601 (2014).

[15] C. Müller, X. Kong, J. M. Cai, K. Melentijević, A. Stacey, M. Markham, D. Twitchen, J. Isoya, S. Pezzagna, J. Meijer, J. F. Du, M. B. Plenio, B. Naydenov, L. P. McGuinness, and F. Jelezko, *Nuclear magnetic resonance spectroscopy with single spin sensitivity,* Nat. Commun. **5**, 4703 (2014).

[16] F. Shi, X. Kong, P. Wang, F. Kong, N. Zhao, R.-B. Liu, and J. Du, *Sensing and atomic-scale structure analysis of single nuclear-spin clusters in diamond,* Nat. Phys. **10**, 21 (2014).

[17] J. Zopes, K. S. Cujia, K. Sasaki, J. M. Boss, K. M. Itoh, and C. L. Degen, *Three-dimensional localization spectroscopy of individual nuclear spins with sub-angstrom resolution,* Nat. Commun. **9**, 4678 (2018).

[18] J. Zopes, K. Herb, K. S. Cujia, and C. L. Degen, *Three-dimensional nuclear spin positioning using coherent radio-frequency control,* Phys. Rev. Lett. **121**, 170801 (2018).

[19] K. Sasaki, K. M. Itoh, and E. Abe, *Determination of the position of a single nuclear spin from free nuclear precessions detected by a solid-state quantum sensor,* Phys. Rev. B **98**, 121405 (2018).

[20] M. H. Abobeih, J. Cramer, M. A. Bakker, N. Kalb, M. Markham, D. J. Twitchen, and T. H. Taminiau, *One-second coherence for a single electron spin coupled to a multi-qubit nuclear-spin environment,* Nat. Commun. **9**, 2552 (2018).

[21] Z. Yang, X. Kong, Z. Li, L. Zhou, K. Yang, P. Yu, P. Wang, Y. Wang, X. Qin, X. Rong, X. Wu, F. Shi, and J. Du, *Two-dimensional nanoscale nuclear magnetic resonance spectroscopy enhanced by artificial intelligence,* arXiv:1902.05676 (2019).

[22] E. L. Rosenfeld, L. M. Pham, M. D. Lukin, and R. L. Walsworth, *Sensing coherent dynamics of electronic spin clusters in solids,* Phys. Rev. Lett. **120**, 243604 (2018).

[23] H. S. Knowles, D. M. Kara, and M. Atatüre, *Demonstration of a coherent electronic spin cluster in diamond,* Phys. Rev. Lett. **117**, 100802 (2016).

[24] J. Cramer, N. Kalb, M. A. Rol, B. Hensen, M. S. Blok, M. Markham, D. J. Twitchen, R. Hanson, and T. H. Taminiau, *Repeated quantum error correction on a continuously encoded qubit by real-time feedback,* Nat. Commun. **7**, 11526 (2016).

[25] M. Pfender, P. Wang, H. Sumiya, S. Onoda, W. Yang, D. B. R. Dasari, P. Neumann, X.-Y. Pan, J. Isoya, R.-B. Liu, *et al., High-resolution spectroscopy of single nuclear spins via sequential weak measurements,* Nat. Commun. **10**, 594 (2019).

[26] K. Cujia, J. Boss, K. Herb, J. Zopes, and C. Degen, *Tracking the precession of single nuclear spins by weak measurements,* Nature **571**, 230– (2019).

[27] C. Slichter, *Principles of Magnetic Resonance,* Springer Series in Solid-State Sciences (Springer Berlin Heidelberg, 1996).

[28] C. Bradley, J. Randall, M. Abobeih, R. Berrevoets, M. Degen, M. Bakker, M. Markham, D. Twitchen, and T. Taminiau, *A ten-qubit solid-state spin register with quantum memory up to one minute,* Physical Review X **9**, 031045 (2019).

[29] A. Laraoui, F. Dolde, C. Burk, F. Reinhard, J. Wrachtrup, and C. A. Meriles, *High-resolution correlation spectroscopy of* ^{13}C *spins near a nitrogen-vacancy centre in diamond,* Nat. Commun. **4**, 1651 (2013).

[30] M. Pfender, N. Aslam, H. Sumiya, S. Onoda, P. Neumann, J. Isoya, C. A. Meriles, and J. Wrachtrup, *Nonvolatile nuclear spin memory enables sensor-unlimited nanoscale spectroscopy of small spin clusters,* Nat. Commun. **8**, 834 (2017).

[31] P. C. Maurer, G. Kucsko, C. Latta, L. Jiang, N. Y. Yao, S. D. Bennett, F. Pastawski, D. Hunger, N. Chisholm, M. Markham, *et al.*, *Room-temperature quantum bit memory exceeding one second,* Science **336**, 1283 (2012).

[32] M. G. Dutt, L. Childress, L. Jiang, E. Togan, J. Maze, F. Jelezko, A. Zibrov, P. Hemmer, and M. Lukin, *Quantum register based on individual electronic and nuclear spin qubits in diamond,* Science **316**, 1312 (2007).

[33] A. P. Nizovtsev, S. Y. Kilin, A. L. Pushkarchuk, V. A. Pushkarchuk, S. A. Kuten, O. A. Zhikol, S. Schmitt, T. Unden, and F. Jelezko, *Non-flipping* ^{13}C *spins near an NV center in diamond: hyperfine and spatial characteristics by density functional theory simulation of the c510[NV]h252 cluster,* New J. Phys. **20**, 023022 (2018).

[34] L. Robledo, L. Childress, H. Bernien, B. Hensen, P. F. A. Alkemade, and R. Hanson, *High-fidelity projective read-out of a solid-state spin quantum register,* Nature **477**, 574 (2011).

[35] D. M. Toyli, C. F. de las Casas, D. J. Christle, V. V. Dobrovitski, and D. D. Awschalom, *Fluorescence thermometry enhanced by the quantum coherence of single spins in diamond,* Proc. Natl. Acad. Sci. **110**, 8417 (2013).

[36] T. H. Taminiau, J. J. T. Wagenaar, T. van der Sar, F. Jelezko, V. V. Dobrovitski, and R. Hanson, *Detection and control of individual nuclear spins using a weakly coupled electron spin,* Phys. Rev. Lett. **109**, 137602 (2012).

[37] S. Kolkowitz, Q. P. Unterreithmeier, S. D. Bennett, and M. D. Lukin, *Sensing distant nuclear spins with a single electron spin,* Phys. Rev. Lett. **109**, 137601 (2012).

[38] N. Zhao, J. Honert, B. Schmid, M. Klas, J. Isoya, M. Markham, D. Twitchen, F. Jelezko, R.-B. Liu, H. Fedder, and J. Wrachtrup, *Sensing single remote nuclear spins,* Nat. Nanotech. **7**, 657 (2012).

[39] J. M. Boss, K. Cujia, J. Zopes, and C. L. Degen, *Quantum sensing with arbitrary frequency resolution,* Science **356**, 837 (2017).

[40] S. Schmitt, T. Gefen, F. M. Stürner, T. Unden, G. Wolff, C. Müller, J. Scheuer, B. Naydenov, M. Markham, S. Pezzagna, *et al.*, *Submillihertz magnetic spectroscopy performed with a nanoscale quantum sensor,* Science **356**, 832 (2017).

[41] A. Laraoui, D. Pagliero, and C. A. Meriles, *Imaging nuclear spins weakly coupled to a probe paramagnetic center,* Phys. Rev. B **91**, 205410 (2015).

[42] T. Gullion, D. B. Baker, and M. S. Conradi, *New, compensated Carr-Purcell sequences,* Journal of Magnetic Resonance **89**, 479 (1990).

[43] W. S. Warren, *Effects of arbitrary laser or NMR pulse shapes on population inversion and coherence,* J. Chem. Phys. **81**, 5437 (1984).

[44] N. Zhao, J.-L. Hu, S.-W. Ho, J. T. K. Wan, and R. B. Liu, *Atomic-scale magnetometry of distant nuclear spin clusters via nitrogen-vacancy spin in diamond,* Nat. Nanotech. **6**, 242 (2011).

[45] C. E. Bradley, J. Randall, M. H. Abobeih, R. C. Berrevoets, M. J. Degen, M. A. Bakker, M. Markham, D. J. Twitchen, and T. H. Taminiau, *A ten-qubit solid-state spin register with quantum memory up to one minute,* Phys. Rev. X **9**, 031045 (2019).

[46] L. Childress, M. V. Gurudev Dutt, J. M. Taylor, A. S. Zibrov, F. Jelezko, J. Wrachtrup, P. R. Hemmer, and M. D. Lukin, *Coherent dynamics of coupled electron and nuclear spin qubits in diamond,* Science **314**, 281 (2006).

[47] J. J. Sakurai, *Modern quantum mechanics; rev. ed.* (Addison-Wesley, Reading, MA, 1994).

[48] S. Stoupin and Y. V. Shvyd'ko, *Thermal expansion of diamond at low temperatures,* Phys. Rev. Lett. **104**, 085901 (2010).

5

A TEN-QUBIT SOLID-STATE SPIN REGISTER

C. E. Bradley*, J. Randall*, M. H. Abobeih, R. C. Berrevoets, M. J. Degen, M. A. Bakker, M. Markham, D. J. Twitchen, T. H. Taminiau

Spins associated to single defects in solids provide promising qubits for quantum information processing and quantum networks. Recent experiments have demonstrated long coherence times, high-fidelity operations and long-range entanglement. However, control has so far been limited to a few qubits, with entangled states of three spins demonstrated. Realizing larger multi-qubit registers is challenging due to the need for quantum gates that avoid crosstalk and protect the coherence of the complete register. In this paper, we present novel decoherence-protected gates that combine dynamical decoupling of an electron spin with selective phase-controlled driving of nuclear spins. We use these gates to realize a 10-qubit quantum register consisting of the electron spin of a nitrogen-vacancy center and 9 nuclear spins in diamond. We show that the register is fully connected by generating entanglement between all 45 possible qubit pairs, and realize genuine multipartite entangled states with up to 7 qubits. Finally, we investigate the register as a multi-qubit memory. We demonstrate the protection of an arbitrary single-qubit state for over 75 seconds - the longest reported for a single solid-state qubit - and show that two-qubit entanglement can be preserved for over 10 seconds. Our results enable the control of large quantum registers with long coherence times and therefore open the door to advanced quantum algorithms and quantum networks with solid-state spin qubits.

The results of this chapter have been published in Phys. Rev. X **9**, 031045 (2019).

*Equally contributing authors.

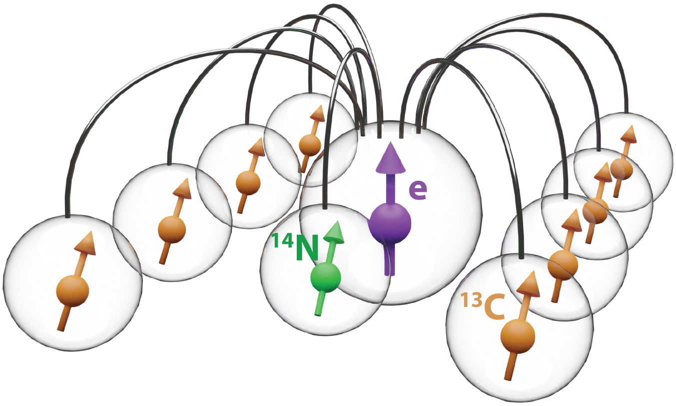

Figure 5.1: Illustration of the 10-qubit register developed in this work. The electron spin of a single NV center in diamond acts as a central qubit and is connected by two-qubit gates to the intrinsic ^{14}N nuclear spin, and a further 8 ^{13}C nuclear spins surrounding the NV center.

5.1. INTRODUCTION

Electron and nuclear spins associated with single defects in solids provide a promising platform for quantum networks and quantum computations [1, 2]. In these hybrid registers, different types of spins fulfill different roles. Electron spins offer fast control [3–13] and high fidelity readout [7, 14, 15], and can be used to control and connect nuclear spins [15–21]. Furthermore, electron-electron couplings enable on-chip connectivity between defects [19, 22, 23], whilst coupling to photons [12, 24–28] allows for the realization of long-range entanglement links [29–31]. Nuclear spins provide additional qubits with long coherence times that can be used to store and process quantum states [16, 17, 21, 24, 32–35].

Recent experiments have demonstrated various schemes for high-fidelity two-qubit gates [34, 36–41], as well as basic quantum algorithms [36, 42] and error correction codes [16, 17]. However, to date, these systems have been restricted to few-qubit registers: the largest reported entangled state contains 3 qubits [16, 17, 43]. Larger quantum registers are desired for investigating advanced algorithms and quantum networks [44–46]. Such multi-qubit registers are challenging to realize due to the required gates that selectively control the qubits and at the same time decouple unwanted interactions in order to protect coherence in the complete register.

In this work, we develop a novel gate scheme based upon selective phase-controlled driving of nuclear spins interleaved with decoupling sequences on an electron spin. These gates enable high-fidelity control of hitherto inaccessible nuclear spin qubits. We combine these gates with previously developed control techniques [14, 16, 47] to realize a 10-qubit register composed of a diamond nitrogen-vacancy (NV) center, its ^{14}N nuclear spin and 8 ^{13}C spins (Fig. 5.1). We show that the register is fully connected by preparing entangled states for all possible pairs of qubits. Furthermore, by also decoupling nuclear-nuclear interactions through echo sequences, we generate N-qubit Greenberger-Horne-Zeilinger (GHZ) states, and witness genuine multipartite entanglement for up to 7 spins. Finally, we investigate the coherence properties of the register. We measure coherence times up to 63(2) seconds and show that an arbitrary single qubit state can be protected for over 75 seconds. Furthermore, we demonstrate that two-qubit entanglement can be preserved for over 10 seconds.

5.2. TWO-QUBIT GATES: THEORY

We consider an NV center in diamond and surrounding ^{13}C nuclear spins. To realize a multi-qubit register, we design single-qubit gates and electron-nuclear two-qubit gates to control the NV ^{14}N spin and several individual ^{13}C spins. Key challenges in these hybrid systems of multiple coupled spins are to maintain coherence on the electron spin qubit and to avoid unwanted crosstalk. In particular, the electron spin continuously couples to all ^{13}C spins through the hyperfine interaction, and the dynamics of the electron spin and nuclear spins typically occur on very different timescales [36]. To address these issues, a variety of decoherence-protected gates, in which decoupling sequences on the electron spin are combined with nuclear spin control, have been investigated [36, 37, 39, 40, 48–52]. Here we develop and demonstrate a novel electron-nuclear two-qubit gate based upon phase-controlled radio-frequency (RF) driving of nuclear spins, interleaved with dynamical decoupling (DD) of the electron spin. We will refer to this scheme as a DDRF gate. Our scheme enables the control of additional ^{13}C spins while offering improved flexibility in dynamical decoupling to optimize the electron spin coherence and avoid unwanted crosstalk.

To design a selective two-qubit gate, we utilize the hyperfine interaction which couples each nuclear spin to the electron spin. As this interaction depends on the relative position of the spin to the NV, different nuclear spins can be distinguished by their precession frequencies [48–50]. In the interaction picture with respect to the electron energy splitting, and neglecting non-secular terms, the Hamiltonian describing the electron and a single ^{13}C nuclear spin is given by [48–50]

$$H = \omega_L I_z + A_\parallel S_z I_z + A_\perp S_z I_x, \tag{5.1}$$

where $\omega_L = \gamma B_z$ is the nuclear Larmor frequency set by the external magnetic field B_z along the NV axis, γ is the ^{13}C gyromagnetic ratio, S_α and I_α are the spin-1 and spin-1/2 operators of the electron and nuclear spins respectively, and $A_\parallel$ and $A_\perp$ are the parallel and perpendicular hyperfine components.

To control the nuclear spin, we apply RF pulses of Rabi frequency Ω, phase ϕ and frequency ω. To target a specific nuclear spin, we set $\omega = \omega_1$, where $\omega_1 = \sqrt{(\omega_L - A_\parallel)^2 + A_\perp^2}$ is the nuclear spin precession frequency when the electron is in the $m_s = -1$ spin projection. In the following we assume $(\omega_L - \omega_1) \gg \Omega$, such that driving of the nuclear spin is negligible while the electron is in the $m_s = 0$ spin projection, and set $A_\perp = 0$ for simplicity (see the Supplemental Material online [53] for the general case). Considering only the $m_s = \{0, -1\}$ subspace, with the addition of RF driving and in a rotating frame at the RF frequency, the Hamiltonian of Eq. 5.1 becomes [36, 53]

$$\begin{aligned} H = {} & |0\rangle\langle 0| \otimes (\omega_L - \omega_1) I_z \\ & + |1\rangle\langle 1| \otimes \Omega(\cos(\phi) I_x + \sin(\phi) I_y), \end{aligned} \tag{5.2}$$

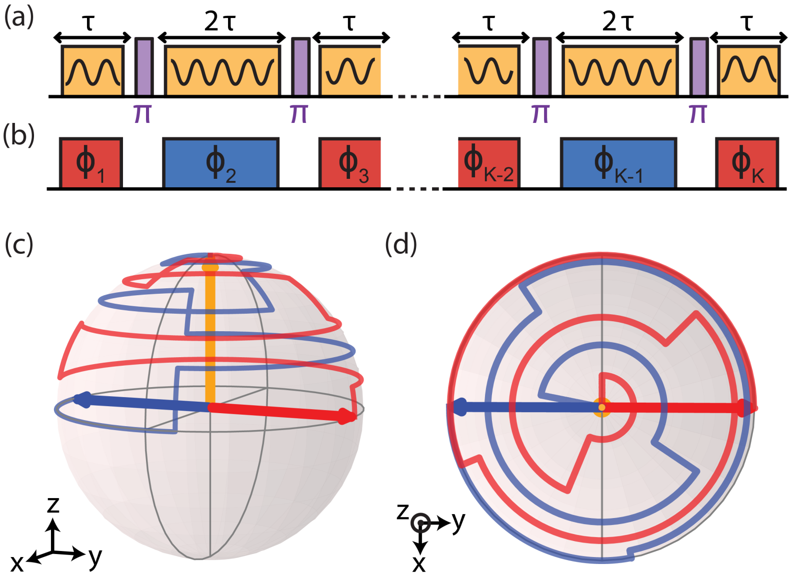

Figure 5.2: (a) Illustration of the pulse sequence employed to realize a DDRF gate. Dynamical decoupling pulses on the electron spin (purple) are interleaved with RF pulses (yellow) which selectively drive a single nuclear spin. (b) Illustration showing that the initial state of the electron spin determines which RF pulses are resonant with the nuclear spin. If the electron spin starts in $|1\rangle$ ($m_s = -1$), the odd RF pulses (red) are resonant. For initial electron state $|0\rangle$ ($m_s = 0$), the even (blue) RF pulses are resonant. The phase of each RF pulse is adapted to create the desired nuclear spin evolution, accounting for periods of free precession according to Eq. 5.3. (c) Nuclear spin trajectory on the Bloch sphere for a conditional rotation with $N = 8$ electron decoupling pulses. Starting from the initial nuclear state $|\uparrow\rangle$ (yellow), the red (blue) path shows the nuclear spin evolution for the case where the electron starts in the state $|1\rangle$ ($|0\rangle$). The final state vectors are anti-parallel along the equator: therefore, the gate is a maximally entangling two-qubit gate. (d) Top-down view of (c).

where $|0\rangle$ ($|1\rangle$) indicates the electron $m_s = 0$ ($m_s = -1$) spin projection. In this picture, for the electron in state $|0\rangle$, the nuclear spin undergoes precession around the $\hat{z}$-axis at frequency $(\omega_L - \omega_1) = A_\parallel$. Conversely, while the electron is in the state $|1\rangle$, the nuclear spin is driven around a rotation axis in the $\hat{x}$-$\hat{y}$ plane defined by the phase of the RF field ϕ.

To simultaneously decouple the electron spin from the environment, we interleave the RF pulses in a sequence of the form $(\tau$ - π - 2τ - π - $\tau)^{N/2}$, where π is a π-pulse on the electron spin, 2τ is the interpulse delay, and N is the total number of electron decoupling pulses (Fig. 5.2(a)) [48–50]. We consider the evolution of the nuclear spin during this sequence separately for the two initial electron eigenstates: $|0\rangle$ and $|1\rangle$ [48–50]. We label each successive RF pulse by integer $k = 1, ..., K$, where $K = N + 1$ is the total number of RF pulses. If the inital electron spin state is $|0\rangle$, only the even k RF pulses will be resonant and drive the nuclear spin (Fig. 5.2(b)). Conversely, for initial state $|1\rangle$, the odd k pulses are resonant. The desired nuclear spin evolution can now be created by setting the phases ϕ_k of the RF pulses.

We construct both an unconditional rotation (single-qubit gate) and a conditional rotation (two-qubit gate). To ensure that the sequential RF rotations build up constructively, the phases of each RF pulse should be set to account for the periods of nuclear spin precession between them, which build up in integer multiples of $\phi_\tau = (\omega_L - \omega_1)\tau$. For the case where the electron starts in the state $|0\rangle$ (even k), the required sequence of phases is $\phi_\tau, 3\phi_\tau, 5\phi_\tau, \ldots$, while for the case where the electron starts in the state $|1\rangle$ (odd k) we require the sequence $0, 2\phi_\tau, 4\phi_\tau, \ldots$. The required phases are therefore given by [53]

$$\phi'_k = \begin{cases} (k-1)\phi_\tau + \pi & k \text{ odd} \\ (k-1)\phi_\tau & k \text{ even}, \end{cases} \tag{5.3}$$

where the (optional) π phase shift for the odd k sequence converts the unconditional rotation into a conditional rotation. By adding a further phase φ to all pulses, we can also set the rotation axis of the gate. The RF pulse phases are thus summarized by $\phi_k = \varphi + \phi'_k$.

With this choice of phases, the total evolution of the two-qubit system is given by $V = V_z \cdot V_{\text{CROT}}$. Here, V_z is an unconditional rotation of the nuclear spin around z [53] and V_{CROT} is a conditional rotation of the nuclear spin depending on the electron state, given by

$$\begin{aligned} V_{\text{CROT}} = &|0\rangle\langle 0| \otimes R_\varphi(N\Omega\tau) \\ &+ |1\rangle\langle 1| \otimes R_\varphi(-N\Omega\tau), \end{aligned} \tag{5.4}$$

where $R_\varphi(\theta) = e^{-i\theta(\cos(\varphi)I_x + \sin(\varphi)I_y)/\hbar}$. V_{CROT} describes a controlled rotation of the nuclear spin with tuneable rotation angle (set by N, Ω and τ) and rotation axis (set by φ). Setting $N\Omega\tau = \pi/2$, a maximally entangling two-qubit operation is achieved, equivalent to a controlled-not (CNOT) gate up to local rotations. Example dynamics for a nuclear spin evolving under such a sequence are shown in Figs. 5.2(c) and (d).

Our design has several advantages. First, the gate allows nuclear spins with small or negligible $A_\perp$ to be controlled, thereby increasing the number of accessible nuclear spin qubits. Second, because the targeted dynamics are achieved by setting the RF phases

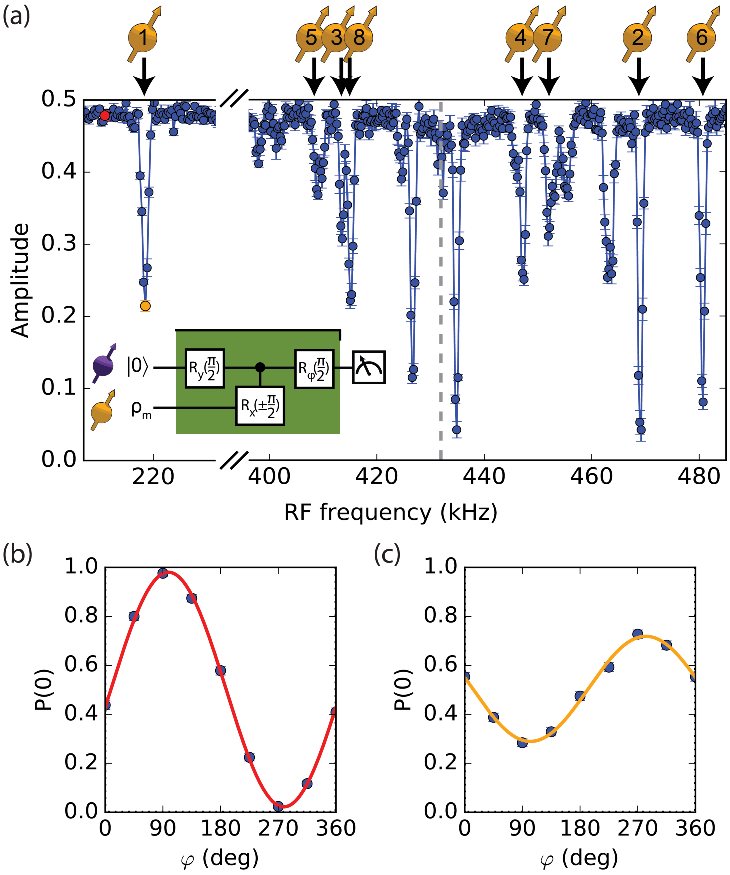

Figure 5.3: (a) Nuclear spin spectroscopy. After preparing the electron in a superposition state, the DDRF gate (controlled $\pm\pi/2$ rotation, see Eq. 5.4) is applied for different RF frequencies ω. The electron spin is then measured along a basis in the equatorial plane defined by angle φ (see inset). Each data point in (a) corresponds to the fitted amplitude A of the function $f(\varphi) = a + A\cos(\varphi + \varphi_0)$, where φ is swept from 0 to 360 deg and φ_0 accounts for deterministic phase shifts induced on the electron by the RF field. By fitting the amplitude, we distinguish such deterministic phase shifts from loss of coherence due to entangling interactions. The signals due to interaction with the 8 ^{13}C spins used in this work are labelled. The dashed gray line indicates the ^{13}C Larmor frequency ω_L. A detailed analysis of the spectrum is given in the Supplemental Material online [53]. (b,c) Example phase sweeps for two data points highlighted in red (b) and orange (c) in (a). Solid lines are fits to $f(\varphi)$. The DDRF gate parameters are $N = 48$ and $\tau = 8\tau_L$, where $\tau_L = 2\pi/\omega_L$ ($\approx 2.3\,\mu$s).

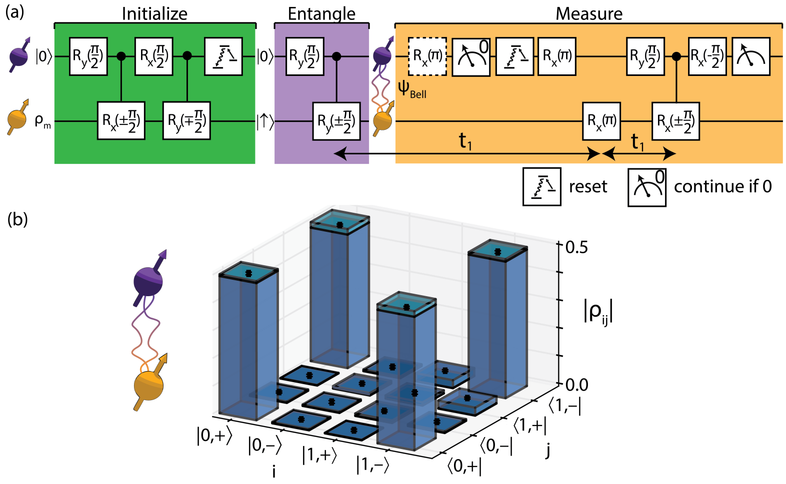

Figure 5.4: (a) Experimental sequence to prepare an electron-nuclear Bell state and determine the expectation value of the two-qubit operator ZX. A series of single and two-qubit gates are used to initialize the nuclear spin [16, 37]. A subsequent $\pi/2$ rotation and two-qubit gate generate the Bell state $\left|\psi_{\text{Bell}}\right\rangle = (|0+\rangle + |1-\rangle)/\sqrt{2}$. A measurement of the electron spin in the Z-basis is followed by an X-basis measurement of the nuclear spin through the electron spin. These measurements are separated by a nuclear spin echo, which is implemented to mitigate dephasing of the nuclear spin. The entire sequence is applied with and without an additional electron π-pulse (dashed box) before the first electron readout, in order to reconstruct the electron state while ensuring that the measurement does not disturb the nuclear spin state [16, 42]. (b) Density matrix of the electron-nuclear state after applying the sequence shown in (a) to qubit C1, reconstructed with state tomography. We correct for infidelities in the readout sequence, characterized in separate measurements [53]. The DDRF gate parameters are $N = 8$, $\tau = 17\tau_L \approx 39.4\,\mu\text{s}$, $\Omega/2\pi = 1.09(3)\,\text{kHz}$, and the total gate duration is 629 µs, compared with the nuclear spin $T_2^* = 12.0(6)\,\text{ms}$. We use error function pulse envelopes with a 7.5 µs rise / fall time for each RF pulse to mitigate pulse distortions induced by the RF electronics [53]. The fidelity with the target Bell state is measured to be $\mathscr{F}_{\text{Bell}} = 0.972(8)$. Lighter blue shading indicates the density matrix for the ideal state $\left|\psi_{\text{Bell}}\right\rangle$.

and amplitudes, the interpulse delay τ of the decoupling sequence can be freely optimized to protect the electron coherence. This is in contrast to the gates described in van der Sar et al. [36], for which τ is restricted to a specific resonance condition for each spin, making multi-qubit control challenging. Third, because our method does not rely on an average frequency shift over the two electron spin states [37], our gates can also be used for selective control of nuclear spins coupled to spin-1/2 defects (such as the negatively-charged group-IV color centers [7, 9, 13, 20, 28, 54, 55]), and via a contact hyperfine coupling, such as for donor spins in silicon [34] and SiMOS quantum dots [21]. Finally, because control is achieved through the RF field, a multitude of avenues for future investigation are opened up, such as parallelizing gates by frequency multiplexing and using shaped and composite pulses to mitigate dephasing and crosstalk [38, 56, 57].

5.3. TWO-QUBIT GATES: EXPERIMENT

Our experiments are performed at 3.7 K using a single NV center in diamond with natural abundance of carbon isotopes (1.1% ^{13}C). Further details of the sample and experimental setup can be found in the Supplemental Material online [53]. As a starting point, we use the DDRF gate to identify and characterize ^{13}C nuclear spin qubits surrounding the NV center. If the electron spin is prepared in a superposition state and the RF frequency is resonant with a nuclear spin in the environment, the entangling interaction (Eq. 5.4) decoheres the electron spin. Therefore, varying the RF frequency (ω) performs spectroscopy of the nuclear spin environment. Fig. 5.3 shows that multiple dips in the electron coherence can be observed, indicating selective interactions with several individual nuclear spins. Importantly, like other RF-based approaches [39, 52], the DDRF sequence is sensitive to nuclear spins with small or negligible $A_\perp$. Besides extending the number of qubits that can be controlled with a single NV center, this also enables the detection of additional spins when using the NV as a quantum sensor, which we exploit in parallel work to realize 3D imaging of large spin clusters (see chapter 4) [58].

To verify the control offered by the DDRF two-qubit gate, we first demonstrate high fidelity ancilla-based initialization and readout by preparation and tomography of a maximally entangled electron-nuclear state. To test the gate, we select a ^{13}C spin (spin C1, Fig. 5.3) with a strong parallel hyperfine component of $A_\parallel/2\pi = 213.154(1)$ kHz, but a weak perpendicular hyperfine component $A_\perp/2\pi = 3.0(4)$ kHz [53]. We exploit the freedom in choosing the interpulse delay by setting τ to an integer multiple of the ^{13}C Larmor period, $\tau_L = 2\pi/\omega_L$, so that unwanted interactions between the electron spin and other ^{13}C spins in the environment are effectively decoupled [47, 59]. The choice of Rabi frequency Ω is a trade-off between obtaining faster gate speeds, maintaining frequency selectivity and minimising additional noise from the electronic hardware [53].

The sequence to perform the state preparation and tomography experiment is shown in Fig. 5.4(a) [16, 37]. We first initialize the electron spin in the state $|0\rangle$ by resonant optical excitation [14]. We then swap the state of the electron spin onto the ^{13}C spin and reset the electron spin. Next, we prepare the electron in a superposition state before performing the DDRF controlled-rotation gate, ideally preparing the electron-nuclear Bell state $\left|\psi_{\text{Bell}}\right\rangle = (|0+\rangle + |1-\rangle)/\sqrt{2}$, where $|\pm\rangle = (|\downarrow\rangle \pm |\uparrow\rangle)/\sqrt{2}$.

To perform quantum state tomography on the two-qubit state, we first measure the electron spin along a chosen axis by appropriate basis rotations followed by Z-basis op-

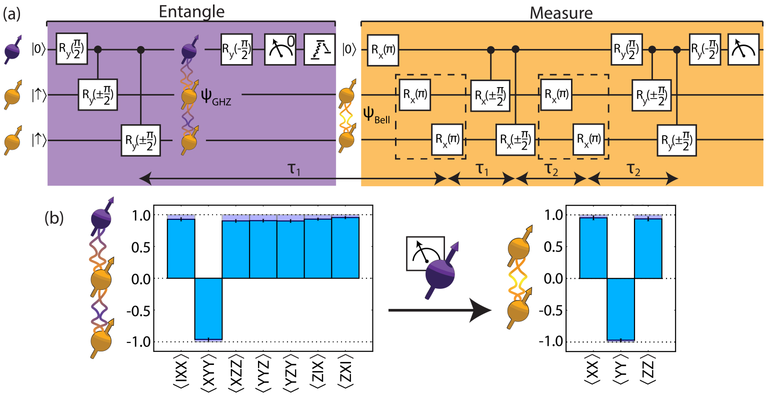

Figure 5.5: (a) Experimental sequence for the preparation of a nuclear-nuclear Bell state and measurement of the two-qubit operator ZZ. After preparation of the electron-nuclear-nuclear GHZ state $|\mathrm{GHZ}_3\rangle = (|0++\rangle + |1--\rangle)/\sqrt{2}$, an X-basis measurement on the ancilla (electron spin) projects the nuclear spins into the Bell state $\left|\Phi^+\right\rangle = (|++\rangle + |--\rangle)/\sqrt{2}$. Measurement of the two-qubit correlations between the nuclear spins is then performed through the electron spin. Spin echoes (dashed boxes) built into the measurement sequence protect the nuclear spins from dephasing errors. (b) Measured expectation values (non-zero terms of the ideal state only) for the electron-nuclear-nuclear state $|\mathrm{GHZ}_3\rangle$, and for the nuclear-nuclear state $\left|\Phi^+\right\rangle$. Blue (purple) bars show the experimental (ideal) expectation values for each operator. The nuclear-nuclear correlations are well preserved after a nondestructive measurement of the electron spin in the X-basis.

tical readout [14]. To mitigate potential dephasing of the nuclear spin induced by the electron spin measurement, we make the electron spin measurement non-destructive by using a short, weak laser pulse and conditioning progression of the sequence on the outcome $|0\rangle$, i.e. the detection of a photon [16, 42] (see Supplemental Material online for all readout parameters [53]). Following appropriate basis rotations, we then use the electron spin to measure the nuclear spin in the X-basis [16]. In this measurement the electron is read out in a single-shot with average fidelity 0.945(2) [14]. We independently characterize the nuclear spin readout, which is then used to correct for readout infidelities in subsequent measurements [53]. In order to reconstruct the full electron-nuclear state, we perform the sequence with and without an additional electron π-pulse before the first readout [53].

The reconstructed density matrix from quantum state tomography is shown in Fig. 5.4(b). The prepared state ρ exhibits a fidelity, $\mathscr{F}_{\mathrm{Bell}} = \left\langle \psi_{\mathrm{Bell}} \right| \rho \left| \psi_{\mathrm{Bell}} \right\rangle = 0.972(8)$ with the target Bell state. Based upon a simple depolarizing noise model, we estimate the two-qubit gate fidelity to be $\mathscr{F}_{\mathrm{gate}} = 0.991(9)$ [53]. Additional characterization measurements in combination with numerical simulations indicate that the remaining infidelity can be mostly attributed to electron spin dephasing due to noise from the electronic hardware [53].

5.4. A 10-QUBIT SOLID-STATE SPIN REGISTER

We now show how the combination of our DDRF gate with previously developed gates and control techniques [16, 37] enables high-fidelity control of a 10-qubit hybrid spin register associated to a single NV-center. Our register is composed of the electron and ^{14}N spins of the NV-center, along with 8 ^{13}C nuclear spins (Fig. 5.1). Our quantum register is connected via the central electron spin. To demonstrate this, we first show that all nuclear spins can be entangled with the electron spin by following the protocol shown in Fig. 5.4(a). For the case of the nitrogen spin, initialization is performed by a measurement-based scheme which heralds the preparation in a particular eigenstate. Compared to previous work [60], we realize an improved initialization fidelity ($\mathscr{F}_{\text{init}} = 0.997(11)$) by pre-preparing the electron in the $m_s = -1$ state instead of a mixed state of $m_s = -1$ and $+1$, and by repeating the measurement-based initialization sequence twice [53]. After initialization, we work in the $m_I = \{0, -1\}$ subspace, and perform operations analogous to those for the ^{13}C nuclear spins, including the two-qubit gates using the DDRF scheme. Genuine entanglement is probed by measuring the non-zero matrix elements of the target state, and confirmed by negativity of the entanglement witness $\mathscr{W}_{\text{Bell}} = 1 - 2\left|\psi_{\text{Bell}}\right\rangle\left\langle\psi_{\text{Bell}}\right|$ [61].

Next, we show that the register is fully connected by preparing entangled states for all possible pairs of spins. To prepare nuclear-nuclear entanglement, we implement a probabilistic measurement-based scheme [62], as shown in Fig. 5.5(a). We first prepare a three-qubit GHZ state comprising the electron and two nuclear spins, $|\text{GHZ}_3\rangle = (|0++\rangle + |1--\rangle)/\sqrt{2}$, before performing a non-destructive X-basis measurement on the electron spin. The measurement ideally prepares the Bell state $\left|\Phi^+\right\rangle = (|++\rangle + |--\rangle)/\sqrt{2}$ on the targeted pair of nuclear spins. Finally, we measure the necessary expectation values in order to reconstruct the non-zero matrix elements of this state and confirm bipartite entanglement (Fig. 5.5(b)).

The measured Bell state fidelities, ranging from 0.63(3) to 0.97(1), are shown in Fig. 5.6. We attribute the variations in the measured values to differences in the two-qubit gate fidelities for each spin. In particular, the lower values measured for ^{13}C spins C7 and C8 are due to short coherence times in combination with long two-qubit gate durations, necessitated by close spectral proximity to other spins [53]. All data is measured using a single set of gate parameters, and using a single hardware configuration, rather than separately optimizing for each pair of qubits.

5.5. GENERATION OF N-QUBIT GHZ STATES

Quantum information processing tasks such as computations and error correction will require the execution of complex algorithms comprising a large number of qubits. An important requirement for a quantum processor is thus the ability to perform operations on many of its constituents within a single algorithm. We test this capability by generating N-qubit GHZ type states, defined as

$$|\text{GHZ}_N\rangle = \frac{1}{\sqrt{2}}\left(|0\rangle \otimes |+\rangle^{\otimes(N-1)} + |1\rangle \otimes |-\rangle^{\otimes(N-1)}\right). \tag{5.5}$$

To generate such states, we follow the sequence shown in Fig. 5.7(a). First, $N-1$ nuclear spins are initialized in the state $|\uparrow\rangle$. Next, we prepare the electron spin in a superposition state, and perform sequential controlled rotation gates between the electron and nuclear spins.

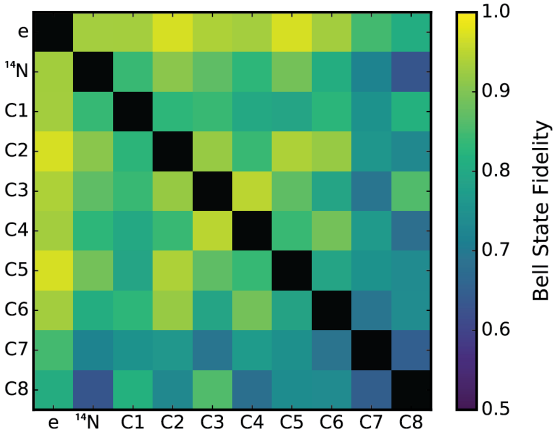

Figure 5.6: Measured Bell state fidelities for all pairs of qubits in the 10-qubit register. Genuine entanglement is confirmed in all cases, as witnessed by a fidelity exceeding 0.5 with the target state. Qubits C1, C7, C8 and ^{14}N are controlled using DDRF gates (section 5.2). Qubits C2, C3, C4, C5, and C6 are controlled using the methods described in Taminiau et al. [37], as their hyperfine interaction parameters enable high-fidelity control using previously optimized gates.

Characterizing the full quantum state for a system of this size is an expensive task due to the dimensionality of the associated Hilbert space. However, we can determine if the state exhibits genuine multipartite entanglement of all N qubits using an entanglement witness with a reduced subset of measurement bases [61]. For a GHZ state with system size N, there exist 2^N operators from which the non-zero elements of the density matrix can be reconstructed by linear inversion, and from which a fidelity with the target state can be calculated. Negativity of the entanglement witness $\mathscr{W}_{\mathrm{GHZ}} = 1/2 - |\mathrm{GHZ}_N\rangle\langle\mathrm{GHZ}_N|$ heralds genuine multipartite entanglement [61]. We determine the required expectation values of products of Pauli operators on the register via the electron spin. In these experiments, the readout sequence is modified slightly. Prior to the readout of the electron spin state, we rotate the nitrogen spin such that the desired measurement basis is mapped to the Z-basis. This ensures that the population in the measurement basis is protected from dephasing during the optical readout of the electron spin, which is caused by the large electron-nitrogen hyperfine coupling in the excited state [53, 63].

As the number of qubits is increased, a new challenge arises: the total sequence time becomes comparable to, or even exceeds the natural dephasing times (T_2^*) of the nuclear spins. In order to preserve the nuclear spin coherence, we insert spin (Hahn) echo pulses (RF π-pulses) into the sequence to refocus each spin at the point of the next operation performed upon it. In the Supplemental Material online [53], we derive a general solution that can be used to algorithmically construct echo sequences that avoid any overlap in gates and that minimize idle time with the electron spin in a superposition state.

In Figs. 5.7(b,c), we show measurements for $N = 5$ and $N = 7$ qubits. In Fig. 5.7(d), we present the measured fidelities with the target GHZ states for 2 to 8 qubits, along with

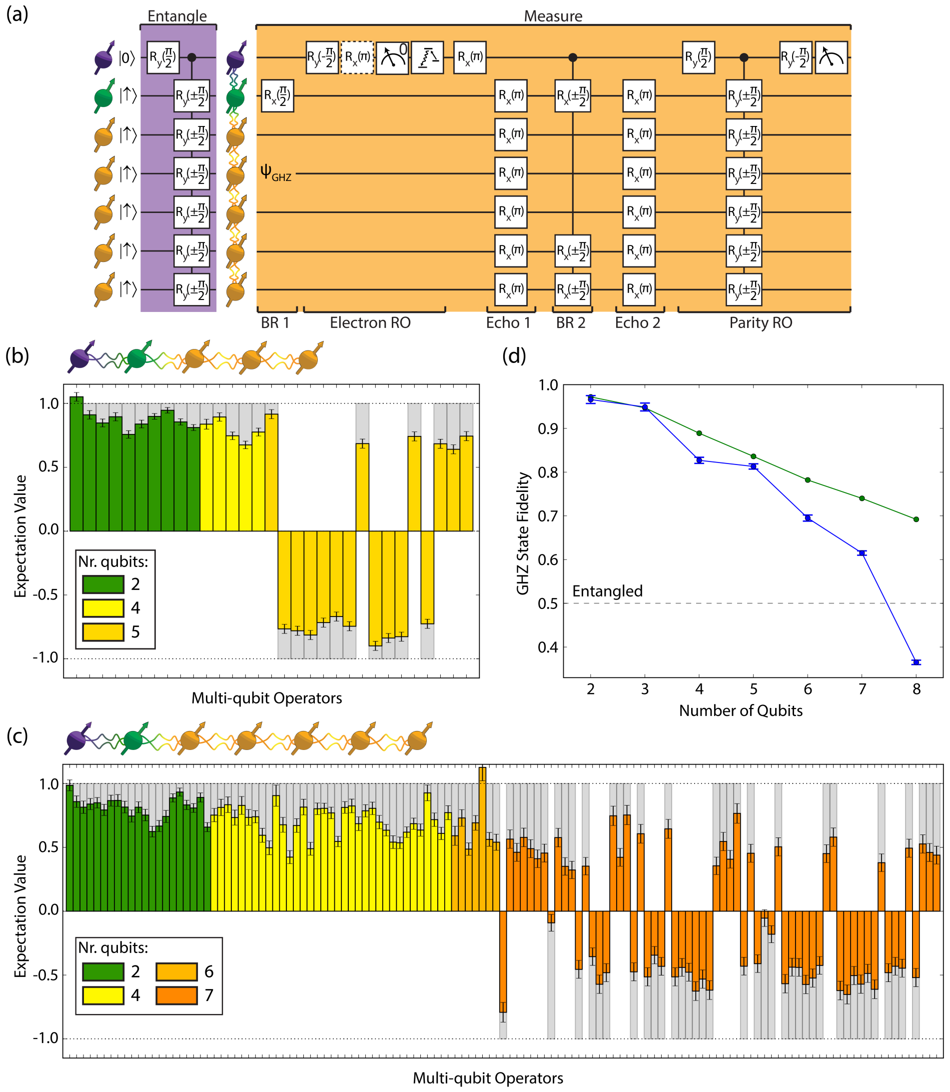

Figure 5.7: (a) Experimental sequence to prepare a 7-qubit GHZ state $|\mathrm{GHZ}_7\rangle$ (purple) and determine the expectation value of the 7-qubit operator $XYYYYZZ$ (orange). The measurement sequence is broken down into basis rotations (BR 1,2), an electron readout (RO), nuclear spin echoes (Echo 1,2), and a multi-qubit readout of the nuclear spins. All operations are applied sequentially (in the same way as shown in Fig. 5.5), but some are shown in parallel for clarity. (b-c) Bar plots showing the measured expectation values (non-zero terms of the ideal state only) after preparing the 5-spin (b) and 7-spin (c) GHZ states. The colors indicate the number of qubits involved, i.e. the number of (non-identity) operators in the expectation value (inset). Gray bars show the ideal expectation values. See the Supplemental Material online [53] for the operator corresponding to each bar. The fidelity with the target state is 0.804(6) (b) and 0.589(5) (c), confirming genuine multipartite entanglement in both cases. (d) Plot of GHZ state fidelity against the number of constituent qubits. A value above 0.5 confirms genuine N-qubit entanglement. The blue points are the measured data, while the green points are theoretical predictions assuming a simple depolarizing noise model whose parameters are extracted from single- and two-qubit experiments. Numerical values are given in the Supplemental Material online [53].

theoretical values as predicted by a depolarizing-noise model based on the individual two-qubit gate fidelities [53]. The growing discrepancy between the measured and predicted values for larger N suggests residual crosstalk between the qubits, which is not taken into account in the model. For registers comprising up to 7 spins we observe negativity of the witness $\mathscr{W}_{\mathrm{GHZ}}$, revealing genuine N-qubit entanglement of up to 7 qubits with high statistical significance.

5.6. A LONG LIVED QUANTUM MEMORY

The nuclear spin qubits surrounding the NV center are promising candidates for quantum memories with long coherence times [32, 64]. Here we investigate the coherence properties of the register under dynamical decoupling and show that an arbitrary single-qubit state can be protected for over 75 seconds. Furthermore, we show that two-qubit entanglement can be preserved beyond 10 seconds.

We first investigate the coherence of individual nuclear spin qubits under dynamical decoupling. After initializing the nuclear spin in the state $|+\rangle$, we prepare the electron in the state $|1\rangle$ (electron $T_1 = 3.6(3) \times 10^3$ s [47]). This has two effects. Firstly, it allows us to perform selective RF π-pulses on the target nuclear spin. Secondly, the magnetic field gradient imposed by the electron-nuclear hyperfine interaction induces a frozen core, which suppresses flip-flop interactions between nuclear spins [65, 66] and thereby reduces the noise the spins are exposed to.

The observed spin-echo coherence times $T_2^{\alpha=1}$, with α the number of RF pulses, vary between 0.26(3) s to 0.77(4) s for the 8 ^{13}C spins. For the ^{14}N spin we find 2.3(2) s, consistent with the smaller gyromagnetic ratio by factor 3.4. The range of coherence times observed for the ^{13}C spins is likely caused by differences in the microscopic environment of each spin. In particular, ^{13}C spins close to the NV center are in the heart of the frozen core, and, generally tend to couple predominantly to the part of the spin environment for which the dynamics are also suppressed most strongly. Spins farther from the NV tend to couple more strongly to the spin environment outside the frozen core. This explanation is consistent with the observation that the spin with the longest $T_2^{\alpha=1}$ of 0.77(4) s is located closest (C1, $r = 0.53(5)$ nm [58]) to the vacancy lattice site, while the shortest $T_2^{\alpha=1}$ of 0.26(3) s is found for a spin at a larger distance (C8, $r = 1.04(4)$ nm [58]). As expected, increasing the number of decoupling pulses leads to an increase in the measured coherence times. For $\alpha = 256$ pulses, the decay time of C5 reaches $T_2^{\alpha=256} = 12.9(4)$ s, while for the ^{14}N spin, we measure $T_2^{\alpha=256} = 63(2)$ s (ee the Supplemental Material online [53]). For the other ^{13}C spins for which we measure $T_2^{\alpha=256}$, we find a range of values from 4(1) to 25(4) seconds [53].

To confirm that arbitrary quantum states can be protected, we prepare the six cardinal states and measure the average state fidelity under dynamical decoupling. The measured decay curves for spin C5 and the ^{14}N spin are shown in Fig. 5.8, where α is varied from 1 to 256. With 256 pulses, we measure a state fidelity exceeding the classical memory bound of $\frac{2}{3}$ at a time of 16.8 s for C5, and at a time of 75.3 s for the ^{14}N spin.

The coherence times demonstrated here are the longest reported for individual qubits in the solid state and exceed values for isolated nuclear spin qubits in isotopically purified materials [24, 32, 33]. More importantly, however, in our register we realize these long coherence times while maintaining access to 10 coupled spin qubits.

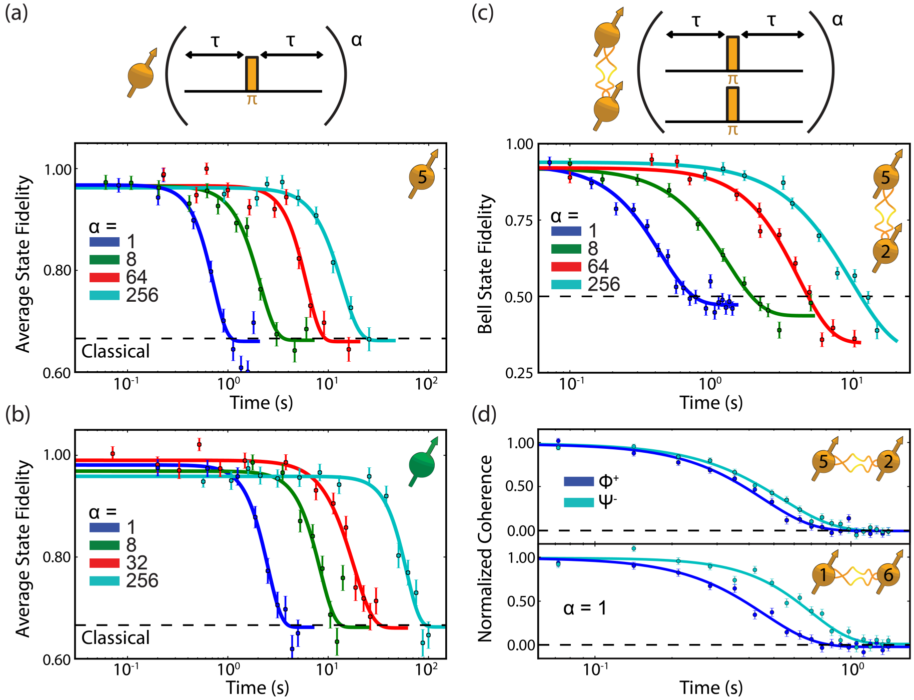

Figure 5.8: (a) Dynamical decoupling for spin C5. With $\alpha = 256$ pulses, the average state fidelity of the six cardinal states is measured to be 0.73(2) after 16.8 s, above the limit of $\frac{2}{3}$ for a classical memory with a confidence of 99.7% (upper-tailed Z test). Solid lines are fit to the function $f(t) = A + Be^{-(t/T)^n}$. The offset A is fixed using the average fidelity of the input states $|\uparrow\rangle$ and $|\downarrow\rangle$, which show no decay on these timescales. B, T and n are fit parameters which account for the decay of the fidelity due to interactions with the nuclear spin bath, external noise and pulse errors. (b) Dynamical decoupling of the ^{14}N spin. For $\alpha = 256$ pulses, the average state fidelity at 75.3 s is 0.73(3), which is above the bound for a classical memory with 99.4% confidence. (c) Dynamical decoupling of a pair of ^{13}C spins prepared in the Bell state $\left|\Phi^+\right\rangle$. Solid lines are fits to $f(t)$, but with A as a free parameter to account for the observed decrease in the ZZ correlations at large pulse numbers, likely due to pulse errors. With 256 decoupling pulses, genuine two-qubit entanglement is witnessed at times up to 10.2 s, where we observe a fidelity of 0.57(2) with the target Bell state (99.9% confidence of entanglement). In addition, interpolation of the fit yields 11.3(8) s as the point where the fidelity crosses 0.5 [53]. (d) Normalized coherence $(\langle XX\rangle \pm \langle YY\rangle)/2\mathcal{N}$, where $\mathcal{N}$ is a normalization factor, for two pairs of ^{13}C spins prepared in both the even and odd parity Bell states $\left|\Phi^+\right\rangle = (|\downarrow\downarrow\rangle + |\uparrow\uparrow\rangle)/\sqrt{2}$ and $|\Psi^-\rangle = (|\downarrow\uparrow\rangle - |\downarrow\uparrow\rangle)/\sqrt{2}$. Solid lines are fits to $f(t)$ with $A = 0$ and $B = 1$. For pair 1, the fitted decay times, T, are 0.45(2) s and 0.54(1) s for the states $\left|\Phi^+\right\rangle$ and $|\Psi^-\rangle$ respectively. For pair 2, the equivalent values are 0.46(2) s and 0.70(3) s.

We exploit the multi-qubit nature of the register to investigate the protection of entangled states of two ^{13}C spin qubits. After preparing the state $\left|\Phi^+\right\rangle = (|{+}{+}\rangle + |{-}{-}\rangle)/\sqrt{2}$ following the sequence shown in Fig. 5.5(a), we again prepare the electron in the state $|1\rangle$. We then measure the Bell state fidelity as a function of total evolution time for $\alpha = 1$ to $\alpha = 256$ pulses. Note that since $\left|\Phi^+\right\rangle$ is an eigenstate of ZZ, its evolution is not affected by the coupling between the two qubits, which is predominantly dipolar and of the form CI_zI_z, with $C = 1.32(4)$ Hz [58]. The measured fidelities are plotted in Fig. 5.8(c). For $\alpha = 256$ decoupling pulses, we confirm the preservation of entanglement for > 10 s, as quantified by a fidelity exceeding 0.5 with the desired Bell state.

With the capability to protect multi-qubit quantum states, it becomes important to consider additional effects that may affect their coherence, such as the presence of correlated noise. As a first experimental step towards understanding such effects, we use entangled states of nuclear spins to explore spatial correlations within the noise environment. We perform experiments on two pairs of ^{13}C spins. We prepare two Bell states for each pair, one exhibiting even ZZ parity, which, written in the Z-basis, is given by $\left|\Phi^+\right\rangle = (|{\downarrow\downarrow}\rangle + |{\uparrow\uparrow}\rangle)/\sqrt{2}$, and another exhibiting odd ZZ parity, $|\Psi^-\rangle = (|{\downarrow\uparrow}\rangle - |{\uparrow\downarrow}\rangle)/\sqrt{2}$. The difference in the coherence times of these two states gives an indication of the amount of correlation in the noise experienced by the two spins [67]. In the case of perfectly correlated noise, one would expect the state $\left|\Phi^+\right\rangle$ to decay at four times the single qubit decay rate (superdecoherence), while the state $|\Psi^-\rangle$ would form a decoherence-free subspace [68, 69]. In contrast, for completely uncorrelated noise, the coherence times for the two states would be identical.

We measure the coherence times for the two Bell states, varying the total evolution time for the case of a single spin-echo pulse ($\alpha = 1$) with the electron spin prepared in the state $|1\rangle$. In Fig. 5.8(d), we plot the normalized coherence signal for both Bell states and for both pairs of qubits. A statistically significant difference between the decay curves for the two Bell states is found for both pairs, where the odd-parity state $|\Psi^-\rangle$ decays more slowly than the even-parity state $\left|\Phi^+\right\rangle$, indicating partly correlated noise in the system. We can relate the size of the effect to the distance between the spins in the pairs, which has been characterized in separate work [58]. This reveals that the pair with a smaller separation (C1 and C6, distance 0.96(3) nm) shows more correlation than the pair with a larger separation (C5 and C2, 1.38(7) nm). This observation is consistent with the idea that spatially close spins tend to couple to the same nuclear spin environment, and therefore experience correlated noise, although large deviations from this rule are expected to be possible for specific cases [67]. Characterizing such correlated noise provides new opportunities to investigate the physics of decoherence in spin baths [67], and to develop and test quantum error correction schemes that are tailored for specific correlated noise [70, 71].

5.7. CONCLUSION

In conclusion, we have developed a novel electron-nuclear two-qubit gate and applied these gates to realize a 10-qubit solid-state spin register that can protect an arbitrary single-qubit state for over one minute. The techniques developed in this work can be readily implemented for multi-qubit control in a variety of other donor and defect platforms, including spin-1/2 [7, 9, 13, 20, 28, 54, 55] and contact hyperfine [21, 34] systems, for which many previous gate designs are challenging to apply [37, 48–50]. Further improvements in selectivity and fidelity of the gates are anticipated to be possible by (optimal) shaping of the RF pulses [38, 56, 57] and by reducing electronic noise. Additionally, the use of direct RF driving opens the possibility to perform gates in parallel on multiple qubits. Combined with already demonstrated long-range optical entanglement [29–31], our multi-qubit register paves the way for the realization of rudimentary few-node quantum networks comprising tens of qubits. This will enable the investigation of basic error correction codes and algorithms over quantum networks [44–46]. Finally, looking beyond quantum information, the gate sequences developed here also enable new quantum sensing methods [58].

REFERENCES

[1] D. D. Awschalom, R. Hanson, J. Wrachtrup, and B. B. Zhou, *Quantum technologies with optically interfaced solid-state spins,* Nat. Photonics **12**, 516 (2018).

[2] F. A. Zwanenburg, A. S. Dzurak, A. Morello, M. Y. Simmons, L. C. L. Hollenberg, G. Klimeck, S. Rogge, S. N. Coppersmith, and M. A. Eriksson, *Silicon quantum electronics,* Rev. Mod. Phys. **85**, 961 (2013).

[3] G. De Lange, Z. Wang, D. Riste, V. Dobrovitski, and R. Hanson, *Universal dynamical decoupling of a single solid-state spin from a spin bath,* Science **330**, 60 (2010).

[4] G. D. Fuchs, V. V. Dobrovitski, D. M. Toyli, F. J. Heremans, and D. D. Awschalom, *Gigahertz dynamics of a strongly driven single quantum spin,* Science **326**, 1520 (2009).

[5] D. J. Christle, A. L. Falk, P. Andrich, P. V. Klimov, J. U. Hassan, N. T. Son, E. Janzén, T. Ohshima, and D. D. Awschalom, *Isolated electron spins in silicon carbide with millisecond coherence times,* Nat. Mater. **14**, 160 (2015).

[6] H. Seo, A. L. Falk, P. V. Klimov, K. C. Miao, G. Galli, and D. D. Awschalom, *Quantum decoherence dynamics of divacancy spins in silicon carbide,* Nat. Commun. **7**, 12935 (2016).

[7] D. D. Sukachev, A. Sipahigil, C. T. Nguyen, M. K. Bhaskar, R. E. Evans, F. Jelezko, and M. D. Lukin, *Silicon-vacancy spin qubit in diamond: a quantum memory exceeding 10 ms with single-shot state readout,* Phys. Rev. Lett. **119**, 223602 (2017).

[8] T. Iwasaki, F. Ishibashi, Y. Miyamoto, Y. Doi, S. Kobayashi, T. Miyazaki, K. Tahara, K. D. Jahnke, L. J. Rogers, B. Naydenov, *et al.*, *Germanium-vacancy single color centers in diamond,* Sci. Rep. **5**, 12882 (2015).

[9] P. Siyushev, M. H. Metsch, A. Ijaz, J. M. Binder, M. K. Bhaskar, D. D. Sukachev, A. Sipahigil, R. E. Evans, C. T. Nguyen, M. D. Lukin, *et al.*, *Optical and microwave control of germanium-vacancy center spins in diamond,* Phys. Rev. B **96**, 081201 (2017).

[10] J. N. Becker, B. Pingault, D. Groß, M. Gündoğan, N. Kukharchyk, M. Markham, A. Edmonds, M. Atatüre, P. Bushev, and C. Becher, *All-optical control of the silicon-vacancy spin in diamond at millikelvin temperatures,* Phys. Rev. Lett. **120**, 053603 (2018).

[11] B. Pingault, D.-D. Jarausch, C. Hepp, L. Klintberg, J. N. Becker, M. Markham, C. Becher, and M. Atatüre, *Coherent control of the silicon-vacancy spin in diamond,* Nat. Commun. **8**, 15579 (2017).

[12] M. E. Trusheim, B. Pingault, N. H. Wan, M. Gündoğan, L. De Santis, R. Debroux, D. Gangloff, C. Purser, K. C. Chen, M. Walsh, J. J. Rose, J. N. Becker, B. Lienhard, E. Bersin, I. Paradeisanos, G. Wang, D. Lyzwa, A. R.-P. Montblanch, G. Malladi, H. Bakhru, A. C. Ferrari, I. A. Walmsley, M. Atatüre, and D. Englund, *Transform-limited photons from a coherent tin-vacancy spin in diamond,* Phys. Rev. Lett. **124**, 023602 (2020).

[13] A. E. Rugar, C. Dory, S. Sun, and J. Vučković, *Characterization of optical and spin properties of single tin-vacancy centers in diamond nanopillars,* Phys. Rev. B **99**, 205417 (2019).

[14] L. Robledo, L. Childress, H. Bernien, B. Hensen, P. F. Alkemade, and R. Hanson, *High-fidelity projective read-out of a solid-state spin quantum register,* Nature **477**, 574 (2011).

[15] J. J. Pla, K. Y. Tan, J. P. Dehollain, W. H. Lim, J. J. L. Morton, F. A. Zwanenburg, D. N. Jamieson, A. S. Dzurak, and A. Morello, *High-fidelity readout and control of a nuclear spin qubit in silicon,* Nature **496**, 334 (2013).

[16] J. Cramer, N. Kalb, M. A. Rol, B. Hensen, M. S. Blok, M. Markham, D. J. Twitchen, R. Hanson, and T. H. Taminiau, *Repeated quantum error correction on a continuously encoded qubit by real-time feedback,* Nat. Commun. **7**, 11526 (2016).

[17] G. Waldherr, Y. Wang, S. Zaiser, M. Jamali, T. Schulte-Herbruggen, H. Abe, T. Ohshima, J. Isoya, J. Du, P. Neumann, *et al.*, *Quantum error correction in a solid-state hybrid spin register,* Nature **506**, 204 (2014).

[18] G. Wolfowicz, P.-A. Mortemousque, R. Guichard, S. Simmons, M. L. Thewalt, K. M. Itoh, and J. J. Morton, *29si nuclear spins as a resource for donor spin qubits in silicon,* New J. Phys. **18**, 023021 (2016).

[19] G. Tosi, F. A. Mohiyaddin, V. Schmitt, S. Tenberg, R. Rahman, G. Klimeck, and A. Morello, *Silicon quantum processor with robust long-distance qubit couplings,* Nat. Commun. **8**, 450 (2017).

[20] M. H. Metsch, K. Senkalla, B. Tratzmiller, J. Scheuer, M. Kern, J. Achard, A. Tallaire, M. B. Plenio, P. Siyushev, and F. Jelezko, *Initialization and readout of nuclear spins via a negatively charged silicon-vacancy center in diamond,* Phys. Rev. Lett. **122**, 190503 (2019).

[21] B. Hensen, W. W. Huang, C.-H. Yang, K. W. Chan, J. Yoneda, T. Tanttu, F. E. Hudson, A. Laucht, K. M. Itoh, T. D. Ladd, *et al.*, *A silicon quantum-dot-coupled nuclear spin qubit,* Nat. Nanotech. **15**, 13 (2020).

[22] F. Dolde, I. Jakobi, B. Naydenov, N. Zhao, S. Pezzagna, C. Trautmann, J. Meijer, P. Neumann, F. Jelezko, and J. Wrachtrup, *Room-temperature entanglement between single defect spins in diamond,* Nat. Phys. **9**, 139 (2013).

[23] T. Yamamoto, C. Müller, L. P. McGuinness, T. Teraji, B. Naydenov, S. Onoda, T. Ohshima, J. Wrachtrup, F. Jelezko, and J. Isoya, *Strongly coupled diamond spin qubits by molecular nitrogen implantation,* Phys. Rev. B **88**, 201201 (2013).

[24] S. Yang, Y. Wang, D. B. Rao, T. H. Tran, A. S. Momenzadeh, M. Markham, D. Twitchen, P. Wang, W. Yang, R. Stöhr, *et al.*, *High-fidelity transfer and storage of photon states in a single nuclear spin,* Nat. Photonics **10**, 507 (2016).

[25] E. Togan, Y. Chu, A. Trifonov, L. Jiang, J. Maze, L. Childress, M. G. Dutt, A. S. Sørensen, P. Hemmer, A. S. Zibrov, *et al.*, *Quantum entanglement between an optical photon and a solid-state spin qubit,* Nature **466**, 730 (2010).

[26] D. J. Christle, P. V. Klimov, F. Charles, K. Szász, V. Ivády, V. Jokubavicius, J. U. Hassan, M. Syväjärvi, W. F. Koehl, T. Ohshima, *et al.*, *Isolated spin qubits in sic with a high-fidelity infrared spin-to-photon interface,* Phys. Rev. X **7**, 021046 (2017).

[27] A. Sipahigil, R. E. Evans, D. D. Sukachev, M. J. Burek, J. Borregaard, M. K. Bhaskar, C. T. Nguyen, J. L. Pacheco, H. A. Atikian, C. Meuwly, *et al.*, *An integrated diamond nanophotonics platform for quantum-optical networks,* Science **354**, 847 (2016).

[28] R. E. Evans, M. K. Bhaskar, D. D. Sukachev, C. T. Nguyen, A. Sipahigil, M. J. Burek, B. Machielse, G. H. Zhang, A. S. Zibrov, E. Bielejec, *et al.*, *Photon-mediated interactions between quantum emitters in a diamond nanocavity,* Science **362**, 662 (2018).

[29] H. Bernien, B. Hensen, W. Pfaff, G. Koolstra, M. Blok, L. Robledo, T. Taminiau, M. Markham, D. Twitchen, L. Childress, *et al.*, *Heralded entanglement between solid-state qubits separated by three metres,* Nature **497**, 86 (2013).

[30] B. Hensen, H. Bernien, A. E. Dréau, A. Reiserer, N. Kalb, M. S. Blok, J. Ruitenberg, R. F. Vermeulen, R. N. Schouten, C. Abellán, *et al.*, *Loophole-free bell inequality violation using electron spins separated by 1.3 kilometres,* Nature **526**, 682 (2015).

[31] P. C. Humphreys, N. Kalb, J. P. Morits, R. N. Schouten, R. F. Vermeulen, D. J. Twitchen, M. Markham, and R. Hanson, *Deterministic delivery of remote entanglement on a quantum network,* Nature **558**, 268 (2018).

[32] P. C. Maurer, G. Kucsko, C. Latta, L. Jiang, N. Y. Yao, S. D. Bennett, F. Pastawski, D. Hunger, N. Chisholm, M. Markham, *et al.*, *Room-temperature quantum bit memory exceeding one second,* Science **336**, 1283 (2012).

[33] J. T. Muhonen, J. P. Dehollain, A. Laucht, F. E. Hudson, R. Kalra, T. Sekiguchi, K. M. Itoh, D. N. Jamieson, J. C. McCallum, A. S. Dzurak, *et al.*, *Storing quantum information for 30 seconds in a nanoelectronic device,* Nat. Nanotechnol. **9**, 986 (2014).

[34] J. P. Dehollain, S. Simmons, J. T. Muhonen, R. Kalra, A. Laucht, F. Hudson, K. M. Itoh, D. N. Jamieson, J. C. McCallum, A. S. Dzurak, *et al.*, *Bell's inequality violation with spins in silicon,* Nat. Nanotech. **11**, 242 (2016).

[35] S. Freer, S. Simmons, A. Laucht, J. T. Muhonen, J. P. Dehollain, R. Kalra, F. A. Mohiyaddin, F. E. Hudson, K. M. Itoh, J. C. McCallum, *et al.*, *A single-atom quantum memory in silicon,* Quantum Science and Technology **2**, 015009 (2017).

[36] T. Van der Sar, Z. Wang, M. Blok, H. Bernien, T. Taminiau, D. Toyli, D. Lidar, D. Awschalom, R. Hanson, and V. Dobrovitski, *Decoherence-protected quantum gates for a hybrid solid-state spin register,* Nature **484**, 82 (2012).

[37] T. H. Taminiau, J. Cramer, T. van der Sar, V. V. Dobrovitski, and R. Hanson, *Universal control and error correction in multi-qubit spin registers in diamond,* Nat. Nanotechnol. **9**, 171 (2014).

[38] X. Rong, J. Geng, F. Shi, Y. Liu, K. Xu, W. Ma, F. Kong, Z. Jiang, Y. Wu, and J. Du, *Experimental fault-tolerant universal quantum gates with solid-state spins under ambient conditions,* Nat. Commun. **6**, 8748 (2015).

[39] S. Zaiser, T. Rendler, I. Jakobi, T. Wolf, S.-Y. Lee, S. Wagner, V. Bergholm, T. Schulte-Herbrüggen, P. Neumann, and J. Wrachtrup, *Enhancing quantum sensing sensitivity by a quantum memory,* Nat. Commun. **7**, 12279 (2016).

[40] T. K. Unden, D. Louzon, M. Zwolak, W. H. Zurek, and F. Jelezko, *Revealing the emergence of classicality using nitrogen-vacancy centers,* Phys. Rev. Lett. **123**, 140402 (2019).

[41] Y.-Y. Huang, Y.-K. Wu, F. Wang, P.-Y. Hou, W.-B. Wang, W.-G. Zhang, W.-Q. Lian, Y.-Q. Liu, H.-Y. Wang, H.-Y. Zhang, *et al.*, *Experimental realization of robust geometric quantum gates with solid-state spins,* Phys. Rev. Lett. **122**, 010503 (2019).

[42] N. Kalb, A. A. Reiserer, P. C. Humphreys, J. J. Bakermans, S. J. Kamerling, N. H. Nickerson, S. C. Benjamin, D. J. Twitchen, M. Markham, and R. Hanson, *Entanglement distillation between solid-state quantum network nodes,* Science **356**, 928 (2017).

[43] S. B. van Dam, J. Cramer, T. H. Taminiau, and R. Hanson, *Multipartite entanglement generation and contextuality tests using nondestructive three-qubit parity measurements,* Phys. Rev. Lett. **123**, 050401 (2019).

[44] B. M. Terhal, *Quantum error correction for quantum memories,* Rev. Mod. Phys. **87**, 307 (2015).

[45] N. H. Nickerson, Y. Li, and S. C. Benjamin, *Topological quantum computing with a very noisy network and local error rates approaching one percent,* Nat. Commun. **4**, 1756 (2013).

[46] N. H. Nickerson, J. F. Fitzsimons, and S. C. Benjamin, *Freely scalable quantum technologies using cells of 5-to-50 qubits with very lossy and noisy photonic links,* Phys. Rev. X **4**, 041041 (2014).

[47] M. H. Abobeih, J. Cramer, M. A. Bakker, N. Kalb, M. Markham, D. Twitchen, and T. H. Taminiau, *One-second coherence for a single electron spin coupled to a multiqubit nuclear-spin environment,* Nat. commun. **9**, 2552 (2018).

[48] S. Kolkowitz, Q. P. Unterreithmeier, S. D. Bennett, and M. D. Lukin, *Sensing distant nuclear spins with a single electron spin,* Phys. Rev. Lett. **109**, 137601 (2012).

[49] T. H. Taminiau, J. J. T. Wagenaar, T. van der Sar, F. Jelezko, V. V. Dobrovitski, and R. Hanson, *Detection and control of individual nuclear spins using a weakly coupled electron spin,* Phys. Rev. Lett. **109**, 137602 (2012).

[50] N. Zhao, J. Honert, B. Schmid, M. Klas, J. Isoya, M. Markham, D. Twitchen, F. Jelezko, R.-B. Liu, H. Fedder, and J. Wrachtrup, *Sensing single remote nuclear spins,* Nat. Nanotech. **7**, 657 (2012).

[51] Z.-Y. Wang, J. Casanova, and M. B. Plenio, *Delayed entanglement echo for individual control of a large number of nuclear spins,* Nat. Commun. **8**, 14660 (2017).

[52] M. Pfender, N. Aslam, H. Sumiya, S. Onoda, P. Neumann, J. Isoya, C. A. Meriles, and J. Wrachtrup, *Nonvolatile nuclear spin memory enables sensor-unlimited nanoscale spectroscopy of small spin clusters,* Nat. Commun. **8**, 834 (2017).

[53] See Supplemental Material at http://link.aps.org/ supplemental/10.1103/PhysRevX.9.031045, which contains experimental details and parameters, all measured coherence times and fidelities, modeling of the expected fidelities, and the generalized theoretical description of the gate dynamics. This part of the paper is not reproduced in this thesis due to length considerations. .

[54] T. Müller, C. Hepp, B. Pingault, E. Neu, S. Gsell, M. Schreck, H. Sternschulte, D. Steinmüller-Nethl, C. Becher, and M. Atatüre, *Optical signatures of silicon-vacancy spins in diamond,* Nat. Commun. **5**, 3328 (2014).

[55] G. Thiering and A. Gali, *Ab initio magneto-optical spectrum of group-iv vacancy color centers in diamond,* Phys. Rev. X **8**, 021063 (2018).

[56] L. M. Vandersypen and I. L. Chuang, *Nmr techniques for quantum control and computation,* Rev. Mod. Phys. **76**, 1037 (2005).

[57] F. Dolde, V. Bergholm, Y. Wang, I. Jakobi, B. Naydenov, S. Pezzagna, J. Meijer, F. Jelezko, P. Neumann, T. Schulte-Herbrüggen, *et al.*, *High-fidelity spin entanglement using optimal control,* Nat. Commun. **5**, 3371 (2014).

[58] M. Abobeih, J. Randall, C. Bradley, H. Bartling, M. Bakker, M. Degen, M. Markham, D. Twitchen, and T. Taminiau, *Atomic-scale imaging of a 27-nuclear-spin cluster using a quantum sensor,* Nature **576**, 411 (2019).

[59] L. Childress, M. G. Dutt, J. Taylor, A. Zibrov, F. Jelezko, J. Wrachtrup, P. Hemmer, and M. Lukin, *Coherent dynamics of coupled electron and nuclear spin qubits in diamond,* Science **314**, 281 (2006).

[60] N. Kalb, J. Cramer, D. J. Twitchen, M. Markham, R. Hanson, and T. H. Taminiau, *Experimental creation of quantum zeno subspaces by repeated multi-spin projections in diamond,* Nat. Commun. **7**, 13111 (2016).

[61] O. Gühne and G. Tóth, *Entanglement detection,* Phys. Rep. **474**, 1 (2009).

[62] W. Pfaff, T. H. Taminiau, L. Robledo, H. Bernien, M. Markham, D. J. Twitchen, and R. Hanson, *Demonstration of entanglement-by-measurement of solid-state qubits,* Nat. Phys. **9**, 29 (2013).

[63] M. Blok, C. Bonato, M. Markham, D. Twitchen, V. Dobrovitski, and R. Hanson, *Manipulating a qubit through the backaction of sequential partial measurements and real-time feedback,* Nat. Phys. **10**, 189 (2014).

[64] N. Kalb, P. C. Humphreys, J. J. Slim, and R. Hanson, *Dephasing mechanisms of diamond-based nuclear-spin memories for quantum networks,* Phys. Rev. A **97**, 062330 (2018).

[65] G. Khutsishvili, *Spin diffusion and magnetic relaxation of nuclei,* Sov. Phys.-JETP **15** (1962).

[66] R. Guichard, S. Balian, G. Wolfowicz, P. Mortemousque, and T. Monteiro, *Decoherence of nuclear spins in the frozen core of an electron spin,* Phys. Rev. B **91**, 214303 (2015).

[67] D. Kwiatkowski and Ł. Cywiński, *Decoherence of two entangled spin qubits coupled to an interacting sparse nuclear spin bath: Application to nitrogen vacancy centers,* Phys. Rev. B **98**, 155202 (2018).

[68] D. A. Lidar, I. L. Chuang, and K. B. Whaley, *Decoherence-free subspaces for quantum computation,* Phys. Rev. Lett. **81**, 2594 (1998).

[69] A. Reiserer, N. Kalb, M. S. Blok, K. J. van Bemmelen, T. H. Taminiau, R. Hanson, D. J. Twitchen, and M. Markham, *Robust quantum-network memory using decoherence-protected subspaces of nuclear spins,* Phys. Rev. X **6**, 021040 (2016).

[70] T. Monz, P. Schindler, J. T. Barreiro, M. Chwalla, D. Nigg, W. A. Coish, M. Harlander, W. Hänsel, M. Hennrich, and R. Blatt, *14-qubit entanglement: Creation and coherence,* Phys. Rev. Lett. **106**, 130506 (2011).

[71] D. Layden, M. Chen, and P. Cappellaro, *Efficient quantum error correction of dephasing induced by a common fluctuator,* Phys. Rev. Lett. **124**, 020504 (2020).

6

FAULT-TOLERANT ENCODING AND MANIPULATIONS OF A COMPLETE LOGICAL QUBIT

M. H. Abobeih, Y. Wang, J. Randall, S. J. H. Loenen, C. E. Bradley, B. M. Terhal, T. H. Taminiau

Quantum error correction (QEC) is essential for reliable large-scale quantum information processing. Pioneering experiments using a variety of physical platforms have demonstrated QEC codes that could correct specific types of errors. However, a full experimental demonstration of a fault-tolerant QEC code capable of correcting any type of single-qubit error is challenging, due to the required number of qubits, control fidelities, and necessity for non-destructive parity measurements. Recently, it has been shown that the smallest fault-tolerant code can be realised using 7 qubits by extending the [[5,1,3]] code with a 'flag' ancilla. Here, we propose, and experimentally demonstrate, a novel scheme for fault-tolerant encoding of the logical qubits of this code using non-destructive parity measurements and flag ancilla measurements. We measure a logical-state fidelity of 95(2)% *for the fault-tolerant encoding scheme compared to* 81(2)% *for the non-fault-tolerant encoding, thus demonstrating a significant improvement using our fault-tolerant scheme. Furthermore, we demonstrate fault-tolerant operations on the logical qubit by applying a set of transversal logical Clifford gates. Our experiments provide the first experimental demonstration of a fault-tolerant logical qubit in the solid-state, a key step towards large-scale quantum information processing.*

6.1. INTRODUCTION

Spin-qubit registers in solids are among the most advanced and promising physical platforms for building large-scale quantum computers and quantum networks, due to their exceptionally long coherence times [1–6], compatibility for on-chip integration [7–9] and suitability to work at relatively high temperatures (few Kelvins) [1, 9, 10]. However, building large-scale quantum computers (or networks) will ultimately require methods to protect the qubits from errors in order to have reliable computations: quantum error correction (QEC) [11–13]. By encoding each data qubit into multiple physical qubits, parity measurements can be used to non-destructively detect (and thereafter correct) the errors [11, 14–17].

At the core of the QEC theory there is the concept of fault tolerance: the circuits used in any stage of the process (encoding, decoding, error extraction, or computing) should not cause errors to spread [16–18]. That is to say, any single error in any logical block remains a single error at the output of the block [19]. For such fault-tolerant circuits, if the error rates in the operations involved are below a certain threshold, we can reliably perform arbitrarily large quantum computations (the threshold theorem) [11, 20, 21].

Experimentally, there has been remarkable progress during the last few years towards implementing QEC codes using various physical platforms (such as superconducting qubits [22–24], ion traps [25, 26] and NV centers [27, 28]). Pioneering experiments have demonstrated error detection codes [29–32] as well as elementary QEC codes that could only correct specific types of errors [22, 27, 28, 33]. More recently, fault-tolerant encoding and post processing QEC of the Bacon-Shor [[9,1,3]] have been demonstrated using trapped ions [26].

Until few years ago, the smallest fault-tolerant QEC code that was known required at least 10 qubits [34], in addition to the ability to perform non-destructive multi-qubit parity measurements, which are crucial for the error-syndrome extractions. These requirements are challenging for all of the current physical platforms [35–37], and therefore have hindered the demonstration of a fault-tolerant QEC code.

Recently Chao and Reichardt [38] proposed a fault-tolerant QEC scheme that uses only 7 qubits in total, see Fig. 6.1c. This is basically the well-known [[5,1,3]] code (the perfect code) with a modification in the error-syndrome measurements, where an extra flag ancilla is used to make the scheme fault tolerant. Concurrently, on the experimental side, we have recently made significant progress in the quantum control and operation of multi-qubit registers. In particular, for our physical platform—spin registers in diamond—we have demonstrated 10-qubit registers with high-fidelity universal control and coherence times up to one minute [6] (see ch. 5). Moreover, we have demonstrated the generation of genuine multipartite entanglement of up to 7 qubits [6] (see ch. 5). Therefore, our system would be a suitable testbed to run and test the smallest fault-tolerant QEC code.

In this chapter, we present and experimentally demonstrate a scheme, that utilizes multiple non-destructive parity measurements in addition to a flag ancilla check, to fault-tolerantly encode the logical eigenstates of the [[5,1,3]] code. Furthermore, we demonstrate fault-tolerant operations on the logical qubit by applying a set of transversal logical gates. These experiments provide the first demonstration of a fault-tolerant complete logical qubit in the solid-state, a key step for large-scale quantum information

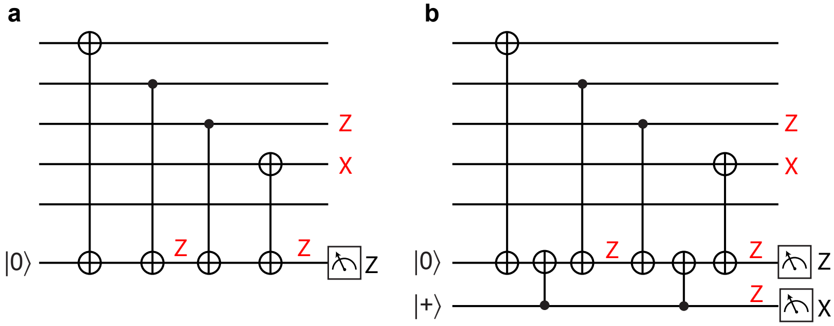

Figure 6.1: Basic idea of flagged error extraction. a) Traditional error extraction scheme (here measuring the $XZZXI$ stabilizer). However, this circuit is non-fault tolerant; a Z error on the ancilla after the second gate will propagate into an $IIZXI$ error on the logical qubit, which is a weight-2 error. This error will be misdiagnosed, leading to a logical error. b) By adding an extra flag ancilla, this circuit can measure the $XZZXI$ stabilizer in a fault-tolerant way; any single fault that can spread into weight two errors will trigger the flag. Furthermore, such errors will be distinguishable by their syndromes and can be fixed [38].

processing.

6.2. THE SMALLEST KNOWN FAULT-TOLERANT QEC CODE

The [5,1,3] code is the smallest distance-3 error correction code (i.e., it can correct arbitrary single qubit errors) [39, 40]. The code is a perfect code, saturating the quantum Hamming bound: it encodes 1 logical qubit with the minimal number of physical qubits. This code is defined by 4 independent stabilizers $s_1 = XZZXI, s_2 = IXZZX, s_3 = XIXZZ, s_4 = ZXIXZ$, which have a cyclic structure, and the logical operators are $X_L = XXXXX$, $Z_L = ZZZZZ$. The ability of this code to correct arbitrary single qubit errors, however, relies on the assumption of perfect error-syndrome extraction. The traditional extraction scheme of the error syndrome, such as the one shown in Fig. 6.1a, is non-fault tolerant [38]; errors on the the ancilla can propagate to weight-2 errors and could lead to logical errors. For example, an IZ error on the second gate in Fig. 6.1a leads to an $IIZXI$ error on the logical qubit, which is a weight-2 error. This error will be misdiagnosed leading to a logical error [38].

There are some extensions of the error extraction schemes which can make this code fault tolerant. For example, "Shor-like" syndrome extraction which requires 4 extra ancilla qubits (10 qubits in total) [34]. Another fault-tolerant extension scheme for the [[5,1,3]] code was proposed by Yoder and Kim [41], and it uses 8 qubits in total. Recently, Chao and Reichardt [38] proposed a simpler scheme which uses only one extra ancilla qubit (flag) to make the code fault-tolerant (7 qubits in total). Figure 6.1 demonstrates the basic idea of the flag-fault tolerance for the [[5,1,3]] code [38]. By adding the flag qubit as shown in Fig. 6.1b, single faults that could lead to correlated errors can be detected and corrected [38].

6.3. FAULT-TOLERANT LOGICAL-STATE ENCODING

The first step for fault-tolerant quantum error correction is the fault-tolerant encoding of the logical states. For distance-3 codes (such as the [[5,1,3]] code used here), fault-tolerant encoding means that a single fault during the preparation circuit leads to the desired logical state plus at most a single-qubit error on output [42]. A fault constitutes the insertion of any Pauli error at a location in the preparation circuit where locations can be a qubit idling step, a qubit measurement, a qubit preparation, or a single or two-qubit gate. In case the location is a two-qubit gate, a single fault is the insertion of any of the 15 Pauli errors after the action of the gate.

One can formulate nondeterministic fault-tolerant state preparation circuits for the [[5,1,3]] code, for example using flag qubits [38]. The circuits previously proposed make heavy use of two-qubit gates between data qubits, which are not native for our system [**?**]. A deterministic fault-tolerant state preparation can be achieved by following a non-fault tolerant state preparation circuit up with several rounds of flag error corrections [42], but the number of parity check measurements is considerable. Here, instead, we present a simpler preparation scheme that uses two extra stabilizer measurements and a flag check to herald the successful fault-tolerant encoding.

Here, we consider the fault-tolerant preparation of the logical state $|-\rangle_L = \frac{1}{\sqrt{2}}(|0\rangle_L - |1\rangle_L)$, but similar circuits can be constructed for the other 5 eigenstates of the logical Pauli operators. The logical state $|-\rangle_L$ is the unique +1 eigenstate of 5 independent weight-3 operators $(p_1, p_2,\ p_3, p_4, p_5)$ given in Table 6.1. This can be understood as $p_1 = -X_L \cdot s_1 \cdot s_2$, and due to the cyclic structure of the code, one can obtain the other 4 operators by performing cyclic permutations on the qubits.

$s_1 = XZZXI$	$p_1 = IZXZI$
$s_2 = IXZZX$	$p_2 = ZIIZX$
$s_3 = XIXZZ$	$p_3 = XZIIZ$
$s_4 = ZXIXZ$	$p_4 = ZXZII$
$X_L = XXXXX$	$p_5 = IIZXZ$

Table 6.1: Measuring p_1 to p_5 is logically equivalent to measure the four stabilizers s_1 to s_4 and the weight-5 logical operator X_L. However, due to the noisy gates, measuring the weight-3 logical operators is preferred.

Measuring p_1 to p_5 and updating the Pauli frame according to the measurement outcomes can prepare $|-\rangle_L$ from an arbitrary density matrix non fault-tolerantly. Instead of starting from a mixed state, we can also start the scheme by initializing the data qubits into the state $|00+0+\rangle$, which is a simultaneous eigenstate of p_1 and p_2 with eigenvalue +1, and then measure p_3 to p_5 (Fig. 6.2a). We refer to this preparation scheme throughout the rest of this chapter as the non-fault-tolerant (NFT) scheme.

The previous scheme is not fault tolerant because some errors on the ancilla will propagate to weight-2 errors that cause a logical error in the encoded state. To design a fault-tolerant scheme that can capture such errors, we specially construct two extra parity checks, $T_1 = p_2 \cdot p_4 \cdot p_5 = IXIYY$ and $T_2 = p_1 \cdot p_3 \cdot p_5 = XIYYI$, in addition to a flag check to make the circuit fault tolerant (see Fig. 6.2). In the proposed scheme, fault-

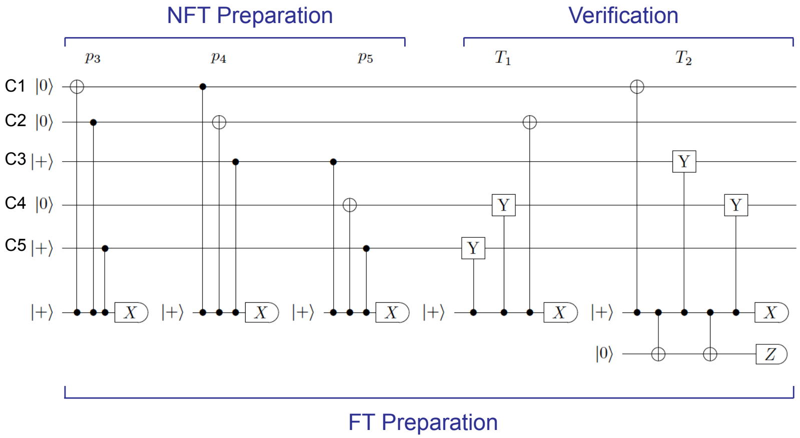

Figure 6.2: The proposed fault-tolerant encoding scheme. The circuit diagram of the the encoding scheme. The first part of the circuit prepares the logical state non-fault-tolerantly. First, the state $|00+0+\rangle$ (a simultaneous eigenstate of p_1, p_2 with eigenvalue +1) is prepared, followed by measuring the logical operators p_3 to p_5. In order to make the scheme fault tolerant, we add extra two stabilizer checks $T_1 = p_2 p_4 p_5$, $T_2 = p_1 p_3 p_5$ and the flag ancilla check. The scheme is fault-tolerant once the following heralding criteria are satisfied: (1) the measurement outcomes of T_1 and T_2 are compatible with the measurement outcomes m_i of the logical operators p_i, i.e. $m_{T_1} = m_2 \times m_4 \times m_5$ and $m_{T_2} = m_1 \times m_3 \times m_5$; (2) the flag is not raised. Otherwise the state is rejected and we start the preparation again. Note that instead of starting with the state $|00+0+\rangle$, the scheme can start from an arbitrary density matrix by measuring p_1 and p_2.

tolerant preparation is heralded by satisfying the following conditions: (1) the measurement outcomes of T_1 and T_2 are compatible with the measurement outcomes m_i of the logical operators p_i, i.e. $m_{T_1} = m_2 \times m_4 \times m_5$ and $m_{T_2} = m_1 \times m_3 \times m_5$; (2) the flag is not raised, i.e., measured to be in $|0\rangle$. Otherwise the state is rejected and we start the preparation again. See section 6.7.1 for a proof of the fault tolerance of this scheme. We refer to this preparation scheme throughout the rest of this chapter as the fault-tolerant (FT) scheme.

6.4. EXPERIMENTAL DEMONSTRATION OF THE ENCODING

In this section, we present the experimental implementation of the encoding scheme as well as the obtained experimental results (for both the fault-tolerant and non-fault-tolerant cases). The scheme requires one ancilla qubit, one flag ancilla qubit and 5 data qubits. We use the NV electron spin as the ancilla qubit, the nitrogen nuclear spin as the flag ancilla, and 5 ^{13}C nuclear-spin qubits as the data qubits. In order to implement the proposed logical state encoding in fig. 6.2, we first translate it into our native experimental gates (see section 6.7.3). To mitigate decoherence of the data qubits, we use multi-spin echoes which can increase the coherence times to several seconds (see chapter 5). Additionally, we ensures that the data qubits are decoupled from each other by using asynchronous echoes to mitigate the nuclear-nuclear coupling effects (see section 6.7.3).

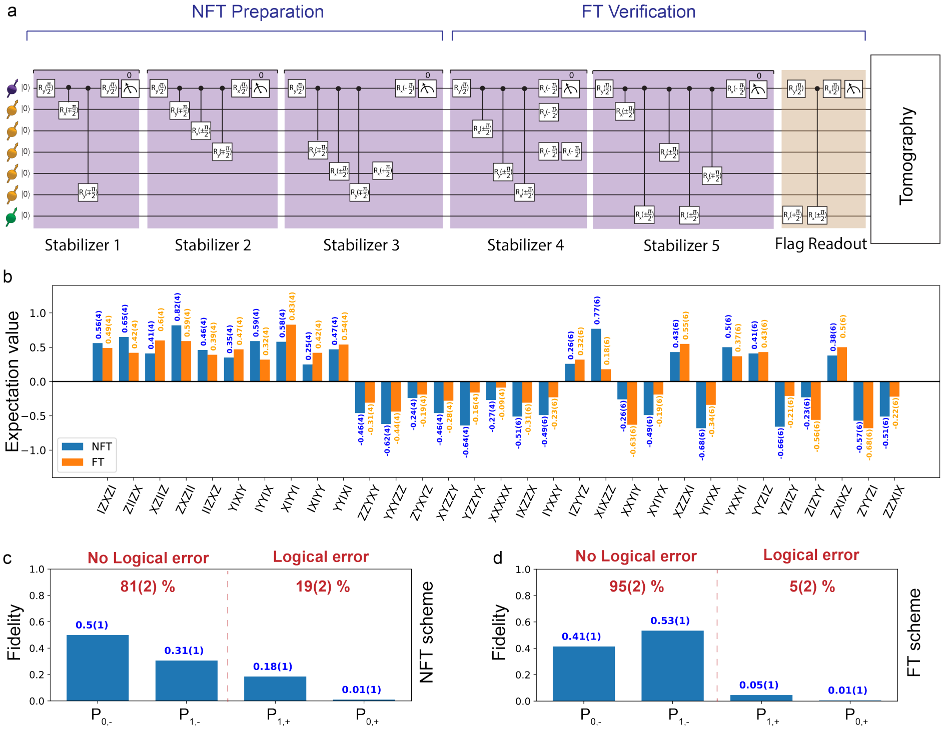

Figure 6.3: Experimental implementation of the encoding scheme and results. a) We convert the circuit diagram in Fig. 6.2 to our experimental gate scheme and compile the circuit to minimize the number of single qubit gates. We use the electron spin as the ancilla qubit as it is directly connected to the nuclear spin qubits. We use 5 ^{13}C nuclear spins as the (data) qubits and the nitrogen spin as the flag ancilla. The ^{13}C nuclear spins are first initialized into $|00000\rangle$ using five sequential swap initialization steps (see ch. 2 for details), and the nitrogen spin is initialized by measurement based initialization [6]. We use multi-spin echoes between the stabilizer measurements (see Fig. 6.5) on the nuclear spins to overcome the dephasing. Note that we run this scheme in a conditional form, we only continue upon measuring the electron spin to be in $m_s = 0$ state (corresponds to +1 eigenvalues of the stabilizers), which directly heralds the fault-tolerant preparation of the state. This way we reduce the measurement errors on the electron spin (ancilla qubit) [28, 43]. Note that this circuit prepares the target state up to single qubit rotations. These rotations are accounted for in the tomography step by updating the Pauli frame of the measured operators. b) Measured expectation values of the 31 multi-qubit operators that define the logical state for the NFT and FT cases. c,d) Combined overlap between the prepared state and the states with zero- and single-qubit Pauli errors with respect to logical $|-\rangle_L$ ($P_{0,-}, P_{1,-}$), and the combined overlap between the prepared state and the states with zero- and single-qubit Pauli errors with respect to logical $|+\rangle_L$ ($P_{0,+}, P_{1,+}$). The FT preparation scheme suppresses the probabilities to have logical errors (two- or three-qubit errors) while increasing the probabilities to have no logical errors (zero or single qubit errors), and therefore improving F_L.

We run both the NFT and FT encoding schemes in Fig. 6.5 and compare the obtained logical state fidelity F_L in both cases. This fidelity represents the probability to have at most a single qubit error in the encoded state (i.e., the overlap between the prepared state and the target state after applying a perfect round of error correction, see section 6.7.2 for details on F_L calculation). To this end, we measure the 31 operators that define the target logical state for both NFT and FT preparation schemes (Fig. 6.5b), and calculate the obtained F_L in both cases (see section 6.7.2). We find that the FT encoding scheme significantly outperforms the NFT one ($F_{L,FT} = 95(2)\%$, $F_{L,NFT} = 81(2)\%$).

To further assess this improvement, we calculate the overlap between the prepared state, ρ_{out}, and the states with zero or single qubit errors with respect to the target state $|-\rangle_L$ (i.e., there is no logical error), given by $P_{0,-}$ and $P_{1,-}$ respectively as

$$P_{0,-} = \mathrm{Tr}\big(|-\rangle_L \langle -|_L \cdot \rho_{out}\big), \tag{6.1}$$

$$P_{1,-} = \sum_{E\in\mathscr{E}} \mathrm{Tr}\big(E|-\rangle_L \langle -|_L E \cdot \rho_{out}\big), \tag{6.2}$$

where $E \in \mathscr{E} = \{X_i, Y_i, Z_i, \, i = 1, 2, \cdots 5\}$. We also calculate the overlap between the prepared state and the states with zero or single qubit errors with respect to the $|+\rangle_L$ (i.e., logical errors), given by $P_{0,+}$ and $P_{1,+}$ respectively as

$$P_{0,+} = \mathrm{Tr}\big(E|+\rangle_L \langle +|_L E \cdot \rho_{out}\big), \tag{6.3}$$

$$P_{1,+} = \sum_{E\in\mathscr{E}} \mathrm{Tr}\big(E|+\rangle_L \langle +|_L E \cdot \rho_{out}\big). \tag{6.4}$$

The combined overlaps between the prepared state and the two cases of logical- or no-logical-error are shown in Fig. 6.3b. From this figure, we note that the FT preparation scheme suppresses the probabilities to have two- or three-qubit errors (logical errors) while increasing the probabilities to have at most a single qubit error, and therefore significantly improving the logical state fidelity F_L.

6.5. FAULT-TOLERANT OPERATIONS ON THE LOGICAL-QUBIT

Here we experimentally demonstrate fault-tolerant manipulations of the encoded logical state by applying fault-tolerant logical gates. Such fault-tolerant gates are important building blocks for fault-tolerant quantum computations. Figure 6.4a shows the basic experimental sequence; after fault-tolerant encoding of the logical state (here $|-\rangle_L$), we apply transversal fault-tolerant logical gates and then perform a tomography of the final state, see Fig. 6.4a. Asynchronous echo sequences are applied between the encoding, logical gate, and tomography steps to mitigate decoherence of the nuclear spins. The logical X and Y gates are done in a transversal way as $X_L = X_1X_2X_3X_4X_5$ and $Y_L = Y_1Y_2Y_3Y_4Y_5$ [20, 44]. The logical Hadamard gate is done following Yoder et al. [44] by applying $H_L = P_\pi H_1H_2H_3H_4H_5$, where P_π is an appropriate permutation of the five data qubits. This permutation is done here by relabelling the qubits and not by applying SWAP gates, and therefore it is transversal (fault-tolerant) [44].

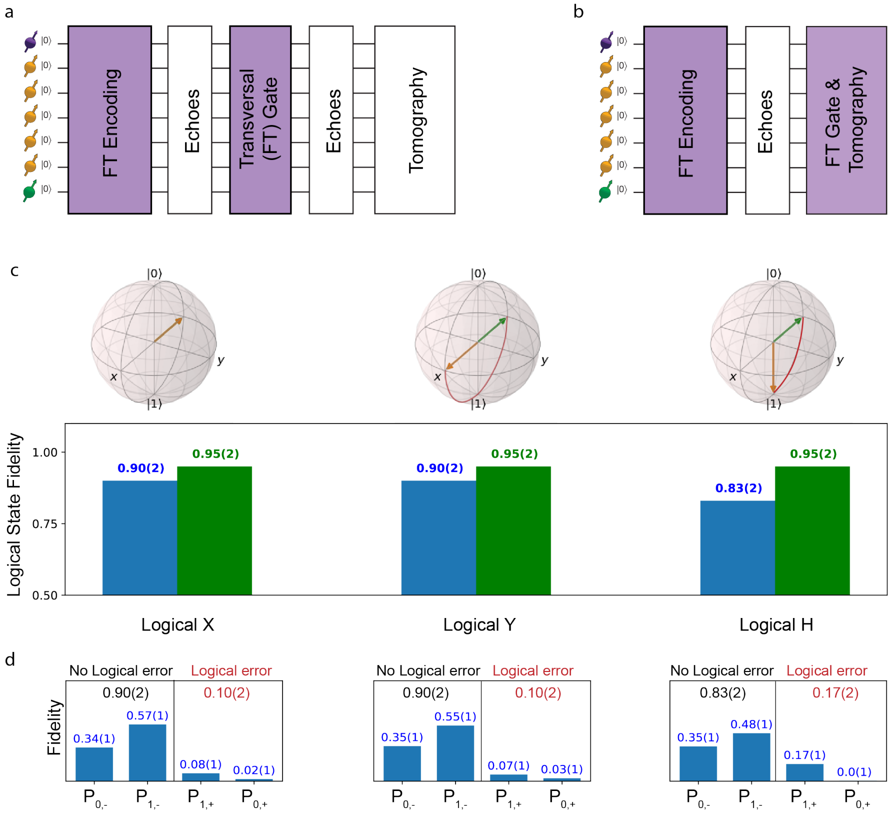

Figure 6.4: Fault-tolerant operations on a logically-encoded qubit. a) Scheme A: after fault-tolerant encoding of a logical state (here $|-\rangle_L$), we apply a transversal fault-tolerant logical gate and then perform a tomography of the final state. In this approach, the logical operations are done by applying five extra gate operations, surrounded by their own echo sequences. We choose to implement this approach as an explicit demonstration and a benchmark. b) Scheme B: an alternative (and generally better) approach is to combine the logical gate with the tomography step (Pauli-frame update). In this approach, the logical operations are still applied in real time, but due to the compilation, they do not come at an extra cost. c) Top: Bloch spheres showing the initial (green) and target (orange) states after applying the logical X, Y, and H gates. Bottom: obtained logical-state fidelities after applying the different logical gates. Blue: scheme A; Green: scheme B. d) Error distribution on the obtained states using the first scheme.

Figure 6.4c shows the obtained logical-state fidelities (with respect to the target state) after applying the logical gates, which demonstrates high-fidelity logical operations. We attribute the observed loss in fidelity to the extra echo stages which lead to an increased sequence time. This causes extra dephasing due to the nuclear-nuclear couplings between the data qubits. We take this into account in the design of our echo sequences by using asynchronous echo sequences to minimize these effects.

In the implementation discussed above, the gates are realized by separately applying an additional set of 5 pulses including extra echo sequences. We choose this approach to provide an explicit demonstration of applying fault-tolerant gates and to benchmark the operations. Clearly, this is not the optimal way to apply transversal logical gates. First, we note that there is a set of logical operators based on three-qubit operators (e.g. $X_L = IIZXZ$), instead of five qubit operators. Second, one would normally compile away such operations: one can simply track the basis changes (Pauli frame) and adapt the next operations accordingly (see Fig. 6.4b). As a reference, Fig. 6.4c also shows the results for such an optimal tracking of the Pauli frame approach, in which the extra transversal logical operations come at no cost, that no fidelity is lost. Finally, note that a $Z_L = ZZZZZ$ operation is trivially implemented as it is automatically compiled in the timing of subsequent gates.

6.6. CONCLUSION AND OUTLOOK

In conclusion, we have experimentally demonstrated fault-tolerant encoding of the smallest fault-tolerant logical qubit. Our results show that the proposed fault-tolerant encoding scheme reduces the probability of logical-qubit errors compared to the non-fault-tolerant scheme. Additionally, we have demonstrated the first fault-tolerant operations on a solid-state logical qubit of a complete error correction code by applying transversal gates. These demonstrations are key building blocks for fault-tolerant quantum computations. The final ingredient missing in the complete fault-tolerant operation of an error-corrected logical qubit is to perform the syndrome extraction in a fault-tolerant way. This requires a FT 4-qubit stabilizer measurement (see Fig. 6.1) and will be the subject of future experiments.

6.7. SUPPLEMENTARY INFORMATION

6.7.1. PROOF OF FAULT-TOLERANCE OF THE PROPOSED SCHEME

We show that a single fault in the circuit in Fig. 6.2 leads to the correct preparation of $|-\rangle_L$ plus at most a single-qubit error, assuming that the conditions for accepting the state are fulfilled. We also note that the modification of this preparation scheme with the additional single-qubit gates (for echoing and/or different gate decompositions) does not change the fault-tolerance argument. In the experimental realization we condition on the preparation runs which give $m_3 = +1, m_4 = +1, m_5 = +1$ since these measurement outcomes are more reliable. Such heralding does not affect the fault-tolerance arguments from section. From now on, we denote controlled-NOT and controlled-Y gates as CX and CY here.

First, it should be noted that for this 5-qubit code any state $|-\rangle_L$ with more than 1 Pauli error is equivalent to either a $|+\rangle_L$ with at most 1 Pauli error or a $|-\rangle_L$ state with at most 1 Pauli error. This is due to the code being perfect: the states $|\pm\rangle_L$ plus any single-qubit error are all orthogonal and there are $2 \times (1+15) = 2^5 = 32$ such states, spanning the full code space. Hence we just need to prove that the circuit does not lead to the state $|+\rangle_L$ with at most 1 Pauli error. For this it is useful to tabulate all weight-3 incarnations of the logical Z_L and logical Y_L as these can bring $|-\rangle_L$ to $|+\rangle_L$, see Table 6.2.

$Z_L \equiv$	$Z_1 Z_2 Z_3 Z_4 Z_5$	$Y_3 Z_4 Y_5$ (cyclic perm.)	$X_2 X_3 Z_5$ (cyclic perm.)
$Y_L \equiv$	$Y_1 Y_2 Y_3 Y_4 Y_5$	$Z_2 Z_3 Y_5$ (cyclic perm.)	$X_1 X_4 Y_5$ (cyclic perm.)
$X_L \equiv$	$X_1 X_2 X_3 X_4 X_5$	$X_2 Y_4 Y_5$ (cyclic perm.)	$Z_1 Z_4 X_5$ (cyclic perm.)

Table 6.2: All weight-3 incarnations of the logical operators. Any cyclic permutation of the logical operator is an equivalent logical operator.

We can assume that the fault appears either in the preparation circuit and the verification circuit is fault-free or vice versa. So we consider these cases separately as follows.

Case A: if the only fault occurs in the verification circuit

Since the only fault occurs in the verification circuit, the preparation circuit prepares the state $|-\rangle_L$ with no errors (assuming noiseless Pauli frame corrections). We prove that the circuit is fault-tolerant through different cases:

- Single-qubit faults on data qubits (in idling or after gates) during the verification. These have the effect of either leading to a single-qubit error on output, or leading to measurement of T_1 or/and T_2 which does not satisfy the consistency check, in which case the state is not accepted.

- A single measurement fault in measurement of T_1 or T_2 or the flag ancilla measurement leads to the state not being accepted.

- A two-qubit fault after one of the two-qubit gates in T_1. If the action of this fault on this ancilla is Z or Y, then it flips the ancilla and the state is not accepted. Hence assume the action on the ancilla qubit is X. If this error PX (where P is some Pauli I, X, Y, Z) occurs after the first CY, it leads to outgoing error $X_2 Y_4 P_5$ which is equivalent to $Y_5 P_5 X_L$, see Table 6.2, hence a single-qubit outgoing error. If PX occurs after the second CY it leads to outgoing error $X_2 P_4$. $X_2 Y_4$ is equivalent to $Y_5 X_L$, see Table 6.2. $X_2 X_4$ and $X_2 Z_4$ lead to the T_2 outcome being flipped, so no acceptance. $P = I$ corresponds to a single-qubit error. If PX occurs after the (last) CX it leads to a single-qubit outgoing error P.

- a two-qubit fault after one of the two-qubit gates in T_2. If the action of this fault on the ancilla qubit is Z or Y, then it flips the ancilla qubit and the state is not accepted. Hence assume that the action on the ancilla qubit is X.

  Consider first the two qubit gates between ancilla and data qubits. If the fault PX occurs after the CX, then it does not flip the flag qubit, and leads to outgoing error $P_1 Y_3 Y_4$ which is equivalent to $X_1 P_1 X_L$ (Table 6.2), hence inducing a single-qubit error. If the fault PX occurs after the first CY it flips the flag qubit and the state is not accepted. If the fault PX occurs after the second CY, it leads to a single qubit error P_4.

Now consider the CX between ancilla and flag ancilla. If the action of the fault is X or Y on the flag ancilla the state is not accepted, hence assume that the action on the flag ancilla qubit is Z. The fault XZ after the first CX will lead to the state not being accepted. The fault XZ after the second CX will lead to an outgoing Y_4 error.

	p_1	p_2	p_3	p_4	p_5	$T_1 = p_2p_4p_5$	$T_2 = p_1p_3p_5$
Y_1		F	F	F			F
X_1		F		F			
Z_1			F				F
Y_2	F		F	F		F	
X_2	F		F				
Z_2				F		F	
Y_3	F			F	F		
X_3				F	F		F
Z_3	F						F
Y_4	F	F			F		
X_4	F	F				F	F
Z_4					F	F	F
Y_5		F	F		F		
X_5			F		F	F	
Z_5		F				F	

Table 6.3: Effect of single qubit errors. F denotes that the eigenvalue is flipped upon application of the error. The errors highlighted in red flip both verification checks.

Case B: if the only fault occurs in the preparation circuit

Now if the fault in the non-fault-tolerant preparation circuit leads to the output $|-\rangle_L$ plus at most a single-qubit error, then, since the verification circuit is perfect, the final output has at most 1 error. Also, we note that any fault in the preparation circuit leads to a $|-\rangle_L$ state with at most 2 Pauli errors and such state can be viewed as a logical $|+\rangle_L$ plus at most a single-qubit error.

We thus need argue what outputs $|+\rangle$ with at most any single-qubit error are caught by the verification circuit. For the output states which are not caught we need to argue that they cannot occur due to a single fault in the preparation circuit.

Note that the output $|+\rangle_L$ is a -1 eigenstate of $p_1, \ldots, p_5$. Clearly the state $|+\rangle_L$ would be caught in the verification test as the product of any three p_is is -1 while it should be $+1$ (assuming Pauli frame corrections). Now we examine what possible single-qubit errors on $|+\rangle_L$ which would lead to passing the verification test which requires both eigenvalues of T_1 and T_2 to be flipped. We can see that these are the errors X_4 and Z_4 on top of $|+\rangle_L$ in Table 6.3.

One can fully characterize these possible bad states $X_4\,|+\rangle_L$ and $Z_4\,|+\rangle_L$ by their syndromes $M_i = \pm 1$, that is, the syndromes of $p_1, \ldots, p_5$ if we were to perfectly measure these checks on these output states. These output syndromes (denoted by capital letters) are as follows

$$X_4\left|\overline{+}\right\rangle: M_3 = M_4 = M_5 = -1, \qquad M_1 = M_2 = +1, \tag{6.5}$$

$$Z_4\left|\overline{+}\right\rangle: M_1 = M_2 = M_3 = M_4 = -1, \qquad M_5 = +1 \tag{6.6}$$

Now we argue that no single fault in the preparation circuit can lead to a state with such output syndromes M_i by looking at various subcases:

1) If the only fault occurs before measuring p_4 and p_5. Then the Pauli corrections in the preparation circuit correctly fix these eigenvalues to be $M_4 = M_5 = +1$ on output, so both syndromes in Eq. (6.5) and Eq. (6.6) are excluded.

2) If the only fault occurs in measuring p_4. Similarly, M_5 is fixed to be $+1$ due to correct Pauli corrections, so that the syndrome in Eq. (6.5) is not possible. Then for the syndrome in Eq. (6.6) we argue as follows:

- A single fault in p_4 can only induce 2-qubit errors on the data qubits C2 and C3. These commute with $p_2 = ZIIZX$, hence M_2 is fixed to be $+1$. The syndrome in Eq. (6.6) is therefore not possible.
- Other single faults can only induce single-qubit errors on the data qubits, and a single-qubit error cannot anti-commute with $p_1 = IZXZI$, $p_2 = ZIIZX$ and $p_3 = XZIIZ$ at the same time, i.e. M_1, M_2 and M_3 cannot be -1 at the same time. The syndrome in Eq. (6.6) is not possible.

3) If the only fault occurs in measuring p_5.

- A single fault can only induce 2-qubit errors Z_4Z_5 and Y_4Z_5 (X_4Z_5 is equivalent to the single-qubit error Z_3), all commute with $p_3 = XZIIZ$ and $p_4 = ZXZII$, i.e. M_3 and M_4 are fixed to be $+1$. The syndromes in Eq. (6.5) and Eq. (6.6) are thus not possible.
- If the fault occurs on an idling location of the data qubits C1 or C2, the induced single-qubit errors commute with $p_5 = IIZXZ$ and the measurement of p_5 is correct, i.e. the syndromes in Eq. (6.5) are not possible since $M_5 = +1$. Because any single-qubit error on C1 or C2 cannot anti-commute with $p_1 = IZXZI$, $p_2 = ZIIZX$, $p_3 = XZIIZ$ and $p_4 = ZXZII$ at the same time, the syndrome in Eq. (6.6) is also excluded.
- Other single faults can only induce a single-qubit error on the data qubits C3, C4 or C5, which cannot anti-commute with $p_3 = XZIIZ$ and $p_4 = ZXZII$ at the same time, i.e. the syndromes in Eq. (6.5) and Eq. (6.6) are not possible.

6.7.2. CHARACTERIZATION OF THE PREPARED STATES

As discussed earlier, the logical state fidelity F_L is defined as the overlap between the prepared state after assuming a perfect round of error correction and the target state. This basically represents the probability to have at most a single qubit error in the prepared state. We would like to verify that this logical state fidelity can be increased by using the proposed fault-tolerant preparation scheme.

Noiseless measurements of p_1 to p_5 project an arbitrary state into the state $E|-\rangle_L$ with E some Pauli error, which can be described by a projector:

$$E|-\rangle_L\langle-|_L E = \prod_{i=1}^{5}\left(\frac{1+m_i\cdot p_i}{2}\right)$$

where $m_i = \pm 1$ is the measurement outcome of p_i, and $m_i = -1$ when E anti-commutes with p_i. Writing $\mathscr{E}$ as the set of all single qubit Pauli errors, i.e. $\mathscr{E} = \{I, X_i, Y_i, Z_i, i = 1, 2, \cdots 5\}$, the logical state fidelity F_L can be calculated as

$$\begin{aligned}
F_L &= \sum_{E\in\mathscr{E}} \mathrm{Tr}\big(E|-\rangle_L\langle-|_L E\cdot\rho_{out}\big)\\
&= \frac{1}{2}+\frac{1}{8}(<p_1>+<p_2>+<p_3>+<p_4>+<p_5>\\
&\qquad +<p_1p_2p_3>+<p_1p_2p_4>+<p_1p_3p_5>+<p_2p_4p_5>\\
&\qquad +<p_3p_4p_5>-<p_1p_2p_5>-<p_1p_3p_4>-<p_1p_4p_5>\\
&\qquad -<p_2p_3p_4>-<p_2p_3p_5>-<p_1p_2p_3p_4p_5>)\\
&= \frac{1}{2}+\frac{1}{8}(<IZXZI>+<ZIIZX>+<XZIIZ>+<ZXZII>\\
&\quad +<IIZXZ>+<YIXIY>+<IYYIX>+<XIYYI>\\
&\quad +<IXIYY>+<YYIXI>+<ZZYXY>+<YXYZZ>\\
&\quad +<ZYXYZ>+<XYZZY>+<YZZYX>+<XXXXX>),
\end{aligned} \tag{6.7}$$

where $<p>= \mathrm{Tr}\big(p\cdot\rho_{out}\big)$ is the expectation value of the operator p, and ρ_{out} is the output density matrix of the full preparation circuit in Fig 6.2.

6.7.3. EXPERIMENTAL IMPLEMENTATION OF THE FAULT-TOLERANT SCHEME

In this section we explain in more detail how to implement the proposed encoding scheme using our physical platform. The scheme requires one ancilla qubit, one flag ancilla qubit and five data qubits. We use the NV electron spin as the ancilla qubit, the ^{14}N nuclear spin as the flag ancilla, and five ^{13}C nuclear spins as the data qubits. The NV electron spin serves well as the ancilla qubit as it can be (non-destructively) read out by optical means and it can be used to directly implement two qubit gates with all of the ^{13}C nuclear-spin qubits as well as the ^{14}N nuclear-spin flag qubit.

In order to implement the proposed logical state encoding in fig. 6.2, we first translate it into our native experimental gates. As discussed in chapter 2, directly applying our gate scheme (i.e. $R_x(\pm\pi/2)$, $R_y(\pm\pi/2)$) leads to an extra basis rotation for the nuclear spins and we have to take this into account. Here, we replace each controlled-gate (CX, CY, CZ) by its equivalent implementation in our gate scheme (see chapter 2) and afterwards compile the circuit to reduce the total number of single-qubit gates. The obtained circuit diagram is shown in Figure 6.5.

Afterwards, we numerically simulate the entire sequence using both the equivalent circuit model (shown in Fig. 6.5) as well as the underlying pulse sequence used in the experiments. Due to the high complexity of the experimental sequence used for the logical state encoding, these simulations are important to verify and optimize the sequence performance (see section 6.7.4 for details).

Another important issue to address here is how to mitigate decoherence of the data qubits. The encoding circuit involves > 30 two-qubit gates (including those required for the initialization and readout of the data qubits); the typical gate time is 0.5 to 1 ms. This makes the total sequence time much longer than the dephasing time of the individual nuclear spins ($T_2^* = 5 - 15$ ms for the carbon spins used here, see ch. 5). An effective way to overcome this dephasing is to use multi-spin echoes, similarly to our previous experiments, which can increase the coherence times to several seconds (see ch. 5). The designed echo sequence should minimize the idle waiting time during which the electron spin is in a superposition state. We found that using two echo stages provides a general solution such that the nuclear spins can refocus at the required points (see the online supplementary material of ref. [6] for details).

An additional challenge here is that the nuclear spins used as the data qubits are also coupled to each other. As the total sequence time is comparable to the nuclear-nuclear coupling strengths [45], we have to account for these effects. From the measured coupling strengths (presented in chapter 4), we find that the most relevant coupling strengths are those between C3, C2 and C3, C5 (8.45(2) Hz and 6.48(2) Hz respectively). An intuitively promising approach to overcome is to use asynchronous echo sequences, i.e. we do not echo all the spins simultaneously. For example, by applying a single echo pulse on C3, it is also decoupled from the other 4 qubits where 2 echo pulses are applied (see Fig. 6.5 for illustration). We simulate the entire encoding scheme including the asynchronous echo sequence and compare the performance to the case with synchronous echoes (see Fig. 6.6). We find that the asynchronous sequence significantly outperforms the synchronous one, and that its performance is close to the case where all the nuclear-nuclear couplings are set to zero in the simulations.

6.7.4. SIMULATIONS OF THE EXPERIMENTAL SEQUENCE

Due to the high complexity of the experimental sequence used for the logical state encoding, it is important to simulate the entire sequence with a realistic system Hamiltonian to verify and optimize the performance.

In chapter 4, we have already demonstrated the characterization and atomic-scale imaging of our quantum system and its spin environment with high accuracy. In short, we have measured the relevant coupling parameters between the electron spins and the closest 27 carbon-13 atoms in the vicinity. In addition, we have measured the nuclear-nuclear coupling between these spins in the environment and resolved their 3D structure, which already gives a compact way to describe the system Hamiltonian. Therefore, this could—in principle—enable us to simulate our system with great accuracy. However, due to the computational requirements to simulate such a large quantum system,

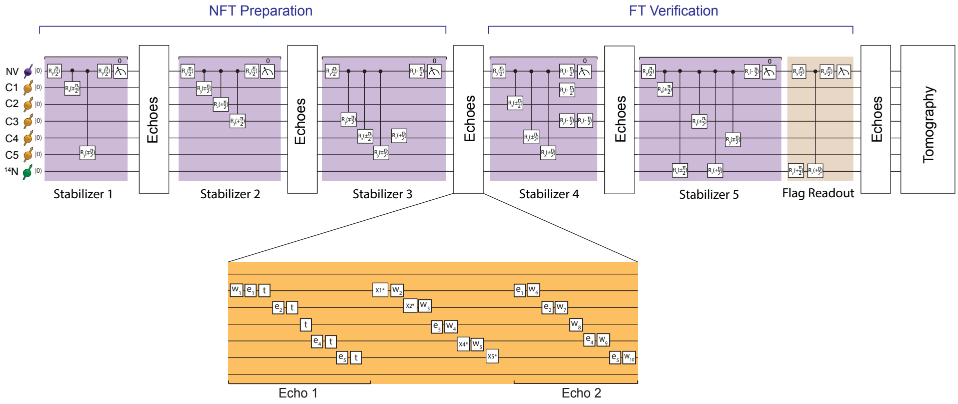

Figure 6.5: Experimental implementation of the logical state encoding scheme. The circuit diagram in Fig. 6.2 is converted to our experimental gate scheme and then compiled to minimize the number of single qubit gates. The electron spin is used as the ancilla qubit as it is directly connected to the nuclear spin qubits. The nitrogen spin is used as the flag ancilla and 5 carbon spins are used as the data qubits. The ^{13}C nuclear spins are first initialized into |00000⟩ using five sequential swap initialization steps (see Ch. 2 for details), and the nitrogen spin is initialized by measurement based initialization [6]. Note that we run this scheme in a conditional form, we only continue upon measuring the electron spin to be in $m_s = 0$ state (corresponds to +1 eigenvalues of the stabilizers), which directly heralds the fault tolerance preparation of the state. This way we reduce the measurement errors on the electron spin (ancilla qubit) [28, 43]. We apply multi-spin echoes on the nuclear spins (between the stabilizer measurements) to mitigate the nuclear-spins decoherence. The echo sequences are applied in asynchronous form: for qubit 3 only a single echo pulse is applied, so that it is also decoupled from the other 4 qubits (2 echo pulses). This simultaneously enhance the nuclear spin coherence time and avoid effects of nuclear-nuclear interactions between the spins involved in the circuit (see section 6.7.4 and Fig. 6.7.4). Boxes boxes $e_1, e_2, ..., e_5$ correspond to spin echo pulses on those spins, with unique lengths calibrated to maximize the pulse fidelity. Boxes $X_1^*, .., X_5^*$ are the rephasing points for the first echo stage, and at these points single-qubit rotations can be applied (in case of a required basis transformation). Boxes $W_1, W_2, ..., W_1 0$ and t are unique waiting duration times derived from a set of simultaneous equations similar to those presented in Ch. 5.

we only consider here the 7 spins involved in the encoding scheme. Consequently, these simulations do not take into account decoherence effects due to the rest of the spin environment.

Fig. 6.6 shows the obtained numerical simulations of the circuit (shown in Fig. 6.5) by applying the underlying pulse sequences and considering the system Hamiltonian as described above. Next, we include the nuclear-nuclear couplings in the simulations and study the performance of the sequence under different echo schemes. Fig. 6.6 shows a clear advantage of using the asynchronous echo sequence to mitigate nuclear-nuclear coupling effects.

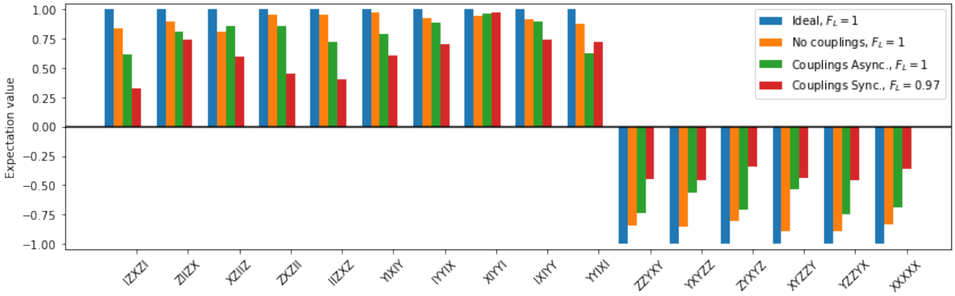

Figure 6.6: Numerical simulations of the underlying pulse sequence of the encoding circuit. Shown are the expectation values of the multi-qubit operators used to calculate F_L as described earlier. Blue bars are the outcomes of the ideal circuit (used here for comparison). No couplings: the nuclear-nuclear couplings are set to zero in the simulations. Couplings Async. (Couplings Sync.): simulations taking into account the nuclear-nuclear couplings and applying the asynchronous (synchronous) echo sequences. These simulations show a clear advantage of using the asynchronous echo sequence to overcome the nuclear-nuclear couplings effects.

REFERENCES

[1] D. D. Awschalom, R. Hanson, J. Wrachtrup, and B. B. Zhou, *Quantum technologies with optically interfaced solid-state spins,* Nat. Photonics **12**, 516 (2018).

[2] M. H. Abobeih, J. Cramer, M. A. Bakker, N. Kalb, M. Markham, D. Twitchen, and T. H. Taminiau, *One-second coherence for a single electron spin coupled to a multi-qubit nuclear-spin environment,* Nat. commun. **9**, 2552 (2018).

[3] N. Bar-Gill, L. M. Pham, A. Jarmola, D. Budker, and R. L. Walsworth, *Solid-state electronic spin coherence time approaching one second,* Nat. Commun. **4**, 1743 (2013).

[4] J. T. Muhonen, J. P. Dehollain, A. Laucht, F. E. Hudson, R. Kalra, T. Sekiguchi, K. M. Itoh, D. N. Jamieson, J. C. McCallum, A. S. Dzurak, and A. Morello, *Storing quantum information for 30 seconds in a nanoelectronic device,* Nat. Nanotech. **9**, 986 (2014).

[5] P. C. Maurer, G. Kucsko, C. Latta, L. Jiang, N. Y. Yao, S. D. Bennett, F. Pastawski, D. Hunger, N. Chisholm, Markham, *et al.*, *Room-Temperature Quantum Bit Memory Exceeding One Second,* Science **336**, 1283 (2012).

[6] C. E. Bradley, J. Randall, M. H. Abobeih, R. C. Berrevoets, M. J. Degen, M. A. Bakker, M. Markham, D. J. Twitchen, and T. H. Taminiau, *A ten-qubit solid-state spin register with quantum memory up to one minute,* Phys. Rev. X **9**, 031045 (2019).

[7] L. Robledo, L. Childress, H. Bernien, B. Hensen, P. F. A. Alkemade, and R. Hanson, *High-fidelity projective read-out of a solid-state spin quantum register,* Nature **477**, 574 (2011).

[8] N. H. Wan, T.-J. Lu, K. C. Chen, M. P. Walsh, M. E. Trusheim, L. De Santis, E. A. Bersin, I. B. Harris, S. L. Mouradian, I. R. Christen, *et al.*, *Large-scale integration of artificial atoms in hybrid photonic circuits,* Nature **583**, 226 (2020).

[9] L. Vandersypen, H. Bluhm, J. Clarke, A. Dzurak, R. Ishihara, A. Morello, D. Reilly, L. Schreiber, and M. Veldhorst, *Interfacing spin qubits in quantum dots and donors—hot, dense, and coherent,* npj Quantum Inf. **3**, 1 (2017).

[10] L. Petit, H. Eenink, M. Russ, W. Lawrie, N. Hendrickx, S. Philips, J. Clarke, L. Vandersypen, and M. Veldhorst, *Universal quantum logic in hot silicon qubits,* Nature **580**, 355 (2020).

[11] J. Preskill, *Reliable quantum computers,* Proc. R. Soc. A **454**, 385 (1998).

[12] N. H. Nickerson, Y. Li, and S. C. Benjamin, *Topological quantum computing with a very noisy network and local error rates approaching one percent,* Nat. Commun. **4**, 1756 (2013).

[13] N. H. Nickerson, J. F. Fitzsimons, and S. C. Benjamin, *Freely Scalable Quantum Technologies Using Cells of 5-to-50 Qubits with Very Lossy and Noisy Photonic Links,* Physical Review X **4**, 041041 (2014).

[14] P. W. Shor, *Fault-tolerant quantum computation,* Proceedings of the 37th IEEE Symposium on foundations of computer science (1996).

[15] M. Nielsen and I. L. Chuang, *Quantum computation and quantum information* (Cambridge University Press, Cambridge, 2000).

[16] D. Gottesman, *An Introduction to Quantum Error Correction and Fault-Tolerant Quantum Computation,* arXiv:0904.2557 [quant-ph] (2009).

[17] B. M. Terhal, *Quantum Error Correction for Quantum Memories,* Rev. Mod. Phys. **87**, 307 (2015).

[18] D. Gottesman, *A Theory of Fault-Tolerant Quantum Computation,* Phys. Rev. A **57**, 127 (1998).

[19] S. J. Devitt, W. J. Munro, and K. Nemoto, *Quantum error correction for beginners,* Rep. Prog. Phys. **76**, 076001 (2013).

[20] D. Gottesman, *Stabilizer Codes and Quantum Error Correction,* arXiv:quant-ph/9705052 (1997).

[21] P. Aliferis, D. Gottesman, and J. Preskill, *Quantum accuracy threshold for concatenated distance-3 codes,* arXiv preprint quant-ph/0504218 (2005).

[22] J. Kelly, R. Barends, A. G. Fowler, A. Megrant, E. Jeffrey, T. C. White, D. Sank, J. Y. Mutus, B. Campbell, Chen, *et al.*, *State preservation by repetitive error detection in a superconducting quantum circuit,* Nature **519**, 66 (2015).

[23] P. Campagne-Ibarcq, A. Eickbusch, S. Touzard, E. Zalys-Geller, N. Frattini, V. Sivak, P. Reinhold, S. Puri, S. Shankar, R. Schoelkopf, *et al.*, *Quantum error correction of a qubit encoded in grid states of an oscillator,* Nature **584**, 368 (2020).

[24] A. Grimm, N. Frattini, S. Puri, S. Mundhada, S. Touzard, M. Mirrahimi, S. Girvin, S. Shankar, and M. Devoret, *Stabilization and operation of a kerr-cat qubit,* Nature **584**, 205 (2020).

[25] D. Nigg, M. Müller, E. A. Martinez, P. Schindler, M. Hennrich, T. Monz, M. A. Martin-Delgado, and R. Blatt, *Quantum computations on a topologically encoded qubit,* Science , 1253742 (2014).

[26] L. Egan, D. M. Debroy, C. Noel, A. Risinger, D. Zhu, D. Biswas, M. Newman, M. Li, K. R. Brown, M. Cetina, *et al.*, *Fault-tolerant operation of a quantum error-correction code,* arXiv:2009.11482 (2020).

[27] G. Waldherr, Y. Wang, S. Zaiser, M. Jamali, T. Schulte-Herbrueggen, H. Abe, T. Ohshima, J. Isoya, P. Neumann, and J. Wrachtrup, *Quantum error correction in a solid-state hybrid spin register,* Nature **506**, 204 (2014).

[28] J. Cramer, N. Kalb, M. A. Rol, B. Hensen, M. S. Blok, M. Markham, D. J. Twitchen, R. Hanson, and T. H. Taminiau, *Repeated quantum error correction on a continuously encoded qubit by real-time feedback,* Nat. Commun. **7**, 11526 (2016).

[29] A. D. Córcoles, E. Magesan, S. J. Srinivasan, A. W. Cross, M. Steffen, J. M. Gambetta, and J. M. Chow, *Demonstration of a quantum error detection code using a square lattice of four superconducting qubits,* Nat. Commun. **6**, 6979 (2015).

[30] D. Ristè, S. Poletto, M.-Z. Huang, A. Bruno, V. Vesterinen, O.-P. Saira, and L. DiCarlo, *Detecting bit-flip errors in a logical qubit using stabilizer measurements,* Nat. Commun. **6** (2015), 10.1038/ncomms7983.

[31] N. M. Linke, M. Gutierrez, K. A. Landsman, C. Figgatt, S. Debnath, K. R. Brown, and C. Monroe, *Fault-tolerant quantum error detection,* Sci. Adv. **3**, e1701074 (2017).

[32] C. K. Andersen, A. Remm, S. Lazar, S. Krinner, N. Lacroix, G. J. Norris, M. Gabureac, C. Eichler, and A. Wallraff, *Repeated quantum error detection in a surface code,* Nat. Phys. , 1 (2020).

[33] T. H. Taminiau, J. Cramer, T. v. d. Sar, V. V. Dobrovitski, and R. Hanson, *Universal control and error correction in multi-qubit spin registers in diamond,* Nat. Nanotech. **9**, 171 (2014).

[34] D. P. DiVincenzo and P. Aliferis, *Effective Fault-Tolerant Quantum Computation with Slow Measurements,* Phys. Rev. Lett. **98**, 020501 (2007).

[35] V. Negnevitsky, M. Marinelli, K. K. Mehta, H.-Y. Lo, C. Flühmann, and J. P. Home, *Repeated multi-qubit readout and feedback with a mixed-species trapped-ion register,* Nature **563**, 527 (2018).

[36] C. Bultink, T. O'Brien, R. Vollmer, N. Muthusubramanian, M. Beekman, M. Rol, X. Fu, B. Tarasinski, V. Ostroukh, B. Varbanov, *et al., Protecting quantum entanglement from leakage and qubit errors via repetitive parity measurements,* Science advances **6**, eaay3050 (2020).

[37] C. K. Andersen, A. Remm, S. Lazar, S. Krinner, J. Heinsoo, J.-C. Besse, M. Gabureac, A. Wallraff, and C. Eichler, *Entanglement stabilization using ancilla-based parity detection and real-time feedback in superconducting circuits,* npj Quant. Inf. **5**, 1 (2019).

[38] R. Chao and B. W. Reichardt, *Quantum error correction with only two extra qubits,* Phys. Rev. Lett. **121**, 050502 (2018).

[39] R. Laflamme, C. Miquel, J. P. Paz, and W. H. Zurek, *Perfect Quantum Error Correcting Code,* Phys. Rev. Lett. **77**, 198 (1996).

[40] E. Knill, R. Laflamme, R. Martinez, and C. Negrevergne, *Benchmarking Quantum Computers: The Five-Qubit Error Correcting Code,* Phys. Rev. Lett. **86**, 5811 (2001).

[41] T. J. Yoder and I. H. Kim, *The surface code with a twist,* Quantum **1**, 2 (2017).

[42] C. Chamberland and M. E. Beverland, *Flag fault-tolerant error correction with arbitrary distance codes,* Quantum **2**, 53 (2018).

[43] S. B. van Dam, J. Cramer, T. H. Taminiau, and R. Hanson, *Multipartite entanglement generation and contextuality tests using nondestructive three-qubit parity measurements,* Phys. Rev. Lett. **123**, 050401 (2019).

[44] T. J. Yoder, R. Takagi, and I. L. Chuang, *Universal fault-tolerant gates on concatenated stabilizer codes,* Phys. Rev. X **6**, 031039 (2016).

[45] M. H. Abobeih, J. Randall, C. E. Bradley, H. P. Bartling, M. A. Bakker, M. J. Degen, M. Markham, D. J. Twitchen, and T. H. Taminiau, *Atomic-scale imaging of a 27-nuclear-spin cluster using a quantum sensor,* Nature **576**, 411 (2019).

7

ENTANGLEMENT OF INTRINSICALLY COHERENCE-PROTECTED SPIN PAIRS

H. P. Bartling, M. H. Abobeih, B. Pingault, M. J. Degen, S. J. H. Loenen, C. E. Bradley, J. Randall, M. Markham, D. J. Twitchen, T. H. Taminiau

Understanding and protecting the coherence of individual quantum systems is a central challenge in quantum science and technology. This challenge is particularly salient for solid-state spin qubits that are embedded in a noisy environment [1–9]. Here, we show that pairs of two identical coupled spins naturally form long-lived qubits that are protected against decoherence. We study three carbon-13 pairs in diamond [3, 10, 11] and realize high-fidelity projective measurements ($F = 98\%$) of their quantum states using a single NV center in their vicinity. We reveal that the spin pairs are robust to external perturbations because they intrinsically combine three physical phenomena: clock states, decoherence-protected subspaces, and a variant on motional narrowing. The resulting inhomogeneous dephasing time is $T_2^* = 1.9(3)$ minutes, the longest reported for an individually controlled qubit [12]. Finally, we develop complete control and realize an entangled state between two spin-pair qubits through projective parity measurements. These long-lived qubits are abundantly and naturally present in diamond and other solids, and provide new opportunities for metrology, quantum sensing [13], quantum information processing [14–16], and quantum networks [17] .

7.1. INTRODUCTION

Over the last decades a rich variety of methods to investigate and protect quantum coherence have been developed in various systems, including atomic and spin ensembles [5–7, 18], as well as individually controlled qubits [1–4, 8, 9, 12, 14, 19]. These methods include the precise tuning of magnetic fields to create magnetic-field insensitive clock states [7, 12, 18, 20, 21], decoherence-protected subspaces to protect against correlated noise [4, 8, 20–22], active dynamical decoupling to mitigate slowly varying noise [3, 5, 6, 9, 14, 19], real-time Hamiltonian estimation [23], quantum error correction [15, 16, 24], and isotopic purification to remove the spin background in solids [6, 9].

A complementary approach is to look for naturally occurring quantum systems that are intrinsically protected from decoherence. Here we investigate a canonical quantum system: a pair of two identical nuclear spins that are coupled together. Such spin pairs are naturally and abundantly present in solids like diamond, silicon, silicon-carbide, silicon-germanium, graphene and MoS_2 [3, 10, 11, 25]. Traditionally, these spin pairs have been regarded as a primary noise source for solid-state spin qubits [26].

In this work, we show that spin pairs themselves can be fully controlled and provide intrinsically long-lived quantum systems. First, we experimentally develop high-fidelity measurement for multiple spin pairs. Then, we reveal and analyze the various regimes and physical phenomena that govern the spin-pair coherence. Finally, we demonstrate complete control over the quantum states of multiple spin pairs by realizing an entangled state between two pairs.

Our experiments reveal that the intrinsic robustness to noise of spin pairs in solids is due to a simultaneous combination of three phenomena. First, the spins in the pair are identical and closely spaced, so that the anti-parallel spin states form a decoherence-protected subspace. Global magnetic field fluctuations cancel, as they affect both spins equally. Second, the interaction of the spins creates a clock state that is first-order insensitive to the remaining local magnetic field fluctuations. Third, due to the resulting long coherence time, fluctuations of the surrounding spin bath become comparatively fast, so that they average out in a phenomenon similar to motional narrowing.

7.2. SYSTEM

The system that we investigate is illustrated in Fig 7.1. We consider three pairs of coupled ^{13}C nuclear spins in the vicinity of an NV center in a diamond at 3.7 K. The NV center spin can be initialized and measured optically (see section 7.7) and is used to create a controllable local magnetic-field gradient for each pair. This enables us to sense and control the spin pairs [3, 10, 11], despite their excellent isolation from all other influences.

A pair of spins is described by four basis states: $|\uparrow\uparrow\rangle$, $|\uparrow\downarrow\rangle$, $|\downarrow\uparrow\rangle$ and $|\downarrow\downarrow\rangle$. We are mainly interested in the dynamics in the antiparallel subspace and define a pseudo-spin spanned by $|\Uparrow\rangle = |\uparrow\downarrow\rangle$ and $|\Downarrow\rangle = |\downarrow\uparrow\rangle$ [3, 10, 11]. The pseudo-spin Hamiltonian is given by:

$$H = X\hat{I}_x + m_s Z\hat{I}_z, \tag{7.1}$$

in which $\hat{I}_z$ and $\hat{I}_x$ are spin–1/2 operators. X is the dipolar coupling between the ^{13}C spins. $m_s = \{-1, 0, +1\}$ is the NV spin projection and $Z \approx A_\parallel^1 - A_\parallel^2$ is due to the difference between the two NV-^{13}C hyperfine couplings (see section 7.8).

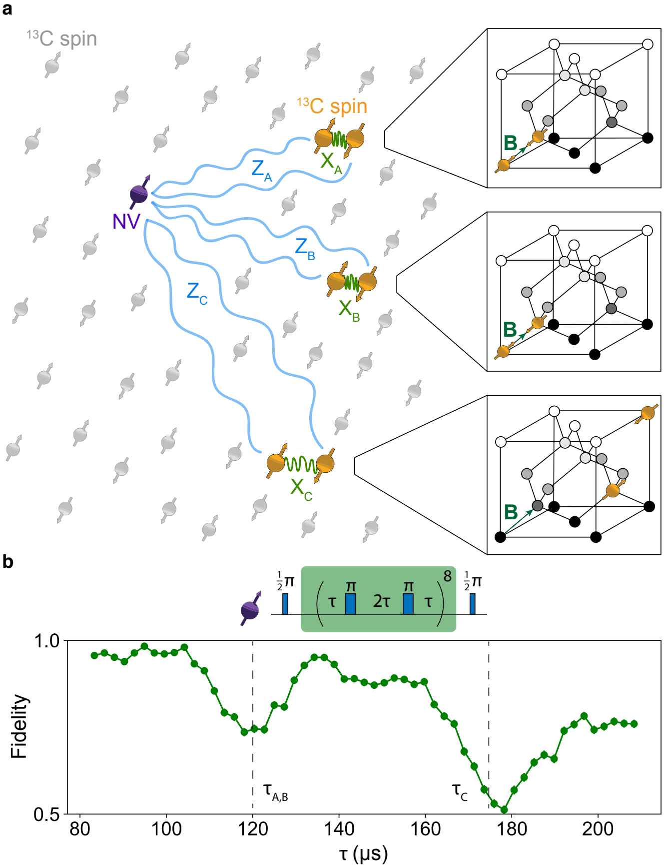

Figure 7.1: **a.** We study three ^{13}C spin pairs (A, B and C) in a diamond. The pairs are detected and controlled using a nearby NV center. The main source of decoherence is the surrounding bath of ^{13}C spins (1.1% abundance). The insets show the structure of the pairs. Pair A and B are nearest-neighbour pairs aligned with the external magnetic field B_z. For pair C we show one of the three possible orientations. **b.** Sensing the pair pseudo-spins [3, 10, 11]. The NV electron spin is prepared in a superposition and a periodic sequence of π pulses is applied. If the interpulse delay is resonant with the dynamics of a pair, a loss of electron coherence is observed. We set $\tau = m2\pi/\omega_L$ with m an integer and ω_L the ^{13}C Larmor frequency to avoid interactions with individual ^{13}C spins. The vertical lines mark the values for τ used in this work for the three pairs ($\tau_A = \tau_B = 120.330$ μs and $\tau_C = 177.026$ μs).

We examine three spin pairs (Fig. 7.1a). Pair A and pair B are both nearest-neighbour pairs oriented along the external magnetic field with dipolar couplings $X_A = X_B = 2\pi \cdot 2080.9900(3)$ Hz and $Z_A = 2\pi \cdot 130(1)$ Hz and $Z_B = 2\pi \cdot 91(2)$ Hz (see measurements below). Pair C has a larger separation between the spins resulting in $X_C = 2\pi \cdot 188.33(2)$ Hz, and $Z = 2\pi \cdot 2802(2)$ Hz. In the following, we focus on developing initialization, control and measurement for pairs A and B, for which $X \gg Z$. For pair C, we have $Z \gg X$, leading to different dynamics and control methods. The control of pair C is developed in section 7.8.

7.3. FULL CONTROL OF SPIN PAIRS

Previous work has demonstrated that the pseudo-spin of pairs can be detected and characterized through dynamical decoupling sequences that toggle the $m_s Z \hat{I}_z$ term by periodically inverting the NV electron spin (Fig. 7.1b) [3, 10, 11]. For an interpulse delay of $2\tau = \pi/\omega_r$, with $\omega_r = \sqrt{X^2 + (Z/2)^2}$, the sequence is resonant with the pseudo-spin dynamics and the effective NV-pair interaction is of the form $\hat{S}_z \hat{I}_z$, with $\hat{S}_z$ the spin operator for the NV electron spin [3, 10, 11]. The NV center thus picks up a phase that depends on the z-projection of the pseudo-spin. We use the NV center as a sensor to detect the spin pairs in its environment by sweeping τ (Fig. 7.1b) [3, 10, 11] and find the resonances for pair A and B ($\tau = 120.330\ \mu$s) and pair C ($\tau = 177.026\ \mu$s).

We start by developing projective single-shot measurements. Unlike all previous work, which was limited to manipulating mixed states of the parallel and antiparallel subspaces [3], these measurements enable us to initialize and read out the complete state of both pairs with high contrast.

Our method is based on repeated non-destructive measurements and illustrated in Fig. 7.2. We let the NV interact with the pair pseudo-spin before reading it out. During the interaction the NV electron spin accumulates a positive (negative) phase if a pair is in $|\Uparrow\rangle$ ($|\Downarrow\rangle$) (Fig. 7.2c). For a pair in the parallel subspace ($|\uparrow\uparrow\rangle$ or $|\downarrow\downarrow\rangle$), the NV spin does not accumulate any phase. We choose τ such that pairs A and B interact with the NV spin simultaneously. Therefore, the NV spin accumulates a phase that depends on which of the 16 possible states the two pairs are in (Fig. 7.2c). By repeatedly applying this sequence, we realize a projective measurement that can distinguish multiple states with high contrast in a single shot.

We construct two types of measurement by setting different interaction times and NV readout axes (Fig 7.2a,b). The 'spin' measurement distinguishes the four pseudo-spin states ($|\Uparrow\Uparrow\rangle, |\Uparrow\Downarrow\rangle, |\Downarrow\Uparrow\rangle, |\Downarrow\Downarrow\rangle$; Fig. 7.2a,c). The 'parity' measurement only distinguishes the pseudo-spin parity of the two pairs ($\{|\Uparrow\Uparrow\rangle, |\Downarrow\Downarrow\rangle\}$ vs $\{|\Uparrow\Downarrow\rangle, |\Downarrow\Uparrow\rangle\}$; Fig. 7.2b,d). Because the pseudo spins evolve as $|\Uparrow\rangle \leftrightarrow |\Downarrow\rangle$ with a frequency $\sim X$ during the NV spin readout, each repetition must be timed to align the measurement axes. This synchronization of repeated non-destructive measurements to the system evolution is similar to the case of repeated measurements on individual spins, e.g. in the context of quantum algorithms [15, 27], atomic frequency locking and quantum Zeno dynamics [28], and weak measurement sequences [29, 30].

We combine these sequences to realize high-fidelity initialization and measurement. We first apply the parity measurement sequence (20 repetitions) to herald preparation

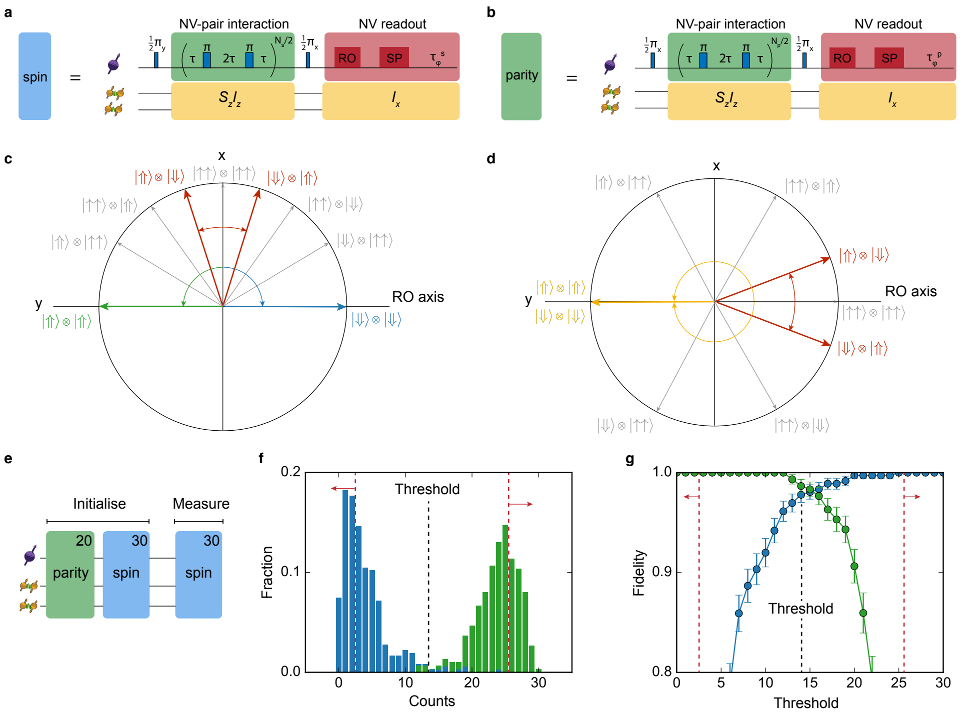

Figure 7.2: **Projective spin and parity measurements. a.** Sequence to measure the pseudo-spin states for pair A and B. The NV electron spin is initialized in $m_s = 0$. The $\hat{S}_z\hat{I}_z$ interaction sequence ($\tau = 120.330$ μs and $N_s = 14$) maps the state of the two pairs onto the NV spin (see (c)). The NV spin is subsequently read out (RO) and reset (SP) to $m_s = 0$. We synchronize subsequent measurements by calibrating a waiting time $\tau^s_\phi = 323.5$ μs to compensate for the $\hat{I}_x$ evolution during NV readout. This ensures that the full sequence duration is a multiple of $1/X$. **b.** Sequence to measure the pseudo-spin parity for pair A and B ($N_p = 20$). We set $\tau^p_\phi = 81$ μs to synchronize subsequent measurements (sequence duration a multiple of $1/(2X)$). **c.** XY-plane of the NV Bloch sphere showing the possible phases accumulated in the spin measurement. The NV spin starts along x and picks up a positive (negative) phase for a pair in |⇑⟩ (|⇓⟩) and no phase for a pair in a parallel state (|↑↑⟩ or |↓↓⟩). Reading out along the y-axis distinguishes the 4 pseudo-spin states (colored). **d.** XY-plane of the NV Bloch sphere under parity readout. The initial state (y-axis) and the readout axis (y-axis) are identical so that the parity of pair A and B is measured. **e.** Measurement sequence to calibrate high-fidelity single-shot readout and initialization. The top right of each block indicates the number of repetitions. The optimal number of spin readouts is 30. **f.** Conditional histograms for 30 spin readouts after initialization in |⇑⟩|⇑⟩ (green) and |⇓⟩|⇓⟩ (blue). The initialization conditions for the 30 preceding spin readouts are indicated in red. **g.** Combined initialization and readout fidelity for |⇑⟩|⇑⟩ (green) and |⇓⟩|⇓⟩ (blue) for 30 spin readouts. We find an optimum of $F = 98.2(7)\%$ for a threshold of 14 out of 30.

in an even parity state (Fig. 7.2e). Then, we apply a spin measurement (30 repetitions) to herald either $|\Uparrow\Uparrow\rangle$ or $|\Downarrow\Downarrow\rangle$. Finally we read out the pseudo-spin state with another spin measurement (30 repetitions). The resulting conditional histograms show well-isolated distributions (Fig. 7.2f) and an optimization of the measurement threshold (Fig. 7.2g) yields a combined initialization and readout fidelity of 98.2(7)% for distinguishing these two states (see section 7.7).

7.4. COHERENCE OF SPIN PAIRS

We now use the developed high-contrast measurements to investigate the coherence of pair A and B. First, we perform a free-evolution experiment with the NV spin in $m_s = -1$ (Fig. 7.3a), for which the NV-pair coupling is on. Because the precession frequency $\sqrt{X^2+Z^2}$ is different for the two pairs ($Z_A \neq Z_B$), this measurement reveals the presence of the two pairs and characterizes their coupling Z to the NV. From the two frequencies observed, we extract $Z_A = 2\pi \cdot 130(1)$ Hz and $Z_B = 2\pi \cdot 91(2)$ Hz (see section 7.7). We obtain the dephasing times from a Fourier transform (Fig. 7.3a): $T_2^*{}_A = 0.26(2)$ s and $T_2^*{}_B = 0.39(6)$ s, one to two orders of magnitude longer than for individual ^{13}C spins in the same environment [14].

Second, we perform the same experiment but with the NV spin in $m_s = 0$, so that the coupling to the NV is effectively turned off. Now both pairs precess with frequency $X_A = X_B = 2080.9900(3)$ Hz (Fig. 7.3b) and a coherent oscillation that extends well past 70 s is observed. To extract the dephasing time, we measure the oscillation amplitude at various times (Fig. 7.3c). The resulting decay yields $T_2^* = 1.9(3)$ minutes (linewidth: 2 mHz), the longest inhomogeneous dephasing time reported for any individually controllable quantum system [12].

To understand the measured dephasing times we add a magnetic-field noise term $\Delta Z(t)$ to the pseudo-spin Hamiltonian:

$$H = X\hat{I}_x + (m_s Z + \Delta Z(t))\hat{I}_z. \tag{7.2}$$

The first mechanism that enhances the coherence is the decoherence-protected subspace formed by the pseudo-spin states: $\Delta Z(t)$ is given by the fluctuations of the magnetic field *difference* between the two spins. The atomic distance between the spins ensures a nearly complete immunity to noise from distant sources, such as the applied magnetic field and the control signals. The main source of noise is therefore the surrounding ^{13}C spin bath. Hence $\Delta Z(t)$ can be approximated as a Gaussian distribution with a correlation time τ_c and variance $b^2 = \frac{1}{4}\sum_k (A_k^1 - A_k^2)^2$, where A_k^1 (A_k^2) is the dipolar coupling of bath spin k to the first (second) spin of the pair. We calculate the typical effective noise strength b (~ 13 Hz) by numerically simulating many spin-bath configurations, and find a reduction of a factor ~ 2 due to the decoherence-protected subspace.

We first analyze the case of the NV electron spin in $m_s = -1$ (Fig. 7.3a). Because $X \gg Z \gg \Delta Z(t)$, the Hamiltonian can be approximated as (see section 7.8)

$$H = (\omega_{-1} + \frac{Z}{\omega_{-1}}\Delta Z(t))\hat{I}_x, \tag{7.3}$$

where $\omega_{-1} = \sqrt{X^2+Z^2}$. The NV $m_s = -1$ state creates a field gradient that slows down spin flip-flops in the bath (a frozen core). Therefore the noise can be treated as quasi-

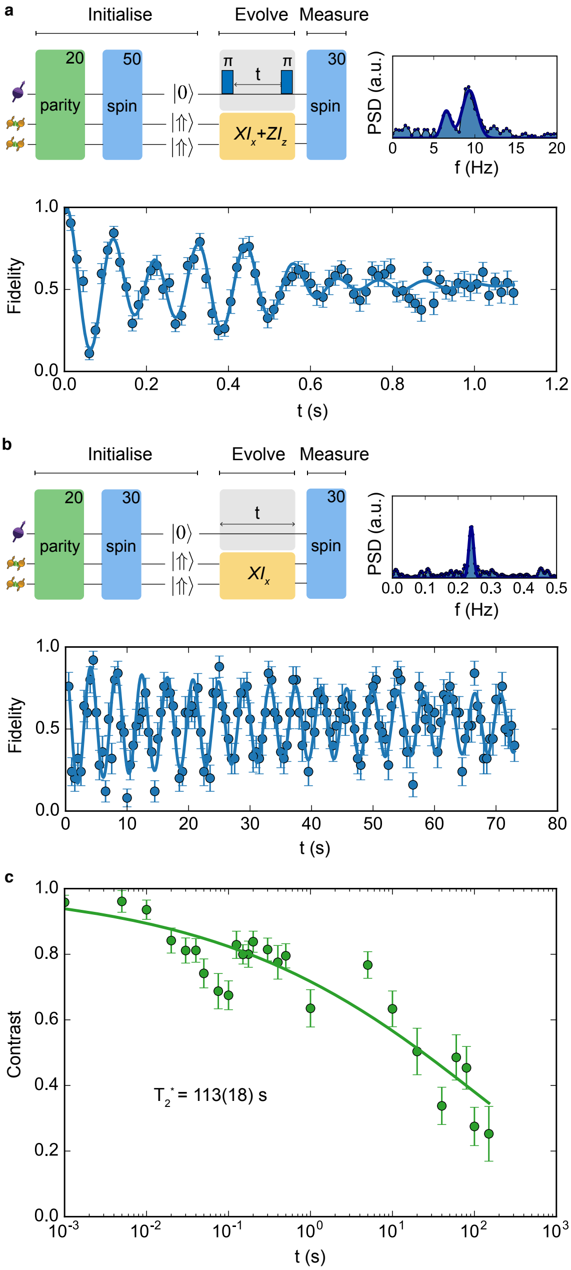

Figure 7.3: **Coherence of pair A and B. a.** Ramsey measurement with the NV in $m_s = -1$. (Top left) Experimental sequence. (Top right) Fourier transform of the signal indicating two frequencies. From the data we obtain the coupling of the pairs to the NV $Z_A = 2\pi\cdot130(1)$ Hz and $Z_B = 2\pi\cdot91(2)$ Hz. **b.** Ramsey measurement with the NV in $m_s = 0$. (Top left) Experimental sequence. (Top right) Fourier transform indicating a single frequency. From the data we obtain $X = 2\pi\cdot2080.9900(3)$ Hz. For a and b an artificial detuning has been applied. **c.** Each data point corresponds to a Ramsey measurement in $m_s = 0$ of which the amplitude is fitted. We then fit the amplitude decay over time, obtaining $T_2^* = 113(18)$ s.

static. The resulting signal decay is Gaussian [31], as experimentally observed (Fig. 7.3a). The dephasing time is then given by [31]

$$T_2^* = \frac{\omega_{-1}}{Z}\frac{\sqrt{2}}{b}. \tag{7.4}$$

In this case, the interaction between the spins enhances the coherence by a factor $\frac{\omega_{-1}}{Z} \approx 20$. Using the measured dephasing times $T_2^*{}_A = 0.26(2)$ s and $T_2^*{}_B = 0.39(6)$ s (Fig. 7.3a) in equation 7.4, we extract effective noise strengths $b_A = 2\pi \cdot 13.9(2)$ Hz and $b_B = 2\pi \cdot 12.5(4)$ Hz. These values are consistent with the inter-pair distance (see section 7.8).

Second, we analyze the case with the NV electron spin in $m_s = 0$, for which the $m_s Z \hat{I}_z$ term is turned off. Since $X \gg \Delta Z(t)$, the Hamiltonian (Eq. 7.2) can be approximated as [32]

$$H = X\hat{I}_x + \frac{\Delta Z^2(t)}{2X}\hat{I}_x. \tag{7.5}$$

The eigenenergies are now first-order insensitive to $\Delta Z(t)$: the spin pair forms a clock state, a second mechanism that suppresses the noise ($X \gg \Delta Z(t)$). Note that, the clock state in this system does not require a specific magnetic field value, due to the decoherence-protected subspace.

The decoherence-protected subspace and clock state alone cannot yet explain the observed $m_s = 0$ dephasing. In particular, for quasi-static noise ($\tau_c \gg X/b^2$) the coherence would be limited to ~ 10 s. However, the increased coherence, in combination with the lack of a frozen core for $m_s = 0$, unlocks a regime in which the nuclear-spin bath fluctuations become relatively fast ($\tau_c \ll X/b^2$). A mathematically equivalent Hamiltonian was analysed theoretically by Dobrovitski et al. [32]. The resulting time constant is

$$T_2^* = \frac{4X^2}{b^4\tau_c}. \tag{7.6}$$

This dependence on the correlation time τ_c reveals a third mechanism, similar to motional narrowing [32], that further enhances the coherence. Inserting the parameters of pair A and B, obtained from the $m_s = -1$ measurement, and a typical value for $\tau_c \sim 0.1$ s [15], inhomogeneous dephasing times of ~ 100 s are predicted, providing an explanation for the observed values. In conclusion, the long dephasing time observed, 4-5 orders of magnitude beyond the value for an individual ^{13}C spin in the same environment, is due to a simultaneous combination of three physical phenomena: a decoherence-protected subspace, a clock state and a mechanism similar to motional narrowing.

To further elucidate the different physical regimes that play a role, we investigate Pair C (Fig. 7.1). Due to the larger separation, this pair has a smaller $X = 2\pi \cdot 188.33(2)$ Hz and larger $Z = 2\pi \cdot 2802(2)$ Hz. We developed initialization and single-shot readout, as well as complete control over this pair (see section 7.8). Importantly, because $Z \gg X$ the clock state can be effectively switched on ($m_s = 0$) and off ($m_s = -1$).

For $m_s = 0$, the situation is similar as for pair A and B and we find $T_2^* = 0.6(1)$ s (Fig. 7.6). The reduced T_2^* compared to Pairs A and B is explained by the smaller coupling X, which makes the clock state less effective. For $m_s = -1$, the clock state is turned off. The noise term $\Delta Z(t)$ now affects the eigenfrequencies directly and linearly. We find

$T_2^* = 18(1)$ ms with Gaussian decay, which does not show a significant improvement over an individual spin. We thus recover the case of an unprotected spin in a quasistatic noise bath. This is further confirmed by the observation that the coherence can be extended by a spin echo ($T_2 = 0.3(2)$ s) and that relaxation is frozen ($T_1 \gg 10$ s, see Fig. 7.6).

7.5. ENTANGLEMENT OF TWO SPIN PAIRS

Finally, we demonstrate the potential of the spin pairs as qubits by demonstrating an entangled state between the pseudo-spins of pairs A and B. We create entanglement through subsequent projective measurements of the YY and ZZ pseudo-spin parity and select outcomes $\langle YY \rangle = +1$ and $\langle ZZ \rangle = -1$ (Fig. 7.4a). The resulting state is $\frac{1}{\sqrt{2}}(|\Uparrow\Downarrow\rangle + |\Downarrow\Uparrow\rangle)$. This state is identical to a 4-spin entangled state $\frac{1}{\sqrt{2}}(|\uparrow\downarrow\downarrow\uparrow\rangle + |\downarrow\uparrow\uparrow\downarrow\rangle)$ that encodes two qubits of information in long-lived pseudo-spin states.

To characterize the resulting state we first measure parity oscillations by varying the evolution time t (Fig. 7.4a). The observed frequency is 4.20(4) kHz, which equals $2X$, as expected (Fig. 7.4b). We use this result to calibrate the time t to measure $\langle YY \rangle$ and $\langle ZZ \rangle$, and we find 105 and 225 μs respectively. To determine the state fidelity, we additionally need to measure $\langle XX \rangle$. We implement the required basis rotations through dynamical decoupling sequences with the NV spin in an eigenstate (for z-rotations) and waiting times (for x-rotations) (Fig. 7.4a). Figure 7.4c shows the measured three pseudo-spin parity operators, which yield an entangled state fidelity of 74(2)% (not corrected for measurement infidelity). This result highlights the high-quality initialization, control and measurements obtained over the spin pairs. Additionally, the realized non-destructive parity measurements are a key primitive for quantum error correction [24].

7.6. CONCLUSION AND OUTLOOK

In conclusion, we have developed complete control over multiple nuclear-spin pairs. These spin pairs provide extremely long-lived quantum states, because they are intrinsically robust to decoherence due to a remarkable combination of three physical phenomena: decoherence-protected subspaces, clock states and motional narrowing. This natural coherence protection makes spin pairs promising qubits for a variety of applications, including quantum sensing [13] and quantum information processing [14]. In particular, due to the small effective coupling to the electron, they might provide robust quantum memories for optically connected quantum networks [17, 22]. Such spin pairs are available at practically any NV center, and are naturally found in a wide variety of other materials. Therefore, our results reveal a new, promising, and abundantly available resource for quantum science and technology.

7.7. METHODS

7.7.1. SAMPLE AND NV CENTER

The experiments are performed on a naturally occurring NV centre at 3.7 K. The diamond was homoepitaxially grown using chemical vapor deposition and cleaved along the $\langle 111 \rangle$ axis (Element Six). There is a natural abundance (1.1%) of ^{13}C. The NV centre was selected on the absence of strongly coupled ^{13}C spins exceeding 500 kHz hyperfine

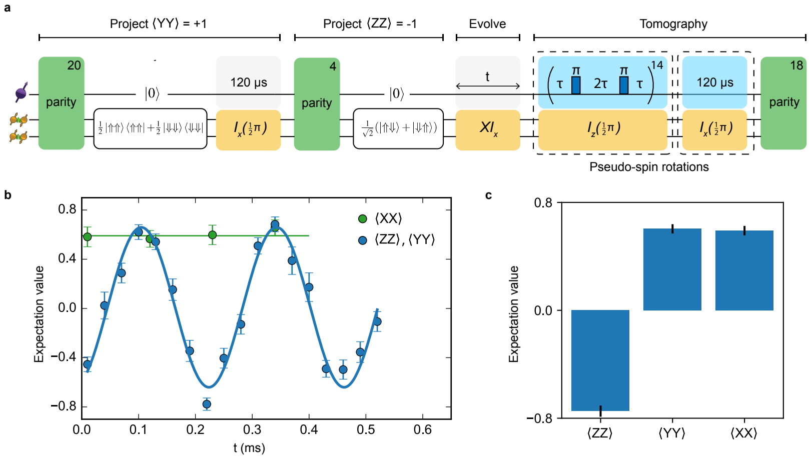

Figure 7.4: **Entanglement of pair A and B. a.** Experimental sequence. A parity readout block implements a measurement of $\langle ZZ\rangle$ in the pseudo-spin basis (Fig. 7.2d). We can thus initialize the entangled state $\frac{1}{\sqrt{2}}|\Uparrow\Downarrow\rangle + |\Downarrow\Uparrow\rangle$ by measuring $\langle YY\rangle$ and $\langle ZZ\rangle$ consecutively. We select on $> 14/20$ and $< 1/4$ counts in the initialization steps. We measure the nonzero correlators by doing pseudo-spin rotations (dashed boxes) before a $\langle ZZ\rangle$ parity measurement. **b.** Parity oscillations show a frequency of 4.20(4) kHz ($\sim 2X$). For $\langle XX\rangle$ no oscillation is observed as the pseudo-spin eigenstates are along x. **c.** Measurement of the three nonzero correlators of the entangled state. The entangled state fidelity is $F = (1 - \langle ZZ\rangle + \langle YY\rangle + \langle XX\rangle)/4 = 74(2)\%$. The results have not been readout corrected.

coupling, but without any other criteria on the spin environment or spin pairs.

The NV electron spin has a dephasing time of $T_2^* = 4.9(2)$ μs and a spin echo time of $T_2 = 1.182(5)$ ms. The electron relaxation ($T_1 > 1$ h) at this temperatures is negligible [3]. We measure the NV spin state in a single shot using spin-selective optical readout. The readout fidelities are 0.905(2) (0.986(2)) for the $m_s = 0$ ($m_s = -1$) state with an average fidelity of $F = 94.6\%$.

7.7.2. INITIALIZATION AND SINGLE-SHOT READOUT FIDELITY

In general, there is an optimum in the number of readouts and the corresponding thresholds used. Independent of the type of pair (A and B or C) and the type of sequence (spin or parity), the approach we take to optimize the readout is the same. First, we initialize the two states that we want to optimally distinguish. We will call those states $|a\rangle$ and $|b\rangle$ for now. Even if the initialization is a two-step process (Fig. 7.2e), the last step is used to either initialize in $|a\rangle$ or $|b\rangle$. For the last initialization step we generally use k repetitions and we denote the number of counts recorded in those repetitions as $N(k)$. The initialization is then defined by $N(k) > N_a$ and $N(k) < N_b$ where N_a and N_b are the thresholds we set for the initialization.

In the readout step, we use m repetitions and obtain $N(m)$ counts. Two histograms are obtained in the readout step (Fig. 7.2e), one corresponding to each initialized state. The histogram at high counts (green in Fig. 7.2f) corresponds to $|a\rangle$ and the histogram at low counts (blue in Fig. 7.2f) corresponds to $|b\rangle$. To optimally distinguish these states, we sweep a threshold T and obtain the total fidelity as

$$\begin{aligned} F &= \frac{F_{|a\rangle} + F_{|b\rangle}}{2} \\ &= \frac{1}{2} P(N(m) \geq T | N(k) > N_a) \\ &+ \frac{1}{2} P(N(m) < T | N(k) < N_b) \end{aligned} \tag{7.7}$$

In Fig. 7.2g the fidelities of the individual states $F_{|a\rangle}$ and $F_{|b\rangle}$ are plotted for a varying threshold T. This is done for a varying number of readouts m to find the optimal number of readouts and corresponding threshold.

It is important to note that the obtained fidelities are combined initialization and readout fidelities, because we do not correct for any infidelity in the initialization. To minimise the infidelity due to initialization we use strict thresholds N_a and N_b, but it cannot be guaranteed that the intialisation infidelity is negligible.

7.7.3. DATA ANALYSIS

The Ramsey data in Fig. 7.3a is fitted to

$$\exp\left(-(t/T)^n\right)[\cos\left(2\pi f_A t + \phi_A\right) + \cos\left(2\pi f_B t + \phi_B\right)] \tag{7.8}$$

We obtain $T = 0.53(4)$ s, $n = 2.1(4)$, $f_A = 9.07(6)$ Hz and $f_B = 7.0(1)$ Hz. We used an artificial detuning of 10 Hz with respect to 2086 Hz. Using $f = \sqrt{(}X^2 + Z^2)$ and $X = 2\pi \cdot 2080.9900(3)$ Hz, the values for f_A and f_B can be used to obtain $Z_A = 2\pi \cdot 130(1)$ Hz and $Z_B = 2\pi \cdot 91(2)$ Hz. To extract the dephasing times we fit the Fourier transform in Fig. 7.3a to

$$a + A\exp\left(-(f + f_A)^2/2\sigma_A^2\right) \tag{7.9}$$

$$+ B\exp\left(-(f + f_B)^2/2\sigma_B^2\right) \tag{7.10}$$

We find $\sigma_A = 0.88(6)$ Hz and $\sigma_B = 0.57(9)$ Hz which gives $T_2^*{}_A = 0.26(2)$ s and $T_2^*{}_B = 0.39(6)$ s.

The Ramsey data in Fig. 7.3b is fitted to

$$\exp\left(-(t/T)^n\right)\cos\left(2\pi f t + \phi\right) \tag{7.11}$$

We obtain $T = 98(44)$ s, $n = 0.5(4)$ and $f = 0.2400(3)$ Hz. We used an artificial detuning of 0.25 Hz with respect to 2081 Hz. Therefore we obtain $X = 2\pi \cdot 2080.9900(3)$ Hz. The Fourier transform is fitted to

$$a + A\exp\left(-(f + f_0)^2/2\sigma_0^2\right) \tag{7.12}$$

We obtain $f_0 = 0.2402(3)$ Hz and $\sigma_0 = 0.0074(3)$ Hz.

The data in Fig. 7.3c is fitted to $\exp(-(t/T)^n)$ obtaining $T = 113(18)$ s and $n = 0.23(2)$.

The data in Fig. 7.4b is fitted to $a + A\cos\left(2\pi f + \phi\right)$. We obtain $f = 4.20(4)$ kHz.

7.8. SUPPLEMENTARY INFORMATION

7.8.1. PSEUDO-SPIN HAMILTONIAN

The Hamiltonian for two ^{13}C spin-$\frac{1}{2}$ particles in the vicinity of an NV center can be written as:

$$H = \omega_L I_z^1 + \omega_L I_z^2 + m_s \mathbf{A}^1 \cdot \mathbf{I}^1 + m_s \mathbf{A}^2 \cdot \mathbf{I}^2 + H_D. \tag{7.13}$$

where $\omega_L = \gamma_c B$ is the ^{13}C spin Larmor frequency, $\mathbf{I}$ are the spin-$\frac{1}{2}$ operators, $m_s = \{-1, 0, +1\}$ are the NV electron spin states and $\mathbf{A}$ is the NV-carbon hyperfine interaction vector. H_D is the dipolar interaction between two ^{13}C spins:

$$H_D = \frac{\mu_0 \gamma_c \gamma_c}{4\pi |\mathbf{r}_{12}|^3} [\mathbf{I}^1 \cdot \mathbf{I}^2 - \frac{3}{|\mathbf{r}_{12}|^2} (\mathbf{I}^1 \cdot \mathbf{r}_{12})(\mathbf{I}^2 \cdot \mathbf{r}_{12})], \tag{7.14}$$

where μ_0 is the vacuum permeability, γ_c is the ^{13}C gyromagnetic ratio, $\mathbf{r}_{12}$ is the vector between the two ^{13}C atoms and θ_{12} the angle between the magnetic field axis and the pair axis. For a large magnetic field ($\gamma_c B \gg \frac{\mu_0 \gamma_c \gamma_c}{4\pi |\mathbf{r}_{12}|^3}$) this can be approximated as:

$$H_D = X(3 I_z^1 I_z^2 - \mathbf{I}^1 \cdot \mathbf{I}^2) \tag{7.15}$$

$$X = \frac{\mu_0 \gamma_c \gamma_c}{8\pi |\mathbf{r}_{12}|^3} (1 - 3\cos^2\theta_{12}). \tag{7.16}$$

Since $\omega_L = \gamma_c B$ is large compared to the dipolar (X) and hyperfine couplings (A^1, A^2) the antiparallel states $|\uparrow\downarrow\rangle$ and $|\downarrow\uparrow\rangle$ form an isolated subspace in which we define a pseudo-spin $\frac{1}{2}$ as $|\Uparrow\rangle = |\uparrow\downarrow\rangle$ and $|\Downarrow\rangle = |\downarrow\uparrow\rangle$ [3, 10, 11, 26]. The Hamiltonian in this subspace is given by [10, 26]

$$H = X\hat{I}_x + m_s Z \hat{I}_z. \tag{7.17}$$

Z originates from the difference of the hyperfine couplings of the two spins to the NV electron spin, and is given by [26]

$$Z = Z_\parallel + Z_\perp = A_\parallel^1 - A_\parallel^2 + \frac{(A_\perp^1)^2 - (A_\perp^2)^2}{\gamma_c B}, \tag{7.18}$$

where $A_\parallel$ and $A_\perp$ are the parallel and perpendicular hyperfine couplings between the NV and the spins of the pair. B is the magnetic field along the NV-axis.

7.8.2. PAIR C CONTROL

Pair C has a dipolar coupling of $X = 2\pi \cdot 188.33(2)$ Hz and a hyperfine gradient of $Z = 2\pi \cdot 2802(2)$ Hz. Therefore we have $Z \gg X$, in contrast to the nearest neigbour pairs described in the main text for which $X \gg Z$. This has two important implications. First, for $m_s = -1$, Z is now the dominant term in the pair frequency $\omega_1 = \sqrt{X^2 + Z^2}$ and thus sets the location of the resonance in Fig. 7.1b. Second, the effective NV-pair interaction during a resonant dynamical decoupling sequence becomes $S_z^{NV} I_x$, a conditional rotation of the pair pseudo-spin around the x-axis [3].

As in the main text, we implement two different sequences to projectively measure pair C, see Fig. 7.5. The spin readout sequence (Fig. 7.5a) allows one to distinguish the pseudo-spin states $\frac{1}{\sqrt{2}}(|\Uparrow\rangle \pm |\Downarrow\rangle)$. The parity readout sequence can distinguish between the parallel and antiparallel subspace of the pair. The measurements can be used to intialize and readout the spin pair. We obtain high fidelity inialization and readout by repeteadly applying these sequences.

For spin pairs with $Z \gg X$, the timing of repeated sequences is complicated by the fact that the evolution frequencies and the eigenstates differ significantly between $m_s = 0$ and $m_s = -1$. Here, we mitigate this by minimizing the NV readout time (RO, $\sim 5\ \mu$s) and applying a fast reset of the NV spin (SP, $\sim 100\ \mu$s), so that the time spent in $m_s = -1$ is minimized. Additionally, the pair is projected into an eigenstate of $m_s = 0$ evolution, and therefore there is no timing requirement after the SP, and we simply concatenate subsequent measurements.

For pairs A and B ($X \gg Z$), dynamical decoupling sequences are required to realize universal single-qubit control for the pseudo spins (Fig. 7.4). For pair C ($Z \gg X$) single-qubit operations can be obtained by letting the system evolve freely. Evolution with the NV electron spin in $m_s = 0$ implements a rotation around the x-axis, and evolution under $m_s = -1$ realizes a rotation around the z-axis. Note that the rotation in $m_s = -1$ is not exactly around the z-axis (i.e., around a slightly tilted axis) because Z is finite. In principle, this can be taken into account and optimized for but this is not done here.

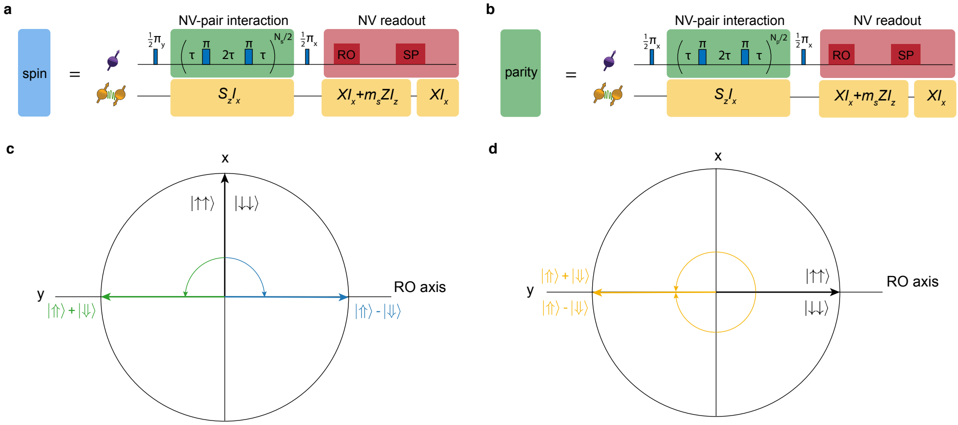

Figure 7.5: **Sequences for Pair C measurements. a.** Sequence to readout the spin state of pair C. The NV readout block (RO) reads out the NV state and the spin pump (SP) re-initializes the NV in $m_s = 0$. During the NV readout and spin pump, the NV can spend an unknown time in $m_s = -1$ which causes dephasing of the pair spin. To minimize this effect, we use a fast readout and spin pump. Note that this is not necessary for the parity readout. $N_s = 8$. **b.** Sequence to measure the parity of the two spins that make up pair C. $N_p = 14$. **c.** XY-plane of the NV Bloch sphere during the NV-pair interaction in a. The NV picks up a positive or negative phase depending on the spin state of the pair and no phase when the pair is in the parallel subspace. **d.** XY-plane of the NV Bloch sphere during the NV-pair interaction in b.

7.8.3. COHERENCE AND RELAXATION OF PAIR C

For pair C the clock state can be turned on ($m_s = 0$) and off ($m_s = -1$) by changing the NV spin state. We measured the pseudo-spin dephasing time T_2^*, the spin echo time T_2 and the relaxation time T_1 for both electron spin states, see Fig. 7.6. Using 10 parity initializations and selecting on $> 7/10$ counts we first initialize the pair in the antiparallel subspace. Then 7 spin readouts are used to initialize $\frac{1}{\sqrt{2}}(|\Uparrow\rangle + |\Downarrow\rangle)$ ($> 4/7$) or $\frac{1}{\sqrt{2}}(|\Uparrow\rangle - |\Downarrow\rangle)$ ($< 3/7$). In Fig. 7.6 blue data corresponds to initialization in $\frac{1}{\sqrt{2}}(|\Uparrow\rangle + |\Downarrow\rangle)$ and green data corresponds to initialization in $\frac{1}{\sqrt{2}}(|\Uparrow\rangle - |\Downarrow\rangle)$. The evolution sequence depends on the measurement performed and is inset in Fig. 7.6b-g. We use 6 spin-readout repetitions to readout the final spin state (calibrated to maximize the fidelity). The coherence and relaxation results are summarised in Table 7.1.

	$m_s = -1$	$m_s = 0$
T_2^* (s)	0.018(1)	0.6(1)
T_2 (s)	0.3(2)	0.7(1)
T_1 (s)	> 10	3.6(7) / 0.9(2)

Table 7.1: **Pair C coherence and relaxation.** Summary of the coherence and relaxation measurements for pair C. The corresponding data is shown in Fig. 7.6. The two numbers for T_1 in $m_s = 0$ correspond to the blue and green fit in Fig. 7.6g respectively.

7.8.4. SPECTROSCOPY AND CONTROL OF THE COMPLETE HILBERT SPACE

Most of the work presented is focused on initializing, controlling and measuring the states in the antiparallel subspace of spin pairs, i.e. $|\uparrow\downarrow\rangle$ and $|\downarrow\uparrow\rangle$. Here we demonstrate that the entire Hilbert space of the spin pairs can be controlled by additionally driving the single-spin-flip transitions.

We focus on pair C. The parity sequence distinguishes between the parallel and antiparallel subspaces (Fig. 7.5). To reveal the transitions between the subspaces, we initialize the pair in the antiparallel subspace, apply a radio frequency (RF) pulse with variable frequency with the NV electron spin in $m_s = -1$, and finally readout the subspace state using a parity measurement (Fig. 7.7b). If the frequency of the RF pulse is resonant with a single-spin transition of the pair, the spin pair changes its subspace, which is reflected in the final NV electron spin state.

The result is shown in Fig. 7.7c. We observe four transitions corresponding to the four possibilities to flip from an antiparallel state to a parallel state: $|\uparrow\downarrow\rangle \rightarrow |\downarrow\downarrow\rangle$, $|\downarrow\uparrow\rangle \rightarrow |\uparrow\uparrow\rangle$, $|\uparrow\downarrow\rangle \rightarrow |\uparrow\uparrow\rangle$ and $|\downarrow\uparrow\rangle \rightarrow |\downarrow\downarrow\rangle$. The corresponding transition frequencies are $\omega_1 \pm X$ and $\omega_2 \pm X$ (Fig. 7.7a).

From the result in Fig. 7.7c we extract $\omega_1 = 429.314(5)$ kHz and $\omega_2 = 432.122(7)$ kHz. Since the frequency of a single spin in $m_s = -1$ is $\omega_{-1} \approx \omega_L - A_\parallel$, we obtain $A_\parallel^1 = 2826(5)$ Hz and $A_\parallel^2 = 18(7)$ Hz. Note that these values assume that $A_\perp$ is of similar magnitude, so that it can be neglected. The frequencies observed are close to the characteristic ^{13}C Larmor frequency ($\omega_L = 432.140$ kHz), further corroborating our assignment of ^{13}C-^{13}C pairs as the source of the signals. These results also reveal that it is possible to selectively initialize, control and measure individual carbon spins that have a negligible coupling to

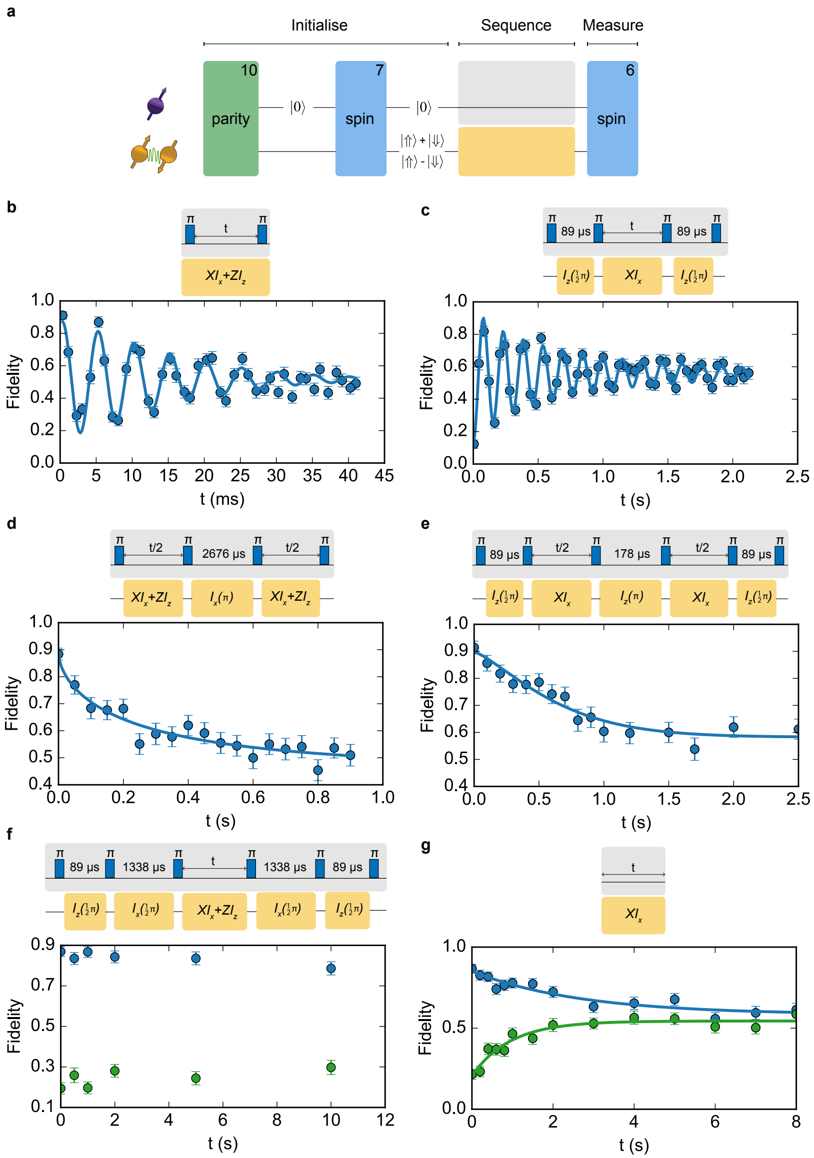

Figure 7.6: **Coherence and relaxation of pair C. a.** Sequence used to initialize the pair C spin state. First, 10 parity readouts ($> 7/10$) initialize the pair in the antiparallel subspace. Then 7 spin readouts initialize the pair in $\frac{1}{\sqrt{2}}(|\Uparrow\rangle + |\Downarrow\rangle)$ ($> 4/7$, blue data) and $\frac{1}{\sqrt{2}}(|\Uparrow\rangle - |\Downarrow\rangle)$ ($< 3/7$, green data). The evolution sequence is given as insets in the corresponding measurements. Finally 6 spin readouts are used to readout the spin state. Figure b,c are fitted to $a + A\exp^{-(t/T)^n}\cos(2\pi f t + \phi)$ and figure d,e,g to $a + A\exp^{-(t/T)^n}$. **b.** Ramsey measurement in $m_s = -1$. $T_2^* = 0.018(1)$ s, $n = 1.4(2)$ and $f = 2808(1)$ Hz. An articial detuning was applied. **c.** Ramsey measurement in $m_s = 0$. $T_2^* = 0.6(1)$ s, $n = 0.7(1)$ and $f = 188.33(2)$ Hz. An articial detuning was applied. **d.** Spin echo measurement in $m_s = -1$. $T_2 = 0.3(2)$ s and $n = 0.6(2)$. **e.** Spin echo measurement in $m_s = 0$. $T_2 = 0.7(1)$ s and $n = 1.3(3)$. **f.** Relaxation measurement in $m_s = -1$. **g.** Relaxation measurement in $m_s = 0$. $T_1 = 3.6(7)$ s and $n = 0.8(2)$ for the blue data $(\frac{1}{\sqrt{2}}(|\uparrow\downarrow\rangle - |\downarrow\uparrow\rangle))$. $T_1 = 0.9(2)$ s and $n = 1.0(2)$ for the green data $(\frac{1}{\sqrt{2}}(|\uparrow\downarrow\rangle + |\downarrow\uparrow\rangle))$.

the NV by using the coupling to neighbouring spins. In this case, spin 2 has a negligible coupling to the NV (18(7) Hz), so that it overlaps in precession frequency with the entire background spin bath. Nevertheless, it can be accessed selectively by using the NV to detect the pseudo-spin dynamics (i.e. flip-flops) with spin 1.

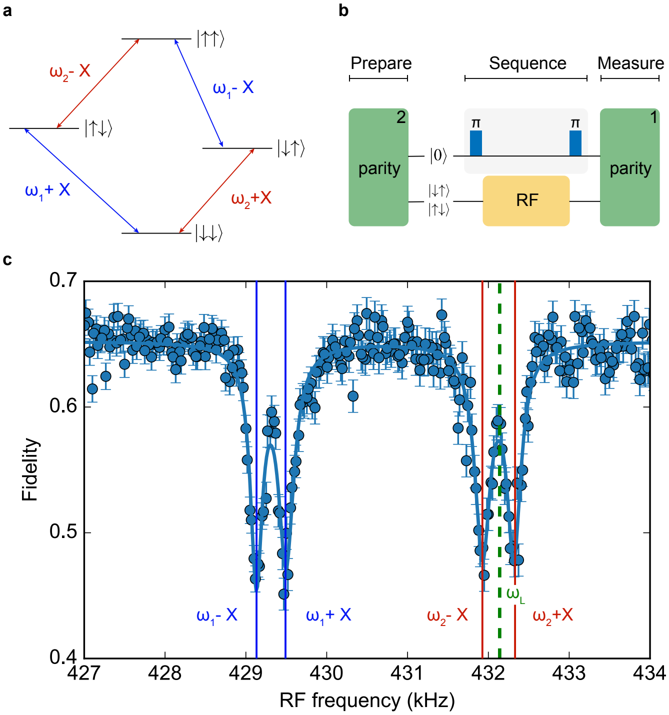

Figure 7.7: **Spectroscopy and control of the complete pair Hilbert space. a.** Level diagram for pair C with the electron spin in $m_s = -1$. ω_1 (ω_2) is the frequency of the first (second) spin of the pair in $m_s = -1$. **b.** Sequence used to access the parallel subspace. First, the pair is initialized in the antiparallel subspace, then an RF pulse with the NV in $m_s = -1$ is applied to flip one of the spins, and finally the subspace population is measured. **c.** Result of the measurement described in b. Four transitions are observed corresponding to the marked transitions in a. The green dashed line corresponds to $\omega_L = 432.140$ kHz. We fit the data to four Lorentzians and extract $\omega_1 = 429.314(5)$ kHz, $\omega_2 = 432.122(7)$ kHz. For the left (right) dip we also obtain $X = 2\pi \cdot 184(3)$ $(2\pi \cdot 194(4))$ Hz.

REFERENCES

[1] K. C. Miao, J. P. Blanton, C. P. Anderson, A. Bourassa, A. L. Crook, G. Wolfowicz, H. Abe, T. Ohshima, and D. D. Awschalom, *Universal coherence protection in a solid-state spin qubit,* Science **1497**, eabc5186 (2020).

[2] T. Van Der Sar, Z. H. Wang, M. S. Blok, H. Bernien, T. H. Taminiau, D. M. Toyli, D. A. Lidar, D. D. Awschalom, R. Hanson, and V. V. Dobrovitski, *Decoherence-protected quantum gates for a hybrid solid-state spin register,* Nature **484**, 82 (2012).

[3] M. H. Abobeih, J. Cramer, M. A. Bakker, N. Kalb, M. Markham, D. J. Twitchen, and T. H. Taminiau, *One-second coherence for a single electron spin coupled to a multi-qubit nuclear-spin environment,* Nat. Commun. **9**, 1 (2018).

[4] M. D. Shulman, O. E. Dial, S. P. Harvey, H. Bluhm, V. Umansky, and A. Yacoby, *Demonstration of entanglement of electrostatically coupled singlet-triplet qubits,* Science **336**, 202 (2012).

[5] M. Zhong, M. P. Hedges, R. L. Ahlefeldt, J. G. Bartholomew, S. E. Beavan, S. M. Wittig, J. J. Longdell, and M. J. Sellars, *Optically addressable nuclear spins in a solid with a six-hour coherence time,* Nature **517**, 177 (2015).

[6] K. Saeedi, S. Simmons, J. Z. Salvail, P. Dluhy, H. Riemann, N. V. Abrosimov, P. Becker, H. J. Pohl, J. J. Morton, and M. L. Thewalt, *Room-temperature quantum bit storage exceeding 39 minutes using ionized donors in silicon-28,* Science **342**, 830 (2013).

[7] G. Wolfowicz, A. M. Tyryshkin, R. E. George, H. Riemann, N. V. Abrosimov, P. Becker, H. J. Pohl, M. L. Thewalt, S. A. Lyon, and J. J. Morton, *Atomic clock transitions in silicon-based spin qubits,* Nat. Nanotechnol. **8**, 561 (2013).

[8] J. T. Muhonen, J. P. Dehollain, A. Laucht, F. E. Hudson, R. Kalra, T. Sekiguchi, K. M. Itoh, D. N. Jamieson, J. C. McCallum, A. S. Dzurak, and A. Morello, *Storing quantum information for 30 seconds in a nanoelectronic device,* Nat. Nanotechnol. **9**, 986 (2014).

[9] P. C. Maurer, G. Kucsko, C. Latta, L. Jiang, N. Y. Yao, S. D. Bennett, F. Pastawski, D. Hunger, N. Chisholm, M. Markham, *et al.*, *Room-temperature quantum bit memory exceeding one second,* Science **336**, 1283 (2012).

[10] N. Zhao, J. L. Hu, S. W. Ho, J. T. Wan, and R. B. Liu, *Atomic-scale magnetometry of distant nuclear spin clusters via nitrogen-vacancy spin in diamond,* Nat. Nanotechnol. **6**, 242 (2011).

[11] F. Shi, X. Kong, P. Wang, F. Kong, N. Zhao, R. B. Liu, and J. Du, *Sensing and atomic-scale structure analysis of single nuclear-spin clusters in diamond,* Nat. Phys. **10**, 21 (2013).

[12] T. P. Harty, D. T. Allcock, C. J. Ballance, L. Guidoni, H. A. Janacek, N. M. Linke, D. N. Stacey, and D. M. Lucas, *High-fidelity preparation, gates, memory, and readout of a trapped-ion quantum bit,* Phys. Rev. Lett. **113**, 2 (2014).

[13] C. L. Degen, F. Reinhard, and P. Cappellaro, *Quantum sensing,* Rev. Mod. Phys. **89**, 1 (2017).

[14] C. E. Bradley, J. Randall, M. H. Abobeih, R. C. Berrevoets, M. J. Degen, M. A. Bakker, M. Markham, D. J. Twitchen, and T. H. Taminiau, *A Ten-Qubit Solid-State Spin Register with Quantum Memory up to One Minute,* Phys. Rev. X **9**, 31045 (2019).

[15] J. Cramer, N. Kalb, M. A. Rol, B. Hensen, M. S. Blok, M. Markham, D. J. Twitchen, R. Hanson, and T. H. Taminiau, *Repeated quantum error correction on a continuously encoded qubit by real-time feedback,* Nat. Commun. **7**, 1 (2016).

[16] G. Waldherr, Y. Wang, S. Zaiser, M. Jamali, T. Schulte-Herbrüggen, H. Abe, T. Ohshima, J. Isoya, J. F. Du, P. Neumann, and J. Wrachtrup, *Quantum error correction in a solid-state hybrid spin register,* Nature **506**, 204 (2014).

[17] B. Hensen, H. Bernien, A. E. Dreaú, A. Reiserer, N. Kalb, M. S. Blok, J. Ruitenberg, R. F. Vermeulen, R. N. Schouten, C. Abellán, *et al.*, *Loophole-free Bell inequality violation using electron spins separated by 1.3 kilometres,* Nature **526**, 682 (2015).

[18] A. W. Young, W. J. Eckner, W. R. Milner, D. Kedar, M. A. Norcia, E. Oelker, N. Schine, J. Ye, and A. M. Kaufman, *A tweezer clock with half-minute atomic coherence at optical frequencies and high relative stability,* Nature **588** (2020).

[19] Y. Wang, M. Um, J. Zhang, S. An, M. Lyu, J. N. Zhang, L. M. Duan, D. Yum, and K. Kim, *Single-qubit quantum memory exceeding ten-minute coherence time,* Nat. Photon. **11**, 646 (2017).

[20] Y. Bae, K. Yang, P. Willke, T. Choi, A. J. Heinrich, and C. P. Lutz, *Enhanced quantum coherence in exchange coupled spins via singlet-triplet transitions,* Sci. Adv. **4**, 1 (2018).

[21] C. Langer, R. Ozeri, J. D. Jost, J. Chiaverini, B. Demarco, A. Ben-Kish, R. B. Blakestad, J. Britton, D. B. Hume, Itano, *et al.*, *Long-lived qubit memory using atomic ions,* Phys. Rev. Lett. **95**, 2 (2005).

[22] A. Reiserer, N. Kalb, M. S. Blok, K. J. van Bemmelen, T. H. Taminiau, R. Hanson, D. J. Twitchen, and M. Markham, *Robust quantum-network memory using decoherence-protected subspaces of nuclear spins,* Phys. Rev. X **6**, 1 (2016).

[23] M. D. Shulman, S. P. Harvey, J. M. Nichol, S. D. Bartlett, A. C. Doherty, V. Umansky, and A. Yacoby, *Suppressing qubit dephasing using real-time Hamiltonian estimation,* Nat. Commun. **5**, 5156 (2014).

[24] B. M. Terhal, *Quantum error correction for quantum memories,* Rev. Mod. Phys. **87**, 307 (2015).

[25] M. Ye, H. Seo, and G. Galli, *Spin coherence in two-dimensional materials,* npj Comput. Mater **5**, 44 (2019).

[26] N. Zhao, S. W. Ho, and R. B. Liu, *Decoherence and dynamical decoupling control of nitrogen vacancy center electron spins in nuclear spin baths,* Phys. Rev. B **85**, 1 (2012).

[27] G. Q. Liu, J. Xing, W. L. Ma, P. Wang, C. H. Li, H. C. Po, Y. R. Zhang, H. Fan, R. B. Liu, and X. Y. Pan, *Single-Shot Readout of a Nuclear Spin Weakly Coupled to a Nitrogen-Vacancy Center at Room Temperature,* Phys. Rev. Lett. **118**, 1 (2017).

[28] N. Kalb, J. Cramer, D. J. Twitchen, M. Markham, R. Hanson, and T. H. Taminiau, *Experimental creation of quantum Zeno subspaces by repeated multi-spin projections in diamond,* Nat. Commun. **7**, 1 (2016).

[29] K. Cujia, J. Boss, K. Herb, J. Zopes, and C. Degen, *Tracking the precession of single nuclear spins by weak measurements,* Nature **571**, 230– (2019).

[30] M. Pfender, P. Wang, H. Sumiya, S. Onoda, W. Yang, D. B. R. Dasari, P. Neumann, X.-Y. Pan, J. Isoya, R.-B. Liu, *et al.*, *High-resolution spectroscopy of single nuclear spins via sequential weak measurements,* Nat. Commun. **10**, 594 (2019).

[31] P. Anderson, P.W.; Weiss, *Exchange Narrowing in Paramagnetic Resonance,* Rev. Mod. Phys. **25** (1953).

[32] V. V. Dobrovitski, A. E. Feiguin, R. Hanson, and D. D. Awschalom, *Decay of Rabi oscillations by dipolar-coupled dynamical spin environments,* Phys. Rev. Lett. **102**, 1 (2009).

8

CONCLUSIONS AND OUTLOOK

In this thesis, we focused on three main research themes. First, we developed novel methods for quantum sensing and atomic-scale imaging of the nuclear-spin environment coupled to the NV center electron spin. This spin environment provides a model system for imaging of single molecules or structures outside the diamond, but also a promising quantum register. Second, we designed and implemented novel methods for high-fidelity control of this spin-environment. Third, we utilized this precise understanding and control for applications in quantum information processing such as the generation of entangled states and quantum error correction. In this chapter, we will give an overview of the future research avenues which are within immediate reach as a result of the work described in this thesis. Afterwards, we will address the bigger picture, i.e., how to move towards atomic-scale imaging of individual structures or molecules outside the diamond, and how to move towards implementing large-scale quantum computations with spins in diamond.

8.1. SUMMARY OF THE RESULTS

In this thesis, we developed novel methods to control complex nuclear-spin systems coupled to the electron spin of an NV center in diamond, and used this for quantum sensing and quantum information processing applications. These well-controlled large spin systems may also form the building blocks of a large-scale quantum network. Here we give a summary of the results presented in the thesis organized by chapter.

- In **chapter 3**, we demonstrated a record-long coherence time of the NV center electron spin (1.5 seconds)—the longest coherence time for single electron spins in the solid state—by precise understanding of (and decoupling from) the interactions with individual ^{13}C nuclear spins and ^{13}C-^{13}C nuclear spin pairs in the environment.

- In **chapter 4**, we used the NV center as a single-spin quantum sensor to demonstrate atomic-scale magnetic resonance imaging of a cluster of 27 ^{13}C nuclear spins in diamond. This experiment provides a proof-of-principle towards the magnetic imaging of single molecules or complex spin structures, an outstanding goals in the field of quantum sensing.

- In **chapter 5**, we developed the NV center and its surrounding ^{13}C nuclear spin environment as a promising quantum register with exceptional coherence properties. We demonstrated a fully connected 10-qubit register with high-fidelity control, coherence times up to one minute, and genuine multipartite entanglement of up to 7 qubits.

- In **chapter 6**, we utilized multiple non-destructive parity measurements to demonstrate fault-tolerant encoding of a complete logical qubit. We showed that fault-tolerant encoding significantly outperforms non-fault-tolerant schemes. Afterwards, we demonstrated fault-tolerant manipulations of the logical qubits by applying a set of transversal (fault-tolerant) gates.

- In **chapter 7**, we introduced ^{13}C-^{13}C nuclear-spin pairs as novel qubits with extraordinary coherence properties. We demonstrated high-fidelity control, single-shot readout, and entanglement of these pairs. Furthermore, we demonstrated a record-long inhomogeneous dephasing time ($T_2^* = 1.9(3)$ minutes)—the longest reported for any individually controllable quantum system.

8.2. NEAR-TERM AVENUES AND PROJECTS

8.2.1. IMPROVED CONTROL OF THE NUCLEAR-SPIN QUBITS

To push the capabilities of this quantum system forward, enabling more complex protocols, it is important to overcome the dominant limitations for local operations in the quantum register. In particular, this performance is currently most limited by two-qubit gate fidelities, cross-talk between different qubits, and the slow logical gate blocks.

In chapter 4, we have already demonstrated the characterization and atomic-scale imaging of our quantum system and its spin environment with high accuracy, which already gives a compact way to describe the full system Hamiltonian. Therefore, this could—in principle—enable simulating this system with high accuracy. Such accurate simulations of the system could be used to develop optimal gate designs that take into account the rest of spin environment and mitigate their effects [1]. Furthermore, when making larger sequences that involve multiple gate operations (and echoes) on many qubits, cross-talk between the spins has a significant effect. One could use such simulations to find the optimal parameters to improve the performance of the whole sequence and to minimize these cross talks. For example, by designing echo sequences that minimize the effects of nuclear-nuclear couplings (see chapter 6).

Additionally, we have seen in chapter 5 that some of the two-qubit gates are mainly limited by a relatively short dephasing time (T_2^*) of the nuclear spins. This can be significantly enhanced by polarizing the other nuclear-spin with which they strongly couple. This can be done by the 'MBI' or 'swap' methods presented earlier or by using other techniques such as dynamic nuclear polarization [2]. Another approach would be to introduce novel two-qubit gate designs that protect both the electron and nuclear spins from decoherence using echoes (i.e., limited by T_2 for both electron and nuclear spins rather than T_2^*).

Another key challenge is that the time of the logical gate cycles are relatively long. This long time is mainly limited by the slow single- and two-qubit gate operations on the nuclear spins. Significant improvements are expected by using by using higher RF powers. However, this will require efficient ways to filter out the background noise from the RF amplifiers which is currently a significant limitation [3]. Additionally, a better method to deliver the RF signals to the sample without direct heating of the sample is required; for example, using an off-chip RF coil may be advantageous [4].

Another promising avenue is to develop gate schemes that can address multiple spins in parallel. For example, multi-tone RF pulses can be used to perform single-qubit rotations on multiple nuclear spins simultaneously. Additionally, the DDRF gate design presented in chapter 5 combined with multi-tone RF pulses might be adapted to perform parallel two-qubit gates, greatly speeding up operations.

8.2.2. MULTIPLE ROUNDS OF QUANTUM ERROR CORRECTION

Overcoming the limitations discussed in the previous section, a better encoding of the fault-tolerant logical qubits presented in chapter 6 can be realized. Additionally, the quality of the stabilizer measurements used for error syndrome extraction will be improved. Therefore, we expect to be able to run a full error-correction cycle on an encoded logical qubit, including active feedback [5], which can then be further extended by applying multiple rounds of error correction (see Fig. 8.1).

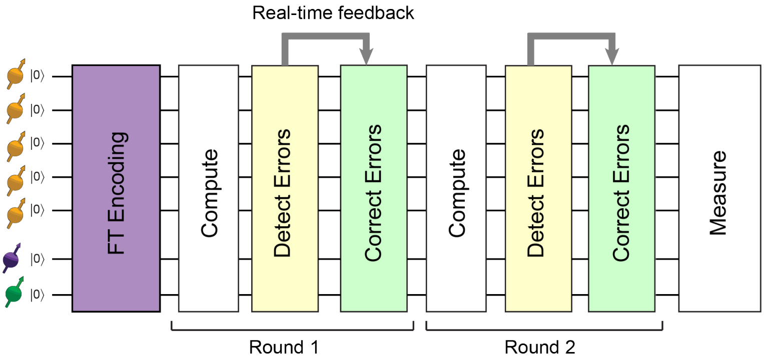

Figure 8.1: Towards active fault-tolerant quantum error correction of a continuously encoded logical qubit. After fault-tolerant encoding of a logical qubit, fault-tolerant operations or computations can be applied (compute). A full round of fault-tolerant error-syndrome measurements can then be applied to detect errors, which can be corrected through a real-time feedback process (via a classical control layer). Multiple rounds of computing, error detection, and error correction can be applied on the logically-encoded qubit.

Furthermore, the proposed improvements in control methods might lead to high-fidelity control of more qubits. This may enable exploring other error correction codes, such as Steane's [[7,1,3]] code with a flag [6], or the smallest fault-tolerant surface code [[9,1,3]] [7].

8.2.3. ATOMIC-SCALE IMAGING BEYOND 27 SPINS

The work presented in chapter 4 has enabled the atomic-scale imaging of a 27-nuclear-spin cluster in the vicinity of an NV center. Imaging more spins surrounding the NV center (i.e., inside the diamond) will enable yet more precise description of the system Hamiltonian and can also provide a resource for other applications such as quantum simulations (see section 8.2.4). Moreover, imaging larger and more complex structures will necessitate the development of more generalized control techniques as required for imaging samples outside the diamond.

In our previous work (chapter 4), the spectral range close to the ^{13}C Larmor frequencies was not studied extensively. We believe that the number of spins that can be detected and imaged can be significantly extended by careful systematic studies of this spectral range but also introducing completely new methods that enable to image more complex and larger systems. For example, by using dynamic nuclear polarization techniques, such as the PulsePol sequence [2, 8], more spins with weaker couplings to the NV electron spin could be initialized. Additionally, it might be possible to use well-controlled nuclear spins to polarize or readout other spins in their vicinity that are more difficult to directly control via the NV center.

Optimized sampling of the measurements and adaptive algorithms based on real-time structure analysis can further reduce the total number of required measurements [9, 10]. Additionally, we have recently introduced deep learning methods to efficiently analyze dynamical decoupling spectroscopy signals [11] and extract the hyperfine coupling parameters with high accuracy. These methods can be further explored to analyze the multi-dimensional spectroscopy data used for the imaging task [10, 12], which could lead to efficient analysis of even larger systems.

8.2.4. QUANTUM SIMULATIONS USING SPINS IN DIAMOND

Analog quantum simulators are special purpose quantum devices used to study certain physical phenomena or dynamics of particular system Hamiltonians. These devices would have the potential to unravel many important problems in physics, such as electron transport in magnetic materials, high-temperature superconductivity and out-of-equilibrium phases of matter [13]. These simulators have been demonstrated in several experimental platforms such as trapped atoms [14, 15] and ions [16], an ensemble of nitrogen-vacancy centers [17], superconducting qubits [18], and quantum dots [19, 20].

Our 27-nuclear-spin ^{13}C cluster provides a promising new platform for such quantum simulators [8]. The dipolar couplings between the ^{13}C nuclear spins naturally realise an interacting spin model. By using the hyperfine shift from the NV electron spin to separate the nuclear spin precession frequencies, flip-flops are strongly suppressed and the Hamiltonian becomes that of the Ising model [8]. It might be possible to use additional selective RF pulses to engineer different Hamiltonians, providing opportunities to study, for example, the ‘driven Ising model’: a periodic Floquet system that exhibits novel physical phenomena such as many body localisation and discrete time crystals [21, 22].

8.3. ATOMIC-SCALE IMAGING OF SAMPLES OUTSIDE DIAMOND

As discussed in chapter 4, magnetic resonance imaging (MRI) of individual molecules or complex spin structures is one of the exciting prospects in the field of quantum sensing [23–26]. Potential future applications include determination of protein structures and other biological samples [27, 28] but also imaging of solid-state systems such as two-dimensional materials [29, 30], accurate characterization of quantum information processing and quantum simulation systems [31–34]. While our work has demonstrated this capability on a model system of 27-nuclear-spin cluster in the vicinity of an NV center quantum sensor, the aim now is to extend this capability to samples outside the diamond.

There are a few challenges to address before such an ambitious goal can be achieved. First, to image samples outside the diamond, near-surface NV centers are needed. However, the properties of the NV centers degrades as they get closer to the surface [35]. This degradation shows up in both the coherence properties (due to paramagnetic surface spins) [35–37] and decreased fluorescence contrast (due to charge state dynamics of the NV center) [38]. These two factors limit the sensitivity of near-surface NV centers as quantum sensors [24, 28]. Recently, there has been a remarkable progress towards improving these coherence properties by using careful etching techniques [28] or by driving the paramagnetic surface environment [36, 37]; however surface engineering might remain important for nano- and atomic-scale sensing applications [38].

The second challenge is how to isolate the samples under study, which is more demanding in the case of single molecules or proteins. Promising techniques include embedding the molecules or the proteins in a spin-free matrix layer [33, 39] or to use immobilization techniques [33, 40]. It is noteworthy that the obtained spectral resolution will be generally limited by the coherence (i.e., linewidth) of the spins in the studied sample. In most cases this is mainly due to coupling to other spins in the environment [34, 41], which can be overcome by using homo- or hetero-nuclear decoupling techniques techniques that decouple the target spins from their environment [34, 41, 42].

The third challenge is to develop spectroscopy and imaging methods that efficiently retrieve the desired structure. What methods are best or most promising is a non-trivial discussion, because the methods might be heavily sample dependent. Promising experimental approaches are weak-measurement techniques [43, 44], two-dimensional spectroscopy methods [9, 10, 45, 46], double echo techniques [34, 47, 48], methods based on dynamic nuclear polarization [2, 43], methods that use reporter spins [49], or combinations thereof. Additionally, new data analysis methods are required to speed up the experimental acquisition and computational analysis, and to optimally extract the desired information. Here, progress has already been made in the form of machine learning based techniques [10–12], sparse sampling of multidimensional spectra [9, 50], and Bayesian inference methods [51]. Further exploration of such methods might lead to a more efficient analysis.

8.4. QUANTUM NETWORKS FOR DISTRIBUTED QUANTUM COMPUTING

Building large-scale quantum computers will ultimately require methods to increase the number of qubits to millions while being able to connect or entangle them. While integrating such a large number of qubits on one device or setup is a significant challenge for all existing experimental platforms, a promising path towards scaling is to take a modular approach. The key idea is to make modules comprising a smaller number of qubits which can be connected through a so-called quantum network to build a larger system [52**?** –56]. This approach is inherently scalable to large sizes by connecting many copies of independent modules, thus avoiding the challenges of a single large structure of ever increasing complexity. Recent theoretical proposal have shown that universal fault-tolerant quantum computations are possible over such a network [54, 55].

The key requirements for building such a quantum network are availability of the basic building module (a quantum register or a quantum node) with high fidelity local operations, well-isolated quantum memories that can be used to store quantum information while creating remote links, and an efficient interface with flying qubits (such as photons or phonons) to connect and entangle remote nodes. Some of these key elements have been demonstrated in a variety of platforms (trapped ions and atoms [57–61], quantum dots [62–64], superconducting qubits [65], optomechanical systems [66], and spins in diamond [3, 67–72].

The NV center in diamond is currently among the most advanced platforms to build such a networks [72, 73]. Deterministic entanglement delivery between distant network nodes has been demonstrated [67]. Moreover, control over nuclear-spins in the vicinity provides good quantum registers with high fidelity control [3, 71] as well as opportunity for well isolated memories [70]. This has led to the demonstration of some key network

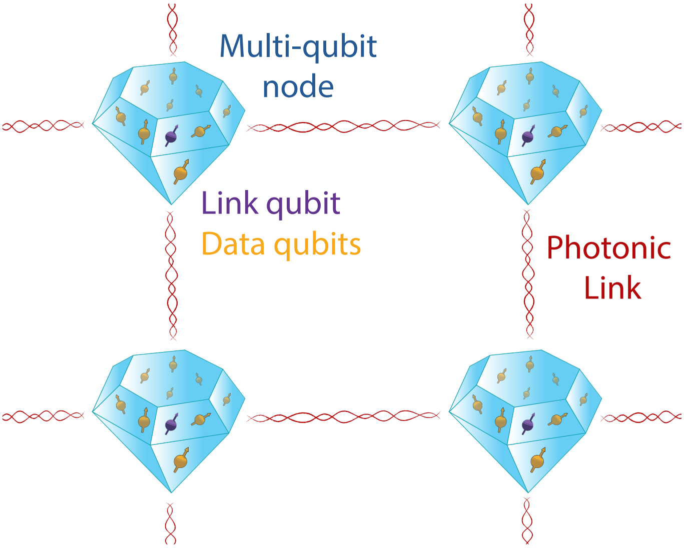

Figure 8.2: Towards distributed quantum computing with diamond quantum networks. Constructing quantum networks with optically active defect centers (such as the NV center in diamond) is a promising approach for large-scale distributed quantum computing. Such a network would consist of multiple nodes that each contain several qubits to store and process quantum states, and that are connected together through optical entanglement links based on photons. Figure credit: C. E. Bradley.

protocols such as quantum teleportation [74] and entanglement distillation [75].

Despite this remarkable progress, there are still some important challenges to overcome before a large scale quantum network can be created. First, the optical entanglement success rate is slow and mainly limited by the small fraction of emitted photons in the NV zero-phonon line [72]. This zero-phonon line emission can—in principle—be enhanced by coupling the NV center to an optical cavity [76–78]. Second, this entanglement generation process is probabilistic, which means that it has to be repeated several times until a successful entanglement between the remote nodes is created. However, during entanglement generation process, present nuclear-spin quantum network memories decohere at a faster rate than that at which entanglement is created. So, we have to find better methods to protect these memories during the entanglement generation process. In the next sections, we will discuss potential solutions.

8.4.1. ROBUST QUANTUM MEMORIES FOR ENTANGLEMENT GENERATION

A key open challenge is to develop quantum memories that can reliably store quantum states during the creation of an entanglement link to other parts in the network. As the entanglement generation process is probabilistic, the process has to be repeated several times until a link is created. Therefore, these quantum memories require long coherence times and excellent isolation from the rest of the system during these attempts. ^{13}C nuclear spins are good candidates for these memories as they have very long coherence times (chapter 5). However, due to the stochastic dynamics of the electron spin during the optical entanglement attempts and the hyperfine coupling—which depends on the electron spin state—the ^{13}C nuclear spins suffer from dephasing which often limits the useful number of entanglement attempts [70, 79].

A promising approach to overcome this challenge is to encode the quantum information in a decoherence-protected subspace of two or more nuclear spins to reduce the effective coupling strengths [70]. Our detailed characterization (chapter 4 can help find such nuclear-spin candidates that would be suitable for this task. Additionally, strongly coupled ^{13}C-^{13}C pairs studied and controlled throughout this thesis (chapters 3, 7) can serve as natural candidates for this task. For example, pairs A and B studied in chapter 7 could be excellent candidates for this as their evolution frequencies have a very small dependence on the electron spin state (< 2 Hz), and therefore they are expected to be very robust for entanglement generation attempts.

Another approach to achieve efficient quantum memories for entanglement is to use isotopically purified samples (i.e., ^{13}C concentration much less than the 1.1% natural abundance). For such samples, the coupling strengths between the NV electron spin and the controllable ^{13}C spins can be very small (< 100 Hz). These weakly coupled ^{13}C spins would therefore be more robust for entanglement generation attempts.

8.4.2. OPTICAL CAVITIES AND OTHER DEFECT CENTERS

As discussed earlier, one of the main challenges for building large-scale quantum networks using the NV center is that the optical entanglement rate is limited by the small fraction of coherent photons emitted (and collected) in the zero-phonon line [72]. This coherent photon emission can, in principle, be enhanced by coupling the NV center to an optical cavity, making use of the Purcell effect [78]. However, the challenge is that the NV center is not very well suited for integration with nanophotonic cavities because of the first order sensitivity of its optical properties to local charge fluctuations, resulting from its structural symmetry; this leads to high spectral diffusion of NV centers close to surfaces [80]. An alternative promising approach relies on coupling the NV centers embedded in microns-thin membranes to fiber-based free space cavities [76–78].

Alternatively, other defect centers that have more favourable optical properties and that are more compatible for integration with nanophotonic structures could be used [81, 82]. Promising candidates include negative and neutral charge state group IV color centers in diamond such as silicon-vacancy (SiV) centers in diamond [83–86], tin-vacancy centers in diamond [87], and Germanium-vacancy centers in diamond [88]; or defect centers in other materials such as silicon carbide [89]. The main challenge for these systems though is to combine the good optical properties with good spin properties, and to enable access to high-fidelity controllable quantum registers and memories. The recent progress, however, suggests that this might be possible [81, 82].

Importantly, the control methods developed in this thesis can likely be extended to these new defect centers. For example, one could use the atomic-scale imaging experiments to develop a good understanding of the nuclear-spin environment in these systems which may enable a well-controlled quantum register. Strongly coupled nuclear-spin pairs are also expected to surround such defects and those could be used as excellent memories during entanglement generation attempts.

REFERENCES

[1] P. Rembold, N. Oshnik, M. M. Müller, S. Montangero, T. Calarco, and E. Neu, *Introduction to quantum optimal control for quantum sensing with nitrogen-vacancy centers in diamond,* arXiv:2004.12119 (2020).

[2] I. Schwartz, J. Scheuer, B. Tratzmiller, S. Müller, Q. Chen, I. Dhand, Z.-Y. Wang, C. Müller, B. Naydenov, F. Jelezko, *et al.*, *Robust optical polarization of nuclear spin baths using hamiltonian engineering of nitrogen-vacancy center quantum dynamics,* Sci. Adv. **4**, eaat8978 (2018).

[3] C. E. Bradley, J. Randall, M. H. Abobeih, R. C. Berrevoets, M. J. Degen, M. A. Bakker, M. Markham, D. J. Twitchen, and T. H. Taminiau, *A ten-qubit solid-state spin register with quantum memory up to one minute,* Phys. Rev. X **9**, 031045 (2019).

[4] J. Zopes, K. S. Cujia, K. Sasaki, J. M. Boss, K. M. Itoh, and C. L. Degen, *Three-dimensional localization spectroscopy of individual nuclear spins with subangstrom resolution,* Nat. Commun. **9**, 4678 (2018).

[5] J. Cramer, N. Kalb, M. A. Rol, B. Hensen, M. S. Blok, M. Markham, D. J. Twitchen, R. Hanson, and T. H. Taminiau, *Repeated quantum error correction on a continuously encoded qubit by real-time feedback,* Nat. Commun. **7**, 11526 (2016).

[6] R. Chao and B. W. Reichardt, *Quantum error correction with only two extra qubits,* Phys. Rev. Lett. **121**, 050502 (2018).

[7] A. G. Fowler, M. Mariantoni, J. M. Martinis, and A. N. Cleland, *Surface codes: Towards practical large-scale quantum computation,* Phys. Rev. A **86**, 032324 (2012).

[8] F. van der Gronden, *Simulating many-body physics using nuclear spin qubits in diamond* (MSc Thesis, Delft, Delft University of Technology, 2020).

[9] M. Kost, J. Cai, and M. B. Plenio, *Resolving single molecule structures with nitrogen-vacancy centers in diamond,* Sci. Rep. **5**, 11007 (2015).

[10] X. Kong, L. Zhou, Z. Li, Z. Yang, B. Qiu, X. Wu, F. Shi, and J. Du, *Artificial intelligence enhanced two-dimensional nanoscale nuclear magnetic resonance spectroscopy,* npj Quantum Inf. **6**, 1 (2020).

[11] K. Jung, M. H. Abobeih, J. Yun, G. Kim, H. Oh, H. Ang, T. H. Taminiau, and D. Kim, *Deep learning enhanced individual nuclear-spin detection,* arXiv:2006.13478 (2020).

[12] N. Aharon, A. Rotem, L. P. McGuinness, F. Jelezko, A. Retzker, and Z. Ringel, *Nv center based nano-NMR enhanced by deep learning,* Sci. Rep. **9**, 1 (2019).

[13] J. I. Cirac and P. Zoller, *Goals and opportunities in quantum simulation,* Nat. Phys. **8**, 264 (2012).

[14] C. Gross and I. Bloch, *Quantum simulations with ultracold atoms in optical lattices,* Science **357**, 995 (2017).

[15] A. Browaeys and T. Lahaye, *Many-body physics with individually controlled rydberg atoms,* Nat. Phys. , 1 (2020).

[16] R. Blatt and C. F. Roos, *Quantum simulations with trapped ions,* Nat. Phys. **8**, 277 (2012).

[17] S. Choi, J. Choi, R. Landig, G. Kucsko, H. Zhou, J. Isoya, F. Jelezko, S. Onoda, H. Sumiya, V. Khemani, *et al.*, *Observation of discrete time-crystalline order in a disordered dipolar many-body system,* Nature **543**, 221 (2017).

[18] K. Xu, Z.-H. Sun, W. Liu, Y.-R. Zhang, H. Li, H. Dong, W. Ren, P. Zhang, F. Nori, D. Zheng, *et al.*, *Probing dynamical phase transitions with a superconducting quantum simulator,* Sci. Adv. **6**, eaba4935 (2020).

[19] T. Hensgens, T. Fujita, L. Janssen, X. Li, C. Van Diepen, C. Reichl, W. Wegscheider, S. D. Sarma, and L. M. Vandersypen, *Quantum simulation of a fermi–hubbard model using a semiconductor quantum dot array,* Nature **548**, 70 (2017).

[20] J. P. Dehollain, U. Mukhopadhyay, V. P. Michal, Y. Wang, B. Wunsch, C. Reichl, W. Wegscheider, M. S. Rudner, E. Demler, and L. M. Vandersypen, *Nagaoka ferromagnetism observed in a quantum dot plaquette,* Nature **579**, 528 (2020).

[21] V. Khemani, R. Moessner, and S. Sondhi, *A brief history of time crystals,* arXiv:1910.10745 (2019).

[22] D. V. Else, C. Monroe, C. Nayak, and N. Y. Yao, *Discrete time crystals,* Annu. Rev. Condens. Matter Phys. **11**, 467 (2020).

[23] R. Schirhagl, K. Chang, M. Loretz, and C. L. Degen, *Nitrogen-vacancy centers in diamond: nanoscale sensors for physics and biology,* Annu. Rev. Phys. Chem. **65**, 83 (2014).

[24] C. L. Degen, F. Reinhard, and P. Cappellaro, *Quantum sensing,* Rev. Mod. Phys. **89**, 035002 (2017).

[25] C. Degen, M. Poggio, H. Mamin, C. Rettner, and D. Rugar, *Nanoscale magnetic resonance imaging,* Proc. Natl. Acad. Sci. **106**, 1313 (2009).

[26] V. P. Bhallamudi and P. C. Hammel, *Nitrogen–vacancy centres: Nanoscale MRI,* Nat. Nanotechnol. **10**, 104 (2015).

[27] F. Shi, Q. Zhang, P. Wang, H. Sun, J. Wang, X. Rong, M. Chen, C. Ju, F. Reinhard, H. Chen, *et al.*, *Single-protein spin resonance spectroscopy under ambient conditions,* Science **347**, 1135 (2015).

[28] I. Lovchinsky, A. O. Sushkov, E. Urbach, N. P. de Leon, S. Choi, K. De Greve, R. Evans, R. Gertner, E. Bersin, Müller, *et al.*, *Nuclear magnetic resonance detection and spectroscopy of single proteins using quantum logic,* Science **351**, 836 (2016).

[29] I. Lovchinsky, J. Sanchez-Yamagishi, E. Urbach, S. Choi, S. Fang, T. Andersen, K. Watanabe, T. Taniguchi, A. Bylinskii, E. Kaxiras, *et al.*, *Magnetic resonance spectroscopy of an atomically thin material using a single-spin qubit,* Science **355**, 503 (2017).

[30] M. J. Ku, T. X. Zhou, Q. Li, Y. J. Shin, J. K. Shi, C. Burch, L. E. Anderson, A. T. Pierce, Y. Xie, A. Hamo, *et al.*, *Imaging viscous flow of the dirac fluid in graphene,* Nature **583**, 537 (2020).

[31] Z.-Y. Wang, J. F. Haase, J. Casanova, and M. B. Plenio, *Positioning nuclear spins in interacting clusters for quantum technologies and bioimaging,* Phys. Rev. B **93**, 174104 (2016).

[32] J. Cai, A. Retzker, F. Jelezko, and M. B. Plenio, *A large-scale quantum simulator on a diamond surface at room temperature,* Nat. Phys. **9**, 168 (2013).

[33] J. Zopes, K. Herb, K. Cujia, and C. Degen, *Three-dimensional nuclear spin positioning using coherent radio-frequency control,* Phys. Rev. Lett. **121**, 170801 (2018).

[34] M. H. Abobeih, J. Randall, C. E. Bradley, H. P. Bartling, M. A. Bakker, M. J. Degen, M. Markham, D. J. Twitchen, and T. H. Taminiau, *Atomic-scale imaging of a 27-nuclear-spin cluster using a quantum sensor,* Nature **576**, 411 (2019).

[35] T. Rosskopf, A. Dussaux, K. Ohashi, M. Loretz, R. Schirhagl, H. Watanabe, S. Shikata, K. M. Itoh, and C. Degen, *Investigation of surface magnetic noise by shallow spins in diamond,* Phys. Rev. lett. **112**, 147602 (2014).

[36] D. Bluvstein, Z. Zhang, C. A. McLellan, N. R. Williams, and A. C. B. Jayich, *Extending the quantum coherence of a near-surface qubit by coherently driving the paramagnetic surface environment,* Phys. Rev. Lett. **123**, 146804 (2019).

[37] S. Sangtawesin, B. L. Dwyer, S. Srinivasan, J. J. Allred, L. V. Rodgers, K. De Greve, A. Stacey, N. Dontschuk, K. M. O'Donnell, D. Hu, *et al.*, *Origins of diamond surface noise probed by correlating single-spin measurements with surface spectroscopy,* Phys. Rev. X **9**, 031052 (2019).

[38] Z. Yuan, M. Fitzpatrick, L. V. Rodgers, S. Sangtawesin, S. Srinivasan, and N. P. de Leon, *Charge state dynamics and optically detected electron spin resonance contrast of shallow nitrogen-vacancy centers in diamond,* arXiv:2005.01142 (2020).

[39] H. J. Mamin, M. H. Sherwood, and D. Rugar, *Detecting external electron spins using nitrogen-vacancy centers,* Phys. Rev. B **86**, 195422 (2012).

[40] A. Sushkov, N. Chisholm, I. Lovchinsky, M. Kubo, P. Lo, S. Bennett, D. Hunger, A. Akimov, R. L. Walsworth, H. Park, *et al.*, *All-optical sensing of a single-molecule electron spin,* Nano lett. **14**, 6443 (2014).

[41] N. Aslam, M. Pfender, P. Neumann, R. Reuter, A. Zappe, F. Fávaro de Oliveira, A. Denisenko, H. Sumiya, S. Onoda, J. Isoya, and J. Wrachtrup, *Nanoscale nuclear magnetic resonance with chemical resolution,* Science **357**, 67 (2017).

[42] A. Ajoy, U. Bissbort, M. D. Lukin, R. L. Walsworth, and P. Cappellaro, *Atomic-scale nuclear spin imaging using quantum-assisted sensors in diamond,* Phys. Rev. X **5**, 011001 (2015).

[43] K. Cujia, J. Boss, K. Herb, J. Zopes, and C. Degen, *Tracking the precession of single nuclear spins by weak measurements,* Nature **571**, 230– (2019).

[44] M. Pfender, P. Wang, H. Sumiya, S. Onoda, W. Yang, D. B. R. Dasari, P. Neumann, X.-Y. Pan, J. Isoya, R.-B. Liu, *et al.*, *High-resolution spectroscopy of single nuclear spins via sequential weak measurements,* Nat. Commun. **10**, 594 (2019).

[45] J. Smits, J. T. Damron, P. Kehayias, A. F. McDowell, N. Mosavian, I. Fescenko, N. Ristoff, A. Laraoui, A. Jarmola, and V. M. Acosta, *Two-dimensional nuclear magnetic resonance spectroscopy with a microfluidic diamond quantum sensor,* Sci. Adv. **5**, eaaw7895 (2019).

[46] Z. Yang, X. Kong, Z. Li, K. Yang, P. Yu, P. Wang, Y. Wang, X. Qin, X. Rong, C.-K. Duan, *et al.*, *Structural analysis of nuclear spin clusters via 2D nanoscale nuclear magnetic resonance spectroscopy,* Adv. Quantum Technol. **3**, 1900136 (2020).

[47] P. London, J. Scheuer, J.-M. Cai, I. Schwarz, A. Retzker, M. B. Plenio, M. Katagiri, T. Teraji, S. Koizumi, J. Isoya, R. Fischer, L. P. McGuinness, B. Naydenov, and F. Jelezko, *Detecting and polarizing nuclear spins with double resonance on a single electron spin,* Physical Review Letters **111**, 067601 (2013).

[48] E. L. Rosenfeld, L. M. Pham, M. D. Lukin, and R. L. Walsworth, *Sensing coherent dynamics of electronic spin clusters in solids,* Phys. Rev. Lett. **120**, 243604 (2018).

[49] A. Sushkov, I. Lovchinsky, N. Chisholm, R. L. Walsworth, H. Park, and M. D. Lukin, *Magnetic resonance detection of individual proton spins using quantum reporters,* Phys. Rev. Lett. **113**, 197601 (2014).

[50] M. Mobli, M. W. Maciejewski, A. D. Schuyler, A. S. Stern, and J. C. Hoch, *Sparse sampling methods in multidimensional NMR,* Phys. Chem. Chem. Phys. **14**, 10835 (2012).

[51] I. Schwartz, J. Rosskopf, S. Schmitt, B. Tratzmiller, Q. Chen, L. P. McGuinness, F. Jelezko, and M. B. Plenio, *Blueprint for nanoscale NMR,* Sci. Rep. **9**, 1 (2019).

[52] H. J. Kimble, *The quantum internet,* Nature **453**, 1023 (2008).

[53] R. Van Meter and S. J. Devitt, *The path to scalable distributed quantum computing,* Computer **49**, 31 (2016).

[54] N. H. Nickerson, Y. Li, and S. C. Benjamin, *Topological quantum computing with a very noisy network and local error rates approaching one percent,* Nat. Commun. **4**, 1756 (2013).

[55] N. H. Nickerson, J. F. Fitzsimons, and S. C. Benjamin, *Freely scalable quantum technologies using cells of 5-to-50 qubits with very lossy and noisy photonic links,* Phys. Rev. X **4**, 041041 (2014).

[56] L. Vandersypen, H. Bluhm, J. Clarke, A. Dzurak, R. Ishihara, A. Morello, D. Reilly, L. Schreiber, and M. Veldhorst, *Interfacing spin qubits in quantum dots and donors—hot, dense, and coherent,* npj Quantum Inf. **3**, 1 (2017).

[57] D. L. Moehring, P. Maunz, S. Olmschenk, K. C. Younge, D. N. Matsukevich, L.-M. Duan, and C. Monroe, *Entanglement of single-atom quantum bits at a distance,* Nature **449**, 68 (2007).

[58] D. Hucul, I. V. Inlek, G. Vittorini, C. Crocker, S. Debnath, S. M. Clark, and C. Monroe, *Modular entanglement of atomic qubits using photons and phonons,* Nat. Phys. **11**, 37 (2015).

[59] I. V. Inlek, C. Crocker, M. Lichtman, K. Sosnova, and C. Monroe, *Multispecies trapped-ion node for quantum networking,* Phys. Rev. Lett. **118**, 250502 (2017).

[60] J. Hofmann, M. Krug, N. Ortegel, L. Gérard, M. Weber, W. Rosenfeld, and H. Weinfurter, *Heralded entanglement between widely separated atoms,* Science **337**, 72 (2012).

[61] W. Rosenfeld, D. Burchardt, R. Garthoff, K. Redeker, N. Ortegel, M. Rau, and H. Weinfurter, *Event-ready bell test using entangled atoms simultaneously closing detection and locality loopholes,* Phys. Rev. Lett. **119**, 010402 (2017).

[62] A. Delteil, Z. Sun, W.-b. Gao, E. Togan, S. Faelt, and A. Imamoğlu, *Generation of heralded entanglement between distant hole spins,* Nat. Phys. **12**, 218 (2016).

[63] N. Samkharadze, G. Zheng, N. Kalhor, D. Brousse, A. Sammak, U. Mendes, A. Blais, G. Scappucci, and L. Vandersypen, *Strong spin-photon coupling in silicon,* Science **359**, 1123 (2018).

[64] F. Borjans, X. Croot, X. Mi, M. Gullans, and J. Petta, *Resonant microwave-mediated interactions between distant electron spins,* Nature **577**, 195 (2020).

[65] A. Narla, S. Shankar, M. Hatridge, Z. Leghtas, K. M. Sliwa, E. Zalys-Geller, S. O. Mundhada, W. Pfaff, L. Frunzio, R. J. Schoelkopf, *et al.*, *Robust concurrent remote entanglement between two superconducting qubits,* Phys. Rev. X **6**, 031036 (2016).

[66] R. Riedinger, A. Wallucks, I. Marinković, C. Löschnauer, M. Aspelmeyer, S. Hong, and S. Gröblacher, *Remote quantum entanglement between two micromechanical oscillators,* Nature **556**, 473 (2018).

[67] H. Bernien, B. Hensen, W. Pfaff, G. Koolstra, M. S. Blok, L. Robledo, T. H. Taminiau, M. Markham, D. J. Twitchen, L. Childress, and R. Hanson, *Heralded entanglement between solid-state qubits separated by three metres,* Nature **497**, 86 (2013).

[68] P. C. Humphreys, N. Kalb, J. P. Morits, R. N. Schouten, R. F. Vermeulen, D. J. Twitchen, M. Markham, and R. Hanson, *Deterministic delivery of remote entanglement on a quantum network,* Nature **558**, 268 (2018).

[69] B. Hensen, H. Bernien, A. E. Dréau, A. Reiserer, N. Kalb, M. S. Blok, J. Ruitenberg, R. F. Vermeulen, R. N. Schouten, C. Abellán, *et al.*, *Loophole-free bell inequality violation using electron spins separated by 1.3 kilometres,* Nature **526**, 682 (2015).

[70] A. Reiserer, N. Kalb, M. S. Blok, K. J. M. van Bemmelen, T. H. Taminiau, R. Hanson, D. J. Twitchen, and M. Markham, *Robust quantum-network memory using decoherence-protected subspaces of nuclear spins,* Phys. Rev. X **6**, 021040 (2016).

[71] T. H. Taminiau, J. Cramer, T. van der Sar, V. V. Dobrovitski, and R. Hanson, *Universal control and error correction in multi-qubit spin registers in diamond,* Nat. Nanotech. **9**, 171 (2014).

[72] D. D. Awschalom, R. Hanson, J. Wrachtrup, and B. B. Zhou, *Quantum technologies with optically interfaced solid-state spins,* Nat. Photonics **12**, 516 (2018).

[73] W. B. Gao, A. Imamoglu, H. Bernien, and R. Hanson, *Coherent manipulation, measurement and entanglement of individual solid-state spins using optical fields,* Nat. Photon. **9**, 363 (2015).

[74] W. Pfaff, B. J. Hensen, H. Bernien, S. B. v. Dam, M. S. Blok, T. H. Taminiau, M. J. Tiggelman, R. N. Schouten, M. Markham, D. J. Twitchen, and R. Hanson, *Unconditional quantum teleportation between distant solid-state quantum bits,* Science **345**, 532 (2014).

[75] N. Kalb, A. A. Reiserer, P. C. Humphreys, J. J. W. Bakermans, S. J. Kamerling, N. H. Nickerson, S. C. Benjamin, D. J. Twitchen, M. Markham, and R. Hanson, *Entanglement distillation between solid-state quantum network nodes,* Science **356**, 928 (2017).

[76] D. Riedel, I. Söllner, B. J. Shields, S. Starosielec, P. Appel, E. Neu, P. Maletinsky, and R. J. Warburton, *Deterministic enhancement of coherent photon generation from a nitrogen-vacancy center in ultrapure diamond,* Phys. Rev. X **7**, 031040 (2017).

[77] M. Ruf, M. J. Weaver, S. B. van Dam, and R. Hanson, *Resonant excitation and Purcell enhancement of coherent nitrogen-vacancy centers coupled to a Fabry-Pérot microcavity,* arXiv:2009.08204 (2020).

[78] E. Janitz, M. K. Bhaskar, and L. Childress, *Cavity quantum electrodynamics with color centers in diamond,* Optica **7**, 1232 (2020).

[79] N. Kalb, P. C. Humphreys, J. J. Slim, and R. Hanson, *Dephasing mechanisms of diamond-based nuclear-spin memories for quantum networks,* Phys. Rev. A **97**, 062330 (2018).

[80] A. Faraon, C. Santori, Z. Huang, V. M. Acosta, and R. G. Beausoleil, *Coupling of nitrogen-vacancy centers to photonic crystal cavities in monocrystalline diamond,* Phys. Rev. Lett. **109**, 033604 (2012).

[81] L. C. Bassett, A. Alkauskas, A. L. Exarhos, and K.-M. C. Fu, *Quantum defects by design,* Nanophotonics **8**, 1867 (2019).

[82] M. Atatüre, D. Englund, N. Vamivakas, S.-Y. Lee, and J. Wrachtrup, *Material platforms for spin-based photonic quantum technologies,* Nat. Rev. Mater. **3**, 38 (2018).

[83] B. Pingault, D.-D. Jarausch, C. Hepp, L. Klintberg, J. N. Becker, M. Markham, C. Becher, and M. Atatüre, *Coherent control of the silicon-vacancy spin in diamond,* Nat. Commun. **8**, 15579 (2017).

[84] A. Sipahigil, R. E. Evans, D. D. Sukachev, M. J. Burek, J. Borregaard, M. K. Bhaskar, C. T. Nguyen, J. L. Pacheco, H. A. Atikian, C. Meuwly, *et al.*, *An integrated diamond nanophotonics platform for quantum-optical networks,* Science **354**, 847 (2016).

[85] D. D. Sukachev, A. Sipahigil, C. T. Nguyen, M. K. Bhaskar, R. E. Evans, F. Jelezko, and M. D. Lukin, *Silicon-vacancy spin qubit in diamond: a quantum memory exceeding 10 ms with single-shot state readout,* Phys. Rev. Lett. **119**, 223602 (2017).

[86] C. Nguyen, D. Sukachev, M. Bhaskar, B. Machielse, D. Levonian, E. Knall, P. Stroganov, R. Riedinger, H. Park, M. Lončar, *et al.*, *Quantum network nodes based on diamond qubits with an efficient nanophotonic interface,* Phys. Rev. Lett. **123**, 183602 (2019).

[87] T. Iwasaki, Y. Miyamoto, T. Taniguchi, P. Siyushev, M. H. Metsch, F. Jelezko, and M. Hatano, *Tin-vacancy quantum emitters in diamond,* Phys. Rev. Lett. **119**, 253601 (2017).

[88] M. K. Bhaskar, D. D. Sukachev, A. Sipahigil, R. E. Evans, M. J. Burek, C. T. Nguyen, L. J. Rogers, P. Siyushev, M. H. Metsch, H. Park, *et al.*, *Quantum nonlinear optics with a germanium-vacancy color center in a nanoscale diamond waveguide,* Phys. Rev. Lett. **118**, 223603 (2017).

[89] N. T. Son, C. P. Anderson, A. Bourassa, K. C. Miao, C. Babin, M. Widmann, M. Niethammer, J. Ul Hassan, N. Morioka, I. G. Ivanov, *et al.*, *Developing silicon carbide for quantum spintronics,* Appl. Phys. Lett. **116**, 190501 (2020).

ACKNOWLEDGEMENTS

Over the past four years, I have had the pleasure to work with many talented and friendly people. It is really those people who made the work in this thesis possible. I am also grateful that I have worked in such a stimulating place as QuTech, this environment really made this adventure fun.

First, I would like to thank my supervisor **Tim Taminiau** for all his support and guidance throughout my PhD. Tim, you are a great supervisor and I believe that I was lucky to work with you. You are also a great and patient teacher. I have learned many things from you during my PhD, but most importantly: to be very critical of our own work and to always keep very high standards. Thank you for all the detailed feedback and suggestions. You are always approachable and it is always fun to come by to have random discussions with you; many times this ended up with great ideas. Thank you for everything! **Ronald**, thank you for being my promotor. I really appreciate all your advice, discussions, and support over the last four years. It was also fun to work with you on teaching Kwantum II. I would also like to thank you for the spirit that you brought to team Diamond (as the founder) and to QuTech (as a director), and for making Delft such a special place in Diamond research.

Slava, thank you for all the nice discussions that we had over these years. I must say that I have learned a lot from you in different subjects: from languages, religion, politics, life, and of course science. Many thanks for your sincere career advice. Slava, you know that I will always remember many quotes from you: "Go make a miracle for yourself"; "Habibi, I told you, you will hit the wall"; "You can never finish improvements, you can only stop them" ... and many others. **Barbara**, thank you for your help with the error correction project. It was great to collaborate with you, and I look forward to finalizing this project together. I would also like to thank all the committee members (**Lieven, Gary, Christian, Martin, Servaas**) for evaluating this thesis and for taking part in the defense ceremony.

Team Diamond, both Tim's and Ronald's groups, is a special group of people. From the first moment I visited for my PhD application, I knew that it would be fun to work with these guys. **Maarten or Maaaarta**, my PhD buddy, and thug life companion. We started our PhDs almost together and we are almost finishing together; it was fun to share this journey with you. Although our paths were not always the same, we always had fun discussing things and sometimes complaining about work or life. Maarten, you know what to do next: go and make a quantum startup and you already know in what ;) - And as you will always say: see you in another life :) **Joe or Dr. Chips**, thank you very much for all the hard and fantastic work that you put into this thesis, I really can't express this in words. It was really fun to work with you on so many projects, but the imaging work will always remain special. Also thanks to you and **Lucy** for the cover design. I wish you guys all the best for your future. **Conor**, it was always fun to work and discuss with you, it was also lovely to share the office with you for the last couple of years; we always had fun discussing so many things about science, other people's work, future of quantum and so on. I always like to listen to your opinion or perspective regarding many things, and of course thanks for all the proof reading; I always like your suggestions. Thanks for everything, and for being such a nice and caring person, and good luck with the last few months of your PhD; and who knows maybe our paths will cross again ;)

I also had the honor to supervise **Hans** and **Sjoerd** during their master's projects. Guys, I learned a lot from you during your projects and really enjoyed working with you. It was also fun to train you on the setup or to try to explain things to you: this certainly helped me understand things better. You know that I will always be proud that you gave me a perfect record (so far) as a recruiter for new PhDs with Tim. Hans, It was fun to see the pairs project going so far. I am sure you will continue to do great work in this direction. Sjoerd, I always admire your organization skills, and that you always pay attention to the very small details. I can't forget you sitting in the lab for hours trying to follow the path of each wire going to the ADwin and the AWG. Good luck studying defects in SiC, and I am sure you will have a great PhD.

Julia, thank you for all your help at the beginning of my PhD. It was really fun to work with you for this short period. I admire your enthusiasm for science communication, and wish you all the best for your career. And thank you for the fantastic Diamond dinner at your place. **Yang**, I enjoyed working with you on the error correction project, and I hope we get this done soon. **Martin**, thanks for all the help with the setup, I'm glad you enjoyed your trip to Egypt! **Valeria**, it was really nice having you here, we were making a good new PhDs team with Maarten and Stephan. I am sorry that you didn't continue, but you know you did the right thing. **Sophie**, it was great to share the office with you. I am glad that your 3-node experiment went well, and good luck with the rest of your PhD. **Guido**, I like your enthusiasm for science in general and the imaging project in particular, and good luck pushing this to the limits. **Damian**, it is great to have you in our group and good luck with Guido in the imaging project. It was nice to share the office with you for that short period. **Nico, Asier**, good luck with your master's projects. **Aletta**, it was nice to have you as a master student in our group, also thanks for your help with the science story, and good luck with your career in outreach. **Floris, Remon**, it was great having you in our group and good luck with your future. **Ben**, I am glad that I got to know you even though it was a very short period, it was also fun to discuss the pairs physics with you.

Arian, I always like to hear your speculations or opinions about different topics (including pandemics). It was also fun to discuss my propositions with you. Thank you for the work you did during your master's, it was certainly helpful for my PhD. And I hope you will manage to entangle Delft and The Hague soon. **Kian**, thank you for organizing the QuTech Thuisje, and for showing me the "secret" button of the coffee machine. I am sure that you and Arian will make the demonstrator project a big success. **Matteo Sr.**, Thank you for the nice Italian pasta and the nice gatherings at your place. And congratulations on the 3-node entanglement, fantastic work. **Simon**, it was really nice having you here, you are such a kind person and it is always fun to discuss with you. And good luck with starting your group: I am sure you are going be a great group leader. **Max**, the cavities expert, I really admire your team management skills, and I think this really made the cavity project possible. Thank you for moderating the diamond journal club over the last years, and good luck with the final steps in your PhD. **Dr. Hans B.**, I really admire what you did, studying medicine and physics simultaneously doesn't seem like a piece of cake, but you did it, and you did very well in both. I am happy that you came back as a PhD student in physics and good luck with your future. **Matteo Jr.**, good luck with tin-vacancy project! **Matthew**, it was great to have you here, and I will always remember our canceled Denver March meeting. **Lorenzo**, it was nice to overlap with you for this short period. **Nina, Yanik, Nicolas**, I wish you all the best with your PhDs.

Norbert, I really admire your efficiency and the number of projects you worked on, and I am glad that you are happy with Google AI. And thank you for your help, it was always fun to discuss and learn from you. **Suzanne**, It was nice to share the office with you, sharing with you the hard times of writing your thesis. It was always fun to see your positive attitude towards things and your enthusiasm for both science and running. **Peter**, you were always a fun and positive person, thank you for your help in debugging when I started. I admire that you made a career shift and I am happy that you are enjoying your work with DeepMind. **Stefan**, it was a pleasure to know you closer, such a nice and caring person. Also thanks for all your advice, and I wish you all the best with Google X. **Bas**, thanks for your help with the ADwin and for introducing me to the Kavli football team. It was nice to see you come back to Delft, and good luck with your future. **Kamiel, Laura, Annick, Thomas, Anna, Anais, Lisanne, Romy, Jesse, Jaco, Jacob, Madelaine, Wouter**, thank you for the fun you brought to our teams. **Marie-Christine**, it was nice to see you coming back to Delft, good luck with your postdoc. **Takashi**, it is always nice to see your fancy grown diamonds.

Outside Team Diamond, there are many people in QuTech that contributed to the fun during this adventure. **Stephan**, you were part of our new PhDs team and it was enjoyable to go running or cooking with you, but also doing the quantum information homework together. We also found the first Egyptian restaurant in Rotterdam together during a random cycle. **Jelmer**, It was fun to share the office for you from day 1 in my PhD until the day you graduated. I hope you enjoy your work at ASML. **Dr. Josh**, it was fun to talk to you about random things, and thank you for the propositions discussion. **Raymond's**, thank you both for all the technical support over the years. **Guoji, Luca, Adriaan, Anne-Marije, Sjaak, Chien, Will, Delphine, Sergey, Kaushik, Tanmoy, Sara, Francesco, Tim, Jake, Mohammad, Gertjan, Hridya, Christian, Floor, Ramiro, Thijs, Xiao, Walter, Oriol, Alessandro, Giordano, Leo, Toeno**, thank you all. **Marja, Chantal** thank you for all the administrative support over the years. **Clara**, thank you for organizing the ICFOnians' gathering in Delft and for your suggestions with the 3D-model design. I am happy that Samuel is no longer scared of me.

There are also some special people that not only entertain you during work but also outside – the QFA team: **Mohsen, Gustavo, Jorge, Anta, Mariyeh, Monique, Cisilia, and Andreia**. You guys were not just colleagues or friends; you were my family here. I think I can't thank you enough for all that you did and for all the fun we had over the years, so let's keep it short. Special thanks to the old Egyptian gang in Delft: **Orabi, Ghandour, Nasr, Yomna, Elham, Marmar, Aya, Tarek, Mostafa, Essam, Bassem, Ghonim, Sharaf, Ragab**. All our gatherings in Mina, dinners, BBQ's, watching movies or football games; it was really fun and I never really felt homesick because of having you around; I shall never forget these days. The new Egyptian/Arabic gang: **Hany, Saad, Fathi, Abdulqader, Muath, Marouen, Abdullah, Motasem, Khobayb, Kadim, Abid, Yasser, Said**, you basically made me survive the second half of my PhD, including going through the last tough year and the Pandemic. Thanks to all of you, we made it through these hard times together. It was always nice to have our PlayStation nights or dinners. **Hany**, I can't thank you enough for what you did over the last period. It was certainly fun to share the flat with you for the last year, it certainly made this 'lockdown' time a bit easier. It was fun to cook together, to watch movies, or to play video-games and of course to make the big weekend gatherings. Good luck with the surface 17 experiment: I am sure you and Jorge will nail it. Special thanks to my dear friends **Osama, Haitham, Ismail, Mahgoub, Doha, Sulaimon, Yaser, karimAllah, Gamal, Ahmed Ashraf, Elmikaty, Amir** for their support over the years.

At the end, I would like to thank my family for their endless and unconditional support. My cousins **Ahmed Saad, Amr, Mahmoud, Ahmed Reda, Yomna, Rasha**; my beloved brothers **Mahmoud, Ali and Abdulrahman**; and my parents **Hamed and Nagah**. You know that I would have never been here without your endless support, love, and prayers.

Mohamed Abobeih
Delft, December 2020

LIST OF PUBLICATIONS

7. *Fault-tolerant encoding and manipulations of a complete logical qubit.*
   M. H. Abobeih, Y. Wang, J. Randall, S. J. H. Loenen, C. E. Bradley, B. M. Terhal, T. H. Taminiau,
   In preparation, tentative title.

6. *Entanglement of intrinsically coherence-protected solid-state spin pairs.*
   H. P. Bartling, **M. H. Abobeih**, B. Pingault, M. J. Degen, S. J. H. Loenen, C. E. Bradley, J. Randall, M. Markham, D. J. Twitchen, T. H. Taminiau,
   In preparation, tentative title.

5. *Deep learning enhanced individual nuclear spin detection.*
   K. Jung*, **M. H. Abobeih***, J. Yun, G. Kim, H. Oh, H. Ang, T. H. Taminiau, D. Kim,
   arXiv:2006.13478 (2020).

4. *Algorithmic decomposition for efficient multiple nuclear spin detection in diamond.*
   H. Oh*, J. Yun*, **M. H. Abobeih**, K. Jung, K. Kim, T. H. Taminiau, D. Kim,
   Scientific Reports **10**, 14884 (2020).

3. *A ten-qubit solid-state spin register with quantum memory up to one minute.*
   C. E. Bradley*, J. Randall*, **M. H. Abobeih**, R. C. Berrevoets, M. J. Degen, M. A. Bakker, M. Markham, D. J. Twitchen, T. H. Taminiau,
   Physical Review X **9**, 031045 (2019). Highlighted in Physical Review X and Nature.

2. *Atomic-scale imaging of a 27-nuclear-spin cluster using a quantum sensor.*
   M. H. Abobeih, J. Randall, C. E. Bradley, H. P. Bartling, M. A. Bakker, M. J. Degen, M. Markham, D. J. Twitchen, T. H. Taminiau,
   Nature **576**,7787 (2019). The 2020 Kavli Delft Publication Prize.

1. *One-second coherence for a single electron spin coupled to a multi-qubit nuclear spin environment.*
   M. H. Abobeih, J. Cramer, M. A. Bakker, N. Kalb, M. Markham, D. J. Twitchen, T. H. Taminiau,
   Nature Communications **9**, 2552 (2018).

---

*Equally contributing authors

CURRICULUM VITÆ

Mohamed ABOBEIH

01/10/1989	Born in Dakahliya, Egypt
09/2006–07/2011	B.Sc. in Electronics and Communications Engineering (with honors), Mansoura University, Egypt
01/2012–03/2013	Military service
10/2013–10/2015	M.Sc. in Optics and Photonics (with distinction) Europhotonics Erasmus Mundus Master's Course 10/2013 – 03/2014: Aix-Marseille University, France 04/2014 – 10/2014: Karlsruhe Institute of Technology, Germany 10/2014 – 10/2015: Universities of Barcelona (UPC, UAB, UB) and The Institute of Photonics Sciences (ICFO), Spain Thesis: Optomechanics with levitating nitrogen-vacancy centers Supervisors: Prof. Romain Quidant & Prof. Martin Wegener
07/2016–01/2021	PhD researcher, Delft University of Technology Thesis: From atomic-scale imaging to quantum fault-tolerance with spins in diamond Group: Taminiau Lab, QuTech and Kavli Institute of Nanoscience Promotor: Prof. dr. ir. Ronald Hanson Co-promotor: Dr. ir. Tim H. Taminiau